UNIVERSITY OF COPENHAGEN
FACULTY OF SCIENCE

Master's Thesis

A Study of Diffractive Scattering with the ATLAS and ALFA Experiment

Alexander Pedersen Lind

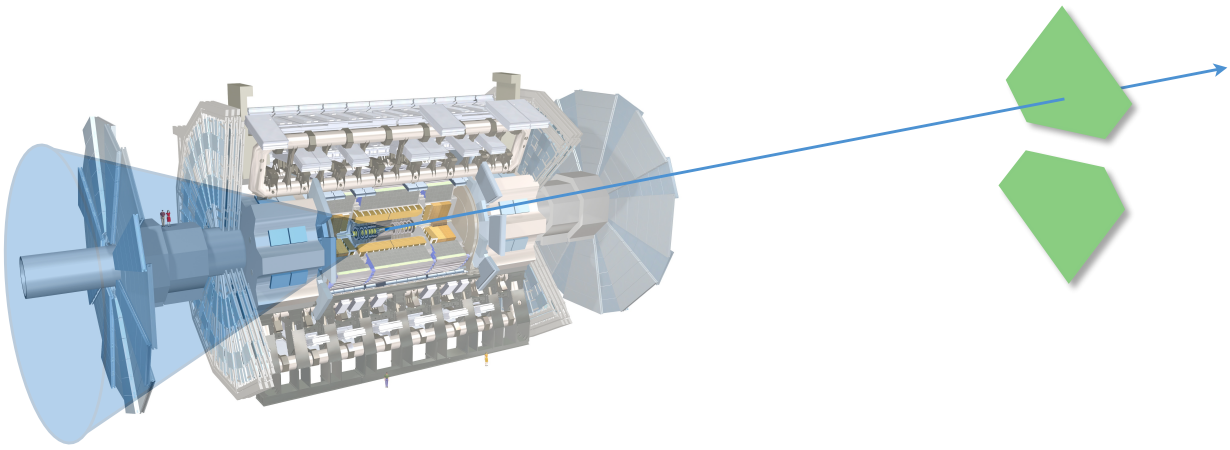

Supervisor: Jørgen Beck Hansen

21 June, 2017

Alexander Pedersen Lind
A Study of Diffractive Scattering with the ATLAS and ALFA Experiment
MSc Thesis, Niels Bohr Institute, University of Copenhagen

SUPERVISOR:
Dr. Jørgen Beck Hansen
Niels Bohr Institute, University of Copenhagen

Typeset using pdfLaTeX with the `classicthesis` package.
Cover art: illustration of the final-state of a single diffractive event with a signal in ATLAS and ALFA (not to scale). Image of ATLAS detector from `[CERN-GE-0803012-02]`, ATLAS Experiment © 2017 CERN.

Thesis submitted on 21 June 2017 for the completion of the degree of Master of Science (MSc) in Physics at the Niels Bohr Institute, University of Copenhagen.

DISCLAIMER: Some of the results and plots presented in this thesis are based on official Run 2 data recorded at the ATLAS experiment in 2015. These are the product of the author's own work and have *not* been officially approved by the ATLAS Collaboration. They are therefore labelled as "Work in Progress" and any replication of these results should clearly reflect this fact.

ABSTRACT

This thesis presents a study of diffractive scattering of high-energy protons. Hadronic diffraction is not well-understood and many alternative approaches exist. The Monte Carlo event generator PYTHIA 8 follows a Pomeron-based approach, where the invariant mass of the diffractive system and the squared momentum transfer t of the system is set up according to a phenomenological Pomeron flux parameterization, which is parameterized by the super-critical Pomeron trajectory, $\alpha(t) = 1 + \varepsilon + \alpha' t$, where the intercept parameter ε and the slope parameter α' can be tuned by the user.

A fast detector response simulation of the ALFA and ATLAS detectors has been developed in the Rivet toolkit for the purposes of this thesis. The developed simulation framework is able to handle the beam transport of diffractively scattered protons as well as impose the kinematic acceptance of the ALFA detector which was found to be approximately $\xi \lesssim 0.22$, with a pseudorapidity coverage of $9 \lesssim |\eta| \lesssim 13$.

The simulation framework has been used in a phenomenological study of single diffraction, in order to study observables most sensitive to the Pomeron flux parameters. Using this information, a statistical fit procedure to determine the Pomeron flux parameters ε and α' has been developed and tested on several generated test samples.

Data recorded at $\sqrt{s} = 13$ TeV, $\beta^* = 90$ m, and $\theta_C = 2 \times 50$ μrad at the ATLAS experiment in the Run 2 period has been analysed. Several structures in the measured single diffractive distributions are observed in data which are not present in the simulation. An investigation into the possible background sources of these structures is presented.

ACKNOWLEDGEMENT

During the past year, I have had the privilege to work on a topic that has been both very exciting and fulfilling, as well as challenging. Many people have helped me during this year and I owe them all a big thanks.

First of all, I would like to thank the *High Energy Physics group at the Niels Bohr Institute* for making me feel welcome and a part of the group, as well as providing both the opportunity and great facilities for carrying out my thesis work. A special thanks to my office mates and all the other students in the group for a nice and relaxed atmosphere.

A big thank you to *Simon Holm Stark*, *Sune Jakobsen*, and *Peter Hansen* for all of your help and answers to all of my questions regarding the ALFA detector, the LHC magnets, and the data analysis.

Thank you to *Torbjörn Sjöstrand* and the *Theoretical Particle Physics group at Lund University*. I am very grateful for your time taken to help me with understanding diffractive theory and the inner workings of PYTHIA as well as your help with the phenomenological aspect of this thesis.

Last, but not least, I would like to thank my supervisor, *Jørgen Beck Hansen*, for your invaluable guidance and support throughout the work and writing of this thesis. The many talks we have had, on physics and things beyond, have been just as inspiring and motivating as they have been enjoyable. Thank you.

CONTENTS

1 INTRODUCTION

"The Monte Carlo simulation has become the major means of visualization of not only detector performance but also of physics phenomena. So far so good. But it often happens that the physics simulations provided by the Monte Carlo generators carry the authority of data itself. They look like data and feel like data, and if one is not careful they are accepted as if they were data."

— J. D. Bjorken [1]

The perhaps apocryphal story goes that at some time in the 4th century BC the ancient greek philosopher Democritus caught the smell of a nearby bakery and postulated that small invisible pieces of bread had floated through the air and into his nose. He called these small pieces for "atoms" [2].

The "atomic model" of Democritus has, however, little in common with modern science. In the 1960s and 1970s a theory emerged that describes all known elementary particles as well as their interactions, with the notable exception of gravity. This theory is known as the *Standard Model of Particle Physics*. In 2012 one of the last missing pieces of the theory, the elusive Higgs boson, was discovered at the Large Hadron Collider (LHC) at CERN [3, 4]. Even though the Standard Model has achieved the status of orthodoxy and has met every experimental test, it is known to be incomplete. It does not explain gravity or the nature of dark matter and dark energy that constitute the majority of the energy present in the Universe. Neither does the Standard Model adequately explain neutrino masses or neutrino oscillations and it is insufficient to explain the matter-antimatter asymmetry in the Universe.

CERN is derived from the historical "Conseil Européen pour la Recherche Nucléaire".

1.1 MOTIVATION AND SCOPE

Hadronic processes such as the proton-proton collisions happening at the LHC, are usually classified into *soft* and *hard processes*. The hard processes are characterized by a large momentum transfer which enables one to use the perturbative regime of *Quantum Chromodynamics (QCD)*. For these kinds of interactions, the theoretical predictions from QCD closely match experimental results. However, when the transferred momentum is small, as is the case for soft processes, this no longer holds. The push has been to search for New Physics at

even higher energies, to discover possible extensions to the Standard Model. But the study of low momentum transfer processes are of equal importance.

Around 25% of all proton-proton collisions at the LHC will be so-called diffractive events, where a hypothetical *Pomeron* will be exchanged between the colliding protons, resulting in the production of particles in a limited region of rapidity. The Pomeron must be a color singlet with quantum numbers of the vacuum as described in the coming chapters. Diffractive scattering is primarily a soft process and therefore non-perturbative in nature. The properties of diffractive scattering and dissociation is well-described by the phenomenology of Pomeron exchange in the form of *Regge theory* – the study of scattering as a function of angular momentum which is allowed to take any complex value. Regge theory, which was developed in the 1960s, predates the quark-gluon model, and it is still not clear how to unite it with QCD. Diffraction has been a steady part of the program at most high energy particle physics experiments, but due to its non-perturbative nature, further insight into the underlying process has been limited. The true nature of the Pomeron has so far remained unattainable. However, in the picture of Ingelman and Schlein [5] the Pomeron takes a partonic substructure and can be treated as a composite particle. In a proton-proton collision the Pomeron can be emitted by one proton and subsequently interact with the other proton in a large momentum transfer process between the constituent partons. This opens up the field of *hard diffraction*. Here the Pomeron is assumed to have both a flux as well as a structure function – the exact shape of which are not known, but different parameterizations exists and are used by Monte Carlo event generators to simulate proton-proton collisions.

The opening quote by J. D. Bjorken is a sobering warning of being careful not to accept the physics simulations provided by Monte Carlo event generators as if they were data. Diffraction is not well-understood and several alternative models exists. The Monte Carlo event generator PYTHIA 8 [6] follows a fairly conventional Pomeron-based approach, which makes use of a Pomeron flux parameterization that can be set by the user. This thesis sets out to study diffractive scattering, with a focus on single diffraction, at the ATLAS and ALFA experiments at the LHC. The final goal of this thesis is to determine which of the available Pomeron flux parameterizations in PYTHIA 8 that best fits the current $\sqrt{s} = 13$ TeV data from the ATLAS and ALFA experiments.

1.2 OUTLINE OF THESIS

This thesis is divided into four major parts along with a fifth part comprised of the appendix.

The first part introduces the theory background necessary for the content of this thesis. A short introduction to the Standard Model is given as well as a description of the physics at hadron colliders. The theory behind diffraction is described in some detail along with the various Pomeron parameterizations used in the Monte Carlo event generator PYTHIA 8 [6].

The second part describes the experimental setup relevant for this study, i.e. the LHC, the ATLAS detector, and the ALFA detector.

The third part presents a phenomenological study of the different Pomeron flux parameterizations in PYTHIA 8 to establish observables which show good sensitivity to the various parameters of the models and to determine how well one can test their validity. For this purpose, a simulation framework has been developed in the Rivet toolkit [7], which will be described in detail. In addition, the acceptance region of the ALFA detector has been studied.

The fourth part is an analysis of the new 13 TeV data from the 2015 Run 2 period using the ALFA sub-detector of the ATLAS experiment at the LHC, along with a comparison of the simulated distributions from the generated proton-proton collisions with measured distributions. Several attempts at reducing the background in the data distributions is presented.

Part I

THEORY

The goal of this thesis is to study diffractive scattering of high-energy protons. To accomplish this we must first gain an understanding of the currently accepted theories of particle physics. This part will therefore first present a short introduction to the Standard Model of particle physics, followed by a walkthrough of diffractive theory and Regge theory. Finally, the phenomenological models and parameterizations for diffraction used in the Monte Carlo event generator PYTHIA will be discussed.

2

THE STANDARD MODEL

The Standard Model (SM) of particle physics is the commonly accepted theory of elementary particles and their interactions through the strong, electromagnetic, and weak force. This chapter will provide a description of the Standard Model, along with a summary of the particles and forces in it.

The information in this chapter is based on references [8], [9], [10], [11], [12], and [13], unless otherwise noted.

2.1 ELEMENTARY PARTICLES AND THEIR INTERACTIONS

The matter particles of the Standard Model (SM) are *fermions* (particles with half-integer spin that follows Fermi-Dirac statistics), and come in two types: *leptons* and *quarks*. There are six leptons, classified according to their electric charge, electron number, muon number, and tau number. Both the leptons and the quarks form three distinct flavor doublets, which are known as the three generations of matter. The six leptons are listed in Table 2.1. There are also six antileptons with all their signs reversed. For example, the anti-electron (known as the *positron*) carries a charge of $+1$. There are in total 12 leptons.

In particle physics it is customary to use natural units, based on universal physical constants, where $c = \hbar = 1$. Energy is usually given in electron-volt, where $1\ eV \approx 1.602 \times 10^{-19}\ J$.

Table 2.1: The spin-1/2 leptons of the SM. Neutrino masses are extremely small and can for most purposes be taken to be zero. Values from [14].

Generation	Name	Flavor	Mass [MeV]	Charge $[e]$
1st	Electron	e	0.5110	-1
	Electron-neutrino	ν_e	0	0
2nd	Muon	μ	105.7	-1
	Muon-neutrino	ν_μ	0	0
3rd	Tau	τ	1.776×10^3	-1
	Tau-neutrino	ν_τ	0	0

Similarly, there are also six flavors of quarks, classified by electric charge, strangeness, charm, beauty, and truth. As already noted, the quarks also fall into three generations, and are listed in Table 2.2. Each quark also have an antiquark, and the quarks comes in three distinct colors, giving 36 quarks in total.

Table 2.2: The spin-1/2 quarks of the SM. Notice that the light quark masses are imprecise and speculative. Values from [14].

Generation	Name	Flavor	Mass [MeV]	Charge $[e]$
1st	Up	u	2.2	$2/3$
	Down	d	4.7	$-1/3$
2nd	Charm	c	1.27×10^3	$2/3$
	Strange	s	96	$-1/3$
3rd	Top	t	173.21×10^3	$2/3$
	Bottom	b	4.18×10^3	$-1/3$

Finally, every interaction (or force) has its mediator, in the form of spin-1 gauge bosons. In the current view, there are just four fundamental forces in nature: *strong*, *electromagnetic*, *weak*, and *gravitational*. To each force belongs a physical theory, however gravity is not yet a part of the Standard Model, as a complete satisfactory quantum mechanical description of gravity is missing. The three forces that are a part of the SM, and their mediators, are listed in Table 2.3. There are eight gluons, one photon, two W bosons, and one Z boson, giving a total of 12 gauge bosons.

Table 2.3: The forces of the SM and their corresponding mediators, the spin-1 gauge bosons. Values from [14].

Force	Mediator	Label	Mass [GeV]	Charge $[e]$
Strong	Gluons (8)	g	0	0
Electromagnetic	Photon	γ	0	0
Weak	W bosons	$W^{\pm}$	80.385	± 1
	Z boson	Z^0	91.188	0

The strong interaction, described by QCD, is the central theory of this study, as diffractive scattering is a QCD phenomenon. Hence, the primary focus of this chapter is on the theory of the strong interaction. However, a brief description of the theory of the electromagnetic and weak interactions is included as the presence of electroweak particles in diffractive scattering can tell us a lot about diffraction and the associated Pomeron, as explained later.

Not listed in any of the tables, is the scalar (spin-0) Higgs boson, with a mass of 125.09 GeV [14]. The Higgs boson was discovered by the ATLAS and CMS experiments at the LHC in 2012 [3, 4]. The Higgs boson was introduced into the SM, to give mass to the massive W and Z bosons, through the Higgs mechanism. The Higgs boson also generates the mass of the fermions through the Yukawa couplings and could generate neutrino masses through the seesaw mechanism.

2.2 QUANTUM FIELD THEORY

The Standard Model (SM) is a quantum field theory (QFT), that combines quantum mechanics with special relativity. A complete review of QFT would be beyond the scope of this thesis, and as such, this section will only serve as a short introduction.

	Small →	
Fast ↓	Classical Mechanics	Quantum Mechanics
	Relativistic Mechanics	Quantum Field Theory

It is not clear how small an elementary particle like the electron actually is, but the size of it will be less than 10^{-18} m

Since elementary particles are extremely small and quantum mechanical in nature, as well as typically extremely fast with velocities comparable to c, they naturally find themselves in the domain of quantum field theory. In QFT, particles are treated as excited states of the underlying physical matter fields. The dynamics of this system can be described by the Lagrangian, $L = T - V$, where T denotes the kinetic energy and V is the potential energy. If we restrict ourselves to local theories, the Lagrangian for a continous field can be written as the spatial integral over a Lagrangian density $\mathcal{L}$. The behavior is then based on the principle of least action, which states that the trajectory, x^μ, followed by the system through some configuration space, is that for which the action,

$$\mathcal{S} = \int L \mathrm{d}t = \int \mathcal{L}(\phi, \partial_\mu \phi, x^\mu) \mathrm{d}^4 x \tag{2.1}$$

is stationary. Here ϕ is the continous field and ∂_μ is the space-time derivative. The trajectory for which the action $\mathcal{S}$ is stationary, will satisfy the Euler-Lagrange equations of motion for the field ϕ,

$$\partial_\mu \left(\frac{\partial \mathcal{L}}{\partial(\partial_\mu \phi)} \right) - \frac{\partial \mathcal{L}}{\partial \phi} = 0 \tag{2.2}$$

As the Lagrangian completely describes the behavior of the field, it can be written in terms of the behavior of the free field $\mathcal{L}_{\text{free}}$ and the interactions of the field $\mathcal{L}_{\text{int}}$ (either with it self or with other fields) by

$$\mathcal{L} = \mathcal{L}_{\text{free}} + \mathcal{L}_{\text{int}} \tag{2.3}$$

The terms in the Lagrangian must be invariant under local gauge transformations. The most general is the Standard Model Lagrangian, which is invariant under the local unitary product symmetry group $\mathrm{SU}(3) \times \mathrm{SU}(2) \times \mathrm{SU}(1)$. The three factors of gauge symmetry will together give rise to the three fundamental interactions in the Standard Model (gravity is excluded).

2.2.1 *Feynman Diagrams and Rules*

The situation for quantum fields is somewhat different compared to that of classical fields, as in QFT the system is allowed to follow all possible paths (or trajectories), though the classical path is often the most dominating with smaller contributions from other paths. These contributions enter as quantum fluctuations (or corrections) around the classical path. So in QFT, instead of having a single uniquely defined path, we have a sum over all possible paths, which can be used to calculate a quantum transition amplitude. This sum is called the Feynman path integral. Expressing the transition amplitude as a perturbative sum is the main idea in *perturbation theory*. Given a Lagrangian (that defines the behavior of the free field as well as its interactions) and by the use of the Feynman path integral, the transition amplitude (i.e. the probability of going from an initial state to a final state) can be calculated by using *Feynman diagrams*.

Feynman diagrams are pictorial representations of the contributions to the transition amplitude, which is also known as the *matrix element* $\mathcal{M}$. For each different path exists a topologically different Feynman diagram. The matrix element $\mathcal{M}$ contains all the dynamical information of the system and is calculated by evaluating the relevant Feynman diagrams, using the Feynman rules appropriate to the interaction in question, whether that be electromagnetic, strong, or weak interaction. In the SM, forces are described as point-like interactions between particles. These points of interactions are drawn in Feynman diagrams, as vertices in space-time with particles going in or out as lines. Each vertex has an associated coupling, that signifies the strength of the interaction, i.e. the probability of that interaction happening. In the following, the QFT formulation of the forces in the SM will be briefly introduced.

2.3 THE ELECTROWEAK THEORY

Electroweak (EW) theory is the unified theory of the electromagnetic interaction (*quantum electrodynamics*, QED) and the weak interaction. The electroweak interactions are mediated by four gauge bosons: the photon γ, the Z^0 boson, and the two $W^{\pm}$ bosons. The four gauge fields are collected under the gauge symmetry $\mathrm{SU}(2) \times \mathrm{U}(1)$. The $\mathrm{SU}(2) \times \mathrm{U}(1)$ symmetry is spontaneously broken into $\mathrm{U}(1)$ in the Higgs mechanism to explain how the heavy gauge bosons ($W^{\pm}$ and Z^0) acquire mass.

All electroweak interactions are characterized by a general, dimensionless, and mass independent coupling strength of $\alpha \approx 1/137$ [14], also known as the fine-structure constant.

The photon couples to electric charge, as seen in the first vertex in Figure 2.1. In electroweak interactions, electric charge is conserved, which means that the sum of charge flowing into a vertex must be equal to the sum of charge flowing out of a vertex.

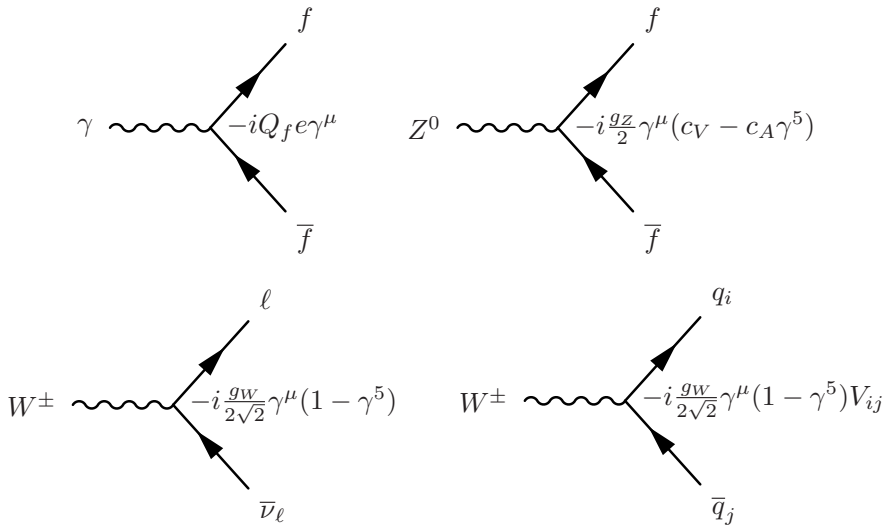

Figure 2.1: The vertices for the electroweak interaction along with their respective couplings, where $g_W \propto g_Z \propto e \propto \sqrt{\alpha}$. Here f is any fermion, ℓ is any charged lepton, and q_i is a quark of flavor i.

In addition to electric charge, all fermions in the SM have a flavor, which is associated with a quantum number called the *lepton number* L_ℓ where $\ell = e, \mu, \tau$. Lepton number is conserved in electroweak interactions and is defined as

$$L_\ell \equiv N(\ell) - N(\overline{\ell}) + N(\nu_\ell) - N(\overline{\nu}_\ell) \tag{2.4}$$

where N is the number of the given particle.

Similarly to lepton numbers, each quark species has a related quantum numbers (known as strangeness, charm, etc.) that are seperately conserved in all types of interactions, except the weak interactions.

The neutral current interactions of the electroweak theory are mediated by the Z^0 boson and conserves both electric charge and flavor quantum numbers. This means that neutral current interactions are always of the form $Z^0 f\overline{f}$ as seen in the vertex in Figure 2.1. When the Z^0 couple to charged leptons, the interaction becomes similar to that of the photon γ, and the two processes will interfere and may collectively be referred to as Z^0/γ^*.

The asterix in γ^* indicates that the photon is off its mass shell.

The charged current interactions are mediated by the $W^\pm$ bosons which has integer electric charge (as opposed to the neutral Z^0) and will therefore not couple directly to fermions and their anti-particles

due to charge conservation. In the leptonic sector, the $W^{\pm}$ bosons couple exclusively to the flavor doublets,

$$\begin{pmatrix} \nu_e \\ e \end{pmatrix}, \quad \begin{pmatrix} \nu_\mu \\ \mu \end{pmatrix}, \quad \begin{pmatrix} \nu_\tau \\ \tau \end{pmatrix} \tag{2.5}$$

which is illustrated by the third vertex in Figure 2.1. In the quark sector, the $W^{\pm}$ must couple to a up-type and a down-type quark in the form of the doublets,

$$\begin{pmatrix} u \\ d' \end{pmatrix}, \quad \begin{pmatrix} c \\ s' \end{pmatrix}, \quad \begin{pmatrix} t \\ b' \end{pmatrix} \tag{2.6}$$

since quarks have fractional charges and charge is conserved. Here, one must take into account the difference between the mass eigenstates and weak isospin eigenstates of the quarks. The weak eigenstates (d', s', b') are linear combinations of the mass eigenstates (d, s, b) as given by the unitary Cabbibo-Kobayashi-Maskawa (CKM) matrix,

$$\begin{pmatrix} d' \\ s' \\ b' \end{pmatrix} = \begin{bmatrix} V_{ud} & V_{us} & V_{ub} \\ V_{cd} & V_{cs} & V_{cb} \\ V_{td} & V_{ts} & V_{tb} \end{bmatrix} \begin{pmatrix} d \\ s \\ b \end{pmatrix} \tag{2.7}$$

Most interactions are within the same generation, but a non-negligible amount of inter-generational mixing does occur, which means that flavor is not strictly conserved in charged current interactions. The biggest mixing of the quarks occur in the first two generations, d and s, while the mixing with b-quarks is very small.

2.4 QUANTUM CHROMODYNAMICS

Quantum chromodynamics (QCD) is the quantum field theory of the strong interaction and is described by the gauge group SU(3). The strong force is characterized by the strong coupling α_s. QCD interactions are mediated by the exchange of the gluons. Central to QCD is the color quantum number, to which the gluons couple. Color charge is conserved in all QCD interactions, in addition to electric charge and flavor quantum numbers. Quarks come in three color charges labelled 'red', 'green', and 'blue', or R, G, and B, with corresponding anti-colors $\overline{R}$, $\overline{G}$, and $\overline{B}$, which is similar to the single ∓ 1 electric charge. (Anti-)quarks therefore carry one (anti-)color charge to which the gluon couple. Unlike the neutral photon, gluons themselves carry color charge and there are eight different color combinations of gluons and hence eight gluons. Only quarks and gluons carry color charge and are therefore the only particles that interact through the strong force. QCD is an unbroken symmetry which leaves the gluon massless.

The Lagrangian of QCD is given by

$$\mathcal{L}_{\text{QCD}} = \overline{q}^i(i\gamma^\mu(D_\mu)_{ij} - m_q\delta_{ij})q^j - \frac{1}{4}G^a_{\mu\nu}G^{\mu\nu}_a \tag{2.8}$$

where q^i denotes a quark field with color index i, γ^μ is a Dirac matrix, m_q allows for the possibility of non-zero quark masses (induced by the Yukawa couplings in the Higgs mechanism), $G^a_{\mu\nu}$ is the gluon field strength tensor for a gluon with color index a, and D_μ is the covariant derivative in QCD,

$$(D_\mu)_{ij} = \delta_{ij}\partial_\mu - ig_s t^a_{ij}A^a_\mu \tag{2.9}$$

where A^a_μ is the gluon field with color index a, t^a_{ij} is proportional to the Hermitian and traceless Gell-Mann matrices of SU(3), and g_s is also known as the strong coupling, and is related to α_s by

$$g_s^2 = 4\pi\alpha_s \tag{2.10}$$

Since the gluons carries color charge themselves, and since gluons couple to color charge, gluons will exhibit self-interaction. The gluon self-coupling arises from the $-\frac{1}{4}G^a_{\mu\nu}G^{\mu\nu}_a$ term in the Lagrangian leading to triple and quartic self-couplings. The possible vertices of QCD are shown in Figure 2.2.

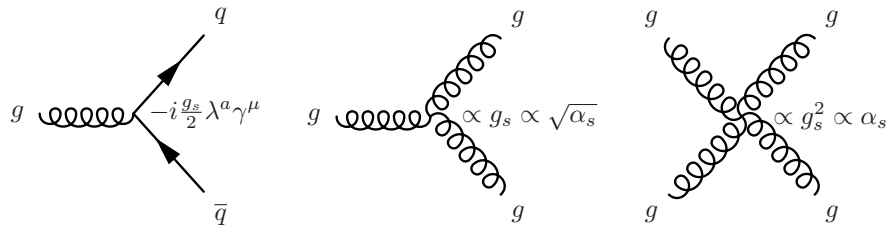

Figure 2.2: The vertices of the QCD interactions along with their respective couplings.

The strong coupling α_s is not constant but depends on the distance scale or, equivalently, the momentum transfer Q^2 of the QCD interaction. The momentum transfer Q^2 in the case of gluon-exchange between two quarks in the t-channel, is shown in the diagram in Figure 2.3. Since the strong coupling α_s depends on the energy scale at which it is probed, it is referred to as a *running coupling*, and the behavior takes the form of

$$\alpha_s(Q^2) \propto \frac{1}{\ln(Q^2/\Lambda^2_{\text{QCD}})} \tag{2.11}$$

where $\Lambda_{\text{QCD}} \approx 200$ MeV is the *QCD scale*. This behavior is seen in Figure 2.4. Numerically, the value of the strong coupling is usually specified at a specific reference scale of the Z^0 boson mass, $Q^2 = M_Z^2$, where $\alpha_s(M_Z^2) \approx 0.12$ [14].

The EM coupling α is also a running coupling and grows with Q^2 despite photons being electrically neutral and hence will not self-interact. Instead, the vacuum polarization of photons will create virtual $e\bar{e}$ pairs leading to screening effects.

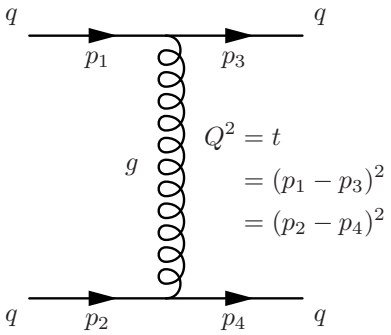

Figure 2.3: Gluon-exchange between two quarks and the associated momentum transfer Q^2.

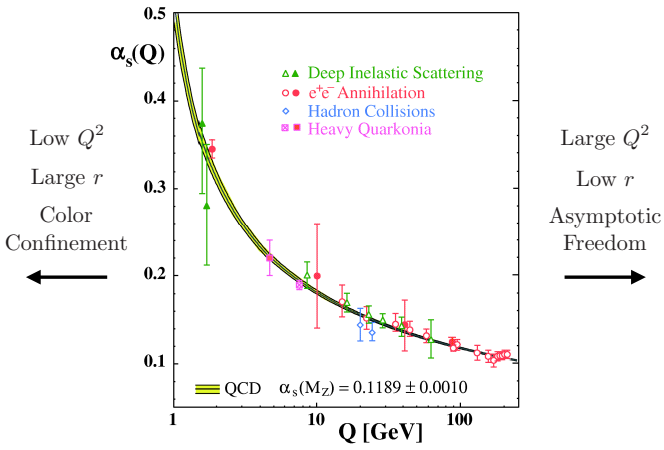

Figure 2.4: The behavior of $\alpha_s(Q^2)$ as a function of the respective energy scale Q^2 along with measurements. Figure from [15].

Distance scale r and momentum transfer Q^2 are inversely related due to the Heisenberg uncertainty principle, $r \sim \hbar c/|Q|$. This means that the strong coupling α_s diverges at large distances. This is manifested in the quark-antiquark potential on the form of

$$V(r) \approx -\frac{a}{r} + br \tag{2.12}$$

where the $1/r$ term is the Coulomb potential and the r term is the color potential. The color potential will dominate at high separation r between the quarks. This is known as *linear color confinement* and means that colored states (e.g. individual quarks and gluons) cannot exist in isolation beyond distances of the order of a few fm. This means that all physically observable states in nature must be color singlet states. All of these color neutral states are called *hadrons* and must be either *baryons*, qqq states like the proton, or *mesons*, $q\bar{q}$ states like the pions. Color confinement is the starting point of *hadronization* as will be discussed in the following chapter.

At low distance scales and larger momentum transfers Q^2, the strong coupling α_s decreases, as seen in Figure 2.4. Hence, at very large energies or very small distances (e.g. in the early Universe, in quark-gluon plasmas, or inside hadrons) the strong coupling essentially vanishes and the quarks no longer feel the strong force between them. The quarks and gluons (collectively known as *partons*) can then propagate freely with virtually no interactions. This is known as *asymptotic freedom*.

2.5 KINEMATICS

The different theoretical approaches to diffraction are based on the identification of the relevant kinematic regimes, as we shall see later. This section will therefore give a short introduction to the kinematics and coordinate system used for high energy pp-collisions.

The usual set of coordinates is

$$p^\mu = (E, \mathbf{p}) = (E, p_x, p_y, p_z) \tag{2.13}$$

Bold-face symbols will in this thesis denote two- and three-vectors.

where the beam of protons is aligned with the z-direction. An important kinematic variable in particle physics is the *rapidity*, defined with respect to the beam axis p_z and using natural units where $c = 1$,

$$y = \frac{1}{2} \ln \left(\frac{E + p_z}{E - p_z} \right) \tag{2.14}$$

where p_z is the momentum along the beam axis z. It is also customary to consider the transverse momentum p_T (i.e. the momentum transverse to the beam axis) defined as

$$p_T = \sqrt{p_x^2 + p_y^2} \tag{2.15}$$

Experimentalists often use p_T to denote the transverse momentum, while phenomenologists and theoreticians tend to use $p_\perp$. Throughout this thesis, p_T will be used.

The transverse mass is defined as

$$m_T = \sqrt{m^2 + p_x^2 + p_y^2} = \sqrt{m^2 + p_T^2} \tag{2.16}$$

which enable us to rewrite the rapidity y as

$$y = \ln \left(\frac{E + p_z}{m_T} \right) = \ln \left(\frac{m_T}{E - p_z} \right) \tag{2.17}$$

If experimentalists cannot measure m they may assume $m = 0$. Instead of rapidity y, they can then measure the pseudorapidity η,

$$\eta = \frac{1}{2} \ln \left(\frac{|\mathbf{p}| + p_z}{|\mathbf{p}| - p_z} \right) = \ln \left(\frac{|\mathbf{p}| + p_z}{p_T} \right) \tag{2.18}$$

since $y \simeq \eta$ in the massless limit. Using that θ is the polar angle, i.e. the angle the three-momentum $\mathbf{p}$ makes with the positive direction of the beam axis z and that $p_z = |\mathbf{p}| \cos(\theta)$ (in spherical coordinates), we can write the pseudorapidity as

$$\begin{aligned} \eta &= \frac{1}{2} \ln \left(\frac{|\mathbf{p}| + |\mathbf{p}| \cos(\theta)}{|\mathbf{p}| - |\mathbf{p}| \cos(\theta)} \right) = \frac{1}{2} \ln \left(\frac{1 + \cos(\theta)}{1 - \cos(\theta)} \right) \\ &= \frac{1}{2} \ln \left(\frac{2 \cos^2(\theta/2)}{2 \sin^2(\theta/2)} \right) = \ln \left(\frac{\cos(\theta/2)}{\sin(\theta/2)} \right) \\ &= -\ln \left[\tan \left(\frac{\theta}{2} \right) \right] \end{aligned} \tag{2.19}$$

which thus only depends on the polar angle, i.e. is a solely geometric quantity.

The concepts of rapidity and pseudorapidity are important in particle physics, since the difference in rapidity, Δy, is invariant under Lorentz boosts,

$$y_2' - y_1' = y_2 - y_1 \tag{2.20}$$

This is however not the case for pseudorapidity,

$$\eta_2' - \eta_1' \neq \eta_2 - \eta_1 \tag{2.21}$$

Both y and η will often be referenced throughout this thesis.

For most purposes in high energy physics, one can equate the rapidity y with the pseudorapidity η without making too large of an error. This is because we usually find ourselves in the massless limit, $E \gg m$. However, if we consider y as a function of the polar angle θ,

$$y = \frac{1}{2} \ln \left(\frac{\sqrt{|\mathbf{p}|^2 \sin^2(\theta) + |\mathbf{p}|^2 \cos^2(\theta) + m^2} + |\mathbf{p}| \cos(\theta)}{\sqrt{|\mathbf{p}|^2 \sin^2(\theta) + |\mathbf{p}|^2 \cos^2(\theta) + m^2} - |\mathbf{p}| \cos(\theta)} \right) \tag{2.22}$$

and compare it with the expression for η in Equation 2.19, we see that for a beam proton with $E = 6500$ GeV and $\theta \to 0$, we get a different behavior for y and η as illustrated in Figure 2.5 and 2.6. For $\theta = 0$, we see that $y_{\text{max}} \simeq 9.5$ while $\eta_{\text{max}} = \infty$. Hence, for protons in the extreme forward direction (which are the particles of interest in this thesis) one should be careful when comparing rapidity and pseudorapidity.

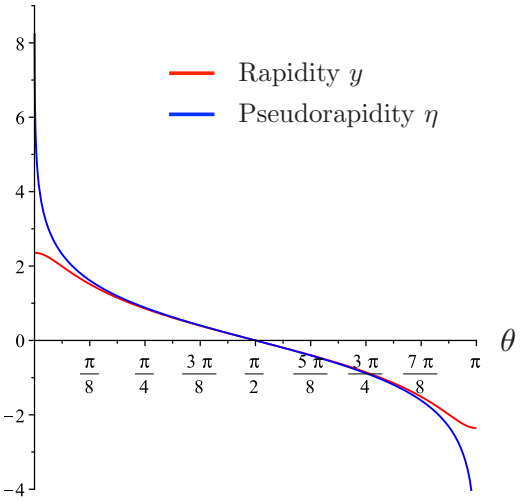

Figure 2.5: Rapidity y and pseudorapidity η as a function of the polar angle θ for a proton with $m_p = 0.938$ GeV and $E = 5$ GeV.

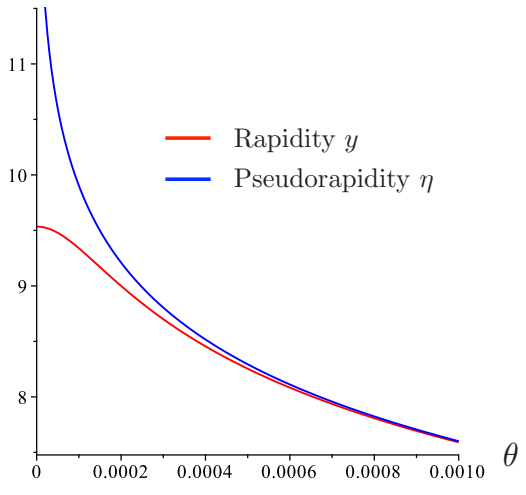

Figure 2.6: Rapidity y and pseudorapidity η as a function of the polar angle θ for a proton with $m_p = 0.938$ GeV and $E = 6500$ GeV. Plotted for low values of θ.

3

PHYSICS AT HADRON COLLIDERS

In the previous chapter we introduced the Standard Model of particle physics, its particle content, and the rules of interactions of these particles. In this chapter, we concern ourselves with the issue of particle production at a hadron collider. We will take a detailed look at the anatomy of hadron collisions as well as the way in which these can be studied through simulation by Monte Carlo event generators.

The content of this chapter is based on references [13], [16], [17], [18], and [19], unless otherwise noted.

3.1 PARTON DISTRIBUTION FUNCTIONS

The proton is not an elementary particle but consists of three valence quarks (two up-quarks and one down-quark) as well as having a time-dependent substructure of a virtual sea of quarks and gluons – see Figure 3.1 and 3.2. For collision energies above the QCD confinement scale $\Lambda_{\text{QCD}} \approx 200$ MeV, it is possible to probe the internal, dynamic structure of the proton through deep inelastic scattering (DIS). The substructure of the proton can be described by parton distribution functions (PDFs), which are a necessary input to almost all theoretical predictions for hadron colliders.

The parton distribution function $f_{i/p}(x, Q^2)$ gives the probability of finding in the proton a parton of flavor i (quarks or gluons) carrying a fraction $x = p/P$ of the proton momentum P with Q being the energy scale of the hard interaction.

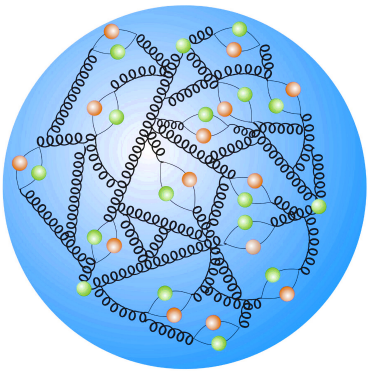

Figure 3.1: An illustration of the virtual quark-gluon sea in the proton. Image credit of Deutsches Elektronen-Synchrotron (DESY).

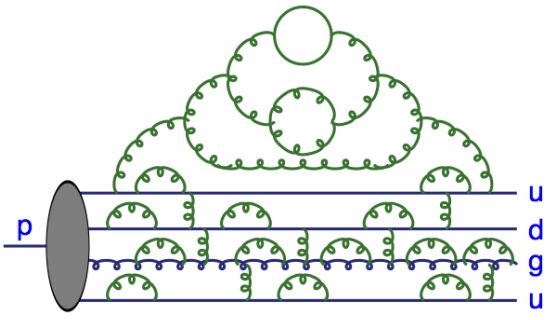

Figure 3.2: The time-dependent substructure of the virtual quarks and gluons in the proton. Image from [17].

In Figure 3.3 the PDFs for the gluon, up, down, and anti-up quark are plotted for two different values of Q^2. If the proton only consisted of the three valence quarks one would expect them to have $x = 1/3$. However, this is far from the case due to the sea of quarks and gluons. The PDFs $f_{i/p}(x, Q^2)$ can be interpreted as the number density of partons of type i in the proton that carries momentum fraction x when probed at energy Q^2. The bumps in the PDFs for the u and d quarks around $x \approx 1/3$ is evidence of the presence of the valence quarks in the proportions as expected. The component of the PDF for the up-quark that does not come from the valence quarks, must then come from the sea quarks. This component is equal to the PDF for the anti-up-quark, $u_S(x, Q^2) = \overline{u}(x, Q^2)$. For very low x, the PDFs show that sea quarks are quite numerous. Already with the gluon, it is clear that the simple picture of only valence quarks do not hold. When probing the proton at higher energy scales Q^2, the valence quark structure becomes less pronounced. One could say that the proton is then probed with finer resolution, and hence is more sensitive to the sea (non-valent) structure.

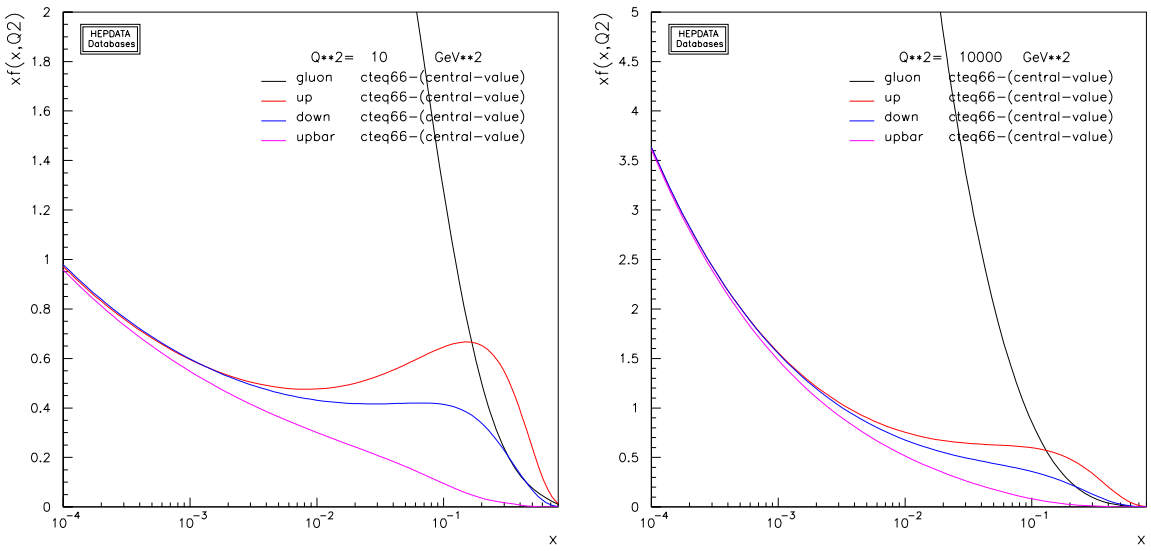

(a) $Q^2 = 10$ GeV^2 **(b)** $Q^2 = 10^4$ GeV^2

Figure 3.3: PDFs from the CTEQ6.6 set for the up ($xu(x)$), down ($xd(x)$), and anti-up ($x\bar{u}(x)$) quarks as well as for the gluon ($xg(x)$). Plotted using the Durham HepData Project PDF plotter, available at `http://hepdata.cedar.ac.uk/pdf/pdf3.html`.

The PDFs can be parameterized as

$$xf_{i/p}(x, Q^2) = A_i x^{a_i} (1 - x)^{b_i} \tag{3.1}$$

The parameter a_i is associated with small-x Regge behavior while b_i is associated with large-x valence counting rules. For example, the high x behavior of the gluon PDF is approximately $xg(x) \sim (1 - x)^6$. Additional factors to the parameterization can be introduced to allow for greater flexibility when fitting data.

3.2 FACTORIZATION THEOREM

From parton distribution functions, we see that pp-collisions are actually interactions between the constituent partons. Now that we know what we are colliding we would also like to understand how to compute the probabilities for the parton-level scattering interactions, at least at the energies that are sufficiently large so that perturbation theory holds. The relevant measure of the probability of a scattering process in particle physics, is the *cross-section* σ, defined as

$$\sigma = \frac{\text{Number of interactions per unit time per target area}}{\text{Incident Flux}} \tag{3.2}$$

To get the cross-section (or probability) for pp-collisions, one can "untangle" the parton-level interactions by using the QCD *factorization theorem* – factorizing the contributions from the parton distribution information and the parton interactions. The factorization theorem is essentially the sum over the possible partons that can be taken out of the protons and then the probability for those particular partons to interact with each other. Hence, cross-sections for a scattering subprocess $a + b \to n$ at hadron colliders can be computed in collinear factorization by

$$\sigma = \sum_{a,b} \int_0^1 \mathrm{d}x_a \mathrm{d}x_b \int f_a(x_a, \mu_F) f_b(x_b, \mu_F) \mathrm{d}\hat{\sigma}_{a+b\to n}(\mu_F, \mu_R) \tag{3.3}$$

where

- $f_i(x_i, \mu_F)$ is the PDF for the parton i with momentum fraction x_i of the parent hadron (in our case the proton) when probed at the factorization scale μ_F, and
- $\hat{\sigma}_{a+b\to n}$ denotes the parton-level cross-section for the production of the final-state n, through the initial partons a and b. It depends on the factorization scale μ_F, the renormalization scale μ_R, and the final-state Lorentz invariant phase-space $\mathrm{d}\Phi_n$. Usually the scales are set to $\mu_F^2 = \mu_R^2 = Q^2$.

3.3 EVENT GENERATORS AND THE STRUCTURE OF AN EVENT

Monte Carlo (MC) event generators are capable of simulating a wide range of the most interesting processes that are expected at hadron colliders such as the LHC. Several general purpose MC event generators exists, such as PYTHIA [6], HERWIG [20], and SHERPA [21], along with numerous more specialised event generators. Common for all the event generators is that they utilize the factorization of different components of hadronic collisions, as per Equation 3.3. This allows for the compartmentalization of the event generation into various specialized subroutines.

In this section, we will give a description of the structure of a typical hadronic event, and the implementation in the Monte Carlo event generators that are used to simulate such collisions.

3.3.1 *Hard Scatter Matrix Element*

Most of hadronic processes of interest involve a large momentum transfer (called *hard processes*), either to produce heavy particles or jets with a large p_T. Therefore the simulation of subprocesses with a large invariant momentum transfer is at the core of every simulation of high energy hadronic processes. Since quarks and gluons are asymptotically free, such reactions can be described by perturbation theory. This makes it possible to compute a lot of the features of the process by using Feynman diagrams.

From the factorization theorem in Equation 3.3, we had the parton-level cross-section $\hat{\sigma}_{a+b\to n}$ which specify the hard subprocess. The parton-level cross-section depends on the matrix element squared $|\mathcal{M}_{a+b\to n}|^2$, by

$$\mathrm{d}\hat{\sigma}_{a+b\to n}(\mu_F,\mu_R) = \frac{1}{2s}|\mathcal{M}_{a+b\to n}|^2(\Phi_n;\mu_F,\mu_R)\mathrm{d}\Phi_n \tag{3.4}$$

where s is the hadronic center-of-mass energy squared. The matrix element can be written as a sum over Feynman diagrams,

$$\mathcal{M}_{a+b\to n} = \sum_i \mathcal{F}^{(i)}_{a+b\to n} \tag{3.5}$$

However, any summation over quantum numbers can be moved outside the square, which allows one to sum over the helicity and color orderings, such that

$$|\mathcal{M}_{a+b\to n}|^2(\Phi_n;\mu_F,\mu_R) = \sum_{h_i,c_j} |\mathcal{M}^{\{ij\}}_{a+b\to n}|^2(\Phi_n,\{h_i\},\{c_j\};\mu_F,\mu_R) \tag{3.6}$$

The factorization theorem holds to all orders in perturbation theory, but when the parton-level (subprocess) cross-section is computed beyond the leading order, there are som subtleties to consider. It is normal to only consider the leading-order (LO) subprocess matrix elements, but with the ever increasing precision of modern particle physics experiments, it can be necessary to go to next-to-leading order (NLO). NLO corrections are, however, beyond the scope of this thesis.

3.3.2 *Parton Showers*

The previous section discussed the generation of a hard subprocess according to the lowest-order matrix elements. This will give a good description of the momenta of the outgoing jets. But to give a more

complete picture of the process and the internal structure of the jets and the distributions of the accompanying particles, any fixed order will be insufficient. The effect of higher orders can be simulated through the use of a *parton shower algorithm*. Higher-order diagrams are increasingly difficult to calculate and the parton shower algorithm can be used to approximate the effect of additional legs and to all higher orders. The algorithm is typically formulated as an evolution in momentum transfer down from the high scales associated with the hard process to the low scales of order ~ 1 GeV, which is associated with the confinement of the partons.

The hard subprocess involves large momentum transfer, and hence the partons involved are highly accelerated. Just like accelerated electric charges will emit QED radiation in the form of photons, the accelerated colored partons will emit QCD radiation in the form of gluons. However, unlike the photon, the gluons themselves carry color charges and can therefore radiate further. This will lead to *parton showers*. The showers correspond to higher-order corrections to the hard subprocess.

Let us consider the almost-collinear splitting of a parton of flavor i into partons j and k. This could be for example, the splitting $q \to q + g$. If the n-parton differential cross-section before splitting is $\mathrm{d}\sigma_n$, then after splitting, it is

Collinear means that the emitted parton is soft (low energy) and hence have an angle to the parent parton going as $\theta \to 0$.

$$\mathrm{d}\sigma_{n+1} \approx \mathrm{d}\sigma_n \frac{\alpha_s}{2\pi} \frac{\mathrm{d}\theta^2}{\theta^2} \, \mathrm{d}z \, \mathrm{d}\phi \, P_{i\to jk}(z, \phi) \tag{3.7}$$

where z is the fraction of the radiating partons momentum carried away by the emitted parton, θ and ϕ are the opening and azimuthal angle of the splitting, and $P_{i\to jk}$ is the *DGLAP splitting kernel* for the branching $i \to j + k$:

$$P_{q\to qg}(z) = \frac{1+z^2}{1-z} \tag{3.8}$$

$$P_{q\to gq}(z) = \frac{1+(1-z)^2}{z} \tag{3.9}$$

$$P_{g\to gg}(z) = \frac{z^4+1+1(1-z)^4}{z(1-z)} \tag{3.10}$$

$$P_{g\to q\bar{q}}(z) = \frac{1+(1-z)^2}{z} \tag{3.11}$$

$$P_{\bar{q}\to \bar{q}g}(z) = P_{q\to qg}(z) \tag{3.12}$$

The splitting kernels are universal, meaning that they allow for a process-independent implementation in MC event generators. These branchings may not just occur for the final-state partons but for the initial-state partons as well. These two categories are referred to as *final* and *initial state radiation* (FSR and ISR), and are handled separately in event generators.

Note that instead of the opening angle θ in Equation 3.7, one can instead use the radiated (off-shell) partons virtuality $Q^2 = z(1-z)\theta^2 E^2 = M^2$ or mass M, or its momentum transverse to the emitting parton $p_T^2 = z^2(1-z)^2\theta^2 E^2$, since

$$\frac{\mathrm{d}\theta^2}{\theta^2} = \frac{\mathrm{d}Q^2}{Q^2} = \frac{\mathrm{d}M^2}{M^2} = \frac{\mathrm{d}p_T^2}{p_T^2} \tag{3.13}$$

We see that z and either of these variables differ in character, as the virtuality Q^2 is "temporal" in that it has memory of the preceding evolution, since the virtuality of the emitting parton decreases for each splitting, while z is purely "spatial", i.e. has no memory of the preceding evolution. The parton shower procedure therefore starts from the high energy final-state partons from the hard subprocess, and then performs an iterative evolution down in one of the temporal evolution variables. This will result in a shower of radiated partons, until all final-state particles reach energies of $\mathcal{O}(\Lambda_{\mathrm{QCD}})$. The divergences in the splitting probability and splitting kernels will in principle result in the emission of infinitely many soft collinear partons. This is not of any consequence for physical measurements since the number of final-state partons above some finite energy threshold is always finite. Therefore, these divergences are avoided in event generators by setting sensible lower limits on z and Q^2.

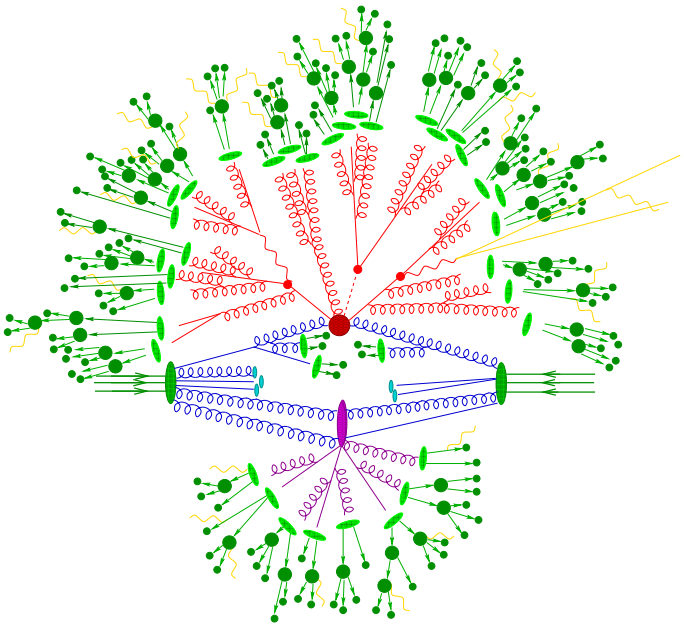

Figure 3.4: Illustration of a hadronic event as generated by a MC event generator. The hard interaction (red blob) is followed by ISR (blue) and FSR (red). Finally hadronization occurs (green). Photon radiation occurs at any stage (yellow). Image from [21].

3.3.3 *Hadronization*

QCD becomes non-perturbative at energies of $\mathcal{O}(\Lambda_{\text{QCD}})$. At this point the parton shower process breaks down. From Section 2.4, we know that, due to color confinement, all particles must exists in color-singlet states. Therefore, Monte Carlo event generators needs a specific model and procedure to enforce a color-neutral recombination of the final-state. Such a model will handle the transition from the partonic "final" state to a complete representation of the actual hadronic final state. The color-singlet primary hadrons may then subsequently decay further.

Monte Carlo event generators generally handle hadronization in three steps:

1. The partonic system is first mapped onto a continuum of high mass hadronic states. This either done through the use of "strings", as in the Lund string model [22] of PYTHIA [6], or by the use of "clusters" as in the cluster model [23] of HERWIG [20];

2. The strings or clusters are then iteratively mapped onto discrete sets of primary hadrons. This is done through string fragmentation or cluster splittings depending on the model used;

3. Finally the primary hadrons will undergo sequential decay into secondaries, resulting in stable products seen in the final state.

The most widely used string model today is the Lund string model, implemented in PYTHIA. In this model, the final-state partons resulting from the hard scatter matrix element, as well as the initial and final state radiation, are connected by color strings. The color strings ensure the conservation of color charge, and may have complicated multi-parton topologies. Simple $q - \overline{q}$ strings form the starting point. As the quarks move apart, linear color confinement implies a potential $V(r) = \kappa r$ at large distances r (see Equation 2.12). The string tension is $\kappa \sim 0.9$ GeV/fm [13]. As the partons move apart, the potential energy in the string increases, eventually allowing virtual $q\overline{q}$ pairs to transition to real particles by absorbing energy from the string. This is referred to as *string breaking* or *string fragmentation*, and is illustrated in Figure 3.5. The process of breaking the strings into separate color-singlet pieces is continued until ordinary hadrons remain, with insufficient energy to cause further string fragmentation.

3.3.4 *Soft Physics, Underlying Event, and Multiparton Interactions*

Apart from the hard subprocess and the associated initial and final state radiation, the pp collision in the Figure 3.4 contains other soft (low energy) activity which is collectively called the *underlying event* (UE). This covers the non-interacting remnants of the colliding protons, often labelled the *beam remnants*, as well as the possibility of *multiple parton interactions* (or *multiparton interactions*, MPI) within the colliding protons besides the hard interaction, as illustrated in Figure 3.6. The soft physics of the underlying event can interfere with the hard subprocess and may obscure the details of the hard interaction, which is most often the process of interest.

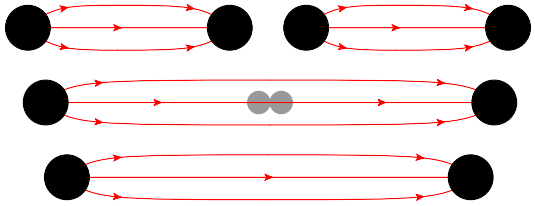

Figure 3.5: Illustration of a color string breaking by quark pair creation in the string field. Image from [13].

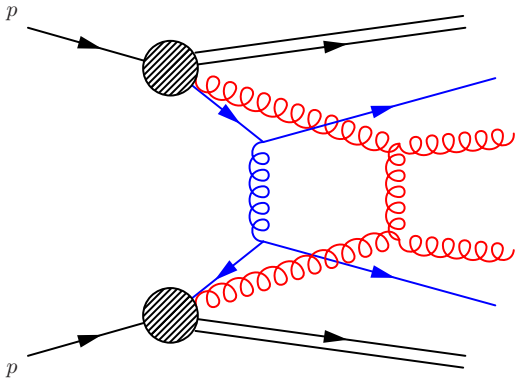

Figure 3.6: Feynman diagram of multiparton interactions (MPIs) in a pp event.

Even in the absence of a hard interaction, soft inclusive physics can occur. Such events are called *minimum bias* events (or simply *min-bias* or MB), which is an experimental term that is used to define a certain class of events that are selected with the minimum possible selection bias. This is to ensure that they are as inclusive as possible. In theoretical context, the term "minimum bias" is often used to denote a specific classes of inclusive soft QCD subprocesses, which are the dominant processes in the experimental context. Minimum bias events make up most of the events observed at hadron colliders. Most studies at hadron colliders focus on heavy resonances (for example the Higgs boson) produced in hard scatter interactions. In these studies, minimum bias events will mostly manifest themselves as a diffusive "noise" of soft particles. However in the study presented in this thesis, diffractive scattering are the processes of interest. Diffraction most often finds itself in the class of soft physics, and hence are often included in the definition of minimum bias events along with non-diffractive events. In the following chapter, the theory, signature, and phenomenology of diffractive events will be described in some detail.

4

DIFFRACTIVE THEORY

This chapter will introduce diffractive scattering of high-energy protons, as hadronic diffraction is the process of interest in this thesis. First, diffractive scattering will be defined in purely particle physics terms. Then the kinematics of scattering processes will be reviewed, with a special focus on diffractive reactions. Relativistic S-matrix theory will be introduced to provide way for a description of Regge theory. Finally, the postulated Pomeron is introduced along with the different phenomenological parameterizations of the Pomeron flux as implemented in Pythia 8.

The information in this chapter is based on references [24], [25], [26], [27], [28], and [29], unless otherwise noted. The reader is referred to these sources for more details and information.

4.1 DEFINITION

A general definition of diffractive scattering can be formulated as:

1. *A high-energy reaction in which no quantum numbers are exchanged between the colliding particles.*

Diffraction is then the phenomenon that takes place as the energy increases, and whenever the resulting outgoing particles have the same quantum numbers as the incident particles. Definition 1 is general enough to cover all cases:

ELASTIC SCATTERING, where the exact same incident particles come out after the interaction (Figure 4.1a),

$$p + p \to p + p \tag{4.1}$$

SINGLE DIFFRACTION (SD), where one of the incoming protons leaves the collision while the other decays into a bunch of final-state particles with the same quantum numbers as the original proton, i.e. only one proton dissociates (Figure 4.1b),

$$p + p \to p + X \tag{4.2}$$

DOUBLE DIFFRACTION (DD), where both protons decay into bunches of multiple particles, each of the bunches carrying the same quantum numbers as their respective parent proton, i.e. both colliding protons dissociate (Figure 4.1c),

$$p + p \to X + Y \tag{4.3}$$

CENTRAL DIFFRACTION (CD), where both protons are intact and are seen in the final state and an additional bunch of particles is produced with the quantum numbers of the vacuum (Figure 4.1d),

$$p + p \to p + X + p \tag{4.4}$$

The request alone of no exchange of quantum numbers is not a sufficient condition for a process to be diffractive. It would not eliminate a possible contamination of processes of non-diffractive origin. However the number of such processes is expected to become asymptotically smaller and smaller at higher energies compared to that of diffractive processes. That is why the definition explicitly demand high-energy processes.

Diffractive scattering processes are often *inclusive*, i.e. some of the final-state particles will escape detector acceptance and are hence left unmeasured. When the entire final-state is not fully measured, it would be difficult to know whether the outgoing system has the same quantum numbers as the incoming particles. Therefore, it is often more convenient to provide a second operational and experimentally more useful definition, which is equivalent to the first:

2. *A diffractive reaction is characterized by a large, non-exponentially suppressed rapidity gap in the final-state.*

Following this definition, a process such as the one in Equation 4.2 is diffractive if a large rapidity gap (i.e. a large angular separation) is observed between the final-state proton p and the system X. However, there may be some events of the type in Equation 4.2 which display a large rapidity gap, although they are of a non-diffractive nature. The number of such events are expected to be exponentially suppressed. Denoting the final-state gap in pseudorapidity space as $\Delta\eta$, then the distribution of diffractive events is roughly

$$\frac{\mathrm{d}N}{\mathrm{d}\Delta\eta} \sim \text{constant} \tag{4.5}$$

while that of non-diffractive events is

$$\frac{\mathrm{d}N}{\mathrm{d}\Delta\eta} \sim e^{-\Delta\eta} \tag{4.6}$$

as the final-state particles in a non-diffractive event is assumed to be uniformly distributed in rapidity and to follow Poisson statistics. The distribution of final-state particles in the (η, ϕ)-plane for non-diffractive events is illustrated in Figure 4.2.

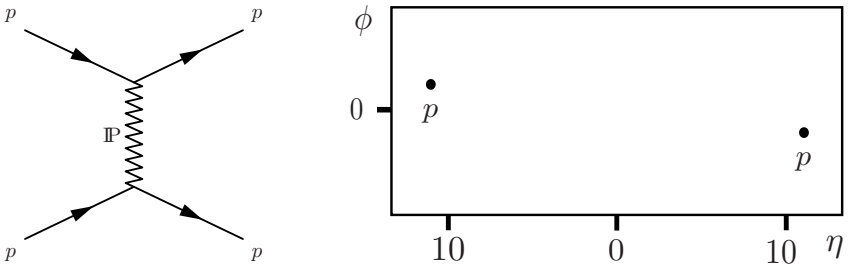

(a) Elastic scattering

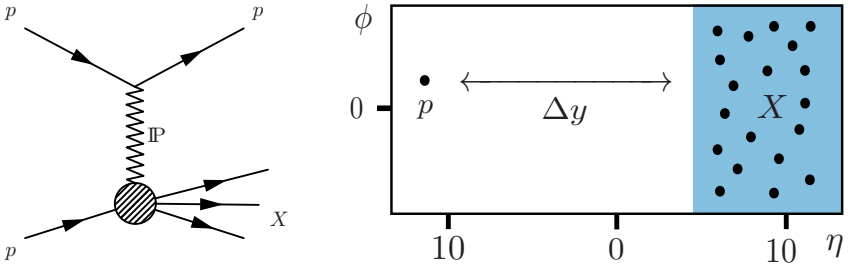

(b) Single diffraction (SD)

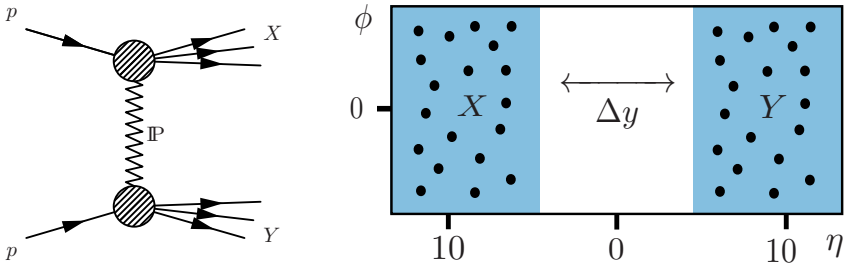

(c) Double diffraction (DD)

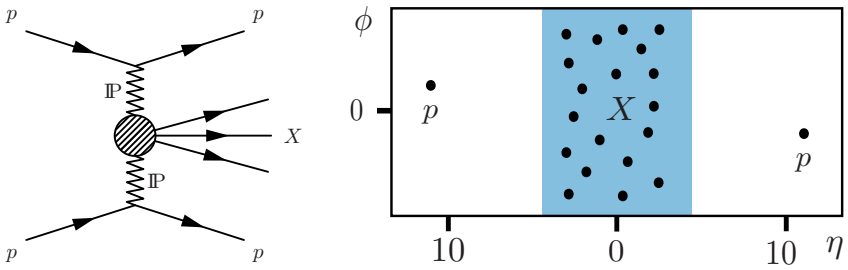

(d) Central diffraction (CD)

Figure 4.1: The four processes covered by diffractive definition 1. The left figures are the relevant Feynman diagrams, and the right figures are the final-state distributions in the (η, ϕ)-plane. These distributions are only for illustrative purposes and to give a general idea of the final-state for each process.

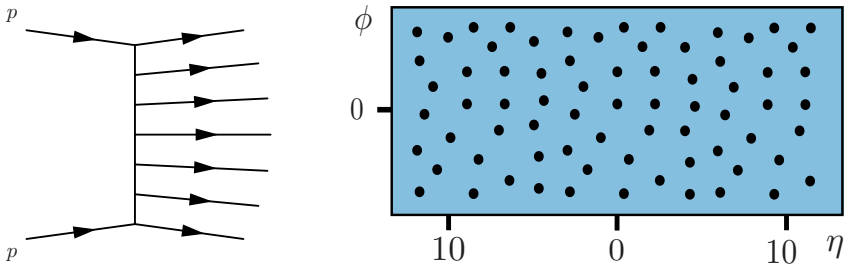

Figure 4.2: Distribution of non-diffractive (ND) events in the (η, ϕ)-plane. Some gaps in rapidity space between particles will occur, but the gap size will be exponentially suppressed. The simplest exchanged particle between the two protons which will lead to a ND event is, in QCD, a single gluon.

Strictly speaking, one should not refer to a specific event as being diffractive or non-diffractive. Instead one should talk about the diffractive and non-diffractive components of the total cross-section. If a specific event is referred to as diffractive, what is really meant is that the event is in a kinematic region (i.e. of rapidity gap or of the relative energy loss ξ as discussed later) where diffraction is the dominant contribution to the total cross-section:

$$\sigma_{\text{tot}} = \underbrace{\sigma_{\text{el}}}_{\text{Elastic}} + \underbrace{\underbrace{\sigma_{\text{sd}} + \sigma_{\text{dd}} + \sigma_{\text{cd}}}_{\text{Diffractive}} + \underbrace{\sigma_{\text{nd}}}_{\text{Non-diffractive}}}_{\text{Inelastic}} \tag{4.7}$$

At $\sqrt{s} = 13$ TeV, pp collisions are expected to have [30]

$$\sigma_{\text{tot}} \approx 100 \text{ mb} \tag{4.8}$$
$$\sigma_{\text{el}} \approx 25 \text{ mb} \tag{4.9}$$
$$\sigma_{\text{sd}} \approx 20 \text{ mb} \tag{4.10}$$
$$\sigma_{\text{nd}} \approx 50 \text{ mb} \tag{4.11}$$

The term *diffraction* was introduced in high-energy physics in 1950s, and borrows from optical terminology. In optics, the intensity I of diffracted light at small angles θ and large wave numbers k, is given by

$$I(\theta) \simeq I(0)(1 - Bk^2\theta^2) \tag{4.12}$$

where B is proportional to the squared radius of the obstacle or the slit in the screen, and $q \simeq k\theta$ is the momentum transfer. As we shall see, diffractive hadronic processes have a similar behavior of the cross-section,

$$\frac{\mathrm{d}\sigma}{\mathrm{d}t} \simeq \left.\frac{\mathrm{d}\sigma}{\mathrm{d}t}\right|_{t=0} e^{-B|t|} \approx \left.\frac{\mathrm{d}\sigma}{\mathrm{d}t}\right|_{t=0} (1 - B|t|) \tag{4.13}$$

for small $|t| \approx \theta^2$. The slope parameter B is proportional to the squared radius of the target hadron, which in our case is the proton with a charge radius, $r_p \approx 0.88$ fm [14].

4.2 TWO-BODY SCATTERING

Consider the two-body process $1+2 \to 3+4$, a special kind of which is the single diffractive inclusive process $1+2 \to 3+X$ (which is the process of interest in this study), where X denotes a system of particles. The kinematics of two-body processes is described by the three *Mandelstam variables*, defined as

$$s = (p_1 + p_2)^2 = (p_3 + p_4)^2 \tag{4.14}$$
$$t = (p_1 - p_3)^2 = (p_2 - p_4)^2 \tag{4.15}$$
$$u = (p_1 - p_4)^2 = (p_2 - p_3)^2 \tag{4.16}$$

The Mandelstam variables obey the identity

$$s + t + u = \sum_{i=1}^{4} m_i^2 \tag{4.17}$$

which can be derived from the definitions and the energy-momentum conservation, $p_1 + p_2 = p_3 + p_4$. Therefore, only two of the Mandelstam variables are independent. The Mandelstam variables can be interpreted as the center-of-mass (CM) energy in the three different channels,

$$1+2 \;\to\; 3+4 \quad (s\text{-channel}) \tag{4.18}$$
$$1+\overline{3} \;\to\; \overline{2}+4 \quad (t\text{-channel}) \tag{4.19}$$
$$1+\overline{4} \;\to\; \overline{2}+3 \quad (u\text{-channel}) \tag{4.20}$$

where a bar indicates the anti-particle with opposite momentum. In the s-channel, we have CM energy $\sqrt{s} = E_{CM}$, and squared momentum transfer $|t| = Q^2$.

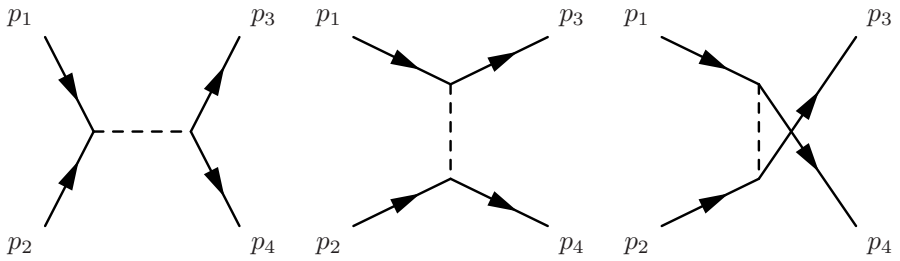

(a) s-channel. **(b)** t-channel. **(c)** u-channel.

Figure 4.3: The three tree-level Feynman diagrams corresponding to the three Mandelstam variables.

If we consider the s-channel process in the center-of-mass (CM) system, we have by definition $\mathbf{p}_1 + \mathbf{p}_2 = 0$, which enables us to write the four-momenta of the particles as

$$p_1 = (E_1, \mathbf{p}) = (E_1, 0, 0, p_z) \tag{4.21}$$
$$p_2 = (E_2, -\mathbf{p}) = (E_2, 0, 0, -p_z) \tag{4.22}$$
$$p_3 = (E_3, \mathbf{p}') = (E_3, \mathbf{p}_T, p'_z) \tag{4.23}$$
$$p_4 = (E_4, -\mathbf{p}') = (E_4, -\mathbf{p}_T, -p'_z) \tag{4.24}$$

where the coordinate system was chosen so that particle 1 and 2 travel along the z-axis. Then by this convention, the s-channel scattering angle θ can be introduced as

$$p'_z = |\mathbf{p}'| \cos\theta \qquad \text{and} \qquad |\mathbf{p}_T| = |\mathbf{p}'| \sin\theta \tag{4.25}$$

The energies E_1, E_2, E_3, and E_4 can be expressed in terms of s as

$$E_{1,2,3,4} = \frac{1}{2\sqrt{s}}(s + m^2_{1,2,3,4} - m^2_{2,1,4,3}) \tag{4.26}$$

Similarly for the momenta, we get:

$$\begin{aligned} \mathbf{p}^2 = p_z^2 &= E_1^2 - m_1^2 \\ &= \frac{1}{4s}\left[s - (m_1 + m_2)^2\right]\left[s - (m_1 - m_2)^2\right] \end{aligned} \tag{4.27}$$

$$\begin{aligned} \mathbf{p}'^2 = \mathbf{p}_T^2 + p'^2_z &= E_3^2 - m_3^2 \\ &= \frac{1}{4s}\left[s - (m_3 + m_4)^2\right]\left[s - (m_3 - m_4)^2\right] \end{aligned} \tag{4.28}$$

4.3 KINEMATICS OF DIFFRACTION

The particular process of interest in this thesis is single diffraction which is part of single-inclusive processes,

$$1 + 2 \to 3 + X \tag{4.29}$$

where X is a system of particles. Reactions of this form are described by three independent variables. It is customary to use the Mandelstam variables s and t (defined in Equation 4.14 and 4.15) as well as the invariant mass of the X system,

$$M_X^2 = (p_1 + p_2 - p_3)^2 \tag{4.30}$$

where it is assumed that X is not a real particle on the mass shell and hence M_X is not fixed.

In the CM system the four-momenta of the three known particles, p_1, p_2, and p_3, can be written as in Equations 4.21-4.23. If we limit

ourselves to the asymptotic case where s and M_x^2 are much larger than the masses of the particles, we have

$$|\mathbf{p}| = p_z \simeq \frac{\sqrt{s}}{2}, \qquad E_1, E_2 \simeq \frac{\sqrt{s}}{2} \tag{4.31}$$

in the limit of $s \gg m_1^2, m_2^2$, and

$$|\mathbf{p}'| \simeq \frac{s - M_X^2}{2\sqrt{s}}, \qquad E_3 \simeq \frac{s - M_X^2}{2\sqrt{s}} \tag{4.32}$$

in the limit $s, M_X^2 \gg m_3^2$. In the case of single diffractive pp-scattering, we will have $m = m_1 = m_2 = m_3$.

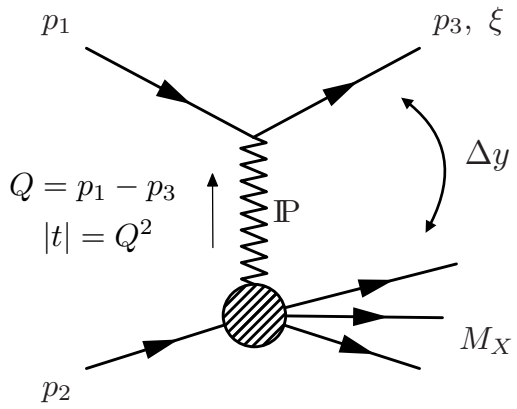

Figure 4.4: Feynman diagram of a single diffractive pp interaction. The common kinematic variables ξ, t, M_X, and Δy are shown.

A kinematic variable of common use when discussing single diffractive processes is the *relative energy loss* ξ, defined as

$$\xi \equiv 1 - \frac{E_3}{E_1} \simeq \frac{M_X^2}{s} \tag{4.33}$$

which will be used extensively throughout this thesis.

Some use the similar Feynman's x_F variable instead, defined as $x_F \equiv |p_3|_z/(p_1)_z$.

The squared momentum transfer t is another commonly used variable in the description of diffractive scattering and will also be frequently referenced in this thesis. From Equation 4.15 we see that

$$\begin{aligned} t &= (p_1 - p_3)^2 = p_1^2 + p_3^2 - 2p_1p_3 \\ &= m_1^2 + m_3^2 - 2E_1E_3 + 2\mathbf{p}_1 \cdot \mathbf{p}_3 \\ &= 2m_p^2 - 2E_1E_3 + 2|\mathbf{p}_1||\mathbf{p}_3|\cos\theta \end{aligned} \tag{4.34}$$

Here θ is the scattering angle between p_1 and p_3 and we have assumed that $m_1 = m_3 = m_p$. We have also used that

$$p^\mu p_\mu = g_{\mu\nu} p^\mu p^\nu = E^2 - \mathbf{p}^2 = m^2 \tag{4.35}$$

where $g_{\mu\nu}$ is the Minkowski metric with signature $(+,-,-,-)$.

In the limit $s, M_X^2 \gg m_p^2$ the transverse momentum of the outgoing scattered particle is

$$\mathbf{p}_T^2 = \mathbf{p}_3^2 \sin^2\theta \simeq -t\left(1 - \frac{M_X^2}{s}\right) \tag{4.36}$$

From Equation 4.33 and 4.36 we see that

$$-t \simeq \frac{p_T^2}{1-\xi} \tag{4.37}$$

Hence, $t \simeq -p_T^2$ for $\xi \simeq 0$. Note that $t \leq 0$.

Another frequently used kinematic variable for describing single diffraction is rapidity y (defined in Equation 2.14) and especially the *rapidity gap* Δy. For very fast particles, i.e. in the limit $p_z \to \infty$, rapidity takes the form:

$$y = \frac{1}{2}\ln\frac{E+p_z}{E-p_z} \simeq \ln\frac{2p_z}{m_T} \tag{4.38}$$

where m_T is the transverse mass, defined as

$$m_T \equiv \sqrt{m^2 + \mathbf{p}_T^2} \tag{4.39}$$

The rapidity of the scattered particle 3 at large s is

$$y_3 = \frac{1}{2}\ln\frac{E_3+p_z'}{E_3-p_z'} \simeq \ln\frac{\sqrt{s}}{m_T} \tag{4.40}$$

The maximum value of y_3 is obtained when $\mathbf{p}_T = 0$,

$$(y_3)_{\max} = \ln\frac{\sqrt{s}}{m} \tag{4.41}$$

The average value of y_X corresponds approximately to a momentum $(p_X)_z \simeq -\sqrt{s}/2$ and to a transverse mass $(M_X)_T \simeq M_X$, hence

$$\langle y_X \rangle \simeq -\ln\frac{\sqrt{s}}{M_X} \tag{4.42}$$

The maximum absolute rapidity of the X system is the rapidity of a particle with momentum $\sim \sqrt{s}/2$ and transverse mass $\sim m$,

$$|y_X|_{\max} \simeq \ln\frac{\sqrt{s}}{m} \tag{4.43}$$

whereas the minimum absolute rapidity corresponds to a particle with momentum $\sim (m/M)\sqrt{s}/2$ and transverse mass $\sim M_X$,

$$|y_X|_{\min} \simeq \ln\frac{m\sqrt{s}}{M_X^2} \tag{4.44}$$

The final-state rapidity gap between the scattered particle 3 and the edge of the rapidity distribution of the X system is then roughly

$$\Delta y \simeq \ln \frac{s}{M_X^2} \tag{4.45}$$

By using the definition of the relative energy loss ξ from Equation 4.33, a relation between ξ and the rapidity gap can be found to be

$$\xi \simeq \mathrm{e}^{-\Delta y} \tag{4.46}$$

It is customary in the literature to use the pseudorapidity gap $\Delta\eta$ here instead. However, one should be careful not to make a too large error in identifying the rapidity y with the pseudorapidity η for a particle with a very small scattering angle θ (see Section 2.5).

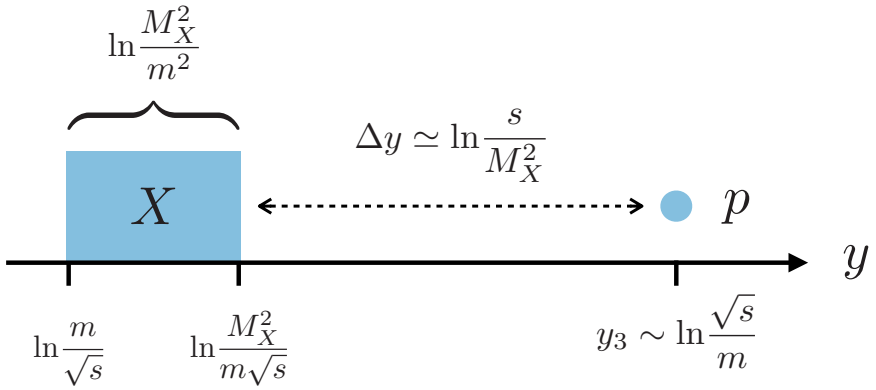

Figure 4.5: Rapidity distribution in the final state of a single diffractive process.

From 4.31 and Equation 4.33, we see that the longitudinal momentum transfer in a single diffractive process with $s, M_X^2 \gg m^2$ is

$$|\Delta p_z| = |p_z - p_z'| \simeq \frac{M_X^2}{2\sqrt{s}} \tag{4.47}$$

According to Good and Walker (1960) [31], the coherence condition between the outgoing and incoming waves that defines diffraction is

$$|\Delta p_z| \lesssim \frac{1}{R} \tag{4.48}$$

where R is the size of the target, which is in our case a proton so that R is of the order of 1 fm. With the appropriate factors of $\hbar$ and c, this corresponds to:

$$|\Delta p_z| \simeq \frac{M_X^2}{2\sqrt{s}} \lesssim 1 \text{ GeV} \quad \Rightarrow \quad \frac{M_X^2}{s} \ll 1 \quad \Rightarrow \quad \xi \sim 0 \tag{4.49}$$

Diffractive events will therefore have a small relative energy loss ξ and hence a large rapidity gap Δy.

4.4 S-MATRIX THEORY

The S-matrix theory was developed in the 1960s as an attempt to completely describe the strong interactions, alternatively to quantum field theory. Some of the methods of S-matrix theory are still useful for describing hadronic phenomena.

The *scattering* matrix (or S-matrix) is the linear operator which transforms the initial or ingoing state $|i\rangle$ of a scattering process into the corresponding final or outgoing state $|f\rangle$:

$$S|i\rangle = |f\rangle \tag{4.50}$$

where the initial state $|i\rangle$ is defined at the time $t = -\infty$ and the final state $|f\rangle$ is defined at $t = \infty$. The states represents plane waves where all the particles can be considered free and non-interacting. The probability for transition is given by,

$$P_{i\to f} = |\langle f|S|i\rangle|^2 \tag{4.51}$$

The S-matrix elements are related to, the arguably most important observable in particle physics, the scattering cross-section. By subtracting the identity operator from S, we can obtain the *transition* matrix T:

$$S = \mathbb{1} + iT \tag{4.52}$$

By enforcing four-momentum conservation, $p_i = p_f$, the S-matrix elements can be written:

$$S_{if} \equiv \langle f|S|i\rangle = \delta_{if} + i(2\pi)^4\delta^4(p_f - p_i)A(i \to f) \tag{4.53}$$

where $A(i \to f)$ is the relativistic *scattering amplitude*, which for a scattering process of the type $1 + 2 \to n$ particles, is related to the differential cross-section by:

$$\mathrm{d}\sigma = \frac{1}{\Phi}|A(i \to f_n)|^2\mathrm{d}\Phi_n \tag{4.54}$$

where Φ is the incident flux and $\mathrm{d}\Phi_n$ is the Lorentz-invariant phase-space (LIPS) measure for n particles in the final-state. The total cross-section is obtained by integrating and summing over all possible numbers of particles n in the final-state.

The general properties assumed for the S-matrix are:

- *relativistic invariance*,
- *unitarity* – $S^\dagger S = SS^\dagger = \mathbb{1}$ which follows from the conservation of probability,

- *analyticity* – the scattering amplitude $A(s,t)$ is an analytical function of the kinematical variables, s and t, when these are continued to complex values,
- *crossing symmetry* – knowing $A(s,t,u)$ in either the s-, t-, or u-channel makes it is possible to analytically continue the amplitude to the other channels.

It is natural to require S to be relativistically invariant. The matrix elements of S can then be expressed in terms of Lorentz-invariant combinations of the kinematic variables in the form of the Mandelstam variables.

4.4.1 *The Optical Theorem*

An important result that follows directly from unitarity is the *optical theorem*. In the case of a $2 \to 2$ elastic scattering, the initial and final states are identical, $|i\rangle = |f\rangle$. In this case, one can find that

$$\sigma_{\text{tot}} = \frac{2}{\Phi} \operatorname{Im} A_{\text{el}}(s, t = 0) \tag{4.55}$$

which is the formulation of the optical theorem for relativistic $2 \to 2$ scattering. The optical theorem can be used to provide a relation between the elastic and total cross-section by

$$\frac{\mathrm{d}\sigma_{\text{el}}}{\mathrm{d}t} \propto \sigma_{\text{tot}}^2 \tag{4.56}$$

Hence, measurements of the differential elastic cross-section $\mathrm{d}\sigma_{\text{el}}/\mathrm{d}t$, can be used to fit and extract the total cross-section.

4.4.2 *The Froissart-Martin Bound*

An important and rigorous theorem found from the theory of the S-matrix, is the Froissart-Martin bound that states that the total cross-section cannot grow faster than $\ln^2(s)$,

$$\sigma_{\text{tot}}(s) \leq c \ln^2\left(\frac{s}{s_0}\right), \quad \text{as } s \to \infty \tag{4.57}$$

where s_0 is an unspecified energy scale and c is a constant bound by

$$c \leq \frac{\pi}{m_\pi^2} \approx 60 \text{ mb} \tag{4.58}$$

where m_π is the pion mass. The Froissart-Martin bound will give an upper bound on the asymptotic (increasing energy) behavior of the total cross-section.

4.5 REGGE THEORY

Regge theory was developed in the 1960s and precedes QCD. It has had significant phenomenological success in describing soft and non-perturbative hadronic processes, for which no alternative theoretical framework is – at least presently – available. The ultimate goal of studying hard diffractive processes is to translate Regge theory into the language of QCD, the theory of strong interactions.

The idea of Regge theory is to introduce into scattering theory, the analytical continuation of scattering amplitudes into the complex angular-momentum plane. Regge theory is based on the general properties of field theory and the relativistic S-matrix: unitarity, crossing symmetry, and analyticity. Let us consider a generic reaction by single-particle exchange in the s- and t-channel (see Figure 4.3a and 4.3b). Our starting point will be the partial-wave expansion of the scattering amplitude in the s-channel, $A(s,t)$, given by

$$A(s,t) = \sum_{\ell=0}^{\infty} (2\ell+1) A_\ell(s) P_\ell(z) \tag{4.59}$$

where

$$A_\ell(s) = \frac{1}{2} \int_{-1}^{+1} \mathrm{d}z P_\ell(z) A(s, t(z,s)) \tag{4.60}$$

and where ℓ is the s-channel angular momentum, $P_\ell(z)$ are the Legendre polynomials, and

$$z \equiv \cos(\theta) = 1 + \frac{2t}{s - 4m^2} \tag{4.61}$$

We can then use crossing symmetry to go to the t-channel:

$$A(s,t) = \sum_{\ell=0}^{\infty} (2\ell+1) A_\ell(t) P_\ell(z_t) \tag{4.62}$$

with

$$z_t \equiv \cos\theta_t = 1 + \frac{2s}{t - 4m^2} \tag{4.63}$$

In the high-energy limit of $s \to \infty$ and keeping t be fixed, we get

$$P_\ell(z_t) \underset{|z_t|\to\infty}{\sim} z_t^\ell \qquad \Rightarrow \qquad A(s,t) \underset{s\to\infty}{\sim} s^\ell \tag{4.64}$$

This leads us to a divergent series for $A(s,t)$. Introducing complex angular momenta allows getting a representation for $A(s,t)$ which is valid in all channels. The relativistic partial-wave amplitude $A_\ell(t)$ can be analytically continued to complex ℓ values. The resulting function, $A(\ell,t)$, will then have simple poles at

$$\ell = \alpha(t) \tag{4.65}$$

where $\alpha(t)$ is called the *Regge trajectory*.

In the presence of a Regge pole, the partial-wave amplitude $A(\ell, t)$ behaves for $\ell \to \alpha(t)$ as

$$A(\ell, t) \underset{\ell \to \alpha(t)}{\sim} \frac{\beta(t)}{\ell - \alpha(t)} \tag{4.66}$$

where $\beta(t)$ is the residue function. The Regge trajectory $\alpha(t)$ takes integer values of ℓ at some non-physical value of t (i.e. for $t > 0$). These Regge poles corresponds to resonances or bound states of increasing angular momentum (i.e. spin) ℓ. The Regge trajectory $\alpha(t)$ (or *Reggeon*) then interpolates such resonances or bound states. Reggeons are collectively denoted by the symbol $\mathbb{R}$.

A simple way to visualize the Regge trajectories, is to expand $\alpha(t)$ in a power series around $t = 0$. Then we get a linear trajectory for small t:

$$\alpha(t) = \alpha(0) + \alpha' t \tag{4.67}$$

where $\alpha(0)$ is the *intercept* and α' is the *slope* of the Regge trajectory. The leading mesonic trajectories, the ρ, the f_2, the a_2, and the ω, are all shown in Figure 4.6. The leading mesonic trajectories all lie on the same trajectory, with an intercept $\alpha(0) \approx 0.5$ and a slope α' of the order of 1 GeV^{-2}.

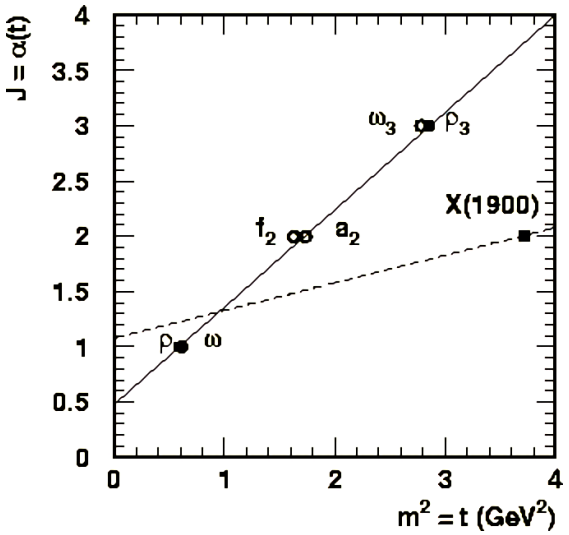

Figure 4.6: Plot of $J = \alpha(t)$ vs. $|t|$ for different observed resonances. The leading mesonic Regge trajectory is indicated by the solid line, while the Pomeron trajectory is indicated by the dashed line. A $J^{PC} = 2^{++}$ glueball candidate state $X(1900)$ observed by the WA91 collaboration is also shown. Figure from [32].

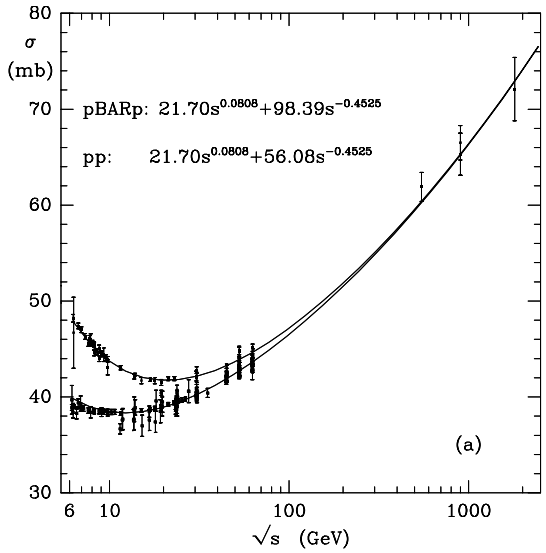

Figure 4.7: The total cross-sections for pp and $p\overline{p}$ scattering as a function of the center-of-mass energy, $\sqrt{s}$. The cross-sections has been fitted with $\sigma_{\text{tot}} = Xs^{\alpha_{\mathbb{P}}(0)-1} + Ys^{\alpha_{\mathbb{R}}(0)-1}$ where X and Y are reaction-dependent free parameters. We see that $\alpha_{\mathbb{P}}(0) \approx 1.08$ and $\alpha_{\mathbb{R}}(0) \approx 0.547$. Figure from [33]. For a recent result see [34].

The scattering amplitude of a two-body scattering process can, in the large s limit and in the case of a single Reggeon exchange, be written as

$$A(s,t) = f(t)s^{\alpha(t)} \tag{4.68}$$

where the function $f(t)$ includes both the residue and the signature factor. The optical theorem then implies that the total cross-section is

$$\sigma_{\text{tot}} \underset{s\to\infty}{\simeq} \frac{1}{s}\,\text{Im}\,A(s,t=0) \underset{s\to\infty}{\sim} s^{\alpha(0)-1} \tag{4.69}$$

in the case of a single-pole contribution. If more than one pole contributes, then the total cross-section is given by a sum of terms of the form

$$\sigma_{\text{tot}} \sim \sum_i A_i s^{\alpha_i(0)-1} \tag{4.70}$$

The high-energy behavior of the total cross-section is then determined by the intercept of the Regge trajectory, as

$$\alpha(0) > 1 \quad \Rightarrow \quad \sigma_{\text{tot}} \text{ increases} \tag{4.71}$$
$$\alpha(0) = 1 \quad \Rightarrow \quad \sigma_{\text{tot}} \text{ constant} \tag{4.72}$$
$$\alpha(0) < 1 \quad \Rightarrow \quad \sigma_{\text{tot}} \text{ decreases} \tag{4.73}$$

The leading mesonic trajectory with an intercept of $\alpha(0) \sim 0.5$, will give a decreasing contribution for low t to the total cross-section, $\sigma_{\text{tot}} \sim s^{-0.5}$. On Figure 4.7 we see that this works for low energies but will not describe the asymptotically increasing total cross-section observed. To describe the increasing total cross-section for higher energies, one needs to introduce the *Pomeron*.

4.6 THE POMERON

The Pomeron is named after one of the founding fathers of hadronic diffractive physics, I. Ya. Pomeranchuk.

To account for the increase in the total pp cross-section an additional Regge trajectory is introduced. This trajectory is known as the *Pomeron*, a hypothetical particle with the quantum numbers of the vacuum, denoted by $\mathbb{P}$. The Pomeron trajectory does not correspond to any meson and is often modelled as

$$\alpha(t) = 1 + \varepsilon + \alpha' t \tag{4.74}$$

where $\varepsilon = 0$ corresponds to a *critical* Pomeron. A Pomeron with $\varepsilon > 0$ is called *supercritical*, and will give rise to an increasing total cross-section. Fits to the total cross-section for different types of elastic scattering [35], indicates that

$$\alpha_{\mathbb{P}}(0) = 1 + \varepsilon = 1.08 \qquad \text{and} \qquad \alpha'_{\mathbb{P}} = 0.25\ \text{GeV}^{-2} \tag{4.75}$$

which will give a $\sim s^{0.08}$ term to the total cross-section.

The framework of Regge theory describes hadronic reactions at high energies in terms of the exchange of 'objects' called Reggeons. A proton may emit (and reabsorb) a Reggeon (for example a positive pion π^+) for a short virtual while, as seen on Figure 4.8. If another proton were to probe this proton at this point, it would interact with the Reggeon. A pion carries color charge and hence a color connection between the two protons would arise. This would result in multiple particle production in the full rapidity space between the two protons. Exchange of mesonic Reggeons will dominate at low interaction energy.

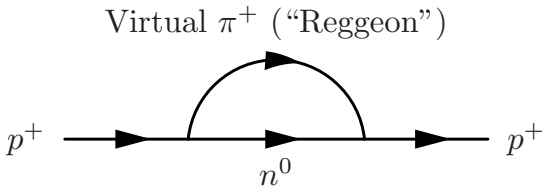

Figure 4.8: Proton emitting and then reabsorbing a virtual Reggeon, in this case a π^+.

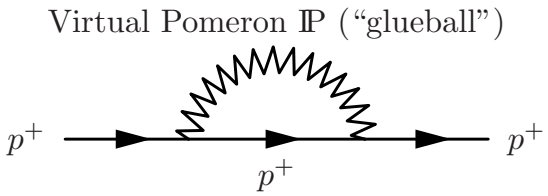

Figure 4.9: Proton emitting and then reabsorbing a virtual Pomeron.

The Reggeon with quantum numbers of the vacuum and which dominates asymptotically (i.e. at high energy) is the Pomeron. A proton may emit (and reabsorb) a Pomeron for a short virtual while, as seen of Figure 4.9, similarly to the Reggeons. This is more likely at high energy. The exchange of other scalar particles with vacuum quantum numbers, contributing to non-diffractive events, is suppressed at high energy. Therefore in Regge theory, the diffractive reactions are those dominated by Pomeron exchange.

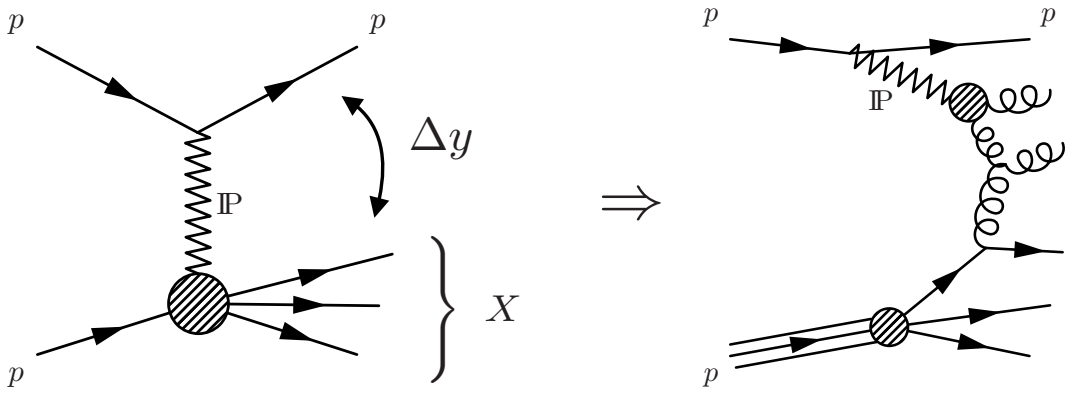

Figure 4.10: Feynman diagrams of a single diffractive pp-scattering by the exchange of a Pomeron with a partonic substructure in the picture of Ingelman and Schlein [5].

In the picture of Ingelman and Schlein [5] the Pomeron takes a partonic substructure. The Pomeron is expected to be a *glueball* state, rather than a conventional resonance. It results from a complicated exchange of gluons (at least two) in a so-called *gluon ladder*. The Feynman diagram for a glueball Pomeron in a single diffractive event is shown in Figure 4.10. The Pomeron trajectory along with a $J^{PC} = 2^{++}$ glueball candidate is shown in Figure 4.6.

4.6.1 *Two-Pomeron Model: A Soft and a Hard Pomeron*

Hadronic processes are usually classified in two distinct classes: *soft processes* and *hard processes*.

The soft processes are characterized by an energy scale of the order of the hadron size $R \sim 1$ fm, as well as a small momentum transfer squared $|t| \sim 1/R^2$. Perturbative QCD is inadequate to describe soft reactions and hence Regge theory has been the go-to framework for soft hadronic processes.

The hard processes are characterized by two energy scales: one is the hadron size, and the other is a hard energy scale. The momentum transfer is of the order of the hard scale and is quite large, $Q^2 \gtrsim 1$ GeV^2. The high momentum transfer allows the use of perturbative QCD. Deep inelastic scattering and events with a large-p_T jet production are two examples of hard processes.

Diffraction most often find itself in the soft regime. However, hard diffraction is of great interest as it opens up the possibility of studying diffractive scattering in a perturbative setting as well as probing the QCD nature of the Pomeron. The ultimate goal is to translate Regge theory into the language of QCD.

The Pomeron that emerges from the fits to the total cross-sections, with an intercept of $\varepsilon \approx 0.08$, is often called the *soft Pomeron*. The soft Pomeron is non-perturbative, and hence very difficult to derive from QCD, but is well known from a large amount of data from the last 60 years.

There also seems to be a *hard Pomeron*, described by the perturbative BFKL equation of QCD, but as of yet is supported by little or no experimental data. A perturbative QCD approach predicts a much higher intercept of $\varepsilon \approx 0.15$ for the hard Pomeron. There are some experimental hints of the existence of the hard Pomeron [36], but a lot still remains to be understood about hard Pomeron exchange.

4.6.2 *The Pomeranchuk Theorem*

The *Pomeranchuk theorem for total cross-sections* states that at high energy the total cross-sections for proton-proton and proton-antiproton scattering become equal,

$$\sigma_{\text{tot}}(pp) \underset{s\to\infty}{\simeq} \sigma_{\text{tot}}(p\overline{p}) \tag{4.76}$$

The theorem is nicely illustrated in Figure 4.7, where the total cross-sections for pp and $p\overline{p}$ scattering is plotted. For increasing center-of-mass energy $\sqrt{s}$, the two cross-sections get asymptotically closer.

The Pomeranchuk theorem can be understood in the context of the Pomeron and the Reggeons. For low interaction energy $\sqrt{s}$, the exchange of mesonic Reggeons (such as the pions) will dominate. But at high energy, the exchange of the Pomeron will dominate. As the Pomeron carry the quantum numbers of the vacuum, it will treat protons and antiprotons alike. This is not the case for the mesonic Reggeons.

4.7 POMERON FLUX PARAMETERIZATION

Hadronic diffraction is not well-understood and many different approaches exist. In this section we will consider the approach followed by the general-purpose event generator PYTHIA 8 [6]. PYTHIA follows a conventional Pomeron-based approach pioneered by Ingelman and Schlein [5] that makes use of the full PYTHIA machinery of parton showers, hadronization, and multiparton interactions. For a full review of the diffractive models in PYTHIA, see references [37] and [38].

The soft diffraction framework in PYTHIA 8 was originally developed for its predeccesor PYTHIA 6, but rewritten and expanded for the new version. The total cross-section is calculated using the Donnachie-Landshoff parameterization [33] which includes both a Pomeron and a Reggeon term. The elastic and diffractive cross-sections are then calculated using the Schuler-Sjöstrand model [30], which is based on Regge theory and gives an exponential t-dependence and an approximate $\mathrm{d}M^2/M^2$ mass dependence. Additional fudge factors are introduced to dampen the cross-section.

The hard diffraction framework in PYTHIA 8 is based on the assumption that the Pomeron exists inside the proton in the Ingelman-Schlein spirit [5]. In this view, a *Pomeron flux* $f_{\mathbb{P}/p}(x_{\mathbb{P}}, t)$ is introduced, where $x_{\mathbb{P}}$ is the Pomeron momentum fraction from the proton, and t is the Pomerons spacelike virtuality. The Pomeron flux can be seen as a parton distribution function (PDF) describing the number density of Pomerons in the proton. In addition, the Pomeron has a partonic sub-

structure and hence has PDFs itself, $f_{i/\mathbb{P}}(x, Q^2)$, similar to the proton. Given these assumptions, the proton PDF can be split into a diffractive and a non-diffractive part, as

$$f_{i/p}(x, Q^2) = f_{i/p}^{\mathrm{ND}}(x, Q^2) + f_{i/p}^{\mathrm{D}}(x, Q^2) \tag{4.77}$$

with the diffractive part $f_{i/p}^{\mathrm{D}}$ being described using the factorization approach of Ingelman and Schlein, as

$$\begin{aligned} f_{i/p}^{\mathrm{D}}(x, Q^2) &= \int_0^1 \mathrm{d}x_{\mathbb{P}} f_{\mathbb{P}/p}(x_{\mathbb{P}}) \int_0^1 \mathrm{d}x' f_{i/\mathbb{P}}(x', Q^2) \delta(x - x_{\mathbb{P}} x') \\ &= \int_x^1 \frac{\mathrm{d}x_{\mathbb{P}}}{x_{\mathbb{P}}} f_{\mathbb{P}/p}(x_{\mathbb{P}}) f_{i/\mathbb{P}}\left(\frac{x}{x_{\mathbb{P}}}, Q^2\right) \end{aligned} \tag{4.78}$$

where

$$f_{\mathbb{P}/p}(x_{\mathbb{P}}) = \int_{t_{\min}}^{t_{\max}} f_{\mathbb{P}/p}(x_{\mathbb{P}}, t)\, \mathrm{d}t \tag{4.79}$$

and where $f_{i/\mathbb{P}}$ is the number density of partons in the Pomeron. Here we have used the Feynman variable for the Pomeron $x_{\mathbb{P}}$, instead of the relative energy loss of the scattered proton ξ. However they have a simple relation,

$$\xi \simeq 1 - x_{\mathbb{P}} \tag{4.80}$$

This model also implements a dynamic gap survival, by evaluating on an event-by-event basis, the possibility for additional multiparton interactions (MPIs) in the pp system. If no further MPIs are found, then the event is diffractive. Only if no additional MPIs are found in the pp system, is the $\mathbb{P}p$ system set up. This is illustrated in Figure 4.11. This means that there will not be any MPIs in the pp system but the model do allow for MPIs in the $\mathbb{P}p$ system.

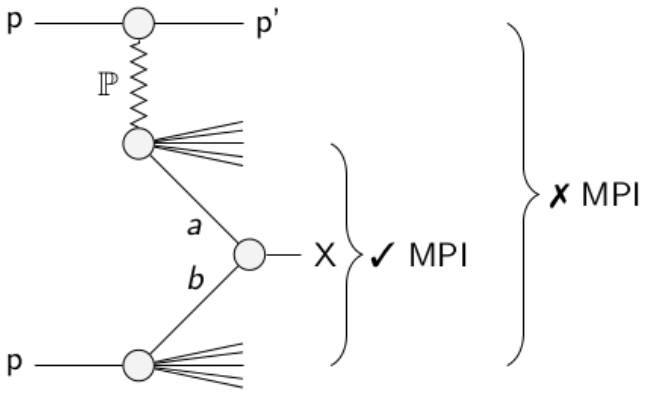

Figure 4.11: Illustration of the dynamic gap survival in the hard diffraction model in PYTHIA. Figure from [38].

Many distributions will be affected by the modelling of the Pomeron flux as well as the Pomeron PDF. These distributions include the relative energy loss ξ, and hence the invariant mass of the diffractive

system M_X and the rapidity gap size Δy. The squared momentum transfer t and hence the scattering angle θ of the surviving proton will also be affected. It was observed in [38] that the distributions will be affected more by the choice of the Pomeron flux parameterization than by the choice of the Pomeron PDF.

Seven different Pomeron flux parameterizations are available in PYTHIA 8, and are shown in Figure 4.12. Three of the seven parameterizations are studied in this thesis. The three includes the Schuler-Sjöstrand [30], the Donnachie-Landshoff [33], and the Minimum Bias Rockefeller (MBR) [39] parameterizations. The Schuler-Sjöstrand parameterization is the default setting in PYTHIA and all three are used in the official Monte Carlo sample generation by both the ATLAS and CMS experiments. In addition, the three differs quite a lot as seen in Figure 4.12, and will hence give a good overall look into diffraction.

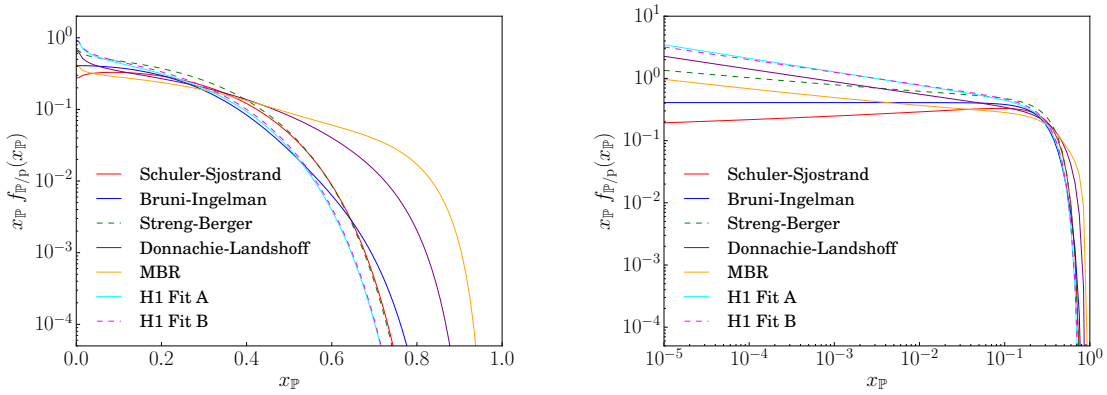

(a) Linear scale **(b)** Logarithmic scale

Figure 4.12: The seven different Pomeron flux parameterizations implemented in PYTHIA 8 on linear (a) and logarithmic (b) scale. Figures from [37].

In the following, the three Pomeron flux parameterizations of interest in this thesis are briefly reviewed.

4.7.1 *The Schuler-Sjöstrand Parameterization*

The Schuler-Sjöstrand parameterization [30] is the default setting in PYTHIA 8. Based on a critical Pomeron with $\varepsilon = 0$ and $\alpha' = 0.25\ \text{GeV}^{-2}$, giving a mass spectrum roughly like $\mathrm{d}M^2/M^2$ and a mass-dependent exponential t-slope that will reduce the rate of low-mass states. The Pomeron flux parameterization is given by

$$f_{\mathbb{P}/p}(\xi, t) = \frac{1}{\xi}(0.02)\sigma^2_{\mathbb{P}p} \exp\left(2t\left[2.3 + 0.25\ln\left(\frac{1}{\xi}\right)\right]\right) \tag{4.81}$$

where $\sigma_{\mathbb{P}p}$ is the assumed Pomeron-proton effective cross-section, as used for multiparton interactions in diffractive systems. By default set

to $\sigma_{\mathbb{P}p} = 10$ mb in PYTHIA. The Schuler-Sjöstrand parameterization in PYTHIA 8 does not allow the user to vary the two parameters of the Pomeron trajectory, ε and α'.

4.7.2 *The Donnachie-Landshoff Parameterization*

A conventional Pomeron description, attributed to Donnachie and Landshoff [33]. Based on a supercritical Pomeron with $\varepsilon > 0$, which will give a stronger peaking towards low-mass diffractive states, and with a power-law t distribution. The Pomeron flux parameterization is given by

$$f_{\mathbb{P}/p}(\xi, t) = \frac{9\beta^2}{4\pi^2}\xi^{1-2\alpha(t)}F_1^2(t) \tag{4.82}$$

where $\beta^2 = 3.43\ \text{GeV}^{-2}$ is the Pomeron-proton coupling and

$$F_1^2 = 0.27\text{e}^{(8.38\ \text{GeV}^{-1})t} + 0.56\text{e}^{(3.78\ \text{GeV}^{-1})t} + 0.18\text{e}^{(1.36\ \text{GeV}^{-1})t} \tag{4.83}$$

The original model only covered single diffraction but has been expanded by analogy to include double and central diffraction. In the Donnachie-Landshoff parameterization, the two parameters of the Pomeron trajectory, ε and α', can be varied.

4.7.3 *The Minimum Bias Rockefeller (MBR) Parameterization*

The MBR model and parameterization [39] follows a renormalized Regge theory model, successfully tested using CDF data. Includes single, double, and central diffraction. The Pomeron flux parameterization is given by

$$f_{\mathbb{P}/p}(\xi, t) = \frac{1}{N_{\text{gap}}(s)}\frac{\beta^2}{16\pi}F_1^2(t)\xi^{1-2\alpha(t)} \tag{4.84}$$

where $\beta^2 = 43.11\ \text{GeV}^{-2}$ is the Pomeron-proton coupling and

$$F_1^2(t) = \left[\frac{4m_p^2 - 2.8t}{4m_p^2 - t}\left(\frac{1}{1 - \frac{1}{1-\frac{t}{0.71}}}\right)^2\right]^2 \tag{4.85}$$

$$\approx 0.9\text{e}^{(4.6\ \text{GeV}^{-1})t} + 0.1\text{e}^{(0.6\ \text{GeV}^{-1})t} \tag{4.86}$$

In the MBR parameterization, the two parameters of the Pomeron trajectory, ε and α', can be varied. There are many additional parameters that can be set for the MBR model (such as N_{gap}) but they will not be studied in this thesis.

Part II

EXPERIMENT

In the previous part, the creation of particles from proton-proton collisions at hadron colliders was described in some detail. This part will provide an explanation of the detection and measurement of the produced and scattered particles. First an overview of the Large Hadron Collider (LHC) at CERN is given, followed by a description of the ATLAS detector and the sub-detectors to the extent relevant to this study. Finally, the ALFA detector will be introduced, which allows for the detection and measurement of the diffractively scattered protons.

5 THE LARGE HADRON COLLIDER

This chapter introduces the Large Hadron Collider (LHC) at CERN. As the ALFA Roman Pots are installed onto the LHC beam pipe, some knowledge of the LHC is required.

5.1 THE CERN ACCELERATOR COMPLEX

The information in this section is based on ref. [40] and [41].

The CERN accelerator complex was established in 1954. The goal was originally to study atomic nuclei but it was soon applied to the study of interactions between subatomic particles. The complex houses the largest particle accelerator ring in the world with a circumference of 26.7 km. The ring was finished in 1988 and up until 2000 housed the Large Electron-Positron Collider (LEP), which was the most powerful accelerator of leptons ever built. The ring now houses the Large Hadron Collider (LHC) which from its onset of operations in 2008 represents the state-of-the-art of particle accelerators.

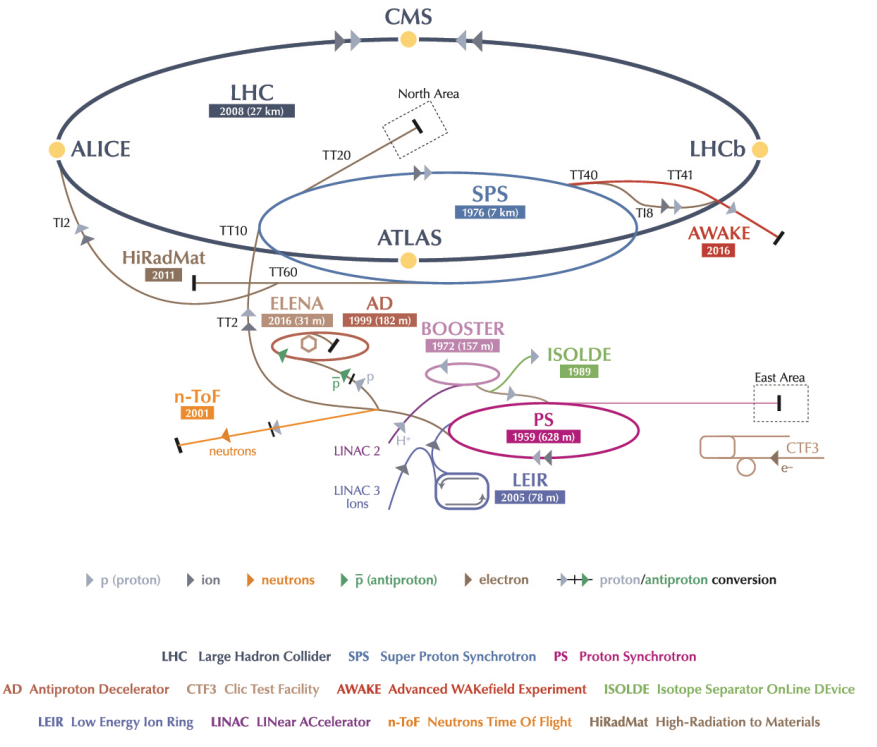

Figure 5.1: Overview of the CERN accelerator complex. Image from [OPEN-PHO-ACCEL-2016-001-2], © 2017 CERN.

The LHC is a two-ring superconducting accelerator and collider installed in a 26.7 km ring located 45 to 170 m below the surface. The LHC is the last step in a larger injection chain that gradually accelerates protons from rest, up to beam energies of 6.5 TeV.

First, a strong electric field is used to strip electrons off of hydrogen atoms to yield protons. The protons are then injected into the Linear Accelerator 2 (Linac2) where an array of three radiofrequency (RF) accelerator tanks will accelerate the protons up to energies of 50 MeV. The beam of protons will then enter a series of three proton synchrotrons – the Proton Synchrotron Booster (PSB), the Proton Synchrotron (PS), and the Super Proton Synchrotron (SPS). The proton beam, leaving the SPS with an energy of 450 GeV, will then enter the LHC.

Once the LHC has reached its target beam energy, the proton beams in the two counter-rotating beam pipes will collide at four interactions points, where the four major LHC experiments are located: ATLAS, CMS, LHCb, and ALICE. The LHC beam pipe is about 3 cm in diameter and has a high vacuum of $\sim 10^{-7}$ Pa to ensure sufficiently long beam lifetimes.

In the first period of operation (Run 1, 2009 to 2013) the LHC collided protons at a center-of-mass energy of $\sqrt{s} = 7$ and 8 TeV. In the ongoing second period of operation (Run 2, 2015 to 2018) the nominal energy has been $\sqrt{s} = 13$ TeV and is expected to reach 14 TeV.

5.2 LUMINOSITY

An important quantity in collider physics (besides the beam energy) is the *luminosity* $\mathcal{L}$ – the number of particles passing down the line per unit time, per unit area. Given a cross-section σ for some process, the total interaction rate $\mathrm{d}N/\mathrm{d}t$ is given by

$$\frac{\mathrm{d}N}{\mathrm{d}t} = \mathcal{L} \times \sigma \tag{5.1}$$

where $\mathcal{L}$ is the instantaneous luminosity. For the LHC, the nominal peak instantaneous luminosity is $\mathcal{L} = 10^{34}\ \mathrm{cm}^{-2}\mathrm{s}^{-1}$ [41]. Integrating over time, will give the total number of collisions (or *events*), as

$$N = \sigma \int \mathcal{L}\mathrm{d}t \tag{5.2}$$

Since both integrated and instantaneous luminosity is denoted by $\mathcal{L}$, we need to rely on the context and the choice of units to distinguish between the two.

where in practice, the integrated luminosity $\int \mathcal{L}\mathrm{d}t$ is the instantaneous luminosity integrated over some LHC run duration, and is measured in units of inverse barn (b^{-1}), where $1\ \mathrm{b} = 10^{-24}\ \mathrm{cm}^2$. The integrated luminosity is a measure of the total amount of data collected during an LHC run, and will be frequently referred to as simply the *luminosity* with the symbol $\mathcal{L}$.

5.3 RUNNING PARAMETERS

This section will give a short introduction to the running parameters and conditions for ensuring collisions. For more in-depth information on the theory behind particle acceleration, the reader is referred to references [42], [43], and [44].

The LHC houses 1232 main superconducting dipole magnets, that are used to bend the paths of the protons. In the linear section around the ATLAS interaction point, a magnetic lattice will focus and tighten the trajectory of the protons inside the beam pipe, to ensure that the stable and precisely aligned beams will collide at the interaction point. This magnetic lattice can be set up into different running configurations, also known as the *optics*. The optics is set depending on the type of run and collisions that should proceed. Naturally, this configuration is of interest to any measurement done with the ALFA detector, as a linear section of magnets is installed in the $\sim$ 240 m between the ATLAS interaction point and the ALFA stations, that will affect the trajectory of an elastically or diffractively scattered proton in the extreme forward direction. Hence, specific running parameters and optics will be requested for studies with ALFA.

To describe the movement of the protons around the LHC ring, a three-dimensional comoving coordinate system is defined and illustrated in Figure 5.2. A position on the reference orbit is given by s with the beam axis in the z-direction. The actual proton orbit can deviate from the reference orbit. The radially outward displacement is denoted by x, while the upward displacement is denoted by y. A given proton can be described by two vectors (u, u') where $u = \{x, y\}$, with u being the position and $u' = \mathrm{d}u/\mathrm{d}z$ being the slope of the particle path relative to the beam axis.

If we ignore energy loss (i.e. momentum dispersion) of the protons, then the oscillating orbits of the protons are given by a single function $\beta(s)$, called the *amplitude function*, which is determined by the configuration of the magnetic lattice. The orbits are given by

$$u(s) = \sqrt{\varepsilon\beta(s)}\cos\left[\Phi(s) - \delta\right] \tag{5.3}$$

$$u'(s) = -\sqrt{\frac{\varepsilon}{\beta(s)}}\left(\sin\left[\Phi(s) - \delta\right] + \sqrt{\varepsilon}\cos\left[\Phi(s) - \delta\right]\right) \tag{5.4}$$

where

- $\Phi(s) = \int_0^s \frac{dz}{\beta(z)}$ is the phase function,
- δ is an arbitrary constant phase shift, and
- ε is the transverse emittance as described below.

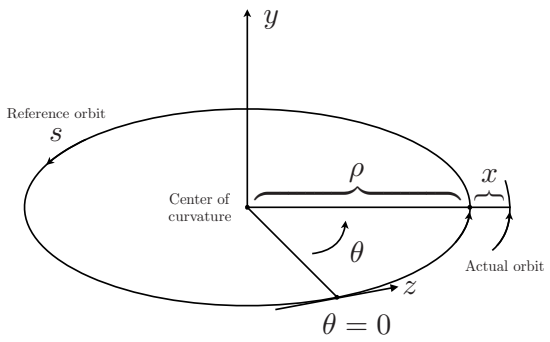

Figure 5.2: Illustration of the LHC comoving coordinate system.

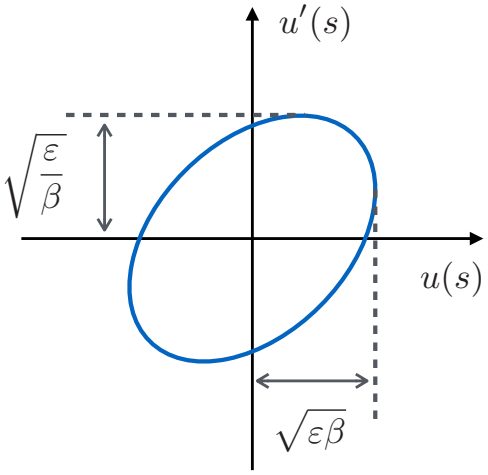

Figure 5.3: The transverse phase space ellipse for a single proton at a particular point on the ring. The ellipse will have an area of $\pi\varepsilon$.

The solutions will map out an ellipse in the transverse phase space (i.e. the (u, u')-plane), centered at zero, but different for each point s along the ring. The ellipse is shown in Figure 5.3. The shape of the ellipse will change with $\beta(s)$, but the area is constant. Here u represents both the horizontal x and the vertical y deviation from the closed orbit of the proton. Hence, $\beta(s)$ represents two different functions $\beta_x(s)$ and $\beta_y(s)$, and likewise will δ represent two different constants. The maximum angular deviation is $u'_{\text{max}} = \sqrt{\varepsilon/\beta}$ and the maximum position deviation is $u_{\text{max}} = \sqrt{\varepsilon\beta}$.

The *transverse emittance* ε is defined as the area (divided by π) of the ellipse that contains a certain fraction (usually 95%) of the beam protons. The emittance is determined solely by the initial conditions. As for the β-function, there exists a separate horizontal ε_x and vertical ε_y emittance. The emittance changes as a function of the beam momentum – increasing the energy of the beam protons will reduce the emittance. Therefore, it is often more useful to consider the *normalized emittance* ε_N, defined as

$$\varepsilon_N = \gamma\beta\varepsilon = \left(\frac{p_0}{m_0 c}\right)\varepsilon \tag{5.5}$$

which is constant during the acceleration of the beam protons. Here β and γ are the relativistic functions.

5.4 BEAM OPTICS AND CROSSING ANGLE

The value of the amplitude function, $\beta(s)$, at the interaction point is referred to as the *optics* of a run with the symbol $\beta^* \equiv \beta(s = 0)$. The value of β^* will refer to the distance from the interaction point (the focus point) where the beam width is twice as wide as at the interaction point.

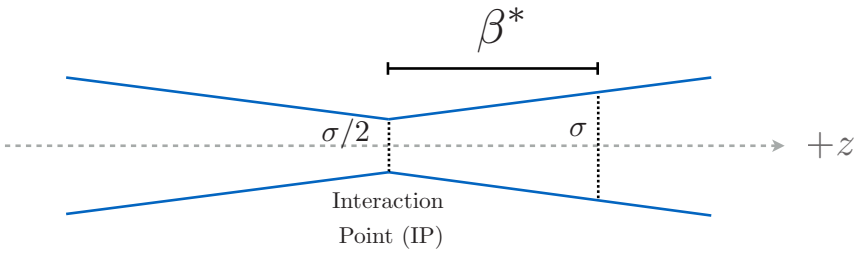

Figure 5.4: Illustration of the optics, β^*, as the distance from the interaction point where the beam width is twice that at the interaction point.

The LHC magnets can be tuned to a different optics for any given run. For most LHC runs, the optics is chosen to have a low β^* value (around 0.55 m) to get as small beams as possible and thereby a large luminosity. This setting is ideal for the search for new physics beyond the SM, as it will provide a large number of total events and therefore more statistics for very rare events which are interesting for Higgs and Beyond the Standard Model (BSM) physics.

However, in the data runs used in this thesis, a large optics of $\beta^* = 90$ m has been used. This will give large beams but low luminosity and small angles of the incoming beam protons.

The low luminosity will result in a small *pile-up* (multiple simultaneous proton-proton collisions per bunch crossing). A low pile-up is necessary for proper reconstruction of tracks in ALFA. In Run 1, during the 2012 data-taking, the peak instantaneous luminosity was $\sim 7 \times 10^{33}$ cm^{-2}s^{-1}, resulting in every hard interaction being accompanied by an average number of pile-up collisions of $\langle\mu\rangle = 20.7$ [45].

The expected average pile-up multiplicity (i.e. number of collisions per bunch crossing), $\langle\mu\rangle$, is given by [46]

$$\langle\mu\rangle = \frac{\mathcal{L} \times \sigma_{\text{inel.}}}{N_{\text{bunch}} \times f_{\text{LHC}}} \tag{5.6}$$

where $\mathcal{L}$ is the instantaneous luminosity, $\sigma_{\text{inel.}}$ is the total inelastic cross-section, and $N_{\text{bunch}} \times f_{\text{LHC}}$ is the average bunch-crossing frequency, which is nominally $(25\text{ ns})^{-1}$ for Run 2 but was $(50\text{ ns})^{-1}$ for Run 1.

Pile-up interactions are often of a soft QCD nature, and can drown out the single diffractive signal in ALFA. We are therefore interested in the pile-up being as low as possible. For the diffractive data runs analyzed in this thesis, the average number of pile-up collisions was $\langle \mu \rangle \approx 0.0863$ at an average instantaneous luminosity $\mathcal{L} \approx 8.21 \times 10^{30}$ cm^{-2}s^{-1} [47].

The small angles of the beam protons will make it possible to neglect the angles of the incoming protons and thereby making it easy to measure the scattering angle of the diffractively scattered protons. In fact, a high β^* is necessary for data taking with the ALFA detector, as the ALFA detector is built to measure scattered protons with very small angles.

Furthermore, to avoid that a given bunch from beam 1 will collide with several bunches from beam 2, the LHC beams will collide with a crossing angle. The crossing angle of the beams are set in the (y, z)-plane and for the data runs of interest in this study, the crossing angle is set to $\theta_C = 2 \times 50$ μrad as seen on Figure 5.5, i.e. each beam will have an angle -50 μrad with respect to the beam axis.

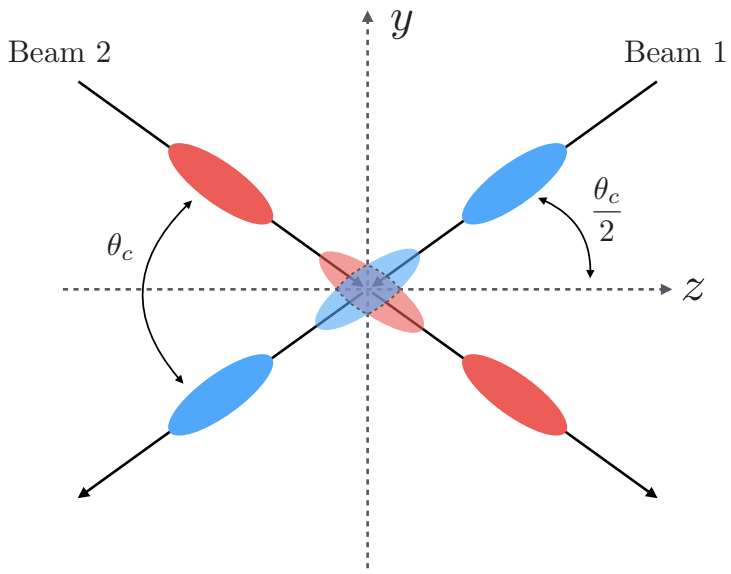

Figure 5.5: Illustration of the beam crossing angle at the LHC.

We will throughout this thesis set the coordinate system such that the ATLAS interaction point IP1 is at $s = 0$ or $z = 0$. The proton beams will have a certain size and hence the interaction vertex will be distributed around the beam spot – the point of bream crossing. Measurements of the position and size of the beam spot for the data run studied in this thesis are shown in Figure 5.6.

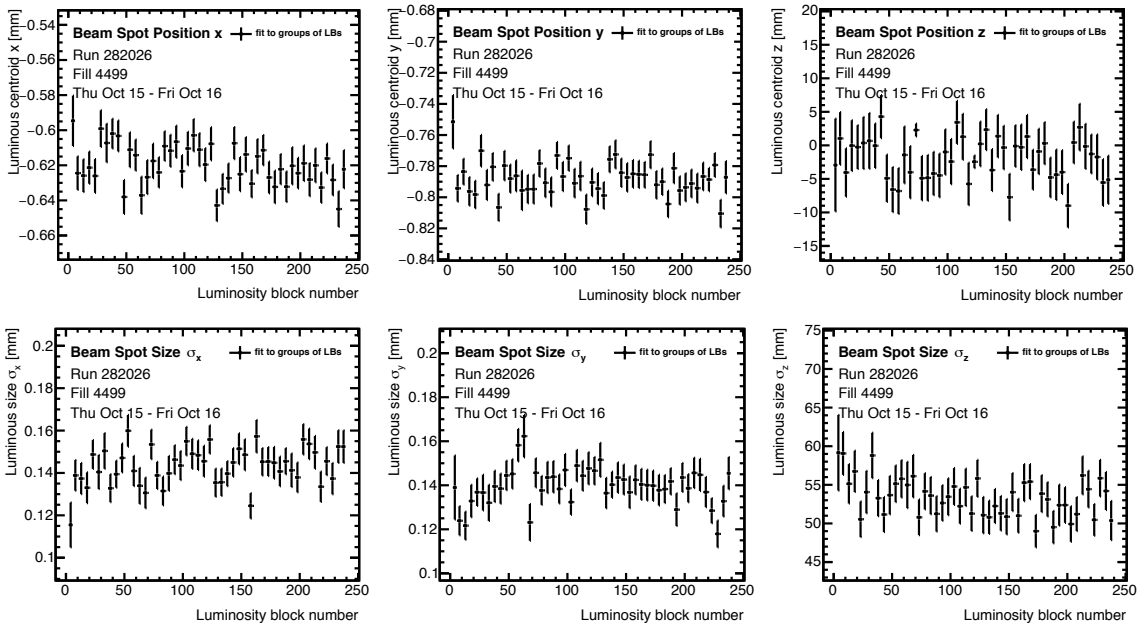

Figure 5.6: Beam spot measurements from the ATLAS inner detector in run 282026 [48].

The average beam spot position and size along with uncertainties are estimated from the graphs in Figure 5.6 and are found to be

$$x_{\text{BS}} = (-0.62 \pm 0.05)\ \text{mm}, \qquad \sigma_{x,\,\text{BS}} = (0.14 \pm 0.05)\ \text{mm} \tag{5.7}$$

$$y_{\text{BS}} = (-0.79 \pm 0.05)\ \text{mm}, \qquad \sigma_{y,\,\text{BS}} = (0.14 \pm 0.05)\ \text{mm} \tag{5.8}$$

$$z_{\text{BS}} = (-3.0 \pm 1.0)\ \text{mm}, \qquad \sigma_{z,\,\text{BS}} = (53.0 \pm 1.0)\ \text{mm} \tag{5.9}$$

These values will be used in both the simulation and data analysis.

The normalized emittances can be used to find the beam divergence for a given run. The beam divergence will contribute to the angles of the diffractively scattered protons and can be found by [49]

$$D_u^{\text{Beam } n} = \sqrt{\frac{\varepsilon_u^{\text{Beam } n}}{\gamma \beta^*}} \qquad \text{where} \quad u = \{x, y\} \tag{5.10}$$

where $\gamma = \frac{E_{\text{Beam}}}{m_p} \approx 6929.64$, $\beta^* = 90$ m, and ε_u are the normalized transverse emittances which are found from wire scans [50] of the beam during data taking. From the LHC eLogBook [51], the normalized emittances for our data runs were found to be

$$\varepsilon_x^{\text{Beam 1}} = (3.5 \pm 0.4)\ \mu\text{m} \times \text{rad} \tag{5.11}$$

$$\varepsilon_y^{\text{Beam 1}} = (3.3 \pm 0.3)\ \mu\text{m} \times \text{rad} \tag{5.12}$$

$$\varepsilon_x^{\text{Beam 2}} = (4.3 \pm 0.4)\ \mu\text{m} \times \text{rad} \tag{5.13}$$

$$\varepsilon_y^{\text{Beam 2}} = (3.5 \pm 0.4)\ \mu\text{m} \times \text{rad} \tag{5.14}$$

with a 10% uncertainty on the wire scans [49]. The beam momentum spread due to the beam divergence, can be found by the simple relation, $\sigma_{p_u} = D_u \times p$.

The measurements of the beam spot widths from before can be used as a stability check of the wire scans. The beam spot width is related to the emittance by [49]

$$\sigma_u = \frac{\sqrt{\beta^*/\gamma}}{\sqrt{1/\varepsilon_u^{\text{Beam 1}} + 1/\varepsilon_u^{\text{Beam 2}}}} \quad \text{where} \quad u = \{x, y\} \tag{5.15}$$

where a Gaussian distribution is assumed for both beams. We get the calculated beam spot widths to be $\sigma_x = 0.16$ mm and $\sigma_y = 0.15$ mm, which are in approximate agreement with the average measured values from Figure 5.6.

5.5 SIMULATION OF BEAM TRANSPORT

Several dipole and quadrupole magnets exists between the ATLAS interaction point and the ALFA Roman Pots, as depicted on Figure 5.7. The knowledge about the magnetic lattice in the LHC between the interaction point and the ALFA detectors, can be used to simulate the trajectories of the diffractively scattered protons in the beam pipe.

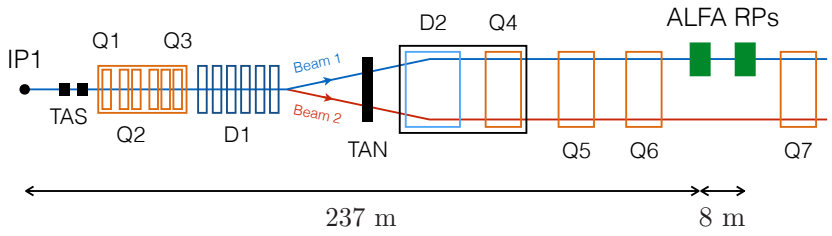

Figure 5.7: Illustration of the magnets between the ATLAS interaction point and the ALFA Roman Pots. Items labelled with a 'D' are dipole magnets, while items labelled with a 'Q' are quadrupole magnets. Reproduction of similar figures from [52] and [53].

The standard package for the simulation of the behavior of charged particles in alternating-gradient accelerators, is `MAD-X` [54] – a general-purpose tool specifically adapted to the design of the LHC. `MAD-X` allows for the use of the *thick lens case* in contrast to the thin lens approximation. `MAD-X` will generate *Twiss files* that contains information on each element of the magnetic lattice (dipoles, quadrupoles, drift spaces, solenoids, bending magnets, beam monitors, etc.). For each element, a large amount of information is stored, including the position s, the values of $\beta(s)$, $\Phi(s)$, and δ in both the horizontal and vertical direction, as well as the aperture survival information. `MAD-X` does not take the LHC collimators into account, however this is not important as the collimators was, for the data runs used in this thesis, retracted far enough away from the beam as to not have an effect on the aperture survival.

The Twiss files generated by MAD-X can be used by the Athena package ForwardTransportFast to simulate the proton trajectories in the LHC beam pipe. ForwardTransportFast will transport particles directly from the interaction point to a specified position s on the beamline. The package reads the given HepMC event collection and appends successfully transported particles to the collection. The package will in the case of the ALFA detector, only transport protons with a positive charge. Other particles that may live long enough and have a large enough energy to reach the ALFA detector, such as antiprotons, charged pions, and muons, will therefore not be simulated by ForwardTransportFast. For this purpose, a more involved simulation using GEANT4 [55] may be necessary. However, a full GEANT4 simulation of ALFA does not exist at present time. ForwardTransportFast is preceded by the older Athena package ALFA_BeamTransport.

The trajectories of protons from the ATLAS interaction point to the ALFA detectors for a collision energy $\sqrt{s} = 13$ TeV, optics of $\beta^* = 90$ m, and a crossing angle $\theta_C = 2 \times 50$ μrad are shown for different proton energies in Figure 5.8 and 5.9. The approximate positions of the quadrupoles and dipoles, that are responsible for the bending and focusing of the protons, are also shown. In addition, kicker magnets in both the vertical and horizontal directions are located between the interaction point and the ALFA stations, to 'kick' the protons into position. The x and y coordinates in the transverse plane for different values of s were found using MAD-X and ForwardTransportFast. The protons were generated with a primary vertex at $(0, 0, 0)$. The protons were generated according to the beam such that $p_x = 0$ and

$$p_y = -\sin(50\ \mu\text{rad}) \times 6500\ \text{GeV} \approx -0.325\ \text{GeV} \tag{5.16}$$

such that $p_T = 0$ relative to the beam. The coverage of the ALFA detector in x and y is roughly shown. A proton with $\xi = 0.16$ but otherwise resembles a beam proton will hit the inner ALFA detector at $z = 237$ m and might just barely hit the outer detector at $z = 245$ m detector. See Figure 8.14 for the exact shape of the ALFA detectors in the transverse plane. Note that the trajectories will also depend on p_x and p_y as well as the interaction vertex, x_{IP} and y_{IP}. The momentum dependence is shown in Figure 5.10 and 5.11, while the vertex dependence is shown in Figure 5.12 and 5.13. Notice that p_x and x_{IP} will only affect the trajectory in the x-direction, and that p_y and y_{IP} will only affect it in the y-direction. This is because the horizontal and vertical betatron oscillations are completely decoupled in a linear section of an accelerator containing only dipoles and quadrupoles. The dependence of the ALFA hit position on energy loss, momentum, and primary vertex will be studied in detail in Section 8.2.

From Figure 5.8 it is seen that with increasing energy loss ξ, the proton deflection in the x-axis direction as well as the y-axis direction increases. The deflection in x is also for protons in events with a non-zero crossing angle. The deflection in y is due to the crossing angle and will be discussed later. The difference in the x-coordinate between the near and far stations, $\Delta x = x_{245\,\mathrm{m}} - x_{237\,\mathrm{m}}$, will likewise grow with ξ.

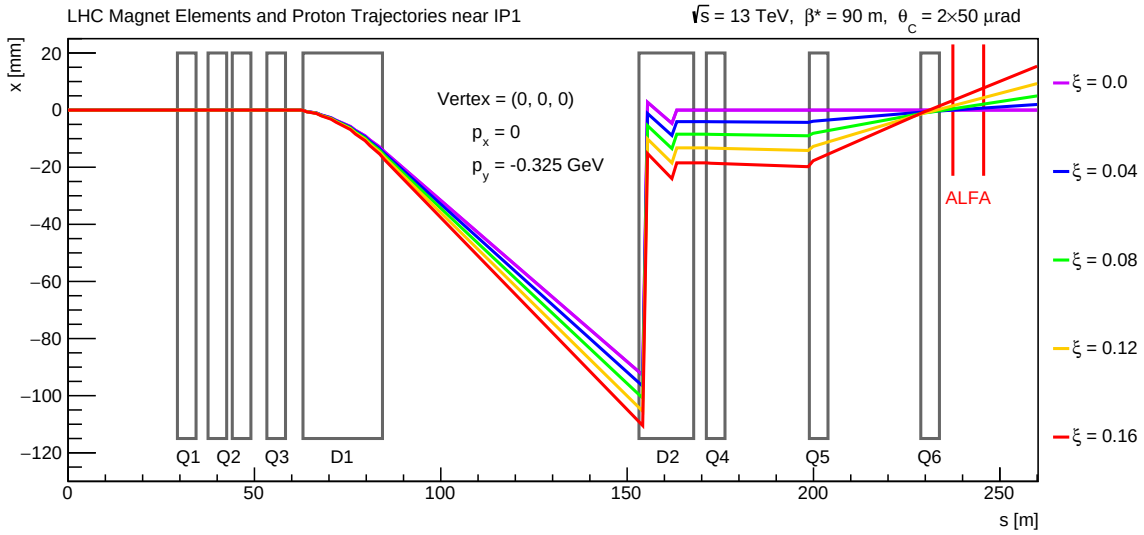

Figure 5.8: Energy dependence of the proton trajectory in the (x, z)-plane.

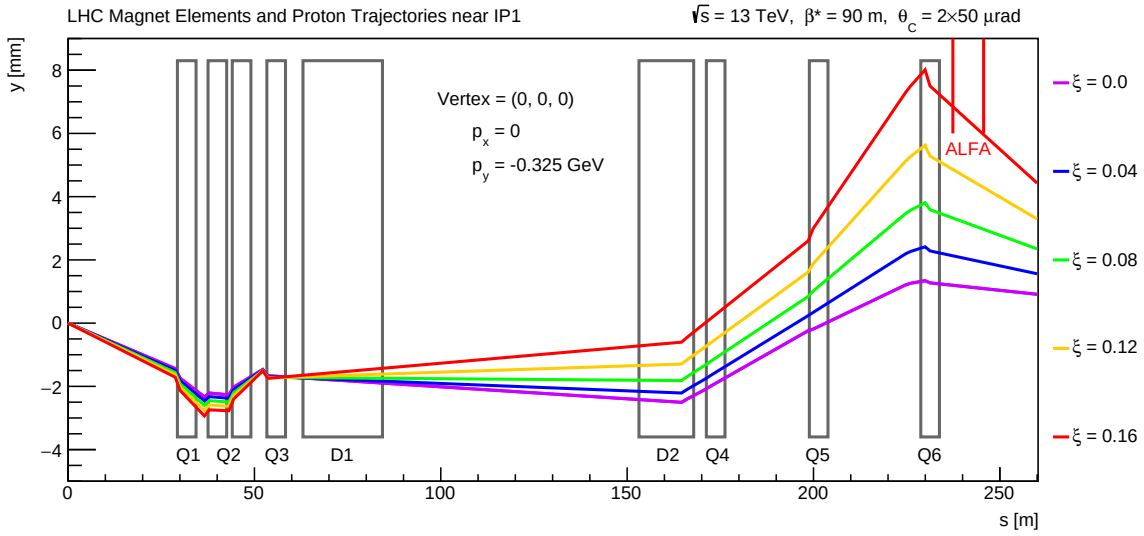

Figure 5.9: Energy dependence of the proton trajectory in the (y, z)-plane.

The small bent in the trajectory in the y-direction (Figure 5.9, 5.11, and 5.13) around the quadrupole triplet (Q1, Q2, Q3) is due to the non-zero crossing angle. A kicker magnet will focus deviating protons in the y-direction right before the ALFA stations.

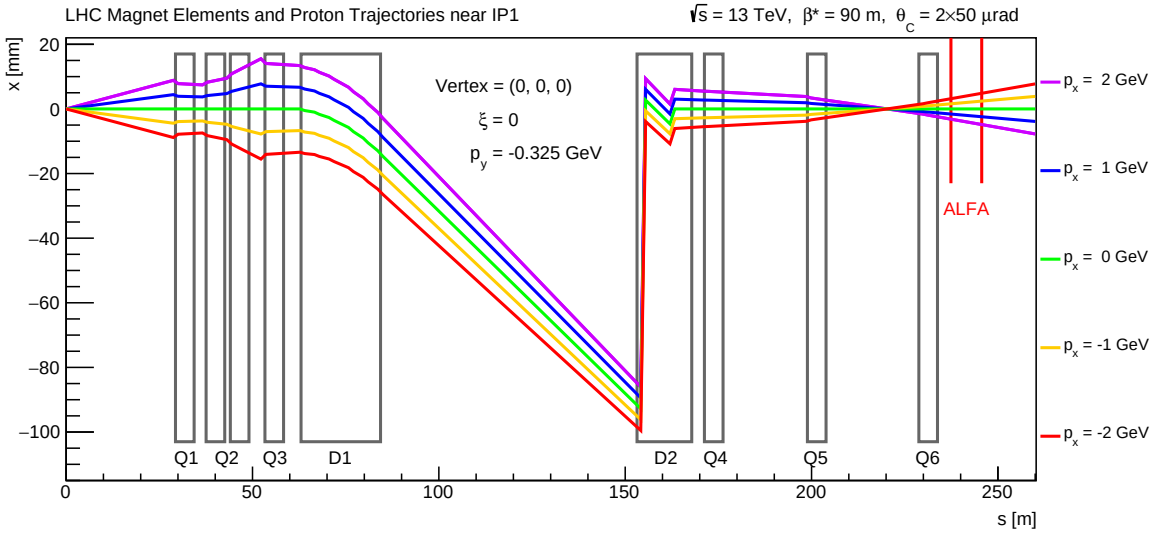

Figure 5.10: p_x dependence of the proton trajectory in the (x, z)-plane.

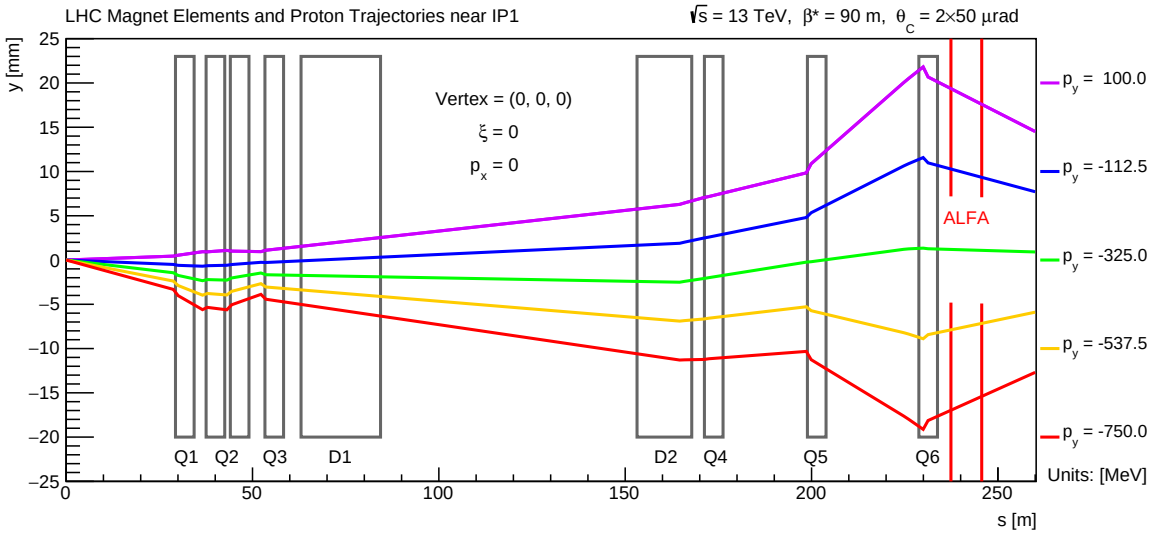

Figure 5.11: p_y dependence of the proton trajectory in the (y, z)-plane.

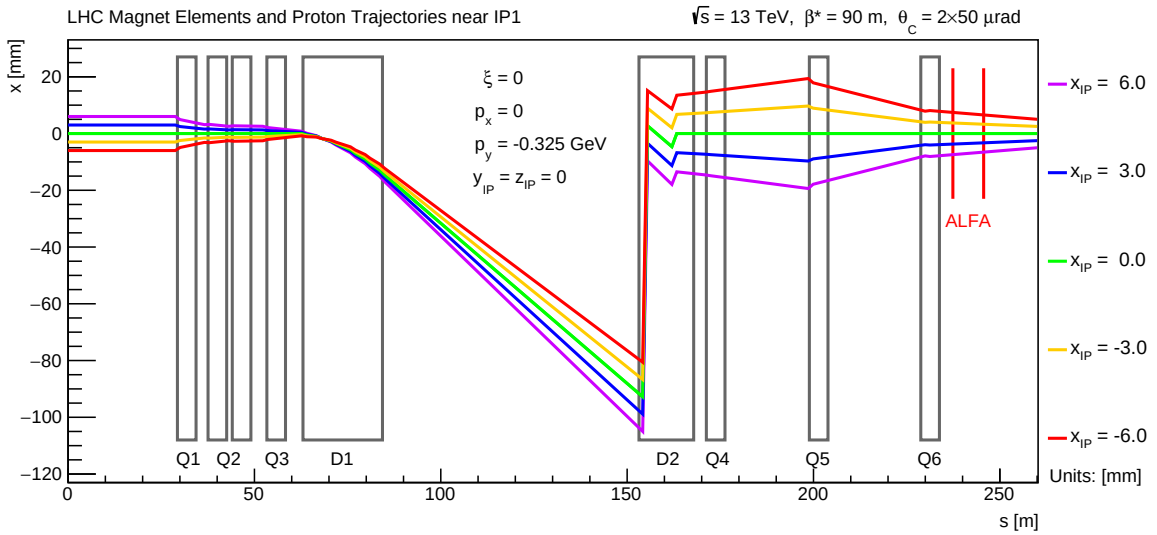

Figure 5.12: x_{IP} dependence of the proton trajectory in the (x, z)-plane.

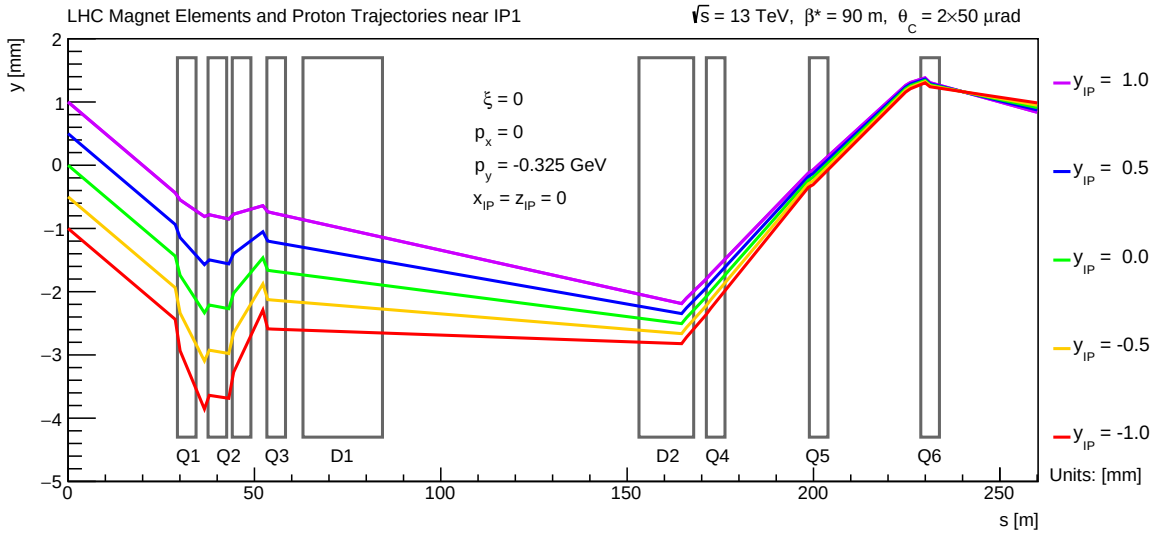

Figure 5.13: y_{IP} dependence of the proton trajectory in the (y, z)-plane.

6

THE ATLAS DETECTOR

The ATLAS detector [52] is one of the two general-purpose detectors at the LHC, with CMS [56] being the other. The ATLAS detector is designed for precision measurements of the Standard Model as well as the observation of new physics at the TeV-scale. ATLAS is installed at IP1 at the LHC, is 44 m long, 25 m in diameter, and weighs about 7000 tonnes. ATLAS has a cylindrical structure, as seen on Figure 6.1, and is described by a coordinate system centered around the nominal interaction point (IP) where the pp-collisions occur. Most of the ATLAS sub-detectors are segmented into bins of η and ϕ, since soft final-state particles are expected to be roughly uniformly distributed in y and ϕ, where the rapidity has been approximated to pseudo-rapidity which allows for a purely geometrical subdivision. Starting from the interaction point, final-state particles will traverse through the layers of the ATLAS detector, passing the inner detector (ID), the calorimeters, and finally the muon spectrometer.

ATLAS stands for 'A Toroidal LHC ApparatuS'.

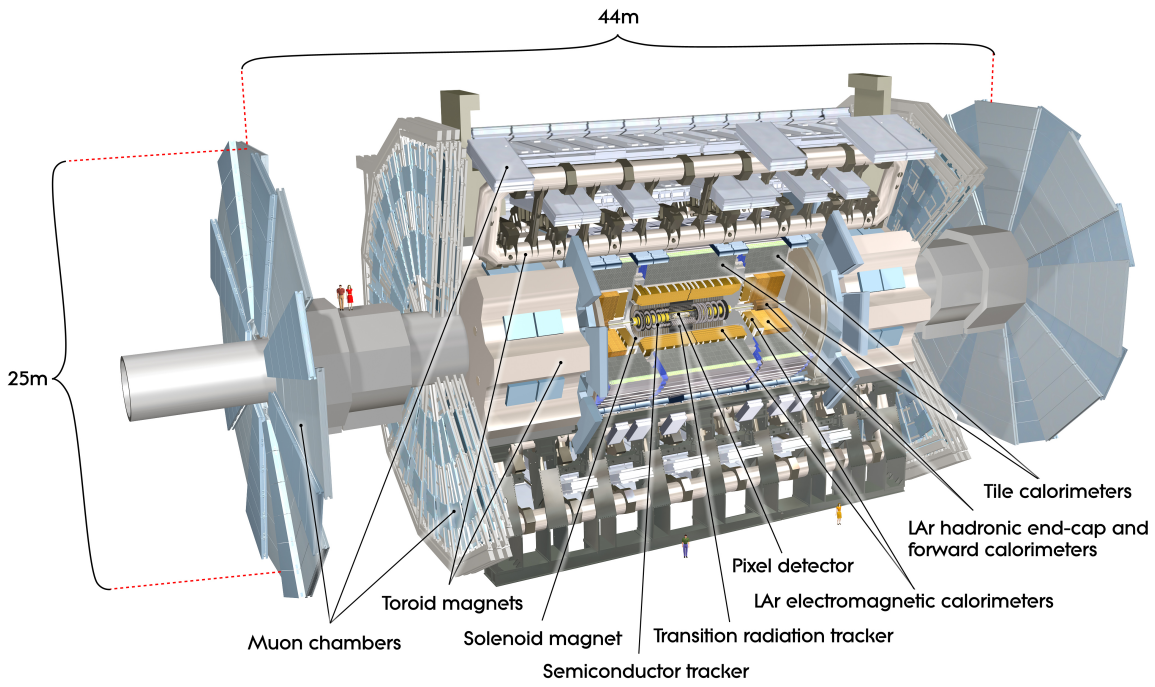

Figure 6.1: Computer generated overview of the ATLAS detector. Image from [CERN-GE-0803012-01], ATLAS Experiment © 2017 CERN.

For the purpose of studying single diffractive scattering, the ATLAS detector is able to measure different properties of the diffractively dissociated system. For this, the inner detector and the calorimeters are of special interest. The inner detector will be able to reconstruct a primary vertex that is necessary for the reconstruction of the kinematics of the diffractively scattered proton. Both the inner detector and the calorimeters are important for the measurement of the large rapidity gap as well as the invariant mass of the dissociated system.

In the following sections, the basic structure of the different components of the ATLAS detector (called 'sub-detectors') are described to some detail, along with their specialized role in the detection and measurement of the different aspects of the final-state of pp-collisions. A full description of the ATLAS detector can be found in ref. [52].

6.1 MAGNET SYSTEM

The ATLAS magnet system is designed to bend charged particles according to the Lorentz force. The bending allows for charge determination of the charged particles as well as a more precise measurement of the momentum.

The innermost magnet is a superconducting solenoid magnet, which consists of a single coil and produces a magnetic field of 2 T in the direction of the beam axis. The solenoid has an axial length of 5.8 m and a radius of 2.5 m. It surrounds the inner detector and is designed to minimize the amount of material in front of the calorimeter to ensure that the energy loss of the particles in the magnet is kept to a minimum.

Beyond the calorimeter system, a three-component toroidal magnet is located. The toroid magnets are air-core magnets that produce an azimuthal magnetic field in the muon spectrometer. The magnets are split into a central ('barrel') part, with an axial length of 25.3 m, and two end-cap parts with a length of 5 m. The toroid magnets provides approximately 0.5 T in the barrel region, and 1 T in the end-cap regions.

6.2 INNER DETECTOR

The ATLAS inner detector (ID) consists of three parts at increasing radial distance from the beam pipe: the pixel detector, the semiconductor tracker (SCT), and the transition radiation tracker (TRT). The three sub-detectors can, in combination, measure the positions of charged particles at different radii from the beam axis. This makes it possi-

ble to fit and reconstruct the particle trajectory. Each ID sub-detector is separated into a barrel part, with cylindrical geometry centered around the interaction point, and two end-cap parts, with axial symmetry, located at each end of the barrel. The entire ID ensures a combined pseudorapidity coverage of $|\eta| < 2.5$. An additional pixel layer, the insertable *B*-layer [57], was installed between the beam line and the older pixel detector during the long shutdown in 2013 and 2014. An cut out of the combined ID before the installation of the insertable *B*-layer is shown in Figure 6.2 and 6.3.

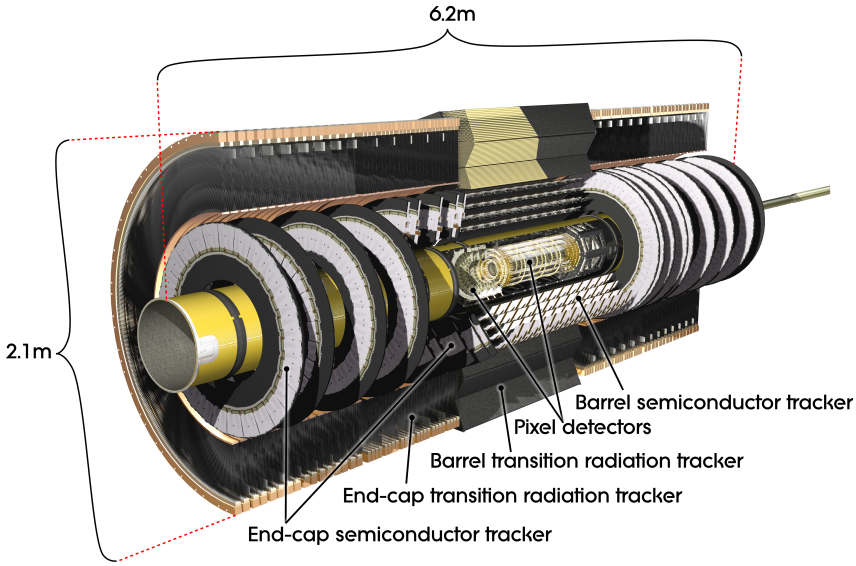

Figure 6.2: Computer generated cut out of the ATLAS inner detector, showing the pixel detector, the SCT, and the TRT. Image from [CERN-GE-0803014-01], ATLAS Experiment © 2017 CERN.

The primary vertex of the interaction can be reconstructed by associating two or more tracks to a possible vertex position. For minimum bias data samples, the charged tracks used in the reconstruction of the primary vertex is usually required to have a $p_T > 100$ MeV. The spatial resolution of the reconstructed vertex will depend on the number of tracks associated to the vertex. The resolution of the x-coordinate for the reconstructed primary vertex in the ID as a function of the number of associated tracks is seen in Figure 6.4. The resolution of the y-coordinate is identical to that of the x-coordinate as the ID is symmetric in the azimuthal angle.

6.2.1 *Pixel Detector*

The pixel detector is located closest to the beam line and consists of semiconductor pixel sensors, effectively acting as solid-state ionisation chambers. The pixel sensors are almost completely depleted of free charge carriers. A charged particle passing through the depleted

regions will generate electron-hole pairs which are then collected by the bias voltage, and detected as small electric currents at the read-out. The pixel sensors have a thickness of 250 μm and a nominal size of 50×400 μm^2. The choice of the $1:8$ rectangular pixel sensors is due to the ID being immersed in a solenoidal magnet field resulting in a bending in the ϕ-direction. Hence, precision in the ϕ-direction is more valuable than in the axial direction – at least for small bending radii. The intrinsic resolution in the transverse direction is 10 μm while it is 115 μm in the longitudinal direction.

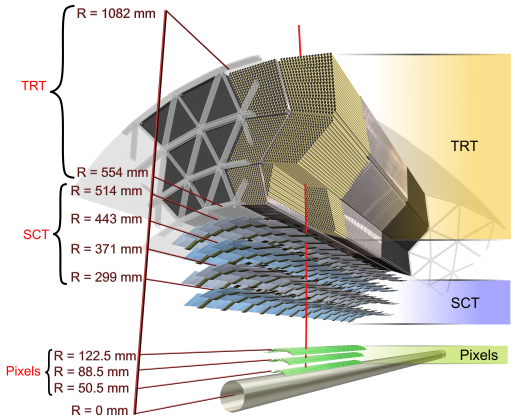

Figure 6.3: Computer generated image of a slice of the ATLAS inner detector. Image from [CERN-GE-0803014-03], ATLAS Experiment © 2017 CERN.

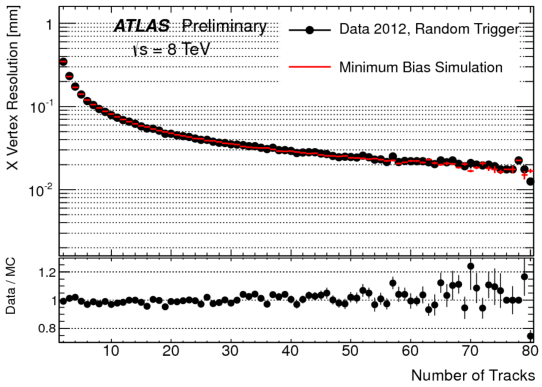

Figure 6.4: The resolution of the x-coordinate of the reconstructed primary vertex by the ID as a function of the number of associated tracks. Figure from [58].

The insertable B-layer (IBL) installed for Run 2, is a single-layer cylindrical pixel detector located between the beam pipe and the three-layer pixel detector at a distance of 31 mm $< R <$ 40 mm from the interaction point. This required the inner radius of the beam pipe to be reduced by 4 mm from 29 to 25 mm. The IBL was installed to improve the reconstruction of the primary and especially secondary vertices. The small distance from the interaction point will furthermore improve the precision of the impact parameters, d_0 and z_0.

6.2.2 *Semiconductor Tracker (SCT)*

The SemiConductor Tracker (SCT) consists of silicon sensors with strip readout rather than the pixel geometry of the pixel detector. This makes it more affordable to cover the larger volume outside the pixel detector with the silicon tracking sensors, but results in an inherently degraded resolution. This is remedied by a pair-wise grouping of sensor modules, that are rotated with a small stereo angle to obtain the z-measurement. A charged particle that traverse one SCT layer, will then effectively cross two silicon strips. The hit resolution is then

given by the effective cross-sectional area of the two strips. Each silicon sensor is 6.36×6.40 cm^2 and consists of 768 read-out strips with a separation of 80 μm. Each layer is double-sided with an angle of 40 μrad between the silicon sensors in the two layers. This results in an intrinsic resolution of 17 μm in the transverse direction, and 580 μm in the longitudinal direction.

6.2.3 *Transition Radiation Tracker (TRT)*

The Transition Radiation Tracker (TRT) is a straw drift tube detector that covers up to $|\eta| < 2.0$. In contrast to the two other ID subdetectors, the TRT uses approximately 300000 long, gas-filled, cylindrical straw tubes (cathodes) with a diameter of 4 mm and with a tungsten wire (anode) running along their centers for charged particle detection. When a charged particle passes a TRT straw, it ionizes the gas atoms inside the straw. The tungsten wires are operated at a large bias voltage which results in the electrons causing an avalanche of secondary ionization which is deposited in the anode wire and read out as an electrical signal. The TRT straw tubes are interleaved with a dielectric foil to enhance the transition radiation of charged particles, which yields much larger signals in the TRT straws than standard minimum ionizing particles, and are used to separate electrons from e.g. pions during the reconstruction. The TRT will only provide hit information in the $(R - \phi)$ plane with an intrinsic resolution of 130 μm. This is a deliberate choice as the solenoid magnet will only bend charged particles in the ϕ direction.

6.3 CALORIMETRY

Calorimeters measure the energy of particles (such as electrons, photons, and hadronic jets) by absorbing them in the detector material. The calorimeters of ATLAS are sampling calorimeters, consisting of alternating layers that absorb and measure the spray of particles. The calorimeter system of ATLAS are grouped into three parts: the electromagnetic (ECAL), hadronic (HCAL), and forward (FCAL) calorimeter. A cut out of the combined calorimeter system is shown in Figure 6.5.

6.3.1 *The Electromagnetic Calorimeter (ECAL)*

The Electromagnetic Calorimeter (ECAL) is a sampling calorimeter with lead as the absorbing material and liquid argon (LAr) as the active material, in which electrodes are embedded for signal detection. The ECAL is located just outside the central solenoid that surrounds the ID. Electrons and photons will interact differently from hadrons as they do not participate in the strong interaction. Electrons lose energy to electromagnetic bremsstrahlung, loosing a factor of

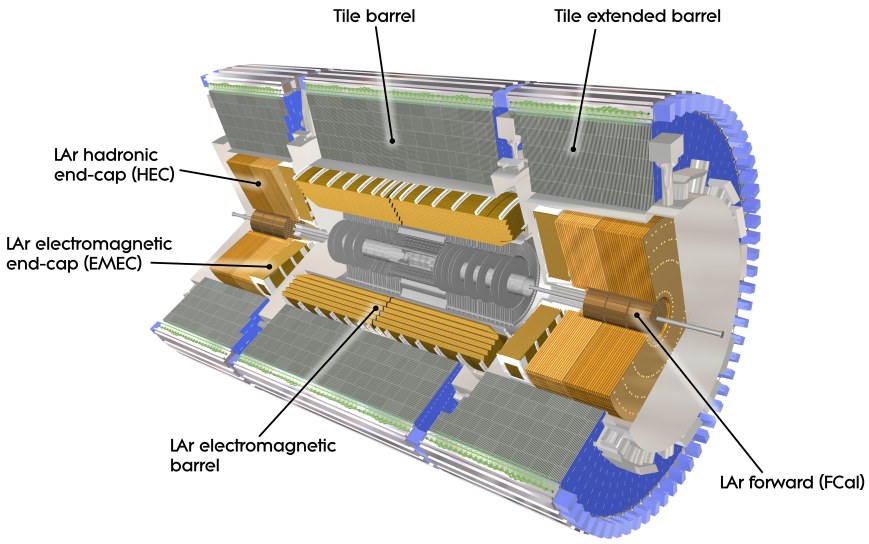

Figure 6.5: Computer generated cut out of the ATLAS calorimeter system, showing the electromagnetic (ECAL), the hadronic (HCAL), and the forward (FCAL) calorimeters. Image from [CERN-GE-0803015], ATLAS Experiment © 2017 CERN.

$1/e$ of their energy over one radiation length X_0. The bremsstrahlung photons will produce e^+e^- pairs after a length $(9/7)X_0$ which gives rise to an electromagnetic (EM) shower. Final-state photons will also generate an EM shower albeit slightly later. The ECAL extends to over $22X_0$ in the barrel region and over $24X_0$ in the end-cap region. The barrel region covers $|\eta| < 1.475$, while the end-cap regions cover $1.375 < |\eta| < 3.2$. The calorimeter uses an accordion geometry to ensure full ϕ coverage with no cracks. The ECAL consists of a presampler followed by three layers in the barrel region and two in the end-cap regions. The presampler consists of an active LAr layer and covers $|\eta| < 1.8$. The purpose of the presampler is to correct the energy of the electrons and photons before they reach the three main layers. The second layer collects the majority of the deposited energy, and the third layer is designed to collect the tails of the EM showers and determine whether there are any punch-through into the HCAL.

6.3.2 *The Hadronic Calorimeter (HCAL)*

The Hadronic Calorimeter (HCAL) is located outside the ECAL and consists of a central Tile calorimeter with the absorbing layers made of steel and the active material made of scintillating tiles, covering the barrel ($|\eta| < 1.0$) and extended barrel ($0.8 < |\eta| < 1.7$) regions. The end-cap calorimeter is based on a copper-LAr sampling calorimeter which covers $1.5 < |\eta| < 3.2$. Final-state hadrons will leave only a small fraction of their energy in the ECAL. The HCAL therefore re-

lies on the strong interaction to measure the energy of the hadrons, where the length scale of the process is characterized by the nuclear interaction length λ, which is the mean free path between inelastic strong interactions. Each strong interaction in the HCAL produce secondary particles (mainly pions) which themselves interact with the calorimeter medium, giving rise to hadronic showers. The central Tile calorimeter consists of three layers while the end-cap LAr calorimeter consists of four layers arranged in wheels, as seen in Figure 6.5. The total length of the calorimeter system in the barrel region is 9.7λ of which the HCAL makes up 7.4λ. The end-cap LAr calorimeter has a length similar to the Tile calorimeter. The large total interaction length of the calorimeter means that there are very little punch-through to the outer muon spectrometer, and that the calorimeter system provides reliable measurements of the total energy inside the η coverage.

6.3.3 *The Forward Calorimeter (FCAL)*

The Forward Calorimeter (FCAL) is a LAr sampling calorimeter installed to ensure high $|\eta|$ coverage and to reduce non-muon radiation into the muon spectrometer. The FCAL extends over $3.2 < |\eta| < 4.9$, ensuring a combined calorimetric coverage of $|\eta| < 4.9$. The FCAL consists of three layers, each with a depth of 45 cm. The first layer uses copper as the absorption material and mainly measures EM showers. The second and third layer uses tungsten as the absorption material and are designed to measure hadronic showers. The FCAL has a total depth of approximately 10λ with a coarser granularity than the ECAL and HCAL.

6.4 MUON SPECTROMETER

The muon spectrometer is the outermost sub-detector system of ATLAS. The only particles that escape the calorimeter system are muons with energies above 5 GeV. This is due to their not participating in the strong interactions (and hence will not leave any energy in the HCAL) and having a large mass compared to the electron and will therefore give off less Bremsstrahlung. The muons are therefore expected to be the only particles to arrive outside the calorimeter, in a second set of tracking detectors. The muon spectrometer relies on the bending of the muons by the large volume of the air-core toroid magnet to achieve excellent stand-alone momentum determination and charge identification of muons with a transverse momentum as high as $p_T \gtrsim 3$ TeV. The muon spectrometer consists of several different kinds of sub-detectors – some used for high precision measurement of the p_T of the muons, and some with a coarser resolution used as triggers in the data-taking process.

6.5 TRIGGER SYSTEM

If the LHC runs with its design bunch spacing of 25 ns, then the rate of bunch crossing happening in the ATLAS detector is 40 MHz, i.e. 40 million proton bunch crossings happen every second. It is not possible to read out and save the information on all of the collisions, nor are all the collisions interesting for a given analysis. Most ATLAS analyses are interested in events with high-p_T objects such as jets, electrons, muons, taus, or missing transverse momentum. To filter out the most interesting events to be saved, a *trigger system* is designed and used. The ATLAS trigger system works in two levels – one more specific than the other.

The first level is the Level 1 trigger, denoted L1, and is implemented in the hardware. The L1 trigger makes a decision on whether to keep or reject an event, based on information from hits in the trigger chambers in the muon spectrometer and energy deposits measured by the trigger towers in the calorimeters. The trigger decision is done by the Central Trigger Processor (CTP) based on this information and uses look-up tables to see whether the trigger requirements are met. The L1 trigger requires around 2.5 μs to reach a decision and will reduce the rate of events to $\sim$ 100 kHz. The trigger forms Regions of Interest (RoIs) which are passed on to the next level.

The second level is the High Level Trigger, denoted HLT, and is a merged collection of the previous Level 2 (L2) and the Event Filter (EF) triggers from Run 1. The HLT relies mostly on the algorithms of the former EF trigger system to make decisions. This includes a requirement of a finer granularity of the calorimeter and an addition of track information from the inner detector. The average rate of the HLT is $\sim$ 1 kHz.

6.6 MINIMUM BIAS TRIGGER SCINTILLATOR

Most of the ATLAS sub-detectors have their own dedicated trigger systems and items. However, the *Minimum Bias Trigger Scintillator* (MBTS) is not associated with any specific sub-detector, but is designed to check and refine noisy and faulty channel maps of ATLAS in the commissioning phase of LHC. The MBTS are scintillation detectors composed of 2 cm thick doped polystyrene. The MBTS are mounted as disks around the LHC beam pipe on both sides of the interaction point, labelled as A and C sides, with B being the barrel region. Each disk consists of 8 wedges, which are composed of an inner ring, covering a pseudorapidity range of $2.76 < |\eta| < 3.86$, as well as an outer ring, covering $2.08 < |\eta| < 2.76$. The light emitted from the scintillator is collected by 8 wavelength shifting optical

fibers (WLS) that are embedded at the edges of the scintillator and connected to photomultipliers. Energy deposits above the threshold of 50 mV corresponding to 0.23 pC [59] will result in the L1 MBTS trigger to fire. The MBTS will trigger on almost all inelastic events. As the MBTS is a very inclusive trigger, the data sample that will trigger the MBTS is called *minimum bias*, and covers the experimental definition given in Section 3.3.4.

6.7 THE LUCID SUB-DETECTOR

LUCID (Luminosity measurements Using Cherenkov Integrating Detector) is a dedicated luminosity monitor for the ATLAS experiment. The LUCID detector is made of two modules installed at $z = \pm 17$ m on both sides of the ATLAS interaction point. Each modules is made of four quartz fibre bundles. When a charged particle traverses the module, the produced Cherenkov radiation is carried to 16 photomultiplier tubes protected by shielding some 2 m aways.

6.8 PARTICLE SIGNATURE IN ATLAS

The ATLAS detector is a general-purpose detector and designed such that most final-state particles will leave a distinct trace. Figure 6.6 shows how the measurements in the ATLAS sub-detectors are combined to identify and measure different types of particles:

PHOTONS are not electrically charged and will therefore not leave any track in the ID. However, they can be identified by creating an electromagnetic shower in the ECAL, where they will deposit all their energy.

ELECTRONS will leave a shower in the ECAL similar to that of photons. Unlike the photons, they are charged particles and will therefore also leave a track in the inner detector.

MUONS have a long enough lifetime to be treated as stable particles in the detector. They will not be stopped by the calorimeters and will therefore reach the muon spectrometer.

CHARGED HADRONS such as protons and charged pions will leave tracks in the ID and will be completely absorbed by the HCAL. They may also deposit some energy in the ECAL.

NEUTRAL HADRONS such as the neutron and neutral pion will not be measured by the ID or ECAL, but will deposit all their energy in the HCAL.

NEUTRINOS interact only through the weak force and will leave the detector without a trace. They can be indirectly measured by the missing transverse energy.

JETS are narrow cones of particles originating from strongly interacting particles that hadronize. Jets will deposit energy in the calorimeters, especially the HCAL. They may leave tracks in the ID.

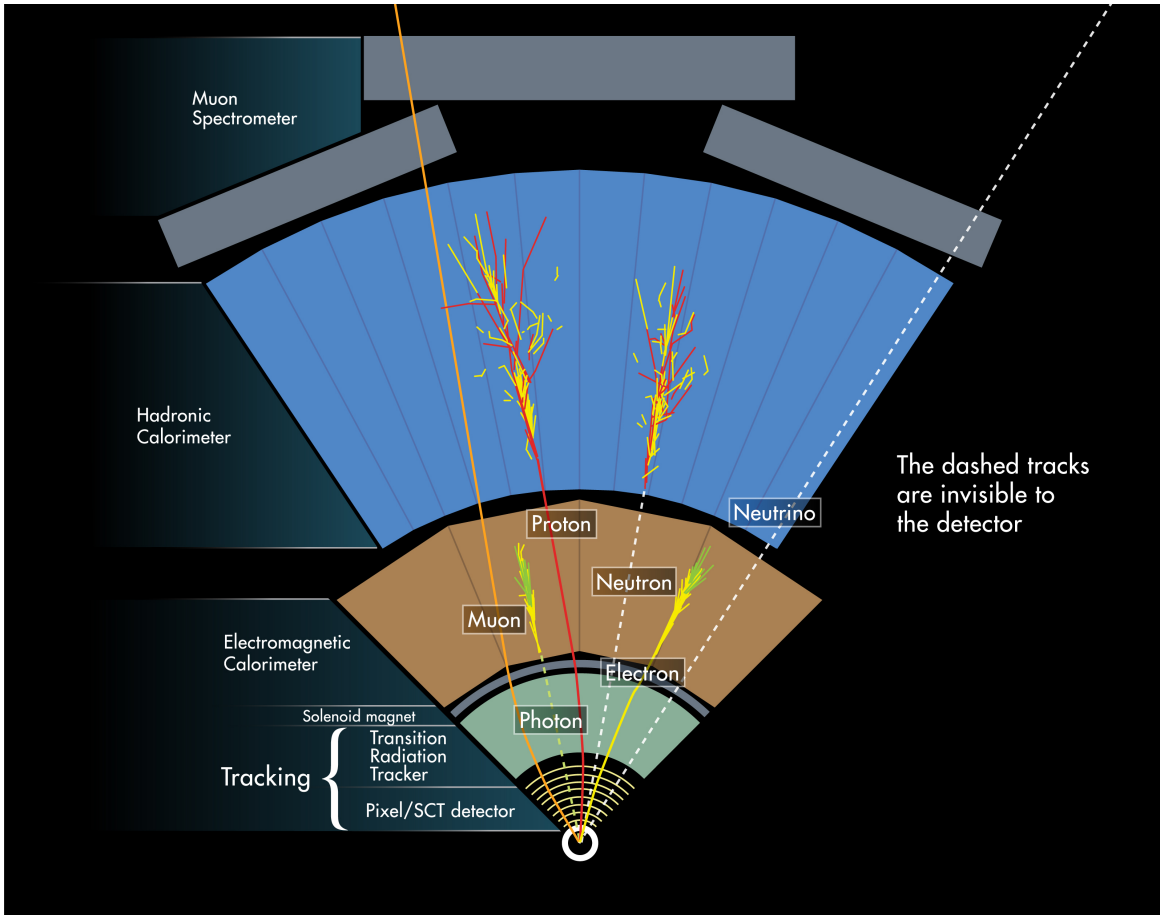

Figure 6.6: Computer generated image representing how different particles are detected in the ATLAS detector. Image from [CERN-EX-1301009], ATLAS Experiment © 2017 CERN.

7

THE ALFA DETECTOR

The ALFA detector is designed to detect and measure protons in the extreme forward direction, making it possible to tag diffractively scattered protons. ALFA consists of eight identical tracking detectors installed in Roman Pots at 237 m and 245 m from the interaction point on either side of ATLAS, pairwise above and below the beam pipe. In Figure 7.1 the positions of the eight ALFA detectors are shown along with the numbering convention used in this thesis. The eight detectors are paired into four stations. Each station consists of two Roman Pots – an upper and a lower – with tracking detectors approaching the beams in the vertical coordinate y. The ALFA detectors are able to measure protons in the transverse plane only few milimetres from the beam in order to reach the small t regime.

ALFA stands for 'Absolute Luminosity for ATLAS'.

This chapter presents an introduction to the ALFA detector, and is based on references [60] and [61], unless otherwise noted.

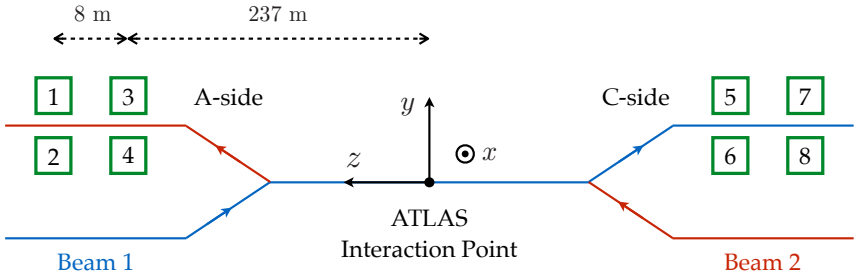

Figure 7.1: Side view of the positions of the eight ALFA stations and the LHC beam configuration with the ATLAS and beam coordinate systems. The ALFA Roman Pots on the A-side are stationed on the outgoing beam 2, while on the C-side they are stationed on the outgoing beam 1.

7.1 MAIN DETECTORS

The main detector (MD) is a tracking detector where traversing protons are detected and their position is measured. The MD consists of ten fibre planes, with two perpendicular layers of 64 scintillating fibres in each layer. The fibers have a size of 0.5×0.5 mm^2 and are coated with aluminium to reduce the amount of light propogating from one fiber to another neighboring fiber, also known as optical cross-talk. The layers of fibers are glued to a titanium substrate. The plates of fibers are arranged with an angle of $\pm 45^\circ$ to the vertical coordinate y in a diamond shape and perpendicular to each other.

The perpendicular planes are referred to as the U- and V-planes. The plates are arranged after each other in the z-direction, i.e. the direction of the beam. This results in a pattern of alternating fibre layers which forms pixels in the u and v coordinates that are rotated 45° with respect to the usual (x, y) coordinates. For one plane with an U and V layer with perpendicular fibres the resulting pixels have a width of $d = 500$ μm which gives a width in the $x - y$ plane of $d_{x,y} = \sqrt{2} \cdot 500$ μm ≈ 707 μm. The theoretical spatial resolution of a single fiber in the (u, v) can be calculated as the Root-Mean-Square (RMS) as

$$\sigma_{u,v} = \sqrt{\int_{-d/2}^{d/2} \frac{(x - x_0)^2}{d} \mathrm{d}x} \overset{x_0=0}{=} \sqrt{\int_{-d/2}^{d/2} \frac{x^2}{d} \mathrm{d}x} = \frac{d}{\sqrt{12}} \approx 144 \ \mu\mathrm{m} \tag{7.1}$$

which is also true in the (x, y) plane due to the geometry. To further improve the resolution, the planes have been staggered with multiples of 1/10 of the fibre width. This results in a final theoretical resolution of the MD of 14.4 μm. In practice the actual resolution is detoriated due to imperfect staggering, cross-talk, noise, and inefficient fibre channels. The actual resolution was measured in several test beams to be around 30 μm. The orientation of the U- and V-planes of the MD with respect to the beam axis is illustrated in Figure 7.2 and 7.3.

7.2 OVERLAP DETECTORS

The overlap detectors (OD) are placed on each side of the MD as shown in Figure 7.2. The OD is dedicated to precisely measure the distance between the upper and lower MDs to align the detectors. This is necessary as the position of the movable Roman Pots that houses the MD and ODs are not fixed from one data taking to another. The ODs consists of three layers of 30 scintillating fibres which are glued to the front and back side of titanium plates. These plates are staggered by 1/3 of the fibre width to improve resolution. The plates are oriented horizontally, since the OD is only used to align in the vertical direction. The ODs are aligned to the MD with an uncertainty that does not exceed 8 μm. The single-track resolution is about 50 μm but can be significantly improved by using many hits. A resolution of 20 μm is achieved with a few thousand tracks. The position of the ODs with respect to the MDs is illustrated in Figure 7.2.

7.3 MULTI ANODE PHOTOMULTIPLIER TUBES

The fibers from both the MDs and ODs are connected to Multi Anode PhotoMultiplier Tubes (MAPMTs) which are located outside the Roman Pots. The scintillation-light signals from the fibers are guided

by means of total internal reflection out of the RP to the photomultiplier tubes. The MAPMTs convert the light signal into an electrical signal that is directed to front-end electronics with signal amplifiers and readout buffers to digitally store signals above a certain threshold. The scintillating fibres are connected to the MAPMTs such that cross-talk between neighboring fibres is reduced.

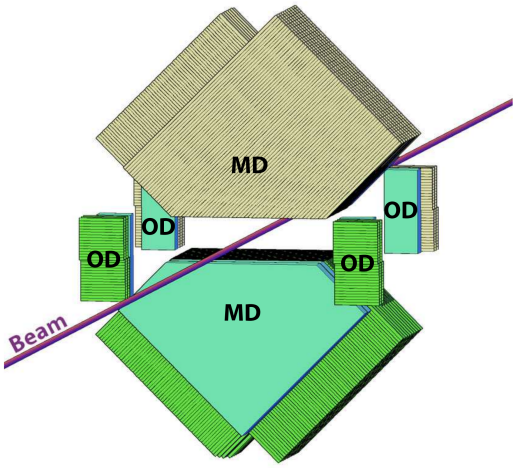

Figure 7.2: A schematic view of a pair of ALFA tracking detectors in the upper and lower Roman Pots. Although not shown, the ODs on either side of each MD, are mechanically attached to the MDs. The orientation of the scintillating fibres are indicated by the dashed lines. The plain layer visible in front of the lower MD, is one of the trigger counters. On the upper detector, the trigger counter is located on the opposite side of the fibres. Image from [53].

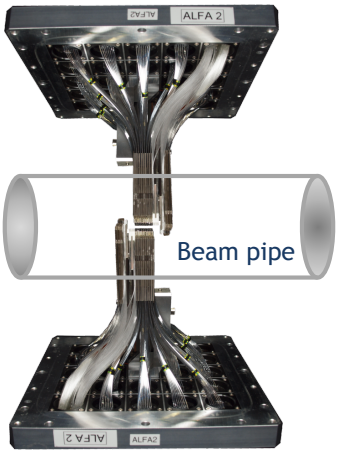

Figure 7.3: Photograph of the side view of one of the ALFA detectors, with the aluminium-coated scintillating fibres clearly visible. The ten layers of scintillating fibres of the MDs are seen in the middle for both the upper and lower detector, while the ODs are located on either side of the MDs. The detectors are located just a few mm from the beam for high β^* runs as pictured here. The orientation of the beam pipe relative to the detectors is also shown. Image from [62].

7.4 TRIGGER COUNTERS

Both the MD and ODs are completed with trigger counters, used to select and trigger on miscellaneous event topologies, e.g. elastically or diffractively scattered protons. The main and overlap trigger counters consists of 3 mm thick plastic scintillator plates that cover the active areas of the MD and ODs. The scintillator plates are painted with a white reflective paint to ensure maximum light yield. Each MD has two separate scintillator plates in order to make local coincidence. The ODs only need one scintillator plate, since the coincidence is obtained from signals in the upper and lower overlap trigger counters. The signals from the trigger tiles are carried to PMTs outside the Roman Pots by clear fibres.

7.5 ROMAN POTS

The tracking detectors (MD and ODs) and the trigger counters are located inside Roman Pots (RPs) which functions as vessels providing a secondary vacuum that allows the ALFA detectors to approach the beam inside the beam pipe. The Roman Pots separate the detectors from the ultra high primary vacuum inside the beam pipe. Each RP has a thin steel window of 0.2 mm thickness at the bottom as a direct separation between the detector and the beam. Two additional steel windows of 0.5 mm thickness are located in front and behind the MD. The secondary vacuum in the RPs reduces the bending of the windows and allows the pots to be moved closer to the beam. The RPs are kept on movable flanges which allows them to be moved close to the beam. Motors are used to achieve the positioning with 5 μm steps. The position is measured by Linear Variable Displacement Transformers (LVDT) which are calibrated by laser measurements. The LVDT is calibrated with respect to the geometric center of the beam pipe and the real beam positions are measured in special runs where the RPs are moved closer to the beam until the bottom RP windows start to scrape the beam edges. The pots needs to be movable as the beam will have different sizes and locations depending on the beam optics, as discussed in Section 5.3 and 5.4. The upper and lower RPs are illustrated in Figure 7.4.

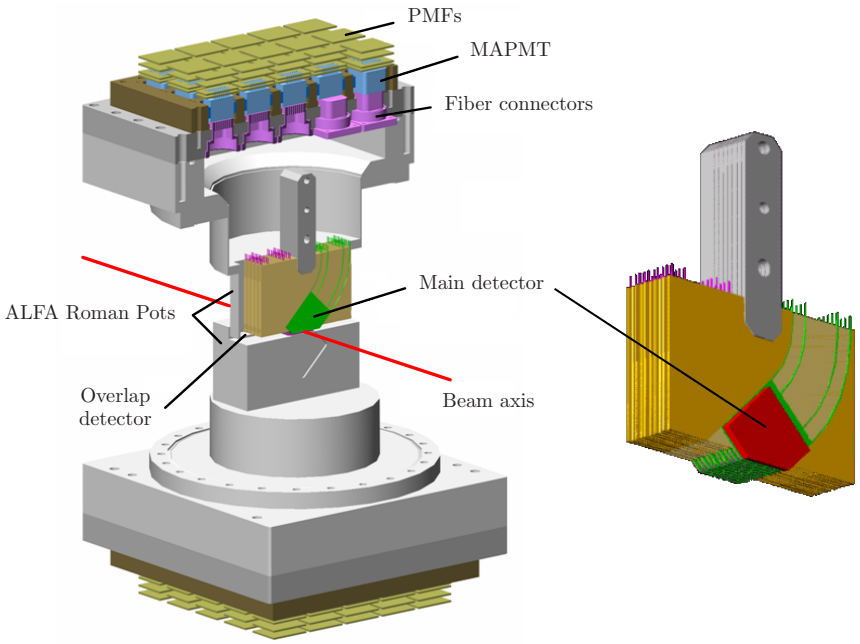

Figure 7.4: A 3D cut-through view of an upper and lower detector and their Roman Pots. For clarity the routing of the fibres to the photodetectors is not shown. Figures from [63] and [64].

7.6 TRACK RECONSTRUCTION

A proton traversing the MD will give a fiber hit in several of the layers. By assuming that the trajectory of the proton is perpendicular to the detector plane, the common overlap region of the hit fibers can be used to reconstruct the proton track. The overlap of fiber hits in the U-plane is illustrated in Figure 7.5. The reconstructed hit position of the proton is the middle of the overlap region and the size of the overlap is a measure of the precision. The track is reconstructed in the fiber (u, v) coordinate system and then translated into (x, y) coordinates by a simple rotation,

$$\begin{pmatrix} x \\ y \end{pmatrix} = \begin{pmatrix} \cos 45^\circ & -\sin 45^\circ \\ \sin 45^\circ & \cos 45^\circ \end{pmatrix} \begin{pmatrix} u \\ v \end{pmatrix} \tag{7.2}$$

The coordinates are given with respect to a precision hole in the titanium plates. This is referred to as the detector coordinate system, and the track coordinates need to be transformed into the beam coordinate system, in which the physics analysis is performed. This is accomplished by an alignment procedure, which uses the distances between the upper and lower detectors along with the rotation of the detector with respect to the beam, to transform the track coordinates. The alignment procedure will be described in detail later.

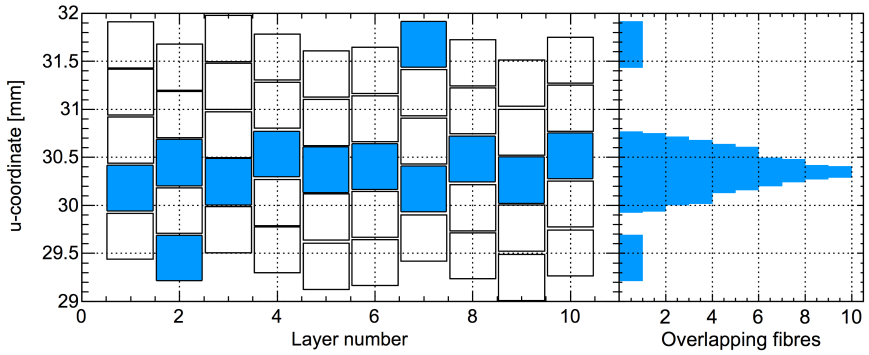

Figure 7.5: Illustration of the principle used to reconstruct tracks in ALFA. Figure from [53].

7.7 NAMING CONVENTION

Several different naming conventions are used for the ATLAS stations and detectors. For the analysis of data, a simple numbering scheme similar to that in Figure 7.1 is normally used. However, each station, Roman Pot, and detector all have separate names. The naming convention for ALFA is shown in Figure 7.6. These names are used throughout this thesis, especially on the hitmaps for each station.

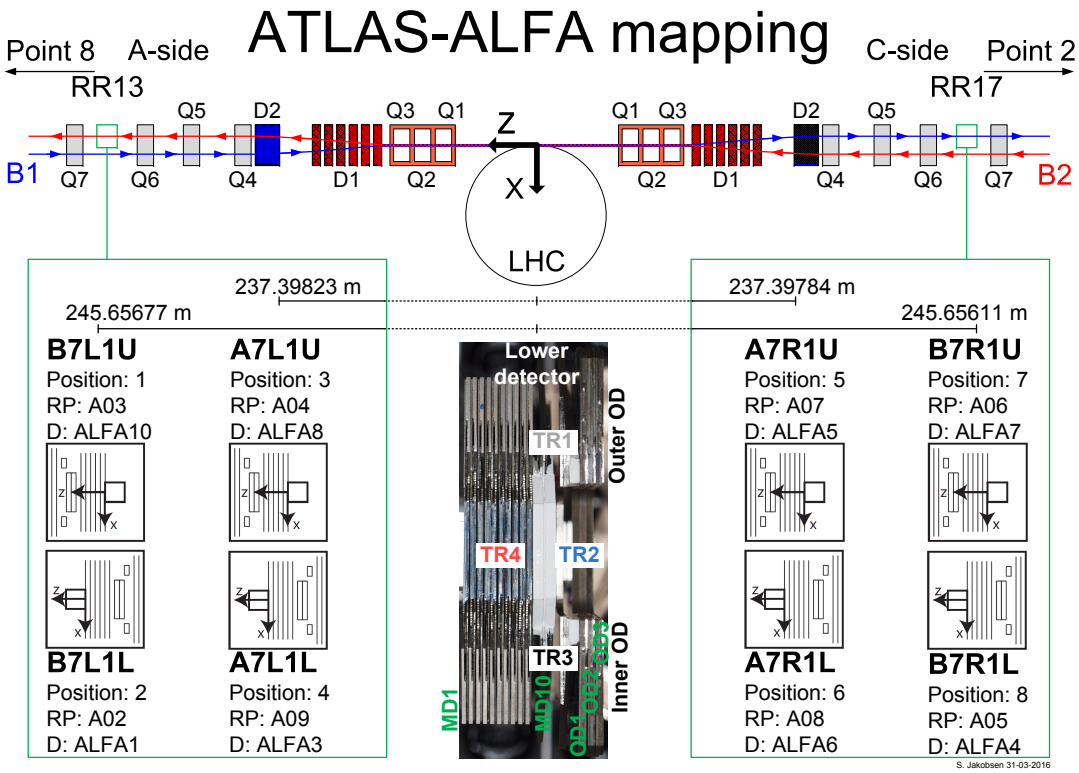

Figure 7.6: Illustration of the ATLAS – ALFA mapping with the ALFA naming convention shown. Figure by Sune Jakobsen, 31 March, 2016.

7.8 EVENT SIGNATURE IN ALFA

In Figure 7.7 the event signature of elastic and diffractive events in both the ATLAS and ALFA detectors are shown. Theoretically, one would assume the two scattered protons in elastic events to be 'back-to-back' and would therefore hit two consecutive ALFA detectors on either side of the interaction point. For single diffractive events, with just one scattered proton and a dissociated system of particles, one would expect the proton to hit two consecutive ALFA detectors on one side with all other ALFA detectors being empty. Some of the particles from the dissociated system may hit ATLAS.

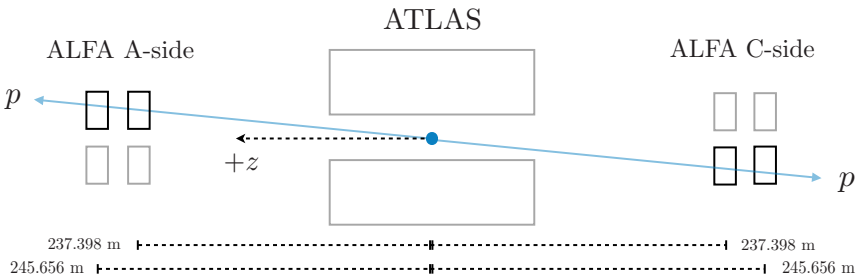

(a) Elastic event

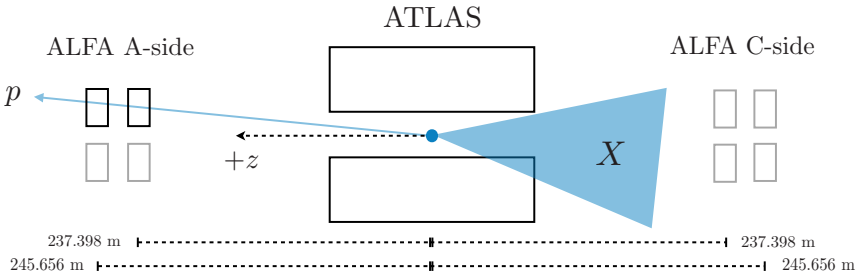

(b) Single diffractive event

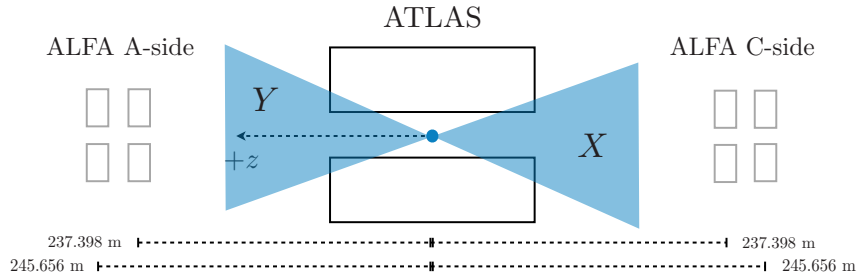

(c) Double diffractive event

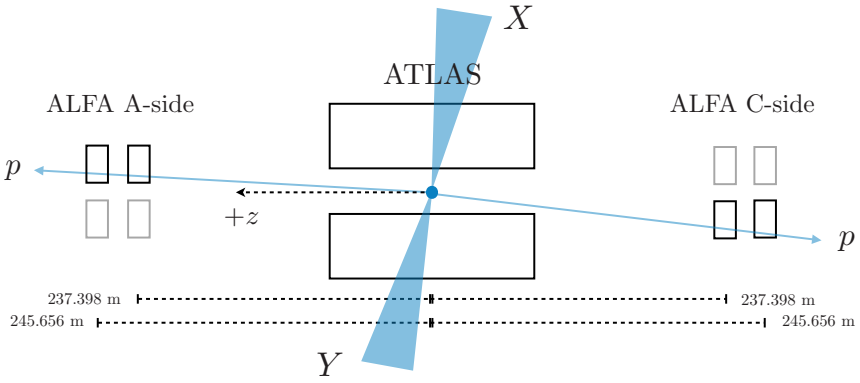

(d) Central diffractive event

Figure 7.7: Simplified illustrations of the event signature in the ATLAS and ALFA detectors for the different types of events happening at IP1.

Part III

SIMULATION

With an understanding of the theory behind diffraction as well as an understanding of the experimental setup for the detection and measurement of diffractive events, we can now embark on a phenomenological study of diffractive scattering. A thorough description of the simulation framework developed for the purposes of this study will be presented, in which the kinematical regions allowed by the ALFA detector will be discussed. The simulation framework will be used to study the observables most sensitive to model parameters. Finally, a study of how well one can test the validity of the models will be presented.

8

SIMULATION FRAMEWORK

For the purposes of this thesis, a simulation framework for single diffractive scattering has been developed, using PYTHIA 8 [6] and the Rivet toolkit [7]. The simulation framework is significantly faster than a full GEANT4 [55] simulation without losing too much in accuracy. Another benefit is that the framework is completely independent of any ATLAS code and software, and can therefore be used by a wider audience. The simulation framework can be easily applied to the analysis of all types of diffraction as well as elastic scattering. However, single diffraction has been the focus of this study.

Single diffractive events have been generated using PYTHIA and then saved as HepMC [65] files. A custom analysis in the Rivet toolkit has been written that reads and analyzes the saved HepMC files. The Rivet analysis handles beam transport of the scattered protons as well as a fast detector simulation of both the ATLAS and ALFA detectors. The various components of the simulation framework will be described to some detail in the following sections.

8.1 GENERATED PYTHIA 8 SAMPLES

The Monte Carlo event generator PYTHIA 8.2 has been used to generate single diffractive events. Single diffractive events can be generated in PYTHIA by setting the QCD process flag,

```
SoftQCD:singleDiffractive = on
```

The Pomeron flux parameterization can then be set by the flag,

```
Diffraction:PomFlux
```

with an integer value where 1 is the Schuler-Sjöstrand parameterization, 4 is Donnachie-Landshoff, and 5 is MBR, as described in Section 4.7. If either Donnachie-Landshoff (4) or MBR (5) is set, then the intercept ε and slope α' of the Pomeron trajectory,

$$\alpha(t) = 1 + \varepsilon + \alpha' t \tag{8.1}$$

can be set. The two parameters can be set within the minimum and maximum values in PYTHIA,

$$\varepsilon_{\text{min}} = 0.02 \qquad \varepsilon_{\text{max}} = 0.15 \tag{8.2}$$

$$\alpha'_{\text{min}} = 0.1 \text{ GeV}^{-2} \qquad \alpha'_{\text{max}} = 0.4 \text{ GeV}^{-2} \tag{8.3}$$

PYTHIA output has been in the form of gzip-compressed HepMC event record files that contains the complete truth information on events. Compression was found to reduce the file sizes to a third of the original.

Multiparton interactions (MPIs) can be toggled in PYTHIA with the `PartonLevel:MPI` flag. All plots in this chapter has been generated with the Schuler-Sjöstrand (1) parameterization that uses fixed parameter values ($\varepsilon = 0$ and $\alpha' = 0.25$ GeV^{-2}) and with MPI toggled on. The effect of MPI and the Pomeron flux parameters will be studied in the phenomenological study in the next chapter.

Two proton beams with a nominal energy of $E_{\text{beam}} = 6.5$ TeV are colliding in the z-direction like it was for the LHC and ATLAS in Run 2 of 2015. The coordinate system in the simulations is the same as for the ATLAS detector. Two sets of simulated samples have been generated – one with an angle between the colliding beams, i.e. a crossing angle as described in Section 5.4, and one with no crossing angle. The beam parameters used in PYTHIA for the different two sets are listed in Table 8.1.

Table 8.1: Beam parameter values used for the event generation of the diffractively scattered protons in PYTHIA 8. B1 = Beam 1, B2 = Beam 2. Note that PYTHIA works in units of GeV and mm.

Parameter	$\theta_C = 0$ μrad	$\theta_C = 2 \times 50$ μrad
E (B1, B2)	6500 GeV	6500 GeV
p_x (B1, B2)	0	0
p_y (B1, B2)	0	$\sin(-50\ \mu\text{rad}) \times E \approx -0.325$ GeV
p_z (B1)	6500 GeV	$\cos(-50\ \mu\text{rad}) \times E$
p_z (B2)	-6500 GeV	$-\cos(-50\ \mu\text{rad}) \times E$

The spread of the interaction vertex can be set according to a simple Gaussian distribution in PYTHIA. The widths of the vertex distributions σ_x, σ_y, and σ_z are taken from beam spot measurements done by the ATLAS inner detector. The beam spot measurements for the data run of interest in this thesis, are seen in Figure 5.6 with the estimated average values listed in Equation 5.7 - 5.9.

PYTHIA also allows for a modest Gaussian beam momentum spread to be set. The beam momentum spread has been found from the beam divergence as calculated according to Equation 5.10 with the emittance values from Equation 5.11 - 5.14. The uncertainties are found from error propagation.

The vertex spread and beam momentum spread are common for all generated PYTHIA samples and can be seen in Table 8.2. Vertex and momentum spread has very little effect on the final-state distributions as seen in Figure 8.1 and 8.2.

Table 8.2: Common parameter values used for the event generation of the diffractively scattered protons in PYTHIA 8. B1 = Beam 1, B2 = Beam 2. Note that PYTHIA works in units of GeV and mm.

Parameter	Value
σ_x	(0.14 ± 0.05) mm
σ_y	(0.14 ± 0.05) mm
σ_z	(53.0 ± 1.0) mm
σ_{p_x} (B1)	(0.0154 ± 0.0009) GeV
σ_{p_y} (B1)	(0.0150 ± 0.0007) GeV
σ_{p_x} (B2)	(0.0171 ± 0.0008) GeV
σ_{p_y} (B2)	(0.0154 ± 0.0009) GeV
σ_{p_z}	0

Note that the beam energy smearing σ_{p_z} has not been set. The reason for this is technical and has to do with Rivet not allowing the center-of-mass energy of analyzed events to differ. This is not a significant problem, as σ_{p_z} will, like the beam momentum spread, have very little effect on final-state distributions. The beam energy smearing can be found from the intrinsic energy uncertainty $\Delta E/E$ and will be roughly $\sigma_{p_z} \approx 734.5$ MeV [66].

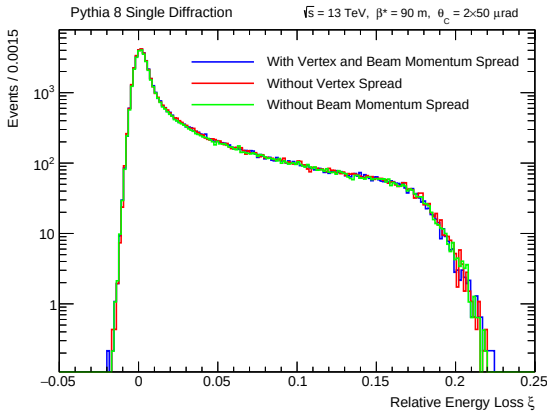

Figure 8.1: ξ distribution with vertex and beam momentum spread (blue), without vertex spread (red), and without beam momentum spread (green). Generated according to Schuler-Sjöstrand.

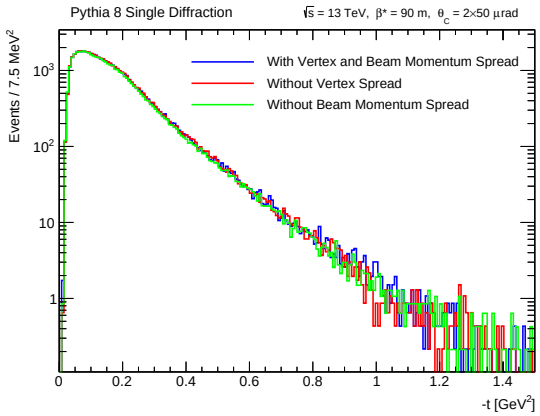

Figure 8.2: t distribution with vertex and beam momentum spread (blue), without vertex spread (red), and without beam momentum spread (green). Generated according to Schuler-Sjöstrand.

8.2 BEAM TRANSPORT OF SCATTERED PROTONS

The simulation framework needs to be able to handle the beam transport of the generated diffractive protons from the interaction point to the ALFA detectors. As explained in Section 5.5, the `MAD-X` software and the `ForwardTransportFast` package can handle the transport. However, the simulation framework developed in this thesis should be fast and independent of any ATLAS software (such as Athena). Hence, a proton transport parameterization has been found with parameters from fits to the output of `ForwardTransportFast`.

The kinematics of the proton at the interaction point can be described by three variables: the energy (E) and the x- and y-components of the three-momentum (p_x and p_y). Alternatively, one could describe the kinematics by the relative energy loss (ξ), the transverse momentum (p_T), and the azimuthal angle (ϕ), since we have

$$\xi = 1 - \frac{E}{\sqrt{s}/2}, \quad p_T = \sqrt{p_x^2 + p_y^2}, \quad \phi = \arctan\left(\frac{p_y}{p_x}\right) \tag{8.4}$$

In most of this thesis, ξ, p_T, and ϕ will be used as they are more relevant for the physics. The scattered protons will be uniformly distributed in ϕ so the interesting distributions are in ξ and in p_T where p_T is related to the momentum transfer, $t \underset{s\to\infty}{\sim} -p_T^2$.

In general a protons coordinates in the transverse plane at any position s along the ring is denoted $u(s)$, where $u = \{x, y\}$, and is related to the protons coordinates and momentum at the interaction point by the transport matrix M_u [67],

$$\begin{pmatrix} u(s) \\ u'(s) \\ (\Delta p)/p \end{pmatrix} = M_u \begin{pmatrix} u^* \\ u^{*\prime} \\ (\Delta p^*)/p \end{pmatrix} \tag{8.5}$$

where we have used the thin lens approximation. Here the asterisk (*) denotes the values at the interaction point, $s = 0$, i.e. $u^* = u(0)$. Note that $u' = \mathrm{d}u/\mathrm{d}s$ which can be expressed by θ_u or p_u. The transport matrix is given by

$$M_u = \begin{pmatrix} \sqrt{\frac{\beta}{\beta^*}}(\cos\Phi + \alpha^* \sin\Phi) & \sqrt{\beta\beta^*}\sin\Phi & D_u \\ \frac{(\alpha^* - \alpha)\cos\Phi - (1+\alpha\alpha^*)\sin\Phi}{\sqrt{\beta\beta^*}} & \sqrt{\frac{\beta}{\beta^*}}(\cos\Phi - \alpha\sin\Phi) & D_u' \\ 0 & 0 & 1 \end{pmatrix} \tag{8.6}$$

where β is the amplitude function, α is the derivative of β, and Φ is the phase function. D is the dispersion which is irrelevant for elastic scattering but is important for diffractive scattering. Notice that the beam transport will not affect the total momentum and hence the

momentum loss of the proton, $(\Delta p)/p = (\Delta p^*)/p$. In the literature on beam transport it is common to use the momentum loss $(\Delta p)/p$ rather than the energy loss ξ. They are however equivalent in the relativistic limit where $E \gg m_p$.

Equation 8.5 is acquired when using the thin lens approximation. `MAD-X` allows for the use of the thick lens case where non-linear terms will enter. This non-linearity will depend on the proton energy loss ξ and will therefore be important for diffractive studies. Hence, we need to find a parameterization with non-linear terms.

In the following, we will use the convention $u_{\mathrm{IP}} \equiv u^*$ and denote the u-coordinate at the ALFA stations at $s \approx 237$ m and $s \approx 245$ m collectively as u_{RP}. The parameterization of the u-coordinate of the proton at the ALFA Roman Pots was found to be

$$\begin{aligned} u_{\mathrm{RP}}\left(u_{\mathrm{IP}}, \frac{p_{u,\,\mathrm{IP}}}{p}, \frac{\Delta p}{p}\right) = {} & F_u\left(\frac{\Delta p}{p}\right) \cdot u_{\mathrm{IP}} \\ & + G_u\left(\frac{\Delta p}{p}\right) \cdot \left[\frac{p_{u,\,\mathrm{IP}}}{p}\right] \\ & + H_u\left(\frac{\Delta p}{p}\right) \end{aligned} \tag{8.7}$$

where F_u, G_u, and H_u are all functions of the momentum loss $\frac{\Delta p}{p}$. Hence, the dependence on the initial position and momentum is linear but with an energy-dependant slope.

Note that the x- and y-coordinates are decoupled, i.e. x_{RP} will not depend on y_{IP} or $p_{y,\,\mathrm{IP}}$, and vice versa. This is because the linear section of the LHC between the ATLAS interaction point and the ALFA Roman Pots only contains dipole and quadrupole magnets (see Figure 5.7), and in such sections, the horizontal and vertical betatron oscillations are completely decoupled [42]. This makes the beam transport parameterization somewhat simpler.

The F_u, G_u, and H_u functions are fitted to the output from the Athena transport package `ForwardTransportFast` as quartic polynomials on the form of

$$\begin{aligned} F_u\left(\frac{\Delta p}{p}\right) = {} & f_{u,\,0} + f_{u,\,1} \cdot \left(\frac{\Delta p}{p}\right) + f_{u,\,2} \times \left(\frac{\Delta p}{p}\right)^2 \\ & + f_{u,\,3} \cdot \left(\frac{\Delta p}{p}\right)^3 + f_{u,\,4} \times \left(\frac{\Delta p}{p}\right)^4 \end{aligned} \tag{8.8}$$

where $f_{u,\,n}$, $g_{u,\,n}$, and $h_{u,\,n}$ are all constant parameters found from the fits. Notice that the units are $[F_u] = 0$ and $[G_u] = [H_u] = \mathrm{mm}$. We end up with 30 parameters in total of the beam transport parameterization for each ALFA station and beam setting. The parameters will

depend on the collision energy ($\sqrt{s}$), optics (β^*), and crossing angle (θ_C). Notably, we have $H_y = 0$ for $\theta_C = 0$ μrad, but a non-zero H_y for $\theta_C = 2 \times 50$ μrad. This was discussed in Section 5.5, where it was found that a non-zero crossing angle would also result in a shift of the protons in the y-direction and not just in the x-direction.

Note that for elastic events, with $\Delta p = 0$, the three functions F_u, G_u, and H_u all reduce to constants. Hence, we lose the non-linearity and revert to the matrix formulation,

$$u_{\text{RP}}\left(u_{\text{IP}}, \frac{p_{u,\text{IP}}}{p}\right) = a \times u_{\text{IP}} + b \times \left(\frac{p_{u,\text{IP}}}{p}\right) + c \tag{8.9}$$

where a, b, and c are the matrix elements from Equation 8.6. The beam transport of elastic protons are therefore a lot simpler than that of diffractive protons.

A particle gun allows us to generate protons where we can scan over values of x_{IP}, y_{IP}, $p_{x,\text{IP}}$, $p_{y,\text{IP}}$, and p. `ForwardTransportFast` using Twiss files from `MAD-X` can then transport the protons down the beam pipe to the ALFA detectors, and will provide values for x_{RP} and y_{RP} at all four ALFA stations.

First we have scanned over different values of momentum loss Δp and for each value then scanned over different values of x_{IP} to see how x_{RP} behaves. In Figure 8.3, x_{RP} as a function of x_{IP} for $\Delta p = 0$ is plotted and fitted with a straight line. For each Δp value, a straight line has been fitted. The slope of the line is F_x and is plotted in Figure 8.4. The function F_x can then be fitted with a quartic polynomial on the form of Equation 8.8. The same has been done for the y-coordinate to find F_y in Figure 8.5 and 8.6.

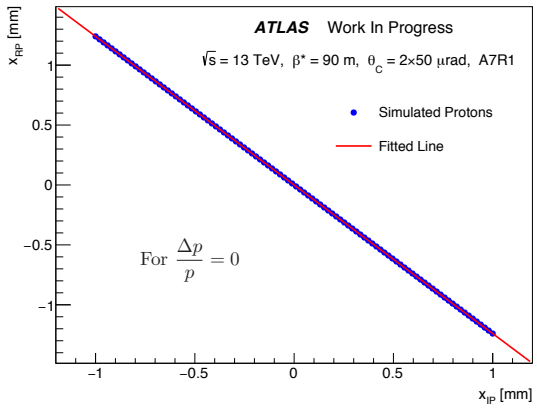

Figure 8.3: x_{RP} as a function of x_{IP} for $\Delta p = 0$. Fitted with a straight line, with slope $F_x(0)$.

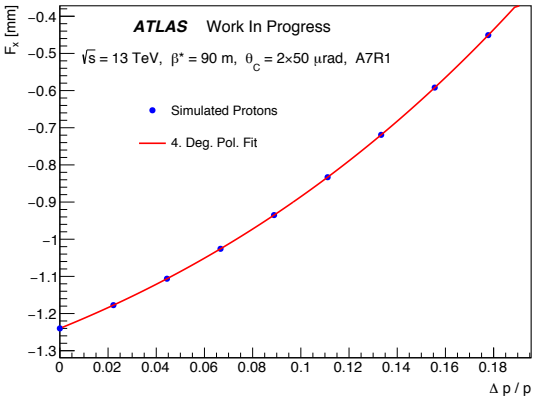

Figure 8.4: The function F_x as a function of $\Delta p/p$. Fitted with a fourth degree polynomial.

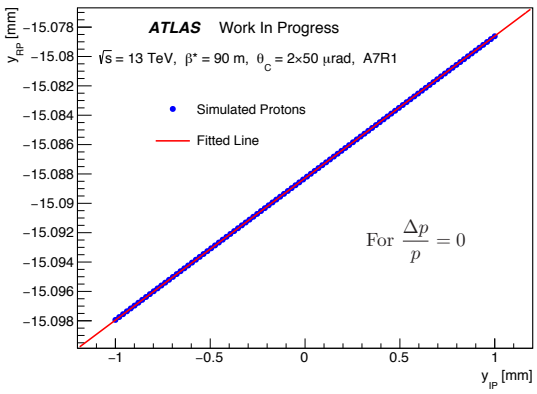

Figure 8.5: y_{RP} as a function of y_{IP} for $\Delta p = 0$. Fitted with a straight line, with slope $F_y(0)$.

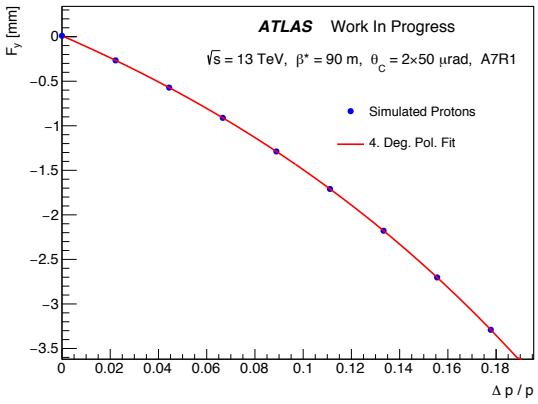

Figure 8.6: The function F_y as a function of $\Delta p/p$. Fitted with a fourth degree polynomial.

The same procedure we used to find F_x and F_y has been used to find G_x and G_y, in Figure 8.7, 8.8, 8.9, and 8.10.

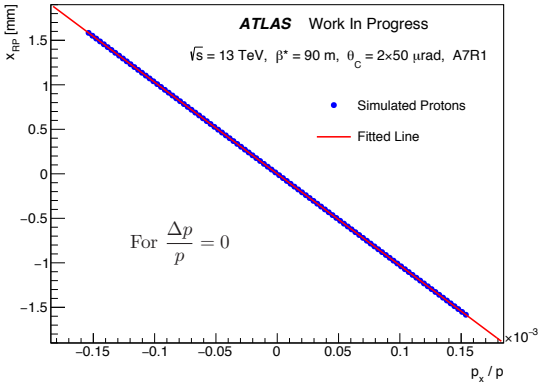

Figure 8.7: x_{RP} as a function of $p_{x,\,\mathrm{IP}}$ for $\Delta p = 0$. Fitted with a straight line, with slope $G_x(0)$.

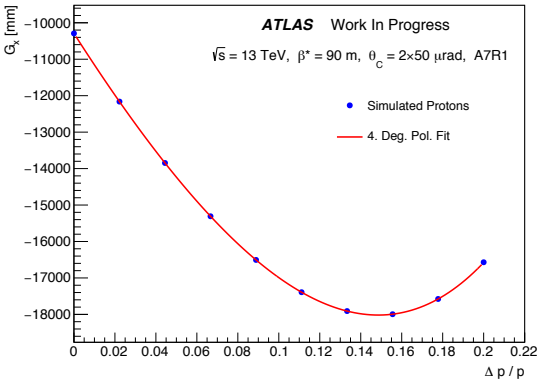

Figure 8.8: The function G_x as a function of $\Delta p/p$. Fitted with a fourth degree polynomial.

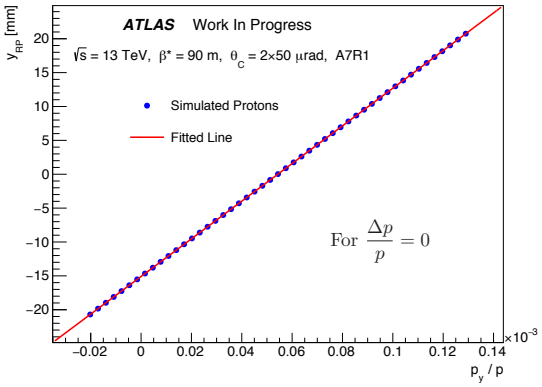

Figure 8.9: y_{RP} as a function of $p_{y,\,\mathrm{IP}}$ for $\Delta p = 0$. Fitted with a straight line, with slope $G_y(0)$.

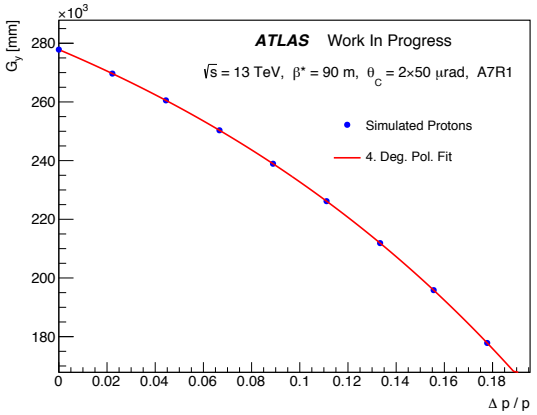

Figure 8.10: The function G_y as a function of $\Delta p/p$. Fitted with a fourth degree polynomial.

Simply keeping $x_{\text{IP}} = y_{\text{IP}} = 0$ and $p_{x,\,\text{IP}} = p_{y,\,\text{IP}} = 0$, while scanning over values of Δp, will give us H_x and H_y as shown in Figure 8.11 and 8.12.

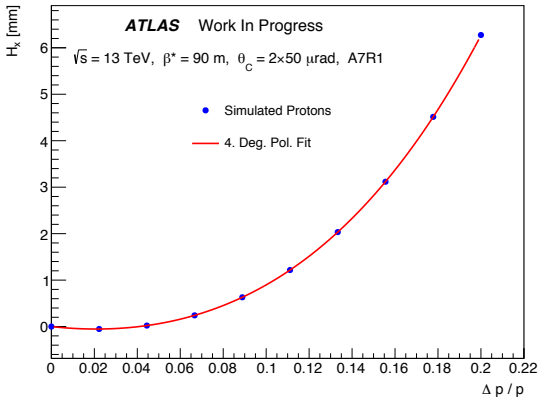

Figure 8.11: The function H_x as a function of $\Delta p/p$. Fitted with a fourth degree polynomial.

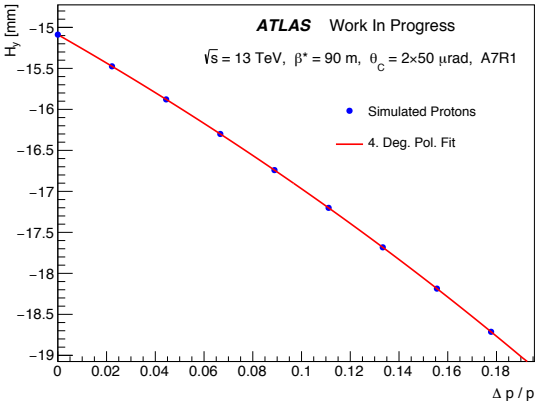

Figure 8.12: The function H_y as a function of $\Delta p/p$. Fitted with a fourth degree polynomial.

Fourth degree polynomials were found to fit the output from `MAD-X` and `ForwardTransportFast` better than e.g. second degree polynomials. In Figure 8.13 the residual for the function H_y for a second degree and a fourth degree polynomial fit are shown. The residual is the difference between the `ForwardTransportFast` output and the respective fit values evaluated at the given $(\Delta p)/p$ values.

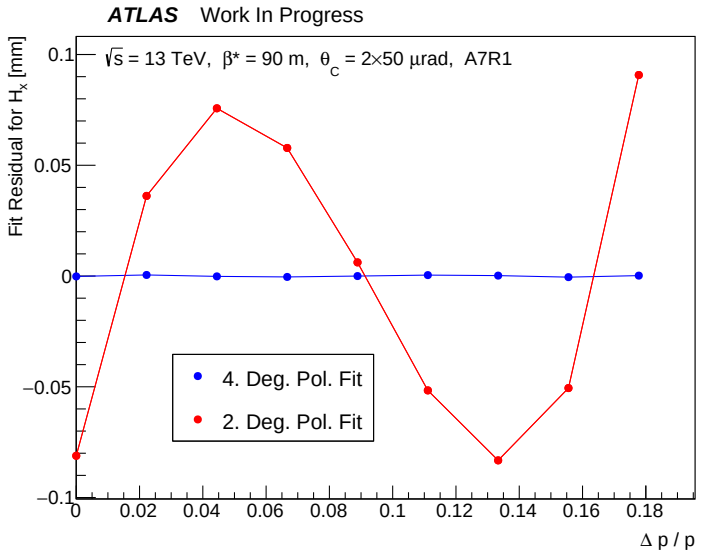

Figure 8.13: The residual for the function H_x, for a second degree polynomial (red) and a fourth degree polynomial (blue).

All beam transport parameters found from the fits are listed in Appendix A.

The diffractively dissociated system, denoted X, in single diffractive systems will on average per event contain about 1.4 protons, 0.8 anti-protons, 12 positive pions, 12 negative pions, and 0.003 of both muons and anti-muons. All of these particles are electrically charged with sufficiently long lifetimes ($\tau \gtrsim 10^{-6}$ s) to allow them to travel to the the ALFA stations and leave a track in the detectors, given that they have a large enough energy ($E \gtrsim 5200$ GeV) and are scattered in the extreme forward direction. In Section 5.5 it was noted that `ForwardTransportFast` is not able to transport negatively charged particles. Particles with the same charge as the positive proton, such as the positive pion and muon, will be affected by the magnetic lattice in the same way as the protons.

The simulation framework as implemented in Rivet will loop over all positively charged protons, pions, and muons in the event, and transport them to the ALFA stations. Events with more than one successfully transported particle will be discarded. In events with exactly one successfully transported particle, the particle will be assumed to be a proton and reconstructed as such. This will naturally introduce a background source, as the ALFA detectors are not able to discern protons from other charged particles. Both positively and negatively charged particles from the system will contribute to the background. Since the simulation framework is only able to transport positively charged particles, any estimation of this background will be smaller than expected. The background of positive particles from the dissociated system was estimated to make up about $(0.13 \pm 0.01)\%$ of selected events, where the events were selected using the full simulation framework. Looping over all particles that may hit the ALFA detectors in each event will also enable the simulation framework to work on non-diffractive events, which are expected to account for a significant part of the background.

A beam proton, with $\xi = 0$, $p_x = 0$ GeV, and $p_y = -0.325$ GeV, will have a small shift in the y-direction due to the crossing angle. The beam positions at the ALFA stations are

$$y_{\text{beam, 237 m}} = 1.1962 \text{ mm} \tag{8.10}$$

$$y_{\text{beam, 245 m}} = 1.0923 \text{ mm} \tag{8.11}$$

These coordinates are in the LHC coordinate system. The beam coordinate system will have the beam at $(x, y) = (0, 0)$ at each position s on the LHC ring.

8.3 ALFA ACCEPTANCE AND DETECTOR SIMULATION

The ALFA detector only covers a small geometrical region of the polar angle, θ, and the azimuthal angle, ϕ. Unlike most of the sub-detectors of ATLAS, ALFA does not cover the entire azimuthal region. The result is that not all diffractively scattered protons will hit ALFA and be measured. The outline of the ALFA main detectors in the transverse plane is seen on Figure 8.14 in blue. The LHC beam screen is illustrated in red.

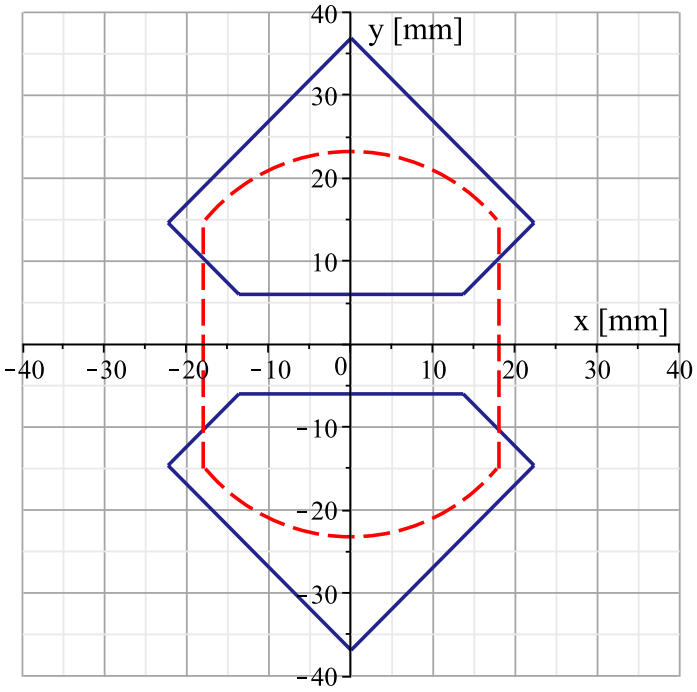

Figure 8.14: Illustration of the shape of the ALFA main detectors (blue) and the LHC beam screen (red) in the plane transverse to the beam direction.

The ALFA Roman Pots are assumed to be displaced about 6 mm in the y-direction from the beam position at $(0, 0)$ in the beam coordinate system. This is the usual setting for diffractive runs. The actual detector positions for our data run are listed in Table 10.1 and has been used for additional accuracy. There is an additional 450 μm from the edge of the ALFA Roman Pots to the ALFA main detectors [49], which needs to be accounted for as well. Note that the beam position in the LHC coordinate system is given by Equation 8.10 and 8.11. Figure 8.14 is therefore in the beam coordinate system.

It is possible to use a single particle gun to generate single protons in the extreme forward direction. The trajectory of these protons down the LHC beam pipe from the ATLAS interaction point (IP1) to the ALFA Roman Pots (RPs) can then be simulated using the Athena package `ForwardTransportFast`, as described in Section 5.5. Varying

the kinematics of the protons in the single particle gun will allow one to check the acceptance as a function of the proton kinematics, for any given beam energy and optics. An understanding of the acceptance regions will not only give insight into the physics that can be analyzed with ALFA but will also provide cuts on the proton kinematics in the simulation framework. Using a single particle gun, one million protons have been simulated, where the kinematics of the protons were scanned over 100 different values each of the three variables: ξ, p_T, and ϕ. The protons were generated at the interaction point set at $(0, 0, 0)$ and then transported down the LHC beam pipe to $z = 237$ m using `ForwardTransportFast`. The accepted variable configurations can then be plotted.

Acceptance of the protons will depend on the beam energy ($\sqrt{s}$), the optics (β^*), as well as the crossing angle (θ_C). The crossing angle will have an interesting effect on the acceptance and therefore both $\theta_C = 0$ μrad and $\theta_C = 2 \times 50$ μrad have been considered for comparison. Note, however, that data considered in this thesis is for $\theta_C = 2 \times 50$ μrad.

The transverse momentum (p_T) is taken relative to the beam axis for both settings of crossing angle. For 0 μrad the beam axis coincide with the z-axis in the LHC coordinate system, while for 2×50 μrad the beam axis is shifted down in the LHC (y, z)-plane with a small angle relative to the z-axis. The four momenta of the beams are listed in Table 8.1. The protons have been generated with a flat distribution in the three kinematic variables, but in data the ξ and p_T distributions are not expected to be described by a flat distribution. Only the ϕ distribution is expected to be flat. This is, however, not important for the acceptance plots as they are inherently physics independent.

There are two versions of the acceptance plots presented. The first is the *LHC acceptance* which is how many protons that survived the aperture down the beam pipe to the first ALFA station at $z = 237$ m. Between IP1 and the ALFA Roman Pots, the magnets situated on the beam pipe can bend the protons so much that they are lost. The second is the *ALFA acceptance* which takes the accepted protons from the LHC acceptance and then adds the additional requirements that protons must hit within the LHC beam screen and the ALFA main detectors. This will naturally reduce the acceptance compared to the LHC acceptance.

For $\theta_C = 0$ μrad the three-dimensional LHC and ALFA acceptance plots are shown in Figure 8.15 and the two-dimensional projections are shown in Figure 8.16 and 8.17. For $\theta_C = 2 \times 50$ μrad the acceptance plots are shown in Figure 8.18, 8.19, and 8.20.

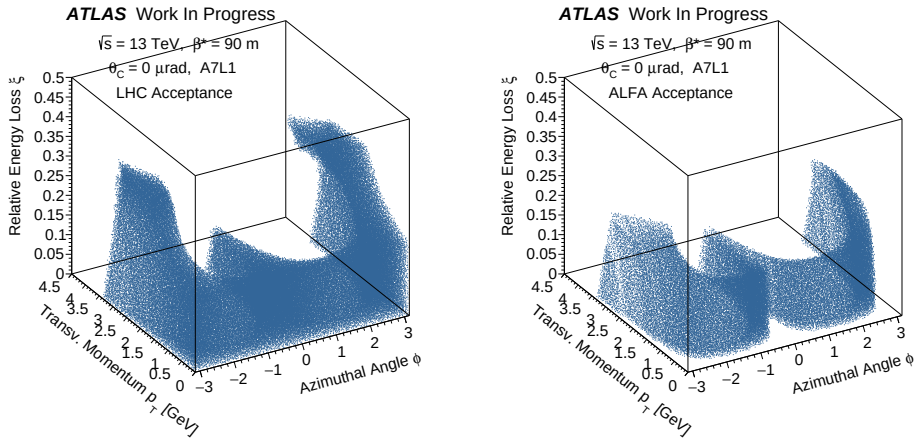

(a) LHC acceptance. **(b)** ALFA acceptance.

Figure 8.15: Three-dimensional acceptance plots for $\sqrt{s} = 13$ TeV, $\beta^* = 90$ m, and $\theta_C = 0$ μrad.

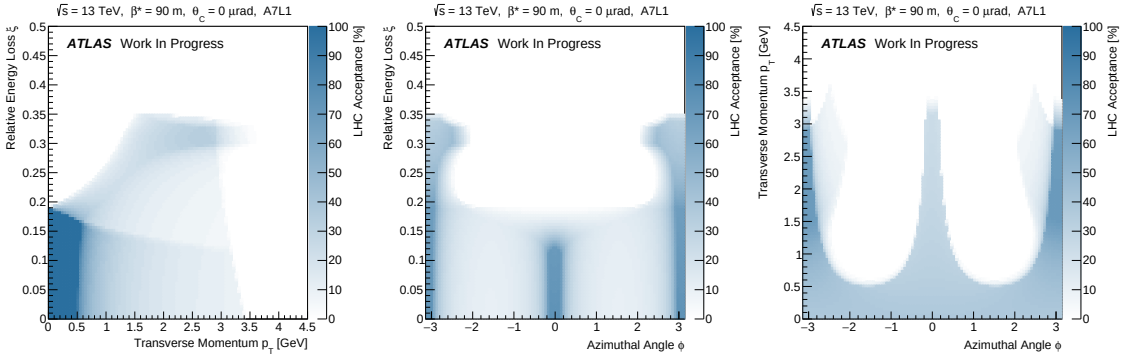

(a) ξ vs. p_T. **(b)** ξ vs. ϕ. **(c)** p_T vs. ϕ.

Figure 8.16: Two-dimensional projections of the LHC acceptance plots for $\theta_C = 0$ μrad.

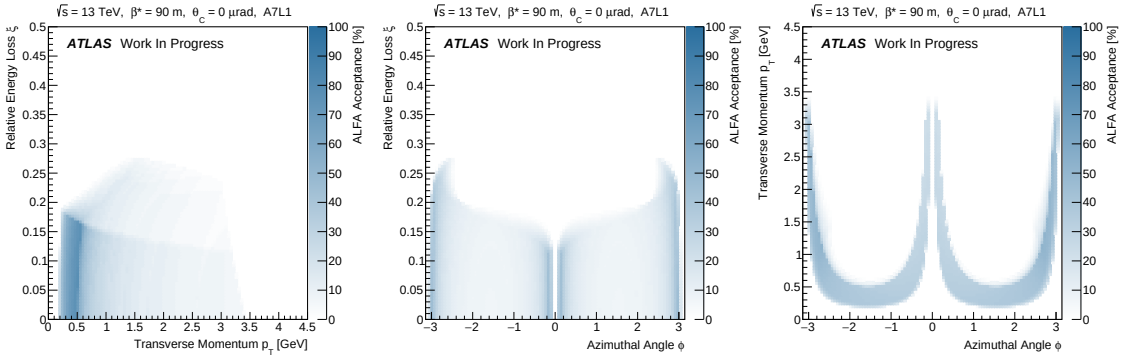

(a) ξ vs. p_T. **(b)** ξ vs. ϕ. **(c)** p_T vs. ϕ.

Figure 8.17: Two-dimensional projections of the ALFA acceptance plots for $\theta_C = 0$ μrad.

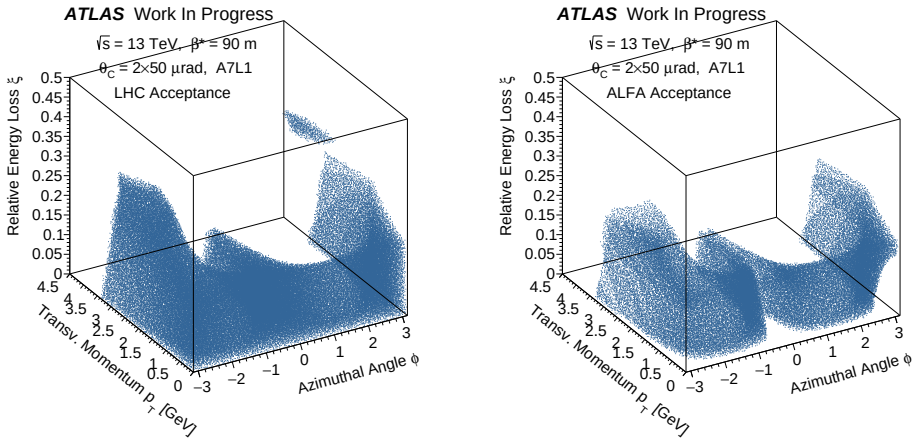

(a) LHC acceptance. **(b)** ALFA acceptance.

Figure 8.18: Three-dimensional acceptance plots for $\sqrt{s} = 13$ TeV, $\beta^* = 90$ m, and $\theta_C = 2 \times 50$ μrad.

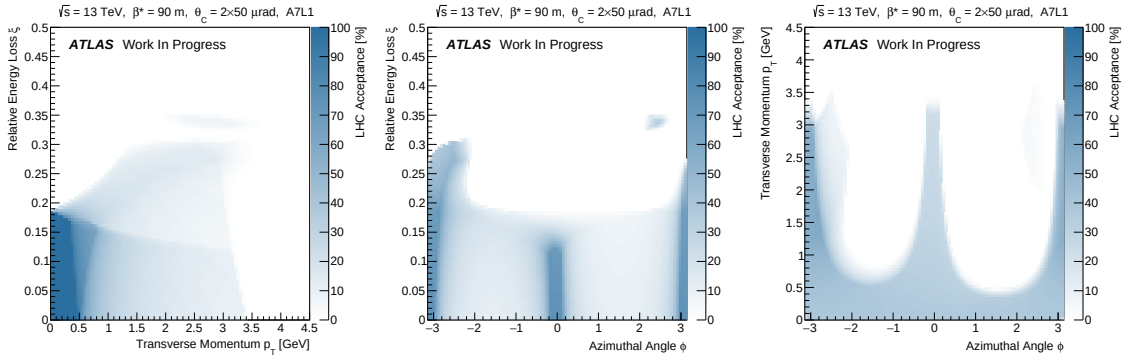

(a) ξ vs. p_T. **(b)** ξ vs. ϕ. **(c)** p_T vs. ϕ.

Figure 8.19: Two-dimensional projections of the LHC acceptance plots for $\theta_C = 2 \times 50$ μrad.

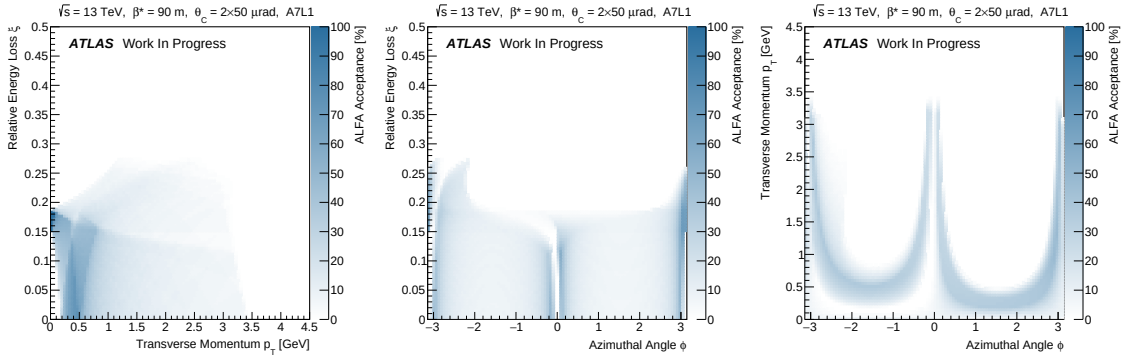

(a) ξ vs. p_T. **(b)** ξ vs. ϕ. **(c)** p_T vs. ϕ.

Figure 8.20: Two-dimensional projections of the ALFA acceptance plots for $\theta_C = 2 \times 50$ μrad.

The acceptance plots in ξ, p_x, and p_y are available in the Appendix in Section B.1 for $\theta_C = 2 \times 50$ μrad.

The LHC acceptance is up to 100% in the region of $\xi < 0.2$ and $p_T < 0.5$ GeV. For $p_T < 0.5$ GeV, the acceptance in ϕ is nearly uniform. Otherwise, the structure seen in ϕ is due to the asymmetry of the ALFA detector in the azimuthal direction. When considering the ALFA acceptance, the acceptance in this region is significantly reduced. For 0 μrad no protons with a $p_T < 0.2$ GeV will hit ALFA as these protons will be too close to the beam axis and will therefore pass between the two main detectors. But for 2×50 μrad the protons may hit ALFA even with a $p_T \approx 0$ GeV, given that they have a $0.135 \lesssim \xi \lesssim 0.185$. To fully understand why, it is necessary to turn to the distributions of hits in the ALFA detectors by looking at ALFA hitmaps. The ALFA hitmaps will be studied in the combined simulation results in Section 8.6.

The protons used to make the acceptance plots were generated at the interaction vertex $(x, y, z) = (0, 0, 0)$. As seen in Section 5.5 the proton trajectory will also depend on the primary vertex from which the protons originate. Hence, the primary vertex will also influence the acceptance. However as seen in the proton trajectory plots (Figure 5.12 and 5.13) as well as in the beam transport fits (Figure 8.3 and 8.5) this dependence is very weak and given the relatively small vertex spread in Table 8.2 the acceptance due to the vertex spread will have no effect in our case.

The ALFA main detectors at $z = 237$ m have a tracking resolution of 30 μm, while the main detectors at $z = 245$ m are assumed to have a resolution of 40 μm due to multiple scattering. The resolution was measured in several test beams [66, 68]. Since multiple scattering and the resulting shower effects will be dependent on the energy of the protons, then so will the resolution at $z = 245$ m. However, this energy dependency has not yet been properly studied.

The simulation framework will first check whether the proton hit (x, y)-coordinate is within acceptance. This is done by using the LHC acceptance plots as essentially "look-up tables" and by requiring the coordinates to be within both the ALFA detector and the beam screen regions as outlined in Figure 8.14. The coordinates are then smeared with a Gaussian function with a width of 30 μm for the near stations and 40 μm for the far stations. If the proton hit is smeared outside the overlap regions of ALFA and the beam screen then the event will be cut. This is to simulate an edge cut that will be used in the data analysis.

8.4 KINEMATIC RECONSTRUCTION OF THE PROTONS

Once the (x, y)-coordinate of the transported proton has been through the acceptance and smearing, it will be given as input to the reconstruction code to get the kinematics of the proton at the interaction point, i.e. the energy, E, and the transverse components of the three-momentum, p_x and p_y. The reconstruction code used in this study is the Copenhagen Reconstruction package, also known as `ALFAReco`. The `ALFAReco` package will be briefly described in this section and the performance and resolution of the reconstruction fits will be shown. For a full run-down of the details on the method used by `ALFAReco` as well as the precision of the package, see ref. [69].

`ALFAReco` utilizes a parameterization of the proton kinematics that is very similar to the one found in Equation 8.7. To handle the reconstruction of a protons kinematics giving its hitmap positions, a χ^2 function is constructed based on the parameterization. The χ^2 function is then minimized using Minuit [70]. The expectation values in the χ^2 function is provided by interpolations of the parameterization that are stored in parameter files. The interpolation is done with the *Akima* method [71]. These parameter files can be constructed with the use of `ForwardTransportFast` and will be read by `ALFAReco` before reconstruction. A parameter file must be created for each different beam setting, i.e. energy ($\sqrt{s}$), optics (β^*), and crossing angle (θ_C). Parameter files for $\sqrt{s} = 13$ TeV, $\beta^* = 90$ m, and both $\theta_C = 0$ μrad and $\theta_C = 2 \times 50$ μrad have been generated for this study. `ALFAReco` along with the parameter file for $\theta_C = 2 \times 50$ μrad will also be used on data. Special care is to be taken to which coordinate system the provided (x, y)-coordinates are expressed in, as the parameter files are generated according to the LHC coordinate system.

The reconstruction resolution of E, p_x, and p_y, from a simulation using `ALFAReco` with the generated parameter file, is shown in Figure 8.21 - 8.26. The resolution is found for simulated single diffractive events. The uncertainty on the reconstruction is primarily from the position smearing at the ALFA detector as described in the previous section, but will also have small contributions from the accuracy of the `ALFAReco` parameterization and the numerical precision of Minuit. The middle 'gap' in the resolution plot for p_y in Figure 8.26 is from the ALFA detector simulation where there is a gap between the detectors. In Figure 8.27 the χ^2 values of the reconstruction fits performed by `ALFAReco` are plotted for simulated single diffractive events. The distribution has been fitted with a χ^2 distribution for a number of degrees of freedom (NDF) of 1, as this is the expected NDF for a single proton fit.

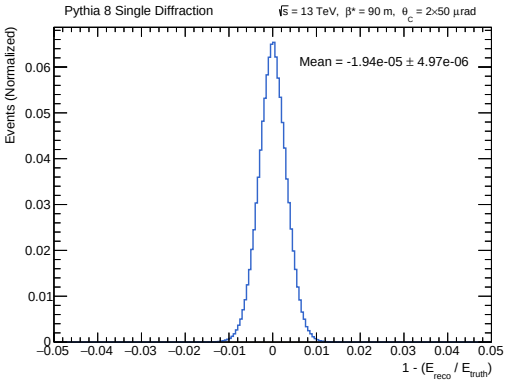

Figure 8.21: The resolution of the reconstructed E from `ALFAReco`.

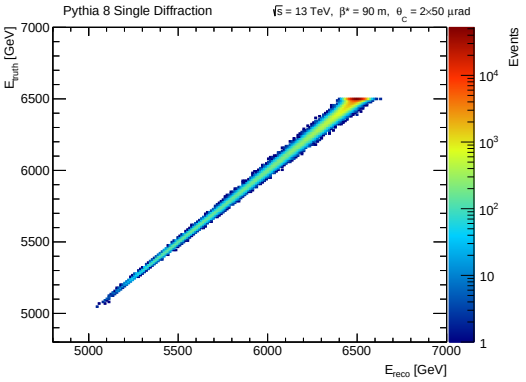

Figure 8.22: The reconstructed E from `ALFAReco` vs. the truth E.

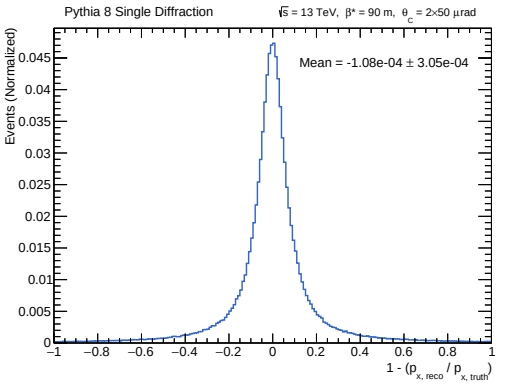

Figure 8.23: The resolution of the reconstructed p_x from `ALFAReco`.

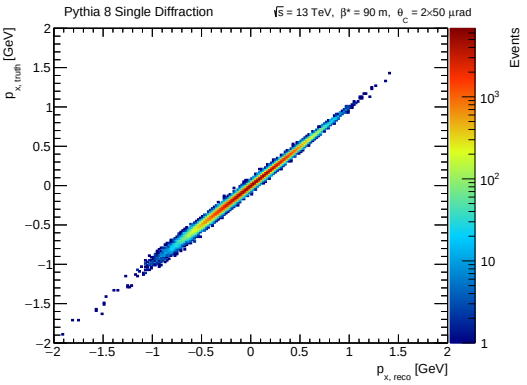

Figure 8.24: The reconstructed p_x from `ALFAReco` vs. the truth p_x.

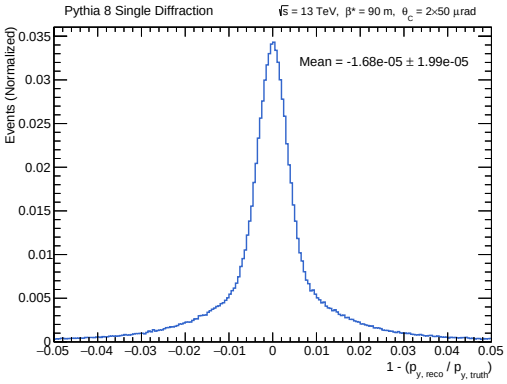

Figure 8.25: The resolution of the reconstructed p_y from `ALFAReco`.

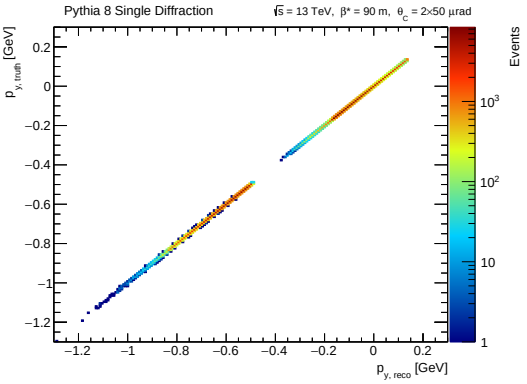

Figure 8.26: The reconstructed p_y from `ALFAReco` vs. the truth p_y.

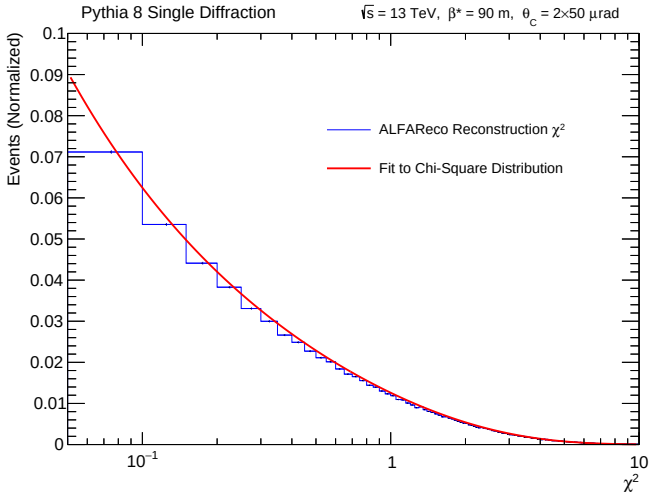

Figure 8.27: The χ^2 of the reconstruction fits from `ALFAReco`, fitted with a χ^2 distribution for a number of degrees of freedom of 1.

8.5 FAST ATLAS DETECTOR SIMULATION

In addition to the ALFA detector simulation, a fast and simple ATLAS detector response simulation in C++ was developed for the purposes of this study. The simulation includes pseudorapidity (η) and transverse momentum (p_T) acceptance for each of the sub-detectors: Inner Detector (ID or Tracker), ECAL, HCAL, FCAL, and Muon Spectrometer (MS). The pseudorapidity coverage of the ATLAS sub-detector systems was discussed in Chapter 6 and is summarized in Table 8.3 as well.

As outlined in Section 6.2, the Inner Detector (ID) detects charged particles (electrons, muons, protons, pions, and charged kaons). The ECAL detects photons and electrons. The HCAL detects hadrons (protons, neutrons, pions, charged kaons, and the neutral K_L). The FCAL detects the same as the ECAL and the HCAL. The Muon Spectrometer only detects muons.

The energy resolution of each ATLAS sub-detector system has also been simulated through the smearing of either the energy or the p_T measurement.

The combined ID system measures the momentum of charged particles using the curvature of the helical trajectory of the particles that is a result of the homogeneous, solenoidal magnetic field inside the ID. This will provide a reconstructed track in the ID system where

the main uncertainty is through the measurement of the hit position. This will give a relative p_T resolution of [42]

$$\frac{\sigma_{p_T}}{p_T} = a \cdot p_T \oplus b \tag{8.12}$$

where the $\oplus$ refers to the addition in quadrature.

All parts of the ATLAS calorimeter (ECAL, HCAL, and FCAL) are sampling calorimeters, where the absorber material that produces the particle shower is distinct from the detector material that measures deposited energy from the shower. This means that the energy measurement is effectively just a counting of the number of particles produced in the shower cascades. The relative energy resolution is therefore given by a Poissonian term [42],

$$\frac{\sigma_E}{E} = \frac{a}{\sqrt{E}} \oplus b \tag{8.13}$$

where a is the stochastic variable and b is the constant term due to non-uniformities and calibration uncertainties.

The main source of uncertainty of the muon momentum measurement in the Muon Spectrometer (MS) is due to multiple scattering in the large volume of the lever arm. To reduce the multiple scattering of the muons, an air-core toroid magnet design has been used instead of using an iron core, though the iron core would enhance the strength and uniformity of the magnetic field. The momentum resolution for the Muon Spectrometer due to multiple scattering is given by [42]

$$\frac{\sigma_{p_T}}{p_T} \propto \text{const.} \tag{8.14}$$

Multiple scattering dominates the resolution at low p_T. For larger values of p_T, the resolution is similar to that of the tracker, in Equation 8.12.

The η and p_T coverage requirements as well as the nominal energy resolution of each sub-detector system are summarized in Table 8.3. The requirements outlined in this table was used to develop the fast and simple simulation of the ATLAS detector that is a part of the simulation framework used in this thesis.

The Minimum Bias Trigger Scintillator has also been simulated by checking for charged particles in the η range, $2.08 < \eta < 3.86$. This is a very simple simulation of the role of the MBTS as a trigger in minimum bias samples. A more thorough simulation would take into account the charge deposited in the MBTS scintillator disks.

Table 8.3: Performance goals of ATLAS and a summary of the requirements of a fast ATLAS simulation. The values are taken from [52].

Sub-detector	η coverage	p_T coverage	Resolution
ID	$\lvert\eta\rvert < 2.5$	$p_T \geq 100$ MeV	$\sigma_{p_T}/p_T = 0.05\% \cdot p_T \oplus 1\%$
ECAL	$\lvert\eta\rvert < 1.37$	$p_T \geq 500$ MeV	$\sigma_E/E = 10\%/\sqrt{E} \oplus 0.7\%$
	$1.52 \leq \lvert\eta\rvert < 2.47$		
	$2.5 \leq \lvert\eta\rvert < 3.2$		
HCAL	$\lvert\eta\rvert < 3.2$	$p_T \geq 500$ MeV	$\sigma_E/E = 50\%/\sqrt{E} \oplus 3\%$
FCAL	$3.2 \leq \lvert\eta\rvert < 4.9$	$p_T \geq 500$ MeV	$\sigma_E/E = 100\%/\sqrt{E} \oplus 10\%$
MS	$\lvert\eta\rvert < 2.7$	$p_T \geq 500$ MeV	$\sigma_{p_T}/p_T = 10\%$

8.6 COMBINED SIMULATION RESULTS

The simulation framework can be used on simulations of single, double, and central diffractive events, as well as elastic events. Note that for elastic events, the simulation framework simplifies significantly, as the acceptance plots in Figure 8.18a and 8.18b are reduced to a 2D plane in p_T and ϕ for $\xi = 0$, and the beam transport is reduced to a simple linear matrix formulation.

In this study, the primary focus is on single diffractive events, as they have a unique signal in ALFA and are the most common diffractive reactions. Hence, simulated events are required to have exactly one hit in two ALFA detectors in one of the four arms, as illustrated in Figure 7.7b. In addition, a requirement of at least two tracks with $p_T > 100$ MeV in the ATLAS inner detector, to simulate the reconstruction of a primary vertex, as well as a requirement of at least one charged particle to hit the MBTS on the opposite side of the ALFA hit, are imposed. A simple cut flow table of simulated single diffractive events, generated according to the Schuler-Sjöstrand Pomeron flux parameterization in Section 4.7.1, is seen in Table 8.4. Note that the acceptance will change according to the Pomeron flux parameterization, as will be discussed in the following chapter.

Table 8.4: Cut flow table for simulated SD events with the Schuler-Sjöstrand Pomeron flux parameterization.

Cut in Simulation	Percentage of passed SD events
At least one hit in ALFA	$(42.75 \pm 0.07)\%$
Exactly one hit in ALFA	$(42.38 \pm 0.07)\%$
At least two tracks in ID	$(24.43 \pm 0.05)\%$
Hit in MBTS on opposite side	$(21.60 \pm 0.05)\%$

8.6.1 *ALFA Hitmaps*

A diffractively scattered proton may hit and be measured by one of the ALFA detectors given that the proton finds itself in the accepted kinematic region. The proton is assumed to hit the ALFA main detectors perpendicular to the layers of scintillating fibres, where the proton track can be reconstructed as outlined in Section 7.6. This will provide a hit position, (x, y), of the proton in the plane transverse to the beam axis at the respective ALFA station.

The resulting hitmaps for simulated single diffractive protons for $\theta_C = 2 \times 50$ μrad in the two stations on the A-side are seen in Figure 8.28a and 8.28b. The distribution of proton hits on the A-side will be similar to that on the C-side. The binning of the hitmaps reflect the 40 μm resolution of the ALFA main detectors. The hitmaps for $\theta_C = 0$ μrad are seen in Figure 8.29a and 8.29b. The hitmaps for elastic events are shown in Figure 8.30a and 8.30b. Note the larger hit multiplicity in the upper detectors for the $\theta_C = 2 \times 50$ μrad single diffractive hitmaps. This was discussed in Section 5.5 and 8.2 and is due to the non-zero crossing angle giving an extra dependence of the y-coordinate on the proton momentum loss.

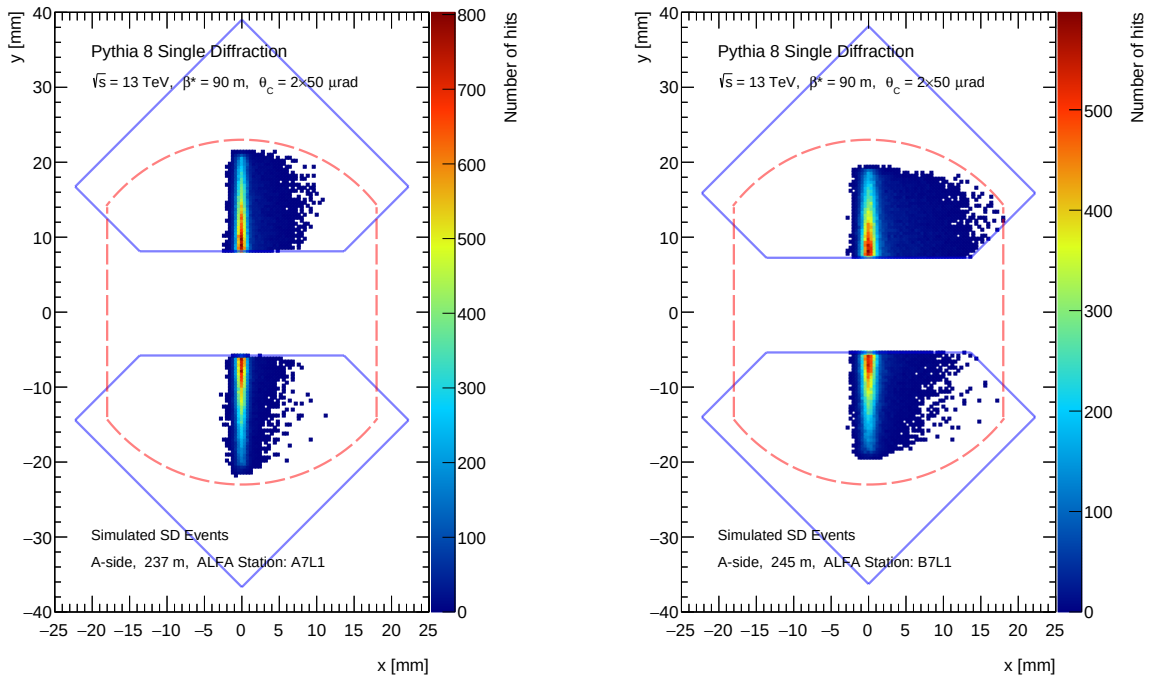

(a) Near station: $z = 237$ m.

(b) Far station: $z = 245$ m.

Figure 8.28: Hitmaps of single diffractively scattered protons for $\theta_C = 2 \times 50$ μrad in the ALFA stations on the A-side. Overlaid with the outline of the ALFA main detector (solid blue line) and the LHC beam screen (dashed red line).

The outline of the ALFA main detector (solid blue line) and the LHC beam screen (dashed red line) is overlaid on top of the hit maps to indicate the edge cuts on the hits.

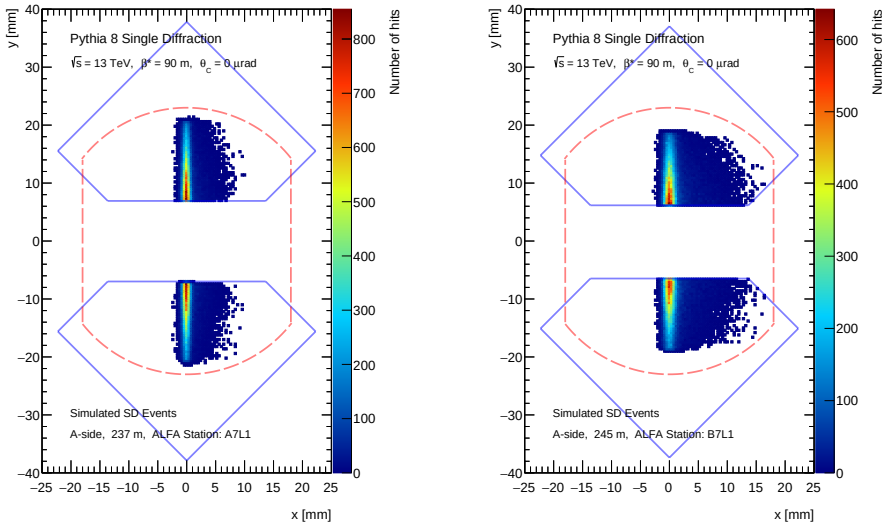

(a) Near station: $z = 237$ m. **(b)** Far station: $z = 245$ m.

Figure 8.29: Hitmaps of single diffractively scattered protons for $\theta_C = 0$ μrad in the ALFA stations on the A-side. Overlaid with the outline of the ALFA main detector (solid blue line) and the LHC beam screen (dashed red line).

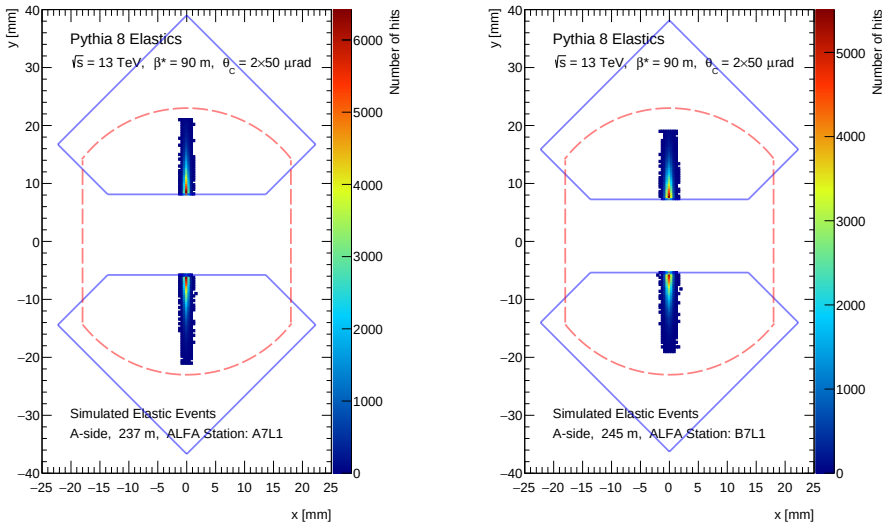

(a) Near station: $z = 237$ m. **(b)** Far station: $z = 245$ m.

Figure 8.30: Hitmaps of elastically scattered protons for $\theta_C = 2 \times 50$ μrad in the ALFA stations on the A-side. Overlaid with the outline of the ALFA main detector (solid blue line) and the LHC beam screen (dashed red line).

The hitmaps can help with the understanding of the acceptance plots in Section 8.3. Protons with $\phi \approx 0$ and $\phi \approx \pm\pi$ will have no ALFA acceptance as the ALFA main detectors are only in the vertical direction. Elastically scattered protons, where we have no energy loss, will all lie on a narrow band or ellipse around $x = 0$ mm, which is narrow in x but has a large spread in y. However, for diffractively scattered protons, a larger energy loss will give larger x and y values. The deflection to higher y values for larger energy loss ξ will also explain why particles with $p_T \approx 0$ GeV and a non-zero energy loss, ξ, may hit the upper detector and therefore be accepted. The more hits in the upper detector compared to the lower detector will also explain the asymmetry seen in ϕ for the acceptance plots, as $\phi \approx +\pi/2$ is in the direction of the upper detector while $\phi \approx -\pi/2$ is in the direction of the lower detector.

It is expected that the hitmaps and the acceptance plots are similar for the ALFA stations on the A-side compared to those on the C-side, as the magnet setup on either side of the ATLAS detector are nearly identical.

The difference between the coordinates in the near and far ALFA stations are shown in Figure 8.31 and 8.32, and illustrates the deflection in x and y. Most particles will be centered around $x = 0$ which corresponds to $\xi \simeq 0$ – i.e. protons that resembles elastically scattered protons as seen in Figure 8.30a and 8.30b. The proton hits as shown in the hitmaps will – alongside the reconstructed primary vertices from which the protons originate – be used by `ALFAReco` to reconstruct the kinematics of the protons, i.e. E, p_x, and p_y.

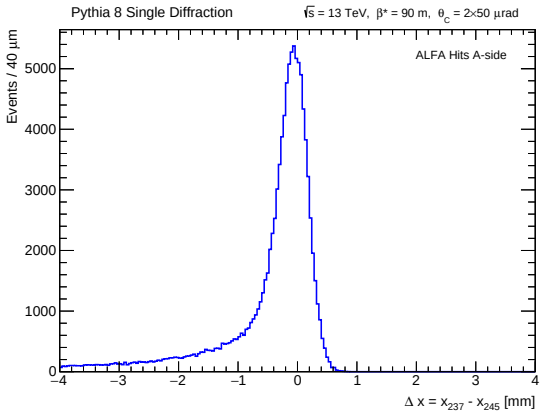

Figure 8.31: Difference in the proton hit x-coordinate between the near and far ALFA station, $\Delta x = x_{237\text{ m}} - x_{245\text{ m}}$, on the A-side.

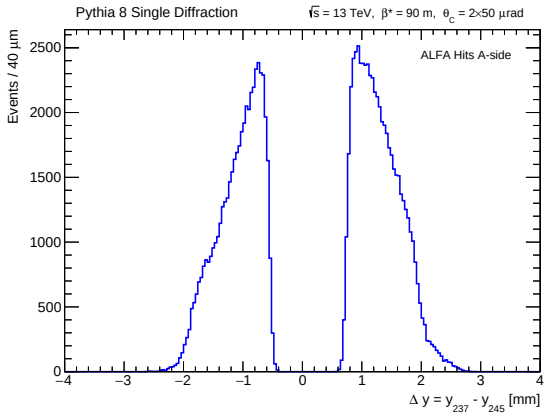

Figure 8.32: Difference in the proton hit y-coordinate between the near and far ALFA station, $\Delta y = y_{237\text{ m}} - y_{245\text{ m}}$, on the A-side.

8.6.2 *Physics Distributions*

The resulting ξ distribution from `ALFAReco` is plotted in Figure 8.33 (in blue) along with the distribution for the truth level (in red). The detector acceptance and simulation restricts the acceptance to $\xi \lesssim 0.22$. The peak is close to $\xi \simeq 0$ indicating the prevalence of low-mass diffractive systems. In the simulation framework, the peak is normal-distributed around $\xi = 0$, rather than sharply peaked. This is a result of the 30 μm and 40 μm detector resolution of the ALFA main detectors. The t distribution is shown in Figure 8.34 where for low $|t|$ we have a small scattering angle, $|t| \sim \theta^2$, that will result in the proton passing between the upper and lower ALFA detectors.

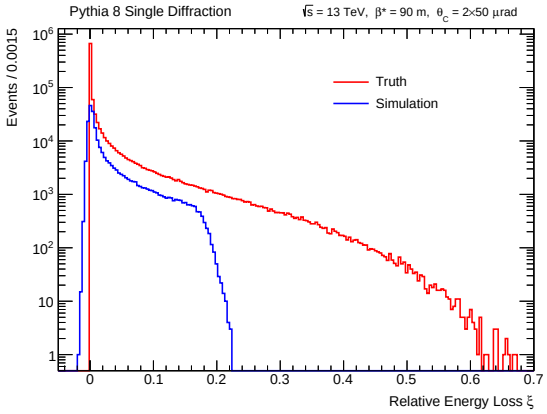

Figure 8.33: ξ distribution for truth level and after all smearing, acceptance, and cuts in the simulation framework.

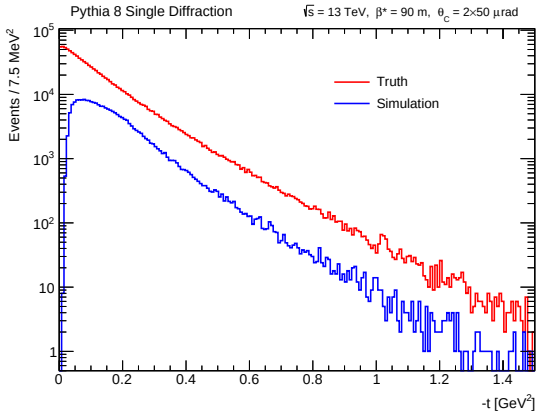

Figure 8.34: t distribution for truth level and after all smearing, acceptance, and cuts in the simulation framework.

The p_x and p_y distributions for the proton at the interaction point are seen in Figure 8.35 and 8.36. The p_y distribution is centered around

$$p_{y,\,\text{beam}} = -\sin(50\ \mu\text{rad}) \times 6500\ \text{GeV} \approx -0.325\ \text{GeV} \qquad (8.15)$$

corresponding to the beam. Protons with a p_y larger than $p_{y,\,\text{beam}}$ will generally hit the upper detector, as $y_{\text{RP}} \propto p_y$. However, protons with a p_y value similar to that of the beam, could hit the upper detector if they have a large energy loss, as already discussed. This is also illustrated in the acceptance plots in Figure 8.18b and 8.20.

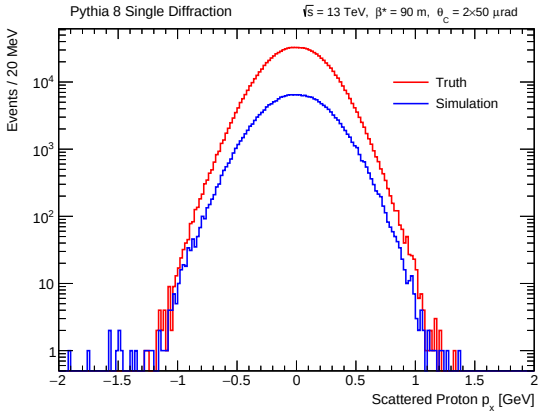

Figure 8.35: p_x distribution for truth level and after all smearing, acceptance, and cuts in the simulation framework.

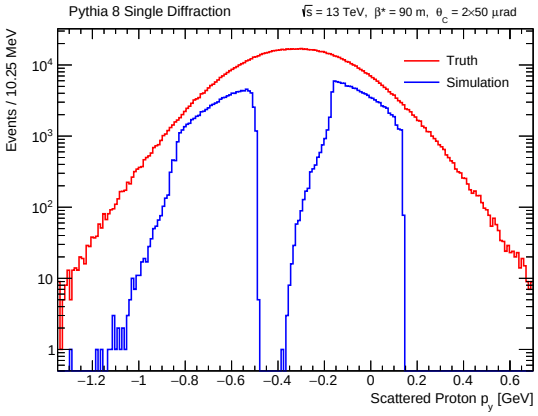

Figure 8.36: p_y distribution for truth level and after all smearing, acceptance, and cuts in the simulation framework.

The p_T distribution is plotted in Figure 8.37 for simulation and truth level. The simulation allows values down to $p_T = 0$ due to the non-zero crossing angle. The ϕ distribution is shown in Figure 8.38 where the truth distribution is uniformly distributed and the simulation distribution reflects the acceptance in Figure 8.20b and 8.20c.

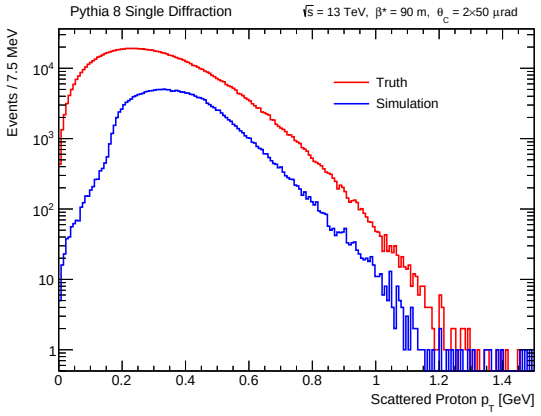

Figure 8.37: p_T distribution for truth level and after all smearing, acceptance, and cuts in the simulation framework.

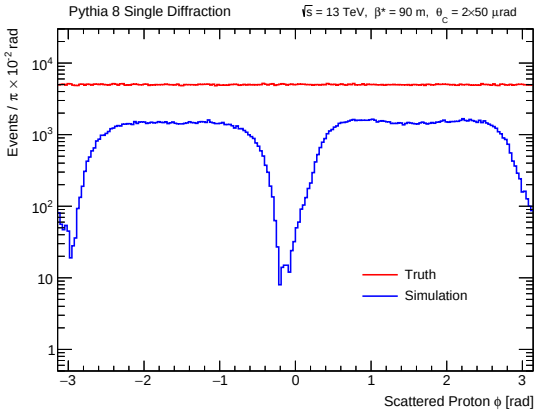

Figure 8.38: ϕ distribution for truth level and after all smearing, acceptance, and cuts in the simulation framework.

The absolute pseudorapidity $|\eta|$ distribution of the diffractively scattered protons is shown in Figure 8.39. Note that the ALFA detector restricts the acceptance to $9 \lesssim |\eta| \lesssim 13$ with most protons (and hence the largest acceptance) in the $9 \lesssim |\eta| \lesssim 11.5$ range.

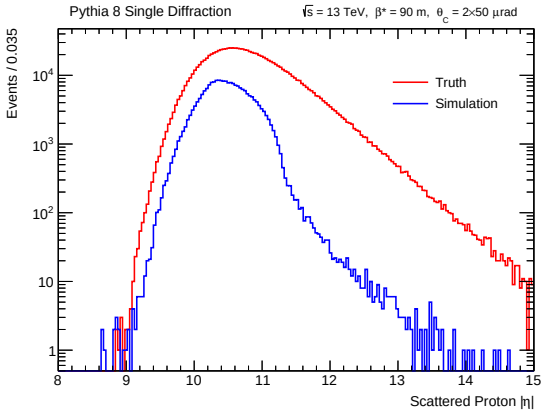

Figure 8.39: $|\eta|$ distribution for truth level and after all smearing, acceptance, and cuts in the simulation framework.

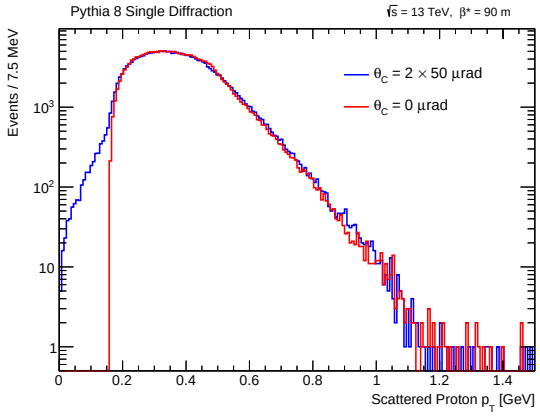

Figure 8.40: p_T distribution for $\theta_C = 2 \times 50$ μrad (in blue) and $\theta_C = 0$ μrad (in red).

The crossing angle θ_C will naturally affect the p_y distribution and therefore the p_T distribution as well. For $\theta_C = 2 \times 50$ μrad the acceptance in p_T extends towards smaller p_T values down to $p_T = 0$, as shown in Figure 8.40. However, the crossing angle will not affect the reconstructed ξ and t distributions, as shown in Figure 8.41 and 8.42.

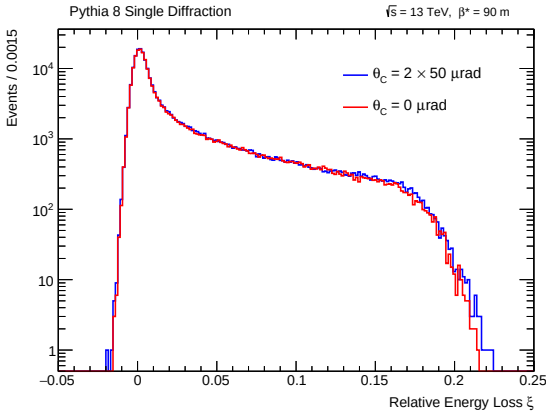

Figure 8.41: ξ distribution for $\theta_C = 2 \times 50$ μrad (in blue) and $\theta_C = 0$ μrad (in red).

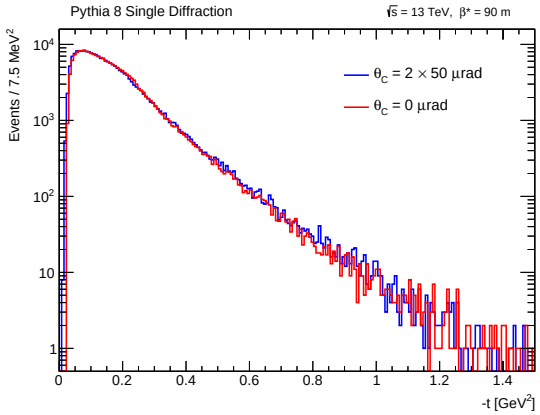

Figure 8.42: t distribution for $\theta_C = 2 \times 50$ μrad (in blue) and $\theta_C = 0$ μrad (in red).

The ξ and t distributions are only affected by the Pomeron flux parameterization. This will be studied in detail in the next chapter by using the simulation framework as outlined in this chapter.

9 PHENOMENOLOGICAL STUDY

This chapter presents a phenomenological study of single diffractive pp events using the simulation framework from the previous chapter. The observables most sensitive to the parameters ε and α' in the Pomeron flux parameterizations in Pythia will be presented, along with a study of some of the possible background sources. Finally, a fit procedure to discern the model parameters ε and α' that best fits data will be introduced and tested on simulated test samples.

9.1 OBSERVABLES SENSITIVE TO MODEL PARAMETERS

The aim of this section is to study the effect of the Pomeron flux parameterization on different observables. The goal is to ideally find observables that are particularly sensitive to the model parameters ε and α'.

To understand the sensitivity of observables to the model parameters, nine different samples for both the Donnachie-Landshoff and the Minimum Bias Rockefeller (MBR) parameterization have been generated. All samples are generated according to the common settings outlined in Section 8.1. In addition, the samples scans over the possible permutations of the three values of the parameters,

$$\varepsilon = \{0.02,\ 0.085,\ 0.15\} \tag{9.1}$$

$$\alpha' = \{0.1,\ 0.25,\ 0.4\}\ \text{GeV}^{-2} \tag{9.2}$$

where we have used the allowed minimum and maximum values along with the default values in Pythia.

The Pomeron flux as defined in Section 4.7 will provide the distribution of single diffractively scattered protons in ξ and t, given some values of the parameters ε and α'. This is seen by considering the predicted cross-section for hard single diffractive events [24],

$$\frac{\mathrm{d}\sigma^{\mathrm{SD}}}{\mathrm{d}\xi \mathrm{d}t} = f_{\mathbb{P}/p}(\xi, t)\ \sigma_{\mathbb{P}/p} \tag{9.3}$$

where factorization has been used. Note that $\sigma_{\mathbb{P}/p}$ is the assumed Pomeron-proton effective cross section, set to 10 mb. Here the probability (expressed as a cross-section) to get a single diffractive pp scattering event is given by the probability of taking a Pomeron out of one of the colliding protons (expressed by the Pomeron flux, $f_{\mathbb{P}/p}$) times

the probability of that Pomeron interacting with the other colliding proton (expressed by $\sigma_{\mathbb{P}/p}$). From Equation 5.2 we know that

$$\frac{\mathrm{d}N}{\mathrm{d}\xi \mathrm{d}t} = \mathcal{L}\frac{\mathrm{d}\sigma}{\mathrm{d}\xi \mathrm{d}t} \tag{9.4}$$

where $\mathcal{L}$ is the integrated luminosity. Hence, the Pomeron flux parameterization will affect the distributions of ξ and t, as well as the distributions of any related observables, e.g. p_T and Δy.

The sensitivity to the model parameters will show itself in two ways: the event count (i.e. the total cross-section) and the shape of the distribution (i.e. the differential cross-section). The event count is the relative number of accepted events. Both types of sensitivity have been studied. The accepted event count in percentage for the nine different samples for each Pomeron flux parameterizations are listed in Table 9.1 and 9.2. Notice that the event count is most sensitive to ε. A larger ε will give a smaller accepted event count, while a larger α' will give a slightly larger event count. The difference in the number of accepted events may be caused by the differences in the shape of the distributions, notably in ξ, p_T (affecting the ALFA acceptance), and the charged track multiplicity n_{ch} (affecting the ATLAS acceptance).

Table 9.1: Accepted event count in percentage for the nine different samples with the Donnachie-Landshoff Pomeron flux parameterization and with MPIs.

	$\varepsilon = 0.02$	$\varepsilon = 0.085$	$\varepsilon = 0.15$
$\alpha' = 0.1$ GeV^{-2}	$(19.44 \pm 0.04)\%$	$(10.11 \pm 0.03)\%$	$(4.08 \pm 0.02)\%$
$\alpha' = 0.25$ GeV^{-2}	$(21.33 \pm 0.05)\%$	$(11.28 \pm 0.03)\%$	$(4.63 \pm 0.02)\%$
$\alpha' = 0.4$ GeV^{-2}	$(21.58 \pm 0.05)\%$	$(11.62 \pm 0.03)\%$	$(4.64 \pm 0.02)\%$

Table 9.2: Accepted event count in percentage for the nine different samples with the Minimum Bias Rockerfeller (MBR) Pomeron flux parameterization and with MPIs.

	$\varepsilon = 0.02$	$\varepsilon = 0.085$	$\varepsilon = 0.15$
$\alpha' = 0.1$ GeV^{-2}	$(21.55 \pm 0.05)\%$	$(16.25 \pm 0.04)\%$	$(11.41 \pm 0.03)\%$
$\alpha' = 0.25$ GeV^{-2}	$(23.16 \pm 0.05)\%$	$(17.64 \pm 0.04)\%$	$(12.55 \pm 0.04)\%$
$\alpha' = 0.4$ GeV^{-2}	$(23.23 \pm 0.05)\%$	$(17.84 \pm 0.04)\%$	$(12.63 \pm 0.04)\%$

The sensitivity in the shape of the distributions will be presented by the following sensitivity plots. The four observables ξ, t, p_T, and Δy are common in studies of diffraction and therefore make a good starting point for studying the sensitivity. Note that the following sensitivity plots does not take the event count into account, but are normalized such that only the difference in shape is illustrated.

The sensitivity plots for the reconstructed relative energy loss ξ are shown in Figure 9.1. Notice that the sensitivity plots to the left are for varying ε while keeping α' constant at the PYTHIA default value $\alpha' = 0.25\ \text{GeV}^{-2}$. The sensitivity plots to the right are for varying α' while keeping ε constant at the default value $\varepsilon = 0.085$. The top sensitivity plots are for the Donnachie-Landshoff Pomeron flux parameterization while the bottom plots are for the Minimum Bias Rockefeller (MBR) parameterization. Furthermore, the sensitivity plots are normalized such that only the sensitivity in the shape of the distributions is illustrated. The sensitivity will therefore not reflect the sensitivity of the relative event count (or acceptance). All sensitivity plots in this section will follow this scheme.

The shape of the ξ distribution is primarily sensitive to ε. Notice that the Donnachie-Landshoff parameterization exhibits a higher sensitivity to ε than the MBR parameterization. This will be evident for all observables that are sensitive to ε.

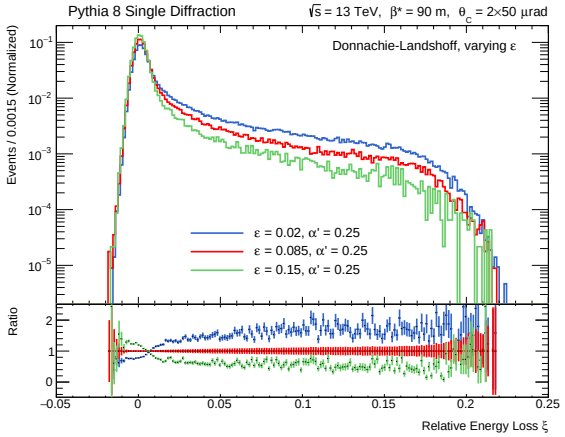

(a) DL – varying ε, keeping α' constant.

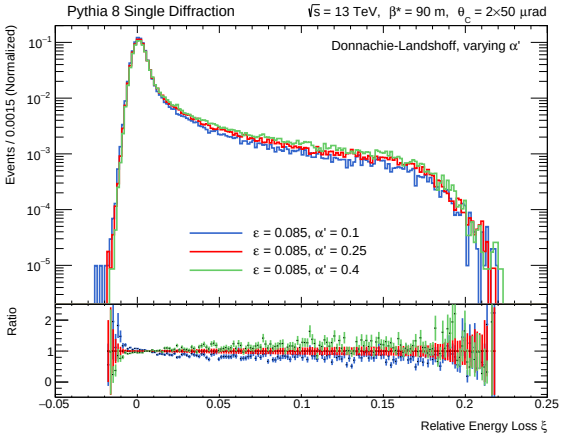

(b) DL – varying α', keeping ε constant.

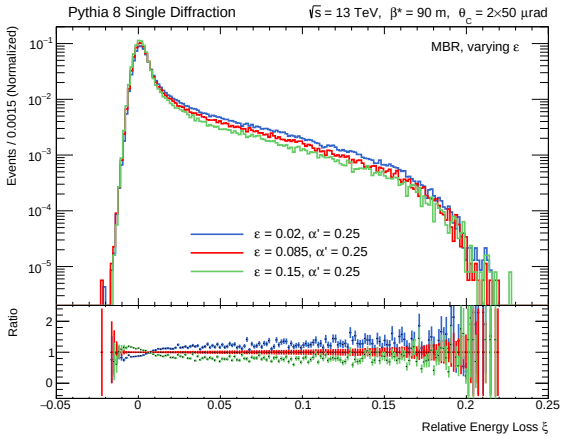

(c) MBR – varying ε, keeping α' constant.

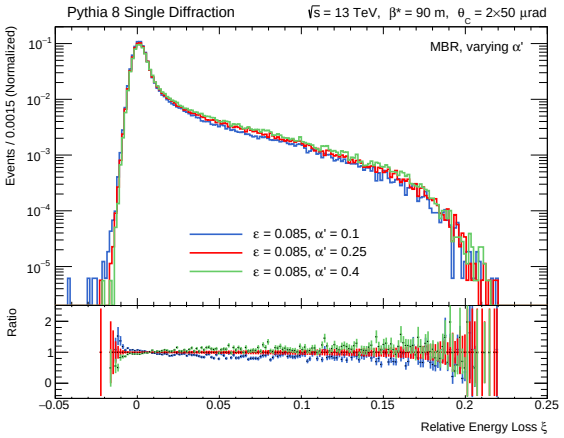

(d) MBR – varying α', keeping ε constant.

Figure 9.1: ξ distributions for different values of the model parameters, ε and α'.

The sensitivity plots for the reconstructed squared momentum transfer t are shown in Figure 9.2. It is seen that t is primarily sensitive to α'. Notice that both Pomeron flux parameterizations exhibit similar sensitivity to α' compared to ε.

The observables ξ and t are not independent as seen in Equation 4.34 and 4.37. Hence, we see a small sensitivity to α' in the ξ distribution and a small sensitivity to ε in the t distribution.

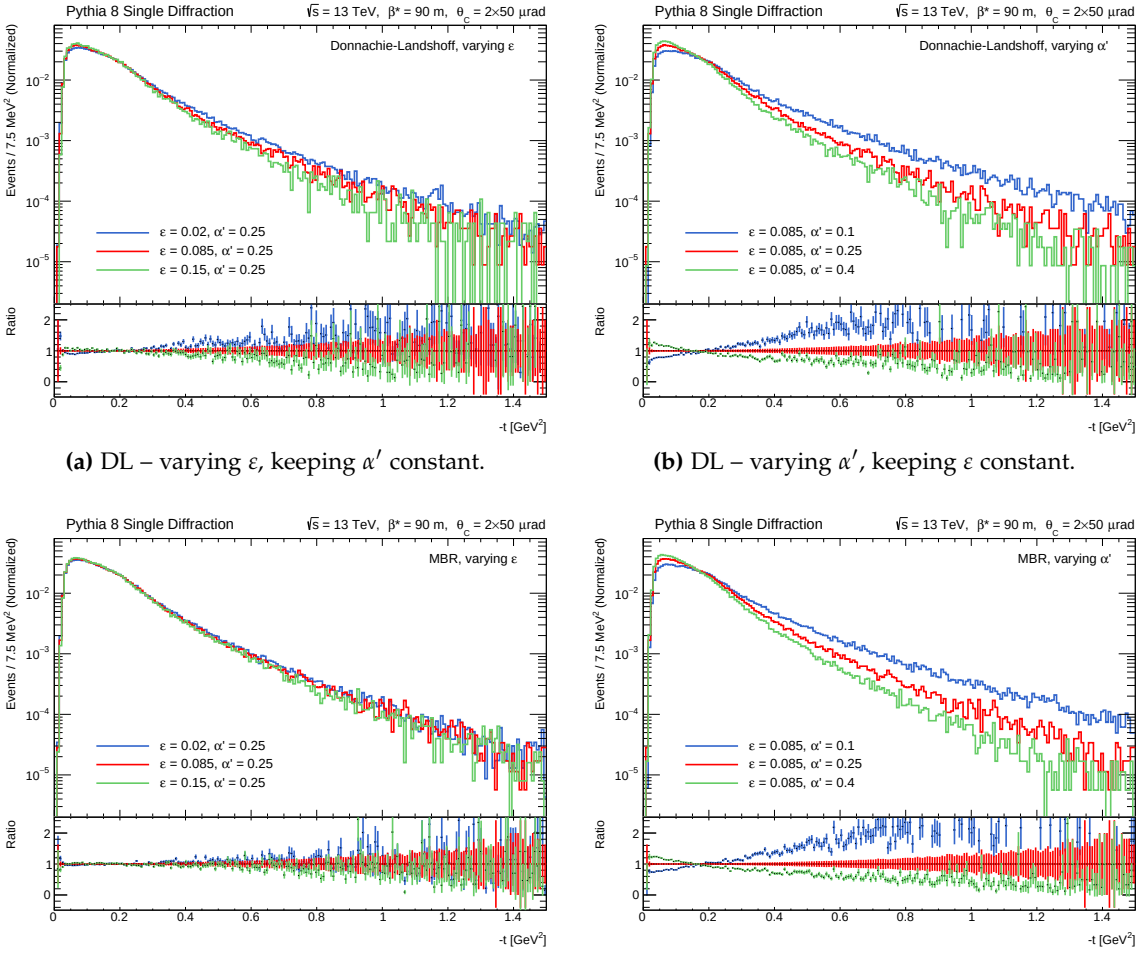

(a) DL – varying ε, keeping α' constant.

(b) DL – varying α', keeping ε constant.

(c) MBR – varying ε, keeping α' constant.

(d) MBR – varying α', keeping ε constant.

Figure 9.2: t distributions for different values of the model parameters, ε and α'.

The correlation plot between the reconstructed ξ and t for a simulated single diffractive sample with the Schuler-Sjöstrand Pomeron flux parameterization is shown in Figure 9.3.

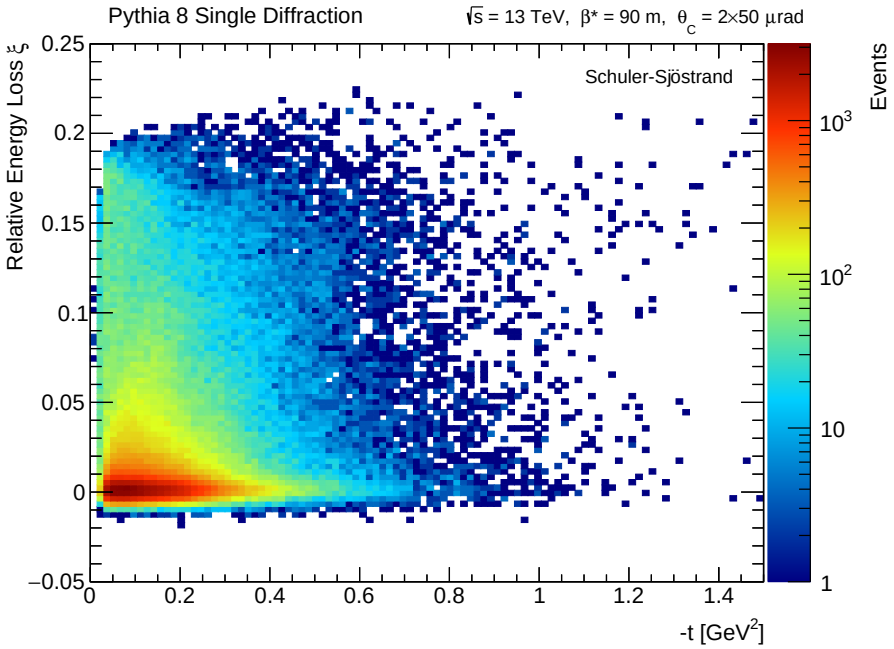

Figure 9.3: Correlation plot of the reconstructed ξ and t for the Schuler-Sjöstrand parameterization.

The sensitivity to the model parameters ε and α' in the ξ vs. t correlation plot are shown in Figure 9.4 and 9.5 respectively. The sensitivity plots have been created by taking the ratio between the correlations plots for the samples with the extreme values of the respective parameter. It is seen that the ε sensitivity is primarily in the ξ direction, while the α' sensitivity is primarily in the t direction.

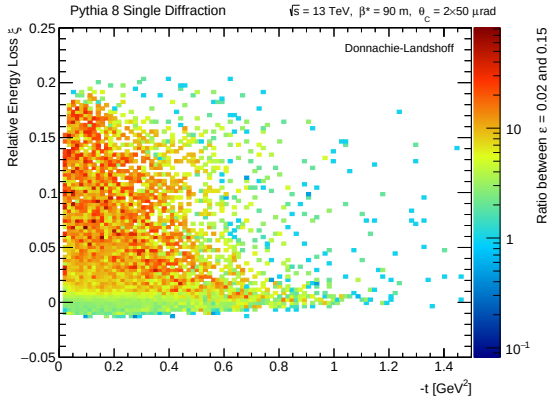

Figure 9.4: Ratio between the correlation plot of the reconstructed ξ and t for $\varepsilon = 0.02$ and $\varepsilon = 0.15$ for the Donnachie-Landshoff parameterization.

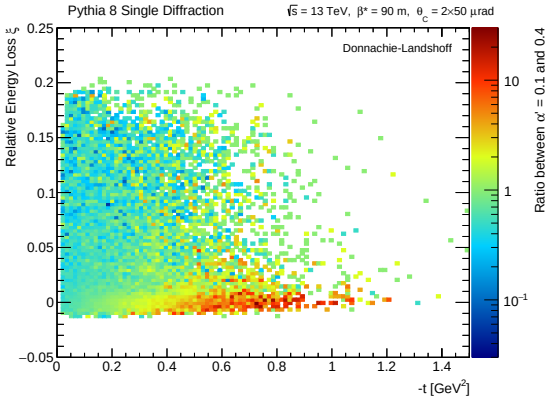

Figure 9.5: Ratio between the correlation plot of the reconstructed ξ and t for $\alpha' = 0.1\ \mathrm{GeV}^{-2}$ and $\alpha' = 0.4\ \mathrm{GeV}^{-2}$ for the Donnachie-Landshoff parameterization.

The sensitivity plots for the reconstructed transverse momentum p_T of the diffractively scattered proton are shown in Figure 9.6. It is seen that p_T is primarily sensitive to α'. This is not surprising since p_T is related to t according to Equation 4.36 and 4.37, such that

$$t \underset{s\to\infty}{\simeq} -p_T^2 \tag{9.5}$$

If p_T is calculated according to the LHC coordinate system, i.e. simply $p_T = \sqrt{p_x^2 + p_y^2}$, then p_T is independent on ξ unlike t. However, if p_T is calculated relative to the beam axis (which is the case here) then p_T is slightly dependent on ξ. This is due to the rotation in the plane of p_y and p_z by the non-zero crossing angle, where p_z is reconstructed from E, p_x, and p_y given by `ALFAReco`. However, due to the crossing angle being of the order of μrad this dependency is rather small.

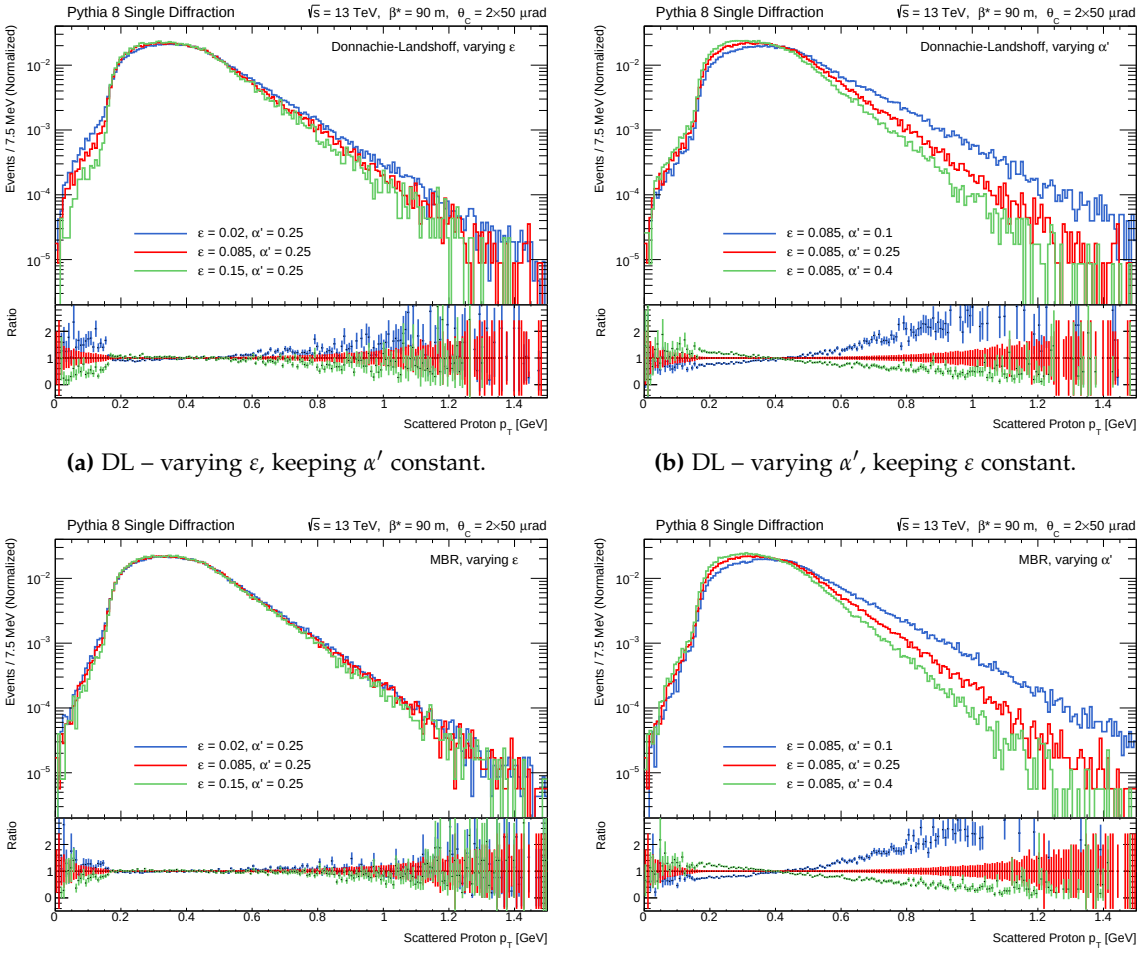

(a) DL – varying ε, keeping α' constant.

(b) DL – varying α', keeping ε constant.

(c) MBR – varying ε, keeping α' constant.

(d) MBR – varying α', keeping ε constant.

Figure 9.6: p_T distributions for different values of the model parameters, ε and α'.

9.1.1 *Rapidity Gap Definitions*

The forward pseudorapidity gap $\Delta\eta^F$ is common in diffractive analyses with just the ATLAS detector [72]. It is defined as the largest pseudorapidity gap from the ATLAS inner detector edge to the first reconstructed track, as illustrated in Figure 9.7. $\Delta\eta^F$ is most sensitive to ε as seen in Figure 9.8. This is expected as ξ and the rapidity gap are related according to Equation 4.46.

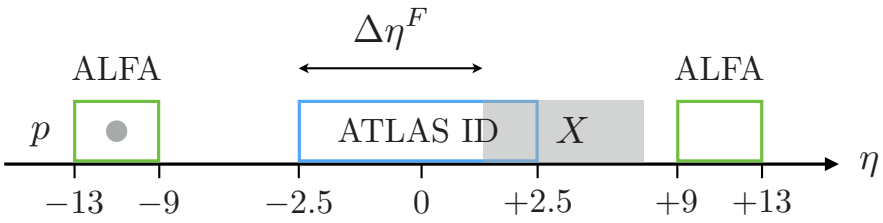

Figure 9.7: Illustration of the forward pseudorapidity gap $\Delta\eta^F$.

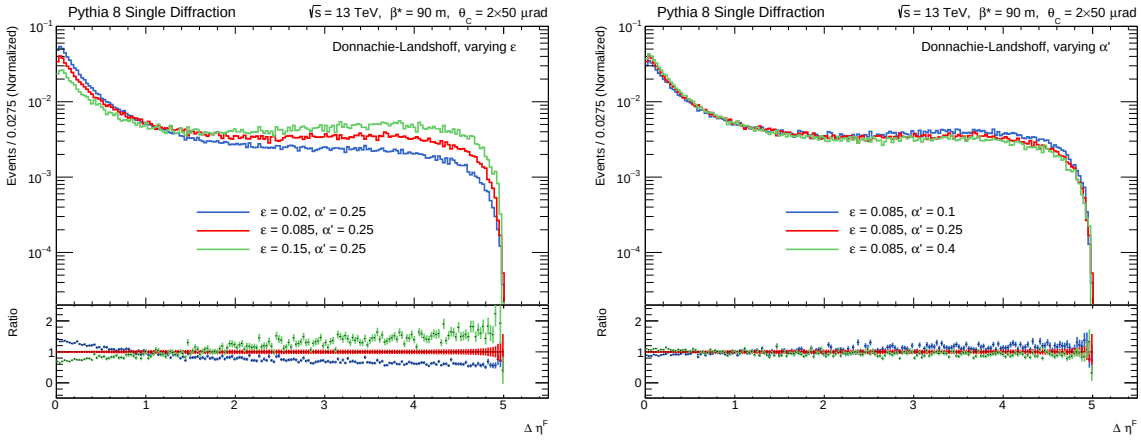

(a) DL – varying ε, keeping α' constant.

(b) DL – varying α', keeping ε constant.

(c) MBR – varying ε, keeping α' constant.

(d) MBR – varying α', keeping ε constant.

Figure 9.8: Forward pseudorapidity gap in ATLAS ID $\Delta\eta^F$ distributions for different values of the model parameters, ε and α'.

By tagging and measuring the rapidity of the diffractively scattered proton it is possible to reconstruct the full rapidity gap Δy in the diffractive system. The definition of the full rapidity gap is illustrated in Figure 9.9. As seen in the sensitivity plots in Figure 9.10 the full rapidity gap Δy is mostly sensitive to ε similar to $\xi \simeq e^{-\Delta y}$ and $\Delta\eta^F$.

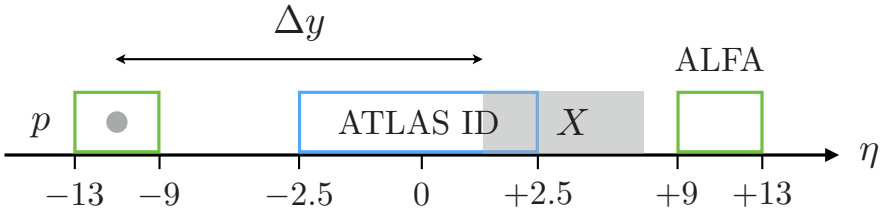

Figure 9.9: Illustration of the full rapidity gap Δy.

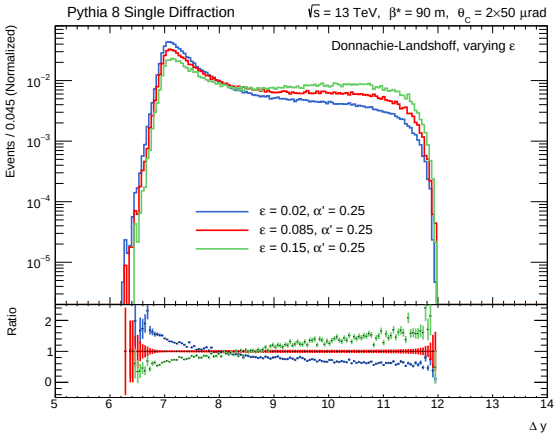

(a) DL – varying ε, keeping α' constant.

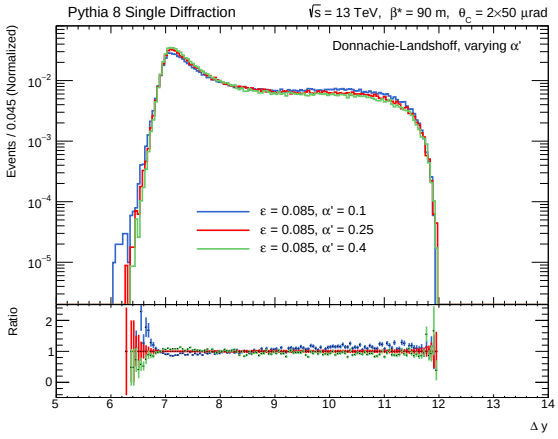

(b) DL – varying α', keeping ε constant.

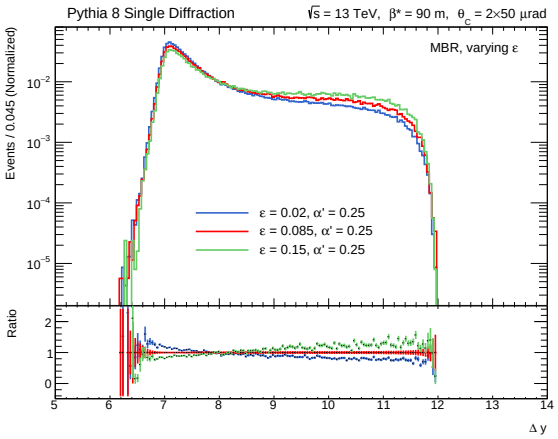

(c) MBR – varying ε, keeping α' constant.

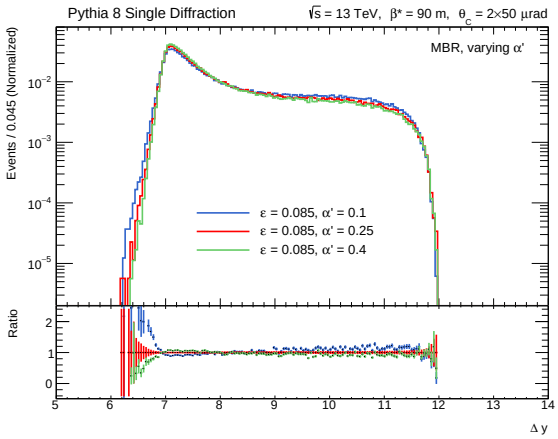

(d) MBR – varying α', keeping ε constant.

Figure 9.10: Rapidity gap Δy distributions for different values of the model parameters, ε and α'.

9.1.2 *Additional Studied Observables*

There are many additional observables related to single diffractive events that may exhibit sensitivity to the model parameters. The ones already presented – ξ, t, p_T, and the rapidity gaps – were found to be the most sensitive. This section will discuss some of the other distributions that were studied.

As seen in Table 9.1 and 9.2, the event count after the acceptance cuts of the simulation framework will depend on the model parameters, and especially on ε. This is partly a result of the kinematic acceptance regions for the diffractively scattered protons, which is reflected in the ξ, t, and p_T distributions. The kinematic acceptance of ALFA is also shown in the distribution of the absolute pseudorapidity $|\eta|$ of the scattered proton. The absolute pseudorapidity $|\eta|$ is related to the scattering angle θ which in turn is related to the squared momentum transfer t. Hence, $|\eta|$ will primarily be sensitive to α'. The dependence of the event count on the model parameters is also partly a result of the acceptance of the diffractively dissociated system – notably the charged multiplicity n_{ch} in the ATLAS inner detector, which is primarily sensitive to ε. This is not surprising, since the multiplicity is tied to the invariant mass M_X of the system which in turn is dependent on the relative energy loss ξ. The diffractively dissociated system is a QCD system of particles and will therefore undergo hadronization. In the Lund string model the average multiplicity of an event after hadronization will behave as a Poissonian multiplicity distribution [17],

$$\langle n_{ch} \rangle \approx c_0 + c_1 \ln(E) \tag{9.6}$$

where c_0 and c_1 are constants and E is the energy in the system. Both the $|\eta|$ and n_{ch} sensitivity plots are shown in the Appendix in Section B.2. The average p_T of the ID tracks as a function of n_{ch}, that is $\langle p_T \rangle (n_{ch})$, was also studied but found to show no significant sensitivity to the model parameters.

Other studied observables include the *linearized* 2*D sphericity* defined as [17]

Linearized sphericity is a collinear safe alternative to sphericity.

$$L^{ab} = \frac{\sum_i \frac{p_i^a p_i^b}{|\mathbf{p}_i|}}{\sum_i |\mathbf{p}_i|} \qquad a, b \in \{x, y, z\} \tag{9.7}$$

This was particularly studied in the transverse plane ($a = x$, $b = y$) along with correlations with the sum of transverse momentum $\sum_i p_i^T$ and the energy loss ξ. The linearized sphericity will naturally be dominated by the high-energy diffractively scattered proton. This can be remedied by setting $p_z = 0$ or by only considering the reconstructed

tracks in the inner detector. However, none of the studied distributions related to the linearized sphericity were found to show any significant sensitivity to ε or α'. The linearized sphericity can be considered in other planes, e.g. the plane extended by the scattered proton and the beam axis. However, these were not studied in this thesis due to time constraints.

9.1.3 *Quantization of Sensitivity*

To quantize the sensitivity to the model parameters of the event count and the shape of the distributions for the different observables, the Chi-Squared (χ^2) test have been used. The χ^2-test can provide the compatibility between the samples for the two extreme cases in the ε and α' ranges (given in Equation 9.1 and 9.2) for each observable. The compatibility will be given in the form of a χ^2-value related to the number of degrees of freedom (NDF). The larger the χ^2/NDF-value the larger the difference and hence the given distribution is more sensitive to the respective parameter.

The χ^2 function describing the ε sensitivity in the event count is just the squared difference,

$$\chi^2_\varepsilon = \frac{(N_{\varepsilon\,\mathrm{max}} - N_{\varepsilon\,\mathrm{min}})^2}{N_{\varepsilon\,\mathrm{max}} + N_{\varepsilon\,\mathrm{min}}} \tag{9.8}$$

where N is the event count (or alternatively the total cross-section σ). A similar χ^2 function can be written for α'.

The values listed in Table 9.1 and 9.2 have been used to estimate the sensitivity in the accepted event count. The event counts for the minimum and maximum parameter values for the studied parameter and the default value for the other parameter have been used. For instance, χ^2_ε is calculated from the event count values for $\varepsilon = 0.02$ and 0.15, and for the default $\alpha' = 0.25\,\mathrm{GeV}^{-2}$. The sensitivity χ^2-values in the accepted event count for the Donnachie-Landshoff (DL) parameterization are

$$\chi^2_{\varepsilon,\,\mathrm{DL}} = 10.7 \tag{9.9}$$

$$\chi^2_{\alpha',\,\mathrm{DL}} = 0.104 \tag{9.10}$$

while for the MBR parameterization we have

$$\chi^2_{\varepsilon,\,\mathrm{MBR}} = 3.14 \tag{9.11}$$

$$\chi^2_{\alpha',\,\mathrm{MBR}} = 0.0753 \tag{9.12}$$

A high χ^2-value indicates a higher sensitivity. It is seen that the event count is more sensitive to ε and that the Donnachie-Landshoff parameterization is more sensitive than MBR.

Note that MPIs in the diffractively dissociated system will slightly affect the accepted event count. This is because MPIs will give a higher chance of a larger charged multiplicity and therefore a higher chance that a particle from the system will hit the inner detector. In Table 8.4 it is listed that the accepted event count of a single diffractive sample for the Schuler-Sjöstrand parameterization with MPIs will, after the selection cuts in the simulation framework, be $(21.60 \pm 0.05)\%$. A similar sample but without MPIs will be $(20.82 \pm 0.05)\%$. This difference is expected to be independent of the model parameters, ε and α', as MPIs will not affect the shapes of the ξ and t distributions.

The χ^2 function describing the ε sensitivity in the shape of a given distribution is given by

$$\chi^2_\varepsilon = \sum_{i \in \text{bins}} \frac{(n_{i,\varepsilon\ \max} - n_{i,\varepsilon\ \min})^2}{\sigma^2_{i,\varepsilon\ \max} + \sigma^2_{i,\varepsilon\ \min}} \tag{9.13}$$

where n_i is the number of events (or alternatively the differential cross-section $\mathrm{d}\sigma$) in bin i of the given distribution. σ_i is the uncertainty on n_i. A similar χ^2 function can be written for α'.

The χ^2/NDF values for the sensitivity in the shapes of the studied distributions are shown in Table 9.3. The χ^2-values have been calculated for the two samples with the extreme values of the given parameter being studied while the other parameter is at the default value. A larger χ^2/NDF value indicates a higher sensitivity to the given model parameter.

Table 9.3: Sensitivity in the shape of the distributions given as χ^2/NDF from the χ^2 test. Listed for samples with MPIs.

	Donnachie-Landshoff (DL)		Minimum Bias Rockefeller (MBR)	
	ε	α'	ε	α'
ξ	$1.413 \times 10^4/158$	$1.786 \times 10^3/163$	$6.279 \times 10^3/157$	$1.976 \times 10^3/163$
t	$1.765 \times 10^3/198$	$7.868 \times 10^3/198$	$6.400 \times 10^2/198$	$1.356 \times 10^4/198$
p_T	$1.826 \times 10^3/197$	$8.666 \times 10^3/199$	$6.553 \times 10^2/197$	$1.478 \times 10^4/199$
Δy	$1.260 \times 10^4/127$	$1.618 \times 10^3/131$	$6.313 \times 10^3/127$	$2.273 \times 10^3/127$
$\Delta\eta^F$	$1.170 \times 10^4/181$	$1.628 \times 10^3/181$	$6.033 \times 10^3/181$	$1.771 \times 10^3/181$
$\lvert\eta\rvert$	$2.281 \times 10^3/141$	$7.832 \times 10^3/137$	$7.155 \times 10^2/140$	$1.362 \times 10^4/139$
n_{ch}	$1.060 \times 10^4/140$	$1.434 \times 10^3/136$	$5.151 \times 10^3/135$	$1.525 \times 10^3/135$

The χ^2-values agree with the previous conclusions on the sensitivity of each distribution. The distributions of ξ, Δy, $\Delta\eta^F$, and n_{ch} are primarily sensitive to ε, while t, p_T, and $|\eta|$ are primarily sensitive to α'. It seems that ξ and p_T are the most sensitive observables. The Donnachie-Landshoff parameterization exhibits a larger sensitivity than the MBR parameterization.

9.1.4 *Effects of Multiparton Interactions*

As discussed in Section 4.7, the model for hard diffraction in PYTHIA implements dynamic gap survival which ensures that MPIs only occur in the $\mathbb{P}p$ system and not in the pp system. Hence, toggling MPI on and off in PYTHIA will have no effect on the shape of the distributions related to the diffractively scattered proton, as illustrated in Figure 9.11 and 9.12.

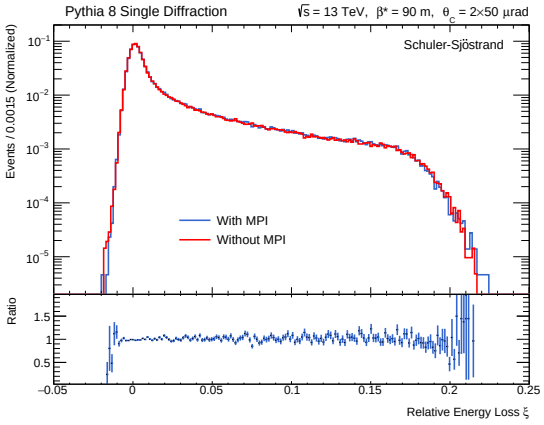

Figure 9.11: Distribution of the reconstructed ξ with and without MPI.

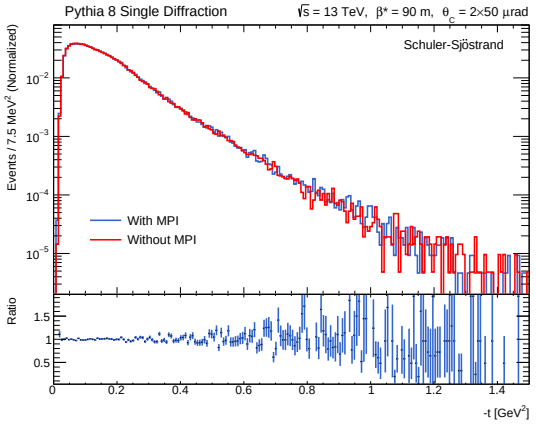

Figure 9.12: Distribution of the reconstructed t with and without MPI.

However, MPIs will naturally give a longer tail towards higher multiplicities in the diffractively dissociated system. This is illustrated in Figure 9.13, where the charged multiplicity n_{ch} is plotted for MPI toggled on and off.

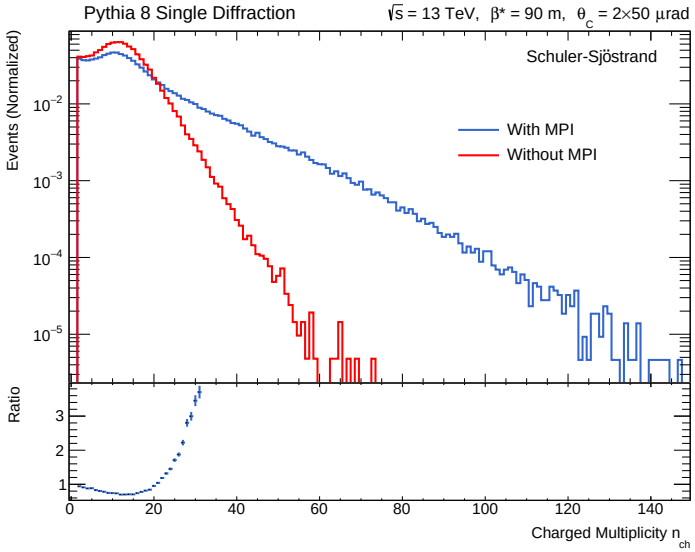

Figure 9.13: Charged multiplicity n_{ch} in the simulated ATLAS inner detector with and without MPI.

9.2 BACKGROUND STUDY

In the previous section, the distributions were plotted for the single diffractive (SD) signal. But some of the other types of events that are illustrated in Figure 7.7, could be reconstructed as single diffractive events, and would then count as background. A good understanding of the possible background contributions is important when fitting for the Pomeron flux parameterization.

- *Non-diffractive (ND) events* may have charged particles with a high enough energy ($E \gtrsim 5200$ GeV), a long enough lifetime ($\tau \gtrsim 10^{-6}$ s), and are scattered in the extreme forward direction so that they hit the ALFA stations and are reconstructed as a diffractive proton. Along with a false proton tag some of the non-diffractive system may hit the ATLAS inner detector and MBTS.
- *Double diffractive (DD) events* could likewise have charged particles hitting ALFA on one side with a signal in the ID and MBTS, with a similar distribution as the ND events.
- *Central diffractive (CD) events* could have one of the scattered protons leaving a well-reconstructed track on one side while the other proton could have missed the ALFA detectors or were not reconstructed.

The contribution of these background channels are seen in Figure 9.14 and 9.15 for the ξ and t distributions, which have been scaled according to the acceptance and relative cross-sections (Equation 4.8 - 4.11). Note that the CD background may be overestimated as it will be dependent on the ALFA track reconstruction efficiency which is not well known and have not been included in the simulation.

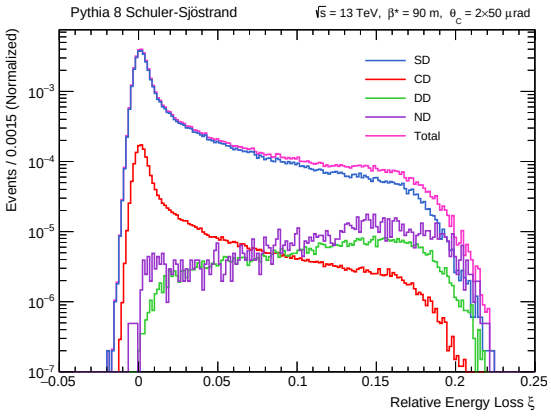

Figure 9.14: ξ distribution for the background channels along with the single diffractive signal and the total distribution.

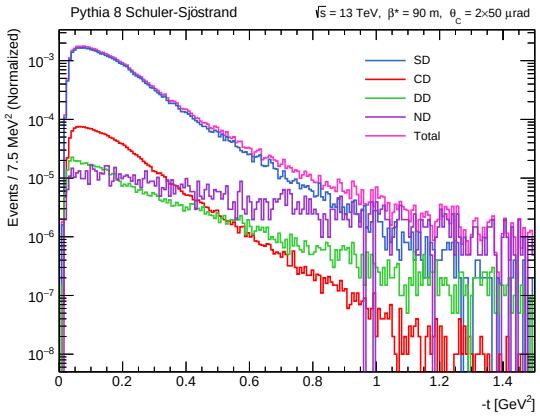

Figure 9.15: t distribution for the background channels along with the single diffractive signal and the total distribution.

The non-diffractive (ND) and double diffractive (DD) background is expected to be significant for large ξ and t values. This region in ξ and t are the most sensitive to the model parameters, as seen in the sensitivity plots in Figure 9.1 and 9.2. The ND events are independent of the Pomeron flux parameterization and will therefore count as a constant term in the fit procedure. However, the DD events are unfortunately dependent on the Pomeron flux parameterization.

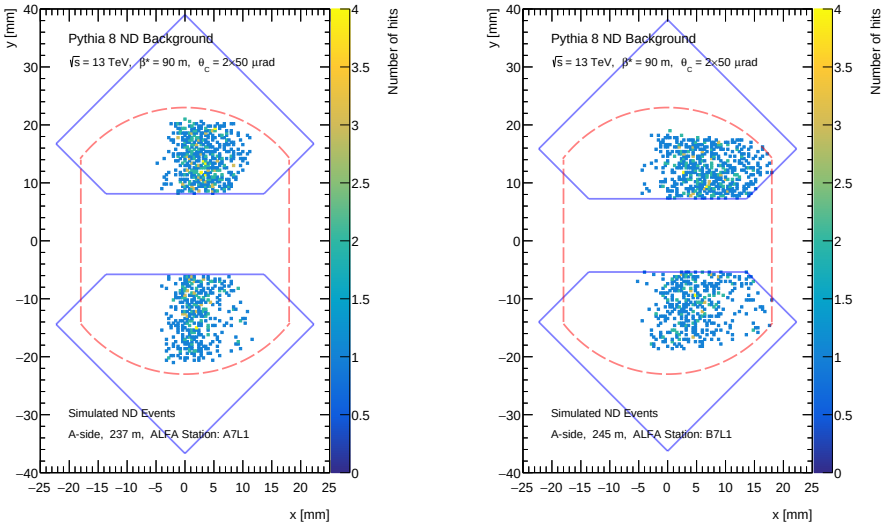

(a) Near station: $z = 237$ m. **(b)** Far station: $z = 245$ m.

Figure 9.16: Hitmaps of the non-diffractive background protons for $\theta_C = 2 \times 50$ μrad in the ALFA stations on the A-side.

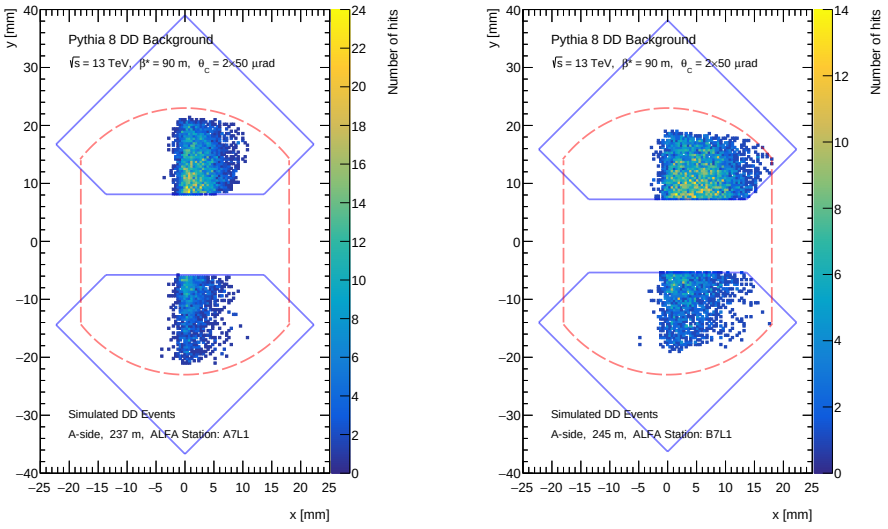

(a) Near station: $z = 237$ m. **(b)** Far station: $z = 245$ m.

Figure 9.17: Hitmaps of the double diffractive background protons (with Schuler-Sjöstrand) for $\theta_C = 2 \times 50$ μrad in the ALFA stations on the A-side.

The hit distribution of the ND background protons are seen in Figure 9.16. In the transverse plane the ND protons coincide with the single diffractive (SD) signal shown in Figure 8.28. The hit distribution of the DD background is shown in Figure 9.17 and is roughly similar to that of the ND background.

The local angle of the protons in the ALFA detector can be expressed as

$$\theta_x = \frac{x_{245\text{ m}} - x_{237\text{ m}}}{d} \tag{9.14}$$

where $d = 8.258$ m is the distance between the near and far ALFA stations. The local angle as a function of the $x_{237\text{ m}}$ hit position for the single diffractive signal is seen in Figure 9.18. Note that the ellipse around $(\theta_x, x_{237\text{ m}}) = (0, 0)$ are the protons with very low energy loss $\xi \simeq 0$, and are therefore nearly elastic (or *quasi-elastic*). The long tail or 'banana' shape extending towards larger θ_x values are for protons with an increasing energy loss ξ.

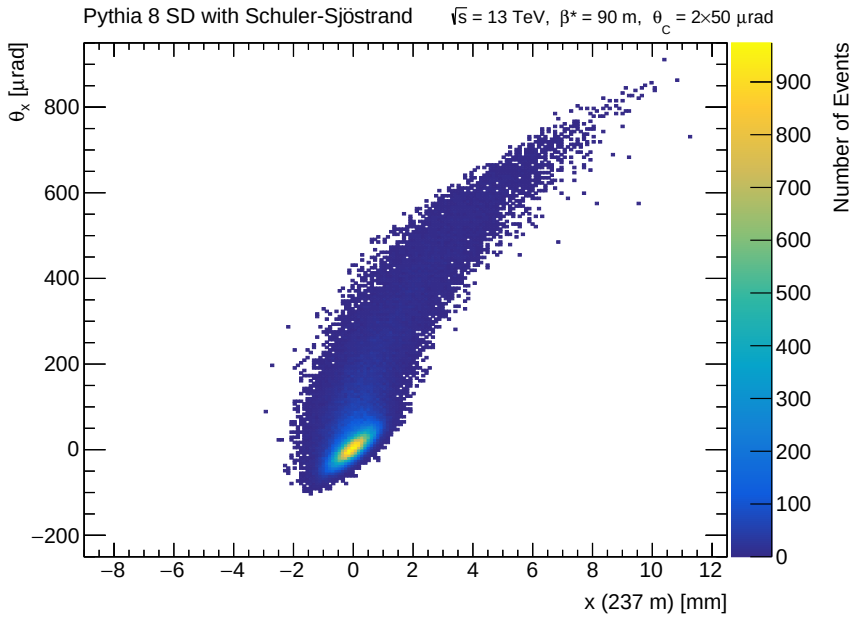

Figure 9.18: Correlation of the single diffractive hit x-coordinate versus the local angle θ_x for the A-side.

The non-diffractive background is shown in Figure 9.19 and the double diffractive background in Figure 9.20. Here hits are roughly uniformly distributed in the single diffractive region.

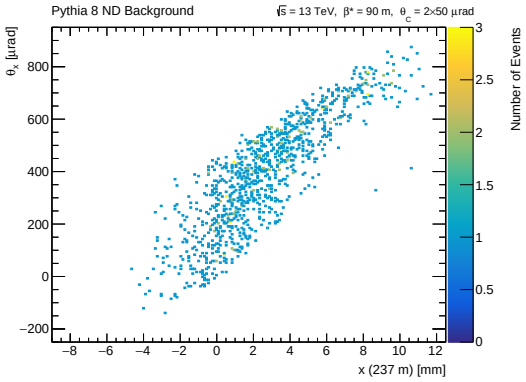

Figure 9.19: Correlation of the non-diffractive hit x-coordinate versus the local angle θ_x for the A-side.

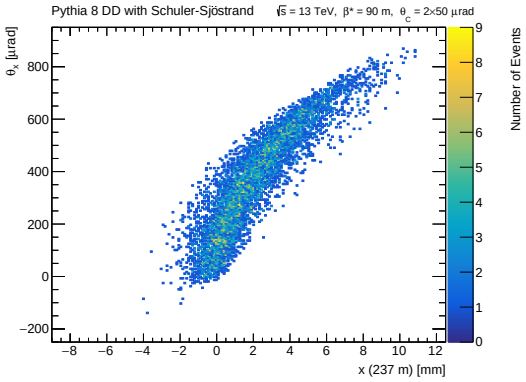

Figure 9.20: Correlation of the double diffractive hit x-coordinate versus the local angle θ_x for the A-side.

The correlation between the reconstructed energy loss ξ and squared momentum transfer t is shown for the non-diffractive background in Figure 9.21 and for the double diffractive background in Figure 9.22. The double diffractive background seems to primarily cluster around large ξ and low t values. The non-diffractive background exhibits similar behavior but the non-diffractive sample generated here is unfortunately plagued by low statistics.

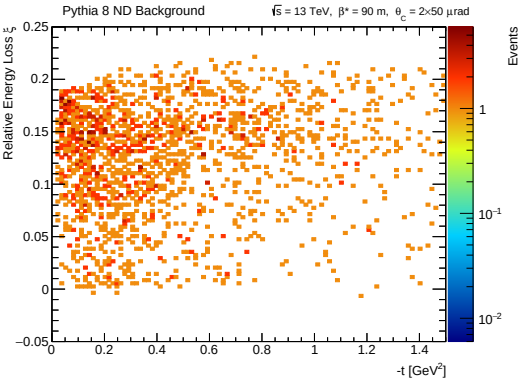

Figure 9.21: Correlation plot of the reconstructed ξ and t for the non-diffractive background.

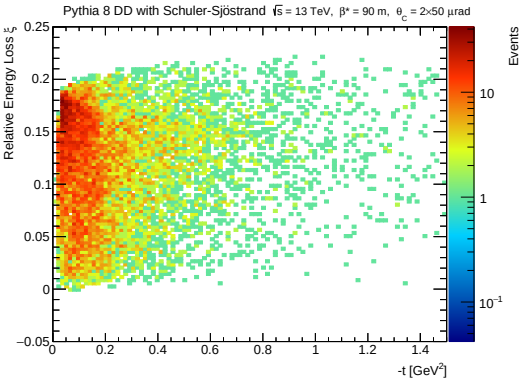

Figure 9.22: Correlation plot of the reconstructed ξ and t for the double diffractive background with the Schuler-Sjöstrand parameterization.

Note that the cluster of events observed at large ξ and low t values in the double diffractive and the non-diffractive background samples may not be representative of the underlying physics (or *truth*) distribution but is rather a consequence of the kinematic acceptance region of ALFA as seen in the ξ vs. p_T acceptance plot in Figure 8.19a, where nearly 100% acceptance is seen for $0.15 \lesssim \xi \lesssim 0.18$ and for low p_T.

It has been shown in this section that the central diffractive background is distributed in a very similar way to the single diffractive signal and is most likely of negligible size. However, the non-diffractive and double diffractive background may be of significance, and have been found to be most easily distinguishable from the single diffractive signal in the correlation plot between ξ and t.

9.3 OPTIMAL OBSERVABLES METHOD

The kinematics of the simulated protons will be determined by the Pomeron flux, which is a distribution over ξ and t. We now allow the Pomeron flux to be a function of the two parameters ε and α' as well,

$$f_{\mathbb{P}/p}(\xi, t; \varepsilon, \alpha') \tag{9.15}$$

The objective is now to possibly construct observables that are maximally sensitive to the model parameters – so-called *optimal observables*.

Mathematically, the Pomeron flux is a scalar function $f_{\mathbb{P}/p} : \mathbb{R}^4 \to \mathbb{R}$. Assuming differentiability, then for such a function, each component of the gradient ∇f will give the rate of change of the function with respect to the standard basis based on the variables. The directional derivative of the function f in some arbitrary direction $\mathbf{u}$ in the basis extended by the variables, will be given by the product of the gradient and the direction,

$$D_{\mathbf{u}} f(\mathbf{a}) = \lim_{h \to 0} \frac{f(\mathbf{a} + h\mathbf{u}) - f(\mathbf{a})}{h} \tag{9.16}$$

$$= \nabla f(\mathbf{a}) \cdot \mathbf{u} \tag{9.17}$$

$$= ||\nabla f(\mathbf{a})|| \cos\theta \tag{9.18}$$

where θ is the angle between the vectors ∇f and $\mathbf{u}$. The direction of steepest ascent, i.e. where the directional derivative is maximal, is the direction where $\theta = 0$, i.e. where ∇f and $\mathbf{u}$ points in the same direction. If we have a small correction $\delta\mathbf{a}$ to the variables around some expansion point $\mathbf{a}$, the Taylor expansion is then

$$f(\mathbf{a} + \delta\mathbf{a}) = f(\mathbf{a}) + \nabla f \cdot \delta\mathbf{a} + \dots \tag{9.19}$$

where the linear correction term $\nabla f \cdot \delta\mathbf{a}$ is maximized when $\delta\mathbf{a}$ is in the same direction as ∇f. This is the idea behind the method of Optimal Observables [73] which can be applied to any reaction where the differential cross-section depends on a certain number of small parameters, and which are to be estimated. The method of Optimal Observables attempts to project onto a single variable the kinematic information which is most sensitive to a particular model parameter. For each parameter, an optimal observable exists.

Optimal observables have previously been applied to studies of anomalous gauge couplings in hadronic collisions [74]. As a short example, consider an extension to the Standard Model (SM) with an anomalous coupling λ. The optimal observable would then be

$$\mathcal{O}(\lambda) = \lim_{\epsilon_\lambda \to 0} \frac{\mathrm{d}\sigma(\mathrm{SM} + \epsilon_\lambda) - \mathrm{d}\sigma(\mathrm{SM})}{\epsilon_\lambda \mathrm{d}\sigma(\mathrm{SM})} \tag{9.20}$$

where $\mathrm{d}\sigma$ is the differential cross-section. Expanding the cross-section in the anomalous coupling λ one can write

$$\mathrm{d}\sigma \approx \mathrm{d}\sigma_0 + \mathrm{d}\sigma_1 \cdot \lambda + \ldots \tag{9.21}$$

where $\mathrm{d}\sigma_0 = \mathrm{d}\sigma(\mathrm{SM})$. The optimal observable would then be

$$\mathcal{O}(\lambda) = \frac{\mathrm{d}\sigma_1}{\mathrm{d}\sigma_0} \tag{9.22}$$

The optimal observable for λ is the relative change in the event probability (cross-section) when the λ parameter is moved from its SM value by some small amount ϵ_λ.

In our case, a certain set of parameter values, $(\varepsilon_0, \alpha'_0)$, will take the role of the expansion point. The first order corrections in the expansion will be the derivatives with respect to the parameter values in question. The Taylor expansion takes the form,

$$\begin{aligned} f_{\mathbb{P}/p}(\xi, t; \varepsilon, \alpha') = {} & f_{\mathbb{P}/p}\big|_{\varepsilon_0, \alpha'_0} \\ & + \left(\frac{\partial f_{\mathbb{P}/p}}{\partial \varepsilon}\bigg|_{\varepsilon_0, \alpha'_0} \right) (\varepsilon - \varepsilon_0) \\ & + \left(\frac{\partial f_{\mathbb{P}/p}}{\partial \alpha'}\bigg|_{\varepsilon_0, \alpha'_0} \right) (\alpha' - \alpha'_0) \\ & + \ldots \end{aligned} \tag{9.23}$$

In this way we can construct optimal observables that are functions of ξ and t as well as the expansion point given by ε_0 and α'_0. The optimal observable that is optimally sensitive to ε, is given by the partial derivative of the Pomeron flux $f_{\mathbb{P}/p}$ with respect to ε,

$$\mathcal{O}_\varepsilon(\xi, t; \varepsilon_0, \alpha'_0) = \left(\frac{\partial f_{\mathbb{P}/p}}{\partial \varepsilon}\bigg|_{\varepsilon_0, \alpha'_0} \right) \Big/ \left(f_{\mathbb{P}/p}\big|_{\varepsilon_0, \alpha'_0} \right) \tag{9.24}$$

where it has been normalized to the Pomeron flux value at the expansion point. The optimal observable for α' is likewise given by

$$\mathcal{O}_{\alpha'}(\xi, t; \varepsilon_0, \alpha'_0) = \left(\frac{\partial f_{\mathbb{P}/p}}{\partial \alpha'}\bigg|_{\varepsilon_0, \alpha'_0} \right) \Big/ \left(f_{\mathbb{P}/p}\big|_{\varepsilon_0, \alpha'_0} \right) \tag{9.25}$$

The Pomeron flux parameterization for both Donnachie-Landshoff and MBR takes the form,

$$f_{\mathbb{P}/p}(\xi, t; \varepsilon, \alpha') \sim \xi^{-1-2\varepsilon-2\alpha' t} \tag{9.26}$$

as seen in Equation 4.82 and 4.84.

The derivatives are then

$$\frac{\partial f_{\mathbb{P}/p}}{\partial \varepsilon} \sim -2\ln(\xi)\xi^{-1-2\varepsilon-2\alpha' t} \sim -2\ln(\xi) f_{\mathbb{P}/p} \tag{9.27}$$

$$\frac{\partial f_{\mathbb{P}/p}}{\partial \alpha'} \sim -2t\ln(\xi)\xi^{-1-2\varepsilon-2\alpha' t} \sim -2t\ln(\xi) f_{\mathbb{P}/p} \tag{9.28}$$

Hence, our optimal observables are given by

$$\mathcal{O}_\varepsilon = -2\ln(\xi) \tag{9.29}$$

$$\mathcal{O}_{\alpha'} = -2t\ln(\xi) \tag{9.30}$$

This explains why ξ is more sensitive to ε and why t is more sensitive to α' as seen in Figure 9.1 and 9.2, since the linear t grows faster than the logarithmic $\ln(\xi)$. It is worth noting here that the optimal observables are maximally sensitive to their respective parameters – not exclusively sensitive to their respective parameters. This means that $\mathcal{O}_\varepsilon$ will also depend on α' and vice versa.

The Pomeron flux parameterization in Equation 9.26 takes a very simple form when expressed in terms of the optimal observables,

$$f_{\mathbb{P}/p}(\mathcal{O}_\varepsilon, \mathcal{O}_{\alpha'}; \varepsilon, \alpha') \sim \exp\left(\mathcal{O}_\varepsilon \varepsilon + \mathcal{O}_{\alpha'}\alpha'\right) \tag{9.31}$$

which holds for both Pomeron flux parameterization models in PYTHIA.

The attempt in this section was to construct observables that are maximally sensitive to the model parameters. However, due to the exponential nature of the Pomeron flux parameterizations it would be necessary to include all terms in the infinitely long Taylor expansion in Equation 9.23 rather than just the linear terms as presented here. This will unfortunately make the optimal observables unviable in the analysis and the following fit procedure. But the optimal observables seems to indicate that ξ already exhibits maximal sensitivity to ε as seen in Equation 9.29.

9.4 FIT PROCEDURE

The primary goals of this thesis is to determine which Pomeron flux parameterization in PYTHIA 8, of the three introduced in Section 4.7, that best fits current $\sqrt{s} = 13$ TeV data at ATLAS and ALFA. This section will present a statistical fit procedure that can estimate the model parameters ε and α' for the Donnachie-Landshoff and MBR parameterization.

The fit procedure will use the sensitivity in the shape of the distributions to fit the parameters. Here the distributions for the reconstructed ξ and p_T will be used as they were particularly sensitive to each their parameter as shown in Section 9.1. We will consider p_T instead of t in this section as p_T is slightly more sensitive than t, and to avoid double counting since ξ and t are not independent of each other (as seen in Equation 4.34).

We are interested in fitting ε and α' in measured ξ and p_T distributions. This can be solved by using the method of least squares [75], where the squared difference between a set of measurements and their predicted values are minimized. The χ^2 function to be minimized takes the general form

$$\chi^2(\varepsilon, \alpha') = \sum_i^n \frac{(O_i - E_i(\varepsilon, \alpha'))^2}{\sigma_{O_i}^2 + \sigma_{E_i}^2} \tag{9.32}$$

where O_i are the observations, and E_i are the expectation values. Note that we allow some uncertainty on the theoretical expectation.

The observations O_i will be the measured $\mathrm{d}N/\mathrm{d}\xi$ and $\mathrm{d}N/\mathrm{d}p_T$, while the expectation values E_i will be based on the Pomeron flux parameterization $f_{\mathbb{P}/p}(\xi, t; \varepsilon, \alpha')$. The full χ^2 function takes the form,

$$\begin{aligned}\chi^2(\varepsilon, \alpha') = &\sum_i^{n_\xi} \left[\frac{\mathrm{d}N_{\text{obs}}}{\mathrm{d}\xi} - E_{\xi,i}(\varepsilon, \alpha')\right]^2 \frac{1}{\sigma_{\xi,\,\text{obs}}^2 + \sigma_{\xi,\,\text{exp}}^2} \\ &+ \sum_i^{n_{p_T}} \left[\frac{\mathrm{d}N_{\text{obs}}}{\mathrm{d}p_T} - E_{p_T,i}(\varepsilon, \alpha')\right]^2 \frac{1}{\sigma_{p_T,\,\text{obs}}^2 + \sigma_{p_T,\,\text{exp}}^2}\end{aligned} \tag{9.33}$$

where we sum over bins of ξ and p_T.

9.4.1 *Minimization with Minuit*

The minimization of the χ^2 function is handled by the Minuit package [70] as implemented in the ROOT data analysis framework. This is done in order to determine the two model parameters, ε and α', for a given sample. Minuit is a physics analysis tool to find the minimum value of a multi-parameter function and analyze the shape of the function around that minimum.

9.4.2 *Expectation Values*

There are many possible ways to find the bin-wise expectation values $E_i(\varepsilon, \alpha')$ for the ξ and p_T distributions. One method is to call PYTHIA and generate a new single diffractive sample for every iteration in the minimization. This will introduce a Poissonian uncertainty on every expectation value. This is computationally very demanding as Minuit will go through several hundreds of iterations. It may be possible to significantly lower the generation time in PYTHIA by disabling procedures that will only affect the dissociated system and not the scattered protons (such as hadronization, ISR, FSR, and MPIs).

An alternative to this method would be to generate a single reference sample, with the PYTHIA default values of $\varepsilon = 0.085$ and $\alpha' = 0.25\ \text{GeV}^{-2}$, and then apply a specific weight to each event,

$$w = \frac{\mathrm{d}\sigma|_{\varepsilon,\alpha'}}{\mathrm{d}\sigma_{\text{ref.}}} \tag{9.34}$$

where $\mathrm{d}\sigma|_{\varepsilon,\alpha'}$ is calculated from the Pomeron flux parameterization. The reference sample is then *reweighted* to a new parameterization based on the Pomeron flux. This is unfortunately complicated by the detector effects and smearing shown in Section 8.6.2.

The method used in this thesis, is to fit the number of events in each ξ and p_T bins for the nine generated samples from Section 9.1 that scanned over different values of ε and α'. A particular non-equidistant binning has been used for the ξ and p_T distributions and is illustrated in Figure 9.23 and 9.24.

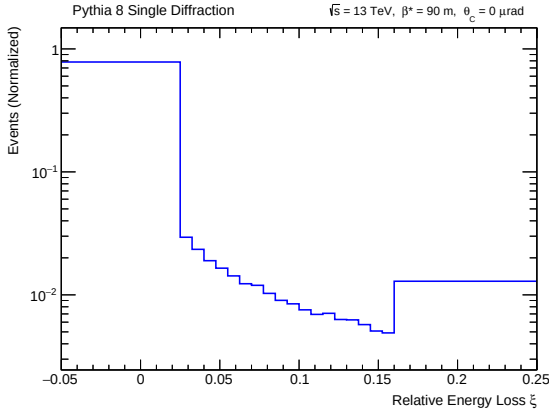

Figure 9.23: Distribution of the reconstructed ξ with the non-equidistant binning used in the fit procedure.

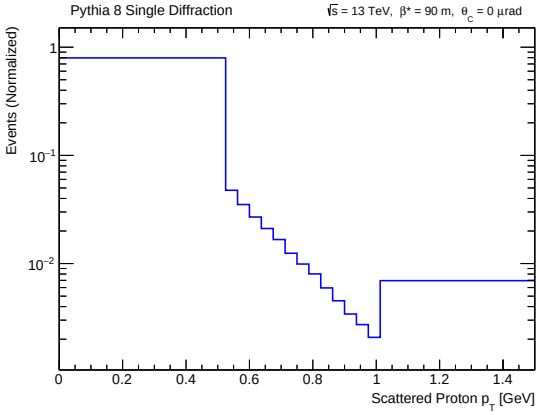

Figure 9.24: Distribution of the reconstructed p_T with the non-equidistant binning used in the fit procedure.

The ranges $0.025 \leq \xi \leq 0.16$ and $0.525\,\text{GeV} \leq p_T \leq 1.0125\,\text{GeV}$ exhibit large sensitivity and does not include the detector smearing seen at low ξ and p_T values nor the low statistics at larger values. The width of the bins in these ranges was chosen to include sufficient statistics while avoiding a too large of a spread of the central ξ and p_T values in each bin. The events outside the ranges are included as overflow and underflow bins which ignores the shape of the distributions.

The normalized number of events for the nine generated samples in each bin in the ξ and p_T distributions are fitted as functions of the model parameters ε and α'. The 2D fit function is modelled after the shape of the Pomeron flux parameterizations,

$$E_i(\varepsilon, \alpha') = a^{b\varepsilon + c\alpha' + d} \tag{9.35}$$

where a, b, c, and d are fit parameters. A set of the fit parameters with uncertainties are found for each bin for both ξ and p_T and are used to construct the expectation values in the χ^2 function in Equation 9.33. A χ^2 function with the sets of fit parameters can be constructed for both the Donnachie-Landshoff and the MBR parameterization. Note that MPIs will not have a significant effect on the ξ and p_T distributions using the non-equidistant binning and will therefore not affect the fits (see Section 9.1.4). The values from the nine samples for the Donnachie-Landshoff parameterization along with the fit surface for two bins in ξ and p_T are shown in Figure 9.25 and 9.26.

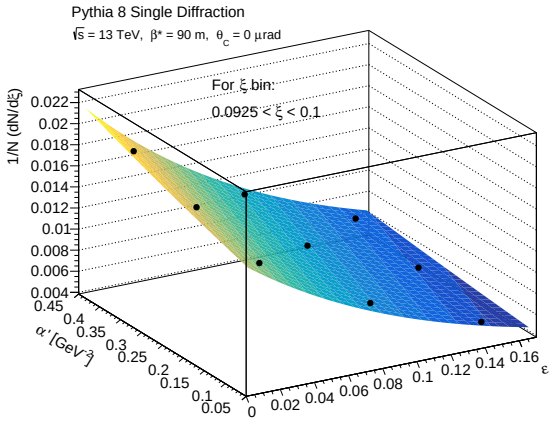

Figure 9.25: The distribution $\mathrm{d}N/\mathrm{d}\xi$ as a function of the model parameters ε and α' for the nine samples (markers) plotted along with the fitted expectation function (surface).

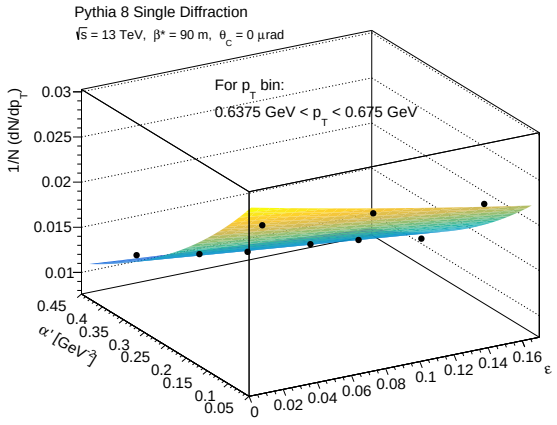

Figure 9.26: The distribution $\mathrm{d}N/\mathrm{d}p_T$ as a function of the model parameters ε and α' for the nine samples (markers) plotted along with the fitted expectation function (surface).

The uncertainties $\sigma_{\xi,\,\mathrm{exp}}$ and $\sigma_{p_T,\,\mathrm{exp}}$ on the expectation values $E_{\xi,i}$ and $E_{p_T,i}$ are found through error propagation of the uncertainties on the fit parameters in Equation 9.35.

9.4.3 *Test Samples with Unknown Parameterization*

Two test samples were generated by the thesis supervisor with Pomeron flux parameterizations that were unknown to the author by the time of development and testing of the fit procedure. This was to ensure a fair test of the fit procedure without bias. Note that the provided test samples were generated without a crossing angle, $\theta_C = 0$ μrad. This makes no difference as the fit procedure is independent on the beam settings. Furthermore, in Section 8.6.2 the crossing angle was found to have little effect on the shape of the ξ and p_T distributions in the region of large ξ and p_T values where the sensitivity was largest.

Test sample 1 contains 3,411,054 events and was generated with the Donnachie-Landshoff parameterization without MPIs and with the true parameter values

$$\varepsilon = 0.04 \tag{9.36}$$

$$\alpha' = 0.15 \text{ GeV}^{-2} \tag{9.37}$$

The fit procedure using the Donnachie-Landshoff parameterizations to find the expectation values found the parameters with a minimum $\chi^2 = 6.27$. This was significantly better than the MBR parameterization which found the parameters with a minimum $\chi^2 = 276.93$. Hence, the fit procedure was able to find the correct Pomeron flux model. The parameters with uncertainties were found to be

$$\varepsilon = 0.042 \pm 0.002 \tag{9.38}$$

$$\alpha' = 0.154 \pm 0.007 \text{ GeV}^{-2} \tag{9.39}$$

which are within 1σ of the true values. The constructed χ^2 as a function of ε and α' for test sample 1 is shown in Figure 9.27 and 9.28.

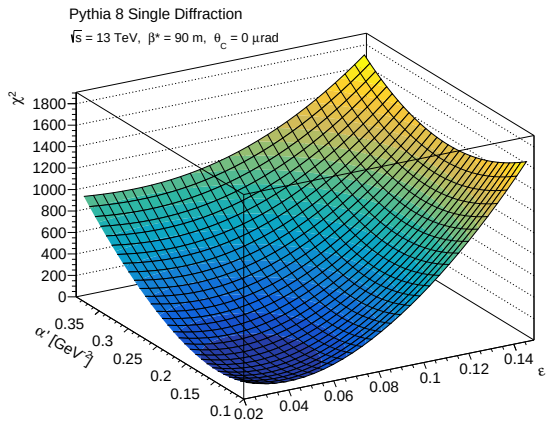

Figure 9.27: The constructed χ^2 as a function of ε and α' for test sample 1.

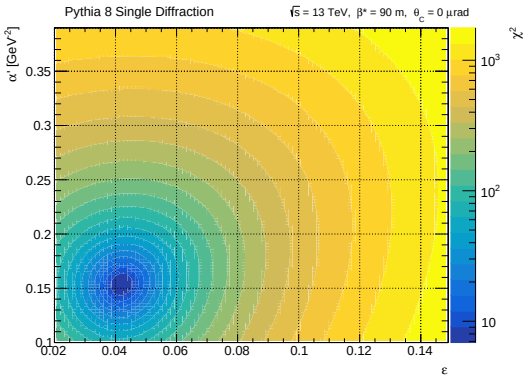

Figure 9.28: The contour lines of the constructed χ^2 for test sample 1.

The contour plot from Minuit for test sample 1 with the true and fitted parameters overlaid is shown in Figure 9.29.

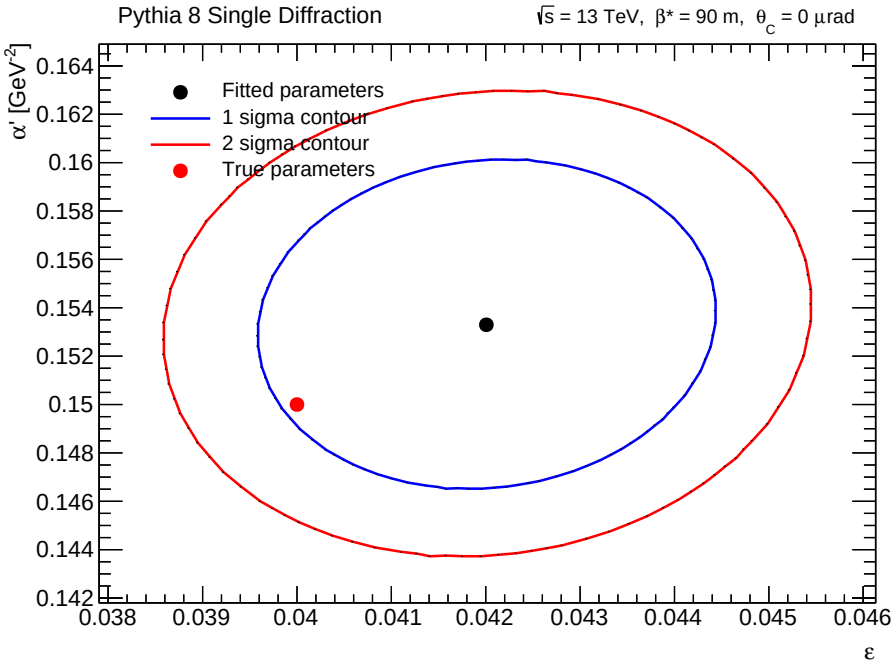

Figure 9.29: Contour plot from Minuit for test sample 1. The true and fitted parameters values are shown.

Test sample 2 contains 2,973,321 events and was generated with the MBR parameterization with MPIs and with the true parameter values

$$\varepsilon = 0.13 \tag{9.40}$$

$$\alpha' = 0.35 \text{ GeV}^{-2} \tag{9.41}$$

The fit procedure using the Donnachie-Landshoff parameterizations found the parameters with a minimum $\chi^2 = 15.89$. With the MBR parameterization the parameters were found with a minimum $\chi^2 = 8.32$. The MBR parameterization then gave the best fit where the parameters with uncertainties were found to be

$$\varepsilon = 0.130 \pm 0.004 \tag{9.42}$$

$$\alpha' = 0.361 \pm 0.004 \text{ GeV}^{-2} \tag{9.43}$$

Here the fit procedure found the exact ε value within 1σ. However, the α' value was only found within 3σ. The constructed χ^2 as a function of ε and α' for test sample 2 is shown in Figure 9.30 and 9.31. The contour plot from Minuit for test sample 2 with the true and fitted parameters overlaid is shown in Figure 9.32.

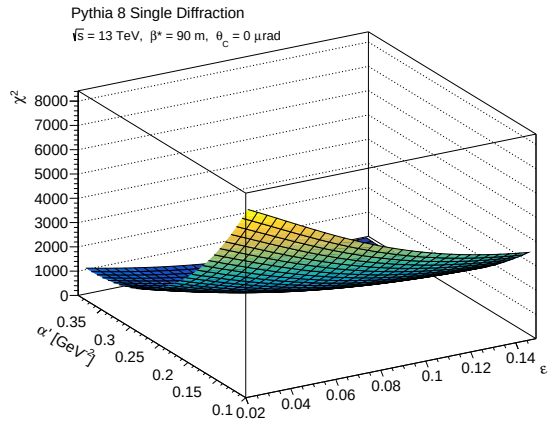

Figure 9.30: The constructed χ^2 as a function of ε and α' for test sample 2.

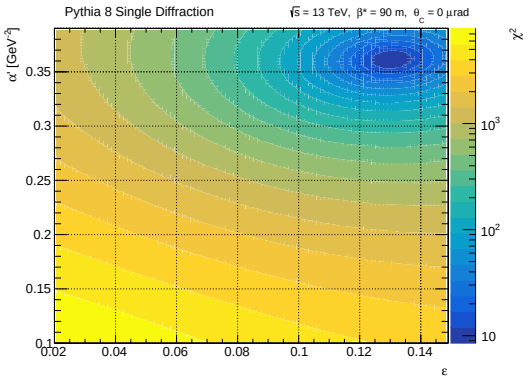

Figure 9.31: The contour lines of the constructed χ^2 for test sample 2.

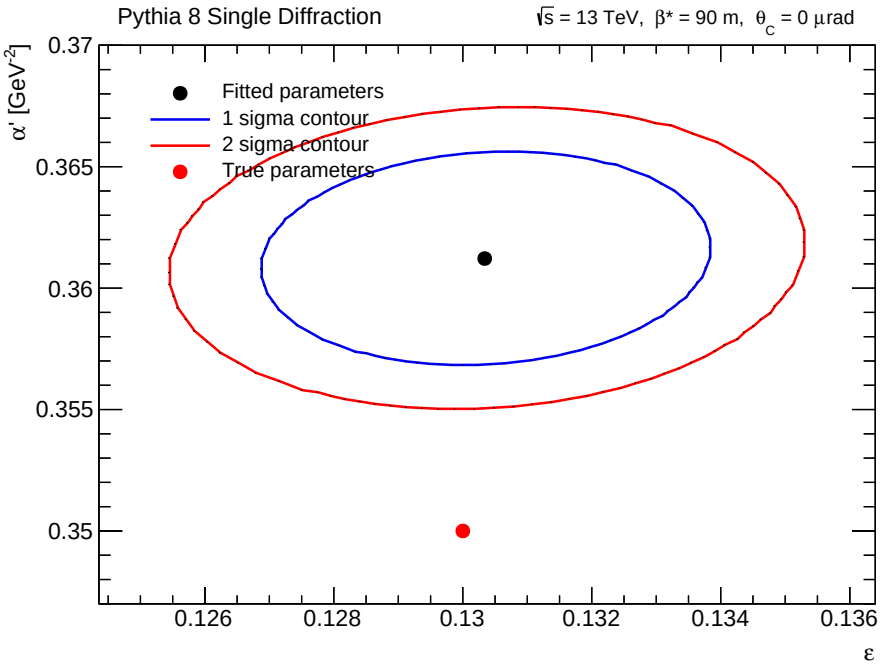

Figure 9.32: Contour plot from Minuit for test sample 2. The true and fitted parameters values are shown.

9.4.4 *Test Samples with Known Parameterization*

Four test samples were generated by the author and therefore had a known parameterization at the time of development and testing of the fit procedure. All four test samples were generated with the Donnachie-Landshoff parameterization and with MPIs. The true parameter values along with the values found from the fit are listed in Table 9.4. The contour plots are shown in Figure 9.33. All found val-

ues are at least within 2σ of the true values. The largest uncertainty is generally in the α' parameter.

Table 9.4: True and fitted parameter values for the four test samples generated by the author.

Test sample	True values	Fitted values
1	$\varepsilon = 0.05$	$\varepsilon = 0.048 \pm 0.003$
	$\alpha' = 0.32\ \text{GeV}^{-2}$	$\alpha' = 0.316 \pm 0.010\ \text{GeV}^{-2}$
2	$\varepsilon = 0.12$	$\varepsilon = 0.119 \pm 0.004$
	$\alpha' = 0.2\ \text{GeV}^{-2}$	$\alpha' = 0.202 \pm 0.012\ \text{GeV}^{-2}$
3	$\varepsilon = 0.03$	$\varepsilon = 0.031 \pm 0.003$
	$\alpha' = 0.15\ \text{GeV}^{-2}$	$\alpha' = 0.158 \pm 0.008\ \text{GeV}^{-2}$
4	$\varepsilon = 0.125$	$\varepsilon = 0.127 \pm 0.005$
	$\alpha' = 0.35\ \text{GeV}^{-2}$	$\alpha' = 0.364 \pm 0.014\ \text{GeV}^{-2}$

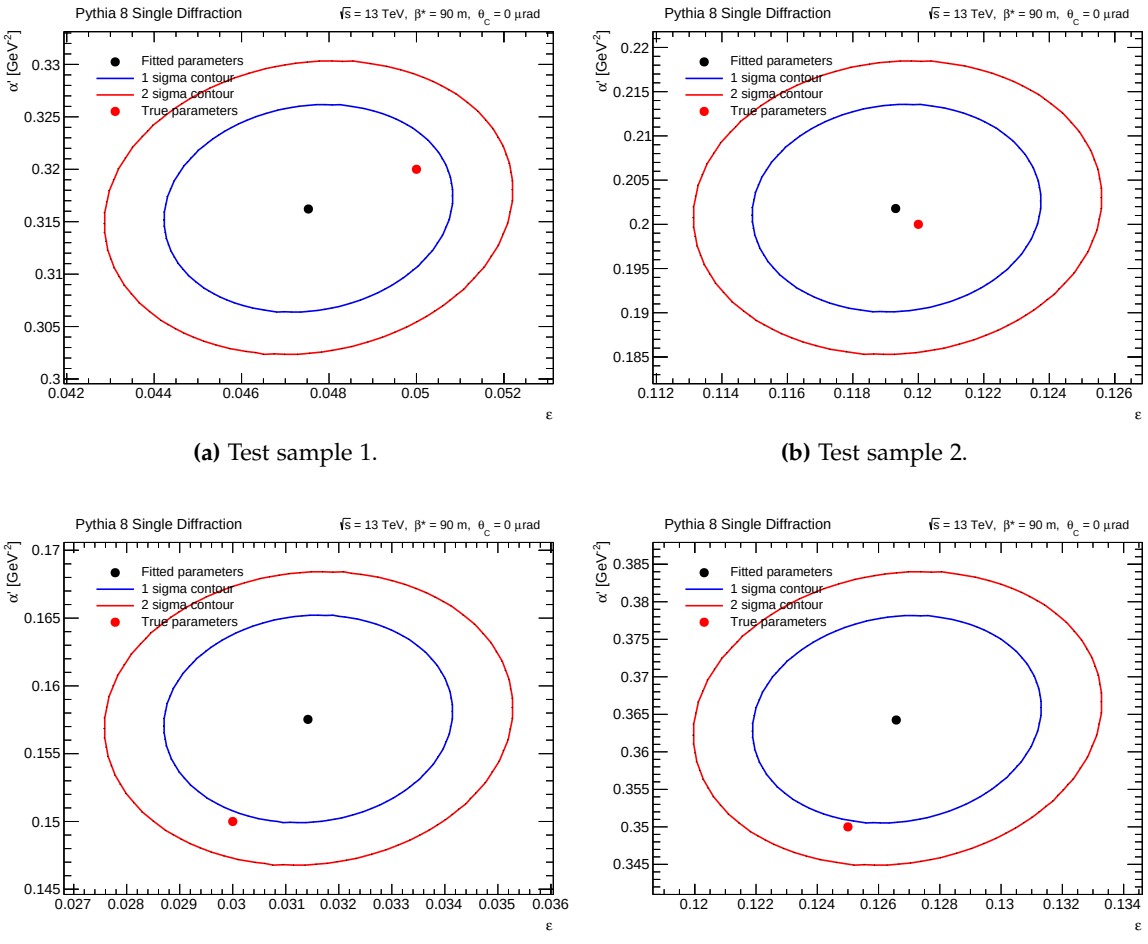

(a) Test sample 1.

(b) Test sample 2.

(c) Test sample 3.

(d) Test sample 4.

Figure 9.33: Contour plots by Minuit of the four test samples generated by the author.

9.4.5 *Conclusions on Fit Performance*

The fit procedure will provide the fitted values for ε and α' with uncertainties from Minuit. The fitted values was found to be generally within at least 2σ of the fit uncertainty for most samples. The fit procedure will also provide a "goodness-of-fit" χ^2 value (i.e. the found minimum χ^2 value) which can be compared between the Donnachie-Landshoff and the MBR parameterizations to find the parameterization model in PYTHIA that gives the best fit.

Since ε and α' will affect the accepted event count, they will also influence the statistical Poissonian uncertainty used in the fit for the expectation value. For instance, for larger ε we saw a lower accepted event count and would therefore see a larger relative uncertainty. This could shift the constructed χ^2 function slightly and introduce an additional systematic uncertainty.

Generating additional samples which scan over more values (e.g. 5 instead of the 3 used here) of the model parameters would naturally improve the resolution and the fits to find the expectation values. The trade-off is time and storage space spent on generating the extra samples. More events generated per sample will also improve the fit with the same consequences.

In Section 9.1 it was found that the Donnachie-Landshoff parameterizations was more sensitive to the model parameters than the MBR parameterization. Hence, the allowed limits on the distributions are larger for Donnachie-Landshoff which makes it easier to fit to data due to allowed freedom to the fit, but could also introduce a larger uncertainty on the fitted parameters. It may even be possible to falsify the MBR parameterization if it is found to be not possible to fit data within the limits of the distributions.

Part IV

DATA ANALYSIS

In the previous part, a statistical fit procedure that allows for the testing of the validity of the phenomenological models of diffraction was presented and utilized on several simulated test samples. This part will present an analysis of the new 13 TeV data from the 2015 Run 2 period using the ATLAS and ALFA experiments at the LHC. Measured distributions will be compared to the simulated distributions from the previous part. Several attempts at reducing the background in data will be presented. Finally, the thesis work is summarized along with some remarks regarding future studies of diffraction.

10 DIFFRACTIVE RUNS

This chapter presents an analysis of data collected from the ATLAS and ALFA experiment at the LHC. The analysis is only preliminary, since the full alignment of the ALFA detectors has not yet been found for the run used in this analysis, and there has not yet been developed a complete and official Monte Carlo simulation for comparison.

The resulting measured distributions from data will be compared to the simulated distributions from the simulation framework that was presented in Chapter 8. As with the simulations, the focus of the data analysis has been exclusively on single diffractive events.

10.1 DATA SAMPLES

The data is from ATLAS run 282026, taken on 15 - 16 October 2015 at the LHC. The run has 14,975,165 events corresponding to an integrated luminosity over the entire run of 111.3 nb^{-1}. The center-of-mass energy of the run was $\sqrt{s} = 13$ TeV and the optics used had a beta function value at the interaction point of $\beta^* = 90$ m. Run 282026 had 671 colliding bunches and the beams collided with a crossing angle of -50 μrad, as already discussed.

Run 282026 took data from LHC fill 4499. Data runs are divided into so-called *luminosity blocks* (lumi-blocks or LBs), which are collections of temporally consecutive events, and roughly amounts to a minute of data taking. For each lumi-block, a data quality flag is set, which signals whether or not that block should be used for analysis. This is described by a so-called *good runs list* (GRL) which are generated for each run.

10.2 DETECTOR ALIGNMENT FROM ELASTIC EVENTS

The precision of the measurement of the diffractively scattered proton kinematics depends strongly on the knowledge of the detector position with respect to the beams. The detector positions were measured during data taking by LVDTs (Linear Variable Differential Transformers) with a precision of 100 - 200 μm. These positions are listed in Table 10.1 and are for the Roman Pot edge. There is an additional 450 μm from the RP edge to the main detector edge. For the analysis, we need to know the detector positions with better precision in order to make use of the tracking precision of 30 μm in the ALFA MDs. This

alignment comes in two steps: a beam-based alignment and an off-line alignment using elastic events.

A beam-based alignment is performed in a separate dedicated LHC fill before the fill in question and will use the same beam settings. Each of the eight ALFA Roman Pots will then be, one at a time, moved from their garage position towards the beam in steps of 10 μm until the LHC beam-loss monitors gives a signal above a certain threshold. Knowing the vertical positions of the upper and lower RP windows with respect to the beam, it is then possible to find the center of the beam as well as the distance between the upper and lower RPs.

After data taking, an off-line alignment procedure is performed to transform reconstructed track positions in the ALFA detectors from the detector coordinate-system to the beam coordinate-system. This alignment procedure is a track-based alignment using proton tracks from elastic-scattering events. The full and final alignment depends on the optics and track reconstruction efficiency and has not yet been found for the data run used in this study. However, a track-based alignment using elastic events has been performed by the author as detailed in the following.

First, elastic events have been selected with the following cuts:

- a *golden* event in the ALFA detectors, i.e. a track in the two upper detectors on one side, and a track in the two lower detectors on the opposite side,
- otherwise empty ALFA detectors,
- beam-screen cut,
- level-1 triggers for elastic events (`L1_ALFA_ELAST15` and `L1_ALFA_ELAST18`),
- veto on level-1 triggers for systematic effects (`L1_ALFA_SYST17` and `L1_ALFA_SYST18`),
- an empty inner detector and calorimeter of ATLAS.

Where the elastic and systematic L1 triggers used here, are the most efficient with a trigger efficiency close to 100% [49]. An additional cut on the horizontal track coordinates of $|x| < 2.5$ mm has been done to remove most of the background from central diffractive events. A perhaps more efficient cut would have been selecting everything within an ellipse in the correlation plots seen in Figure 10.1 and in Figure 10.3, which is one of the usual selection criteria for elastic events. However, for this simple alignment procedure, the cut in $|x|$ had a similar effect.

For the alignment of each ALFA detector, three parameters are necessary: the rotation angle around the beam axis, and the horizontal and vertical position offsets. The distribution of tracks from elastic-scattered protons will form a narrow ellipse in the (x, y)-plane, with its major axis in the vertical direction and with an aperture gap between the upper and lower detectors. The distribution of track hits in the (x, y)-plane for one of the detectors is seen in Figure 10.2. A linear fit to the profile histogram of the track distribution will give the small rotation angle θ_z around the beam axis. Each detector will have a rotation angle on the order of a few mrad. The values from the fits are listed in Table 10.1.

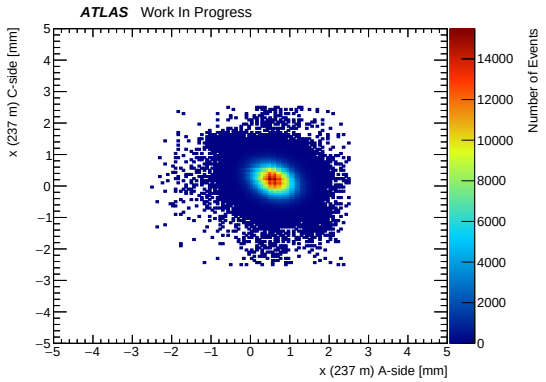

Figure 10.1: Correlation plot of the horizontal reconstructed track positions for the inner detectors. The track coordinates are in the detector coordinate system.

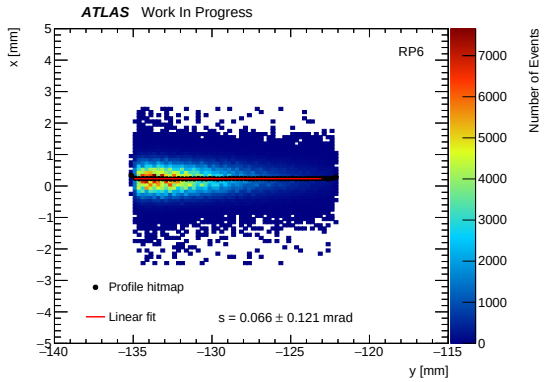

Figure 10.2: Linear fit to a profile histogram of the track pattern in the $x - y$-plane for RP6 (B7R1U) to determine the rotation angle around the beam axis. The track coordinates are in the detector coordinate system.

The horizontal position offset Δx can be found from the mean value of a Gaussian fit to the projection of the horizontal track position in each detector, as seen in Figure 10.4. The values of Δx are also listed in Table 10.1.

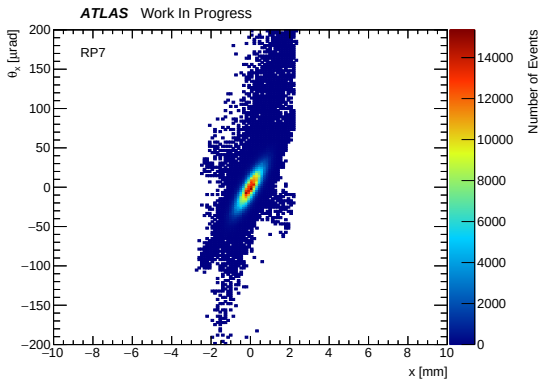

Figure 10.3: Correlation of reconstructed horizontal track position versus the local angle for RP7 (B7R1L).

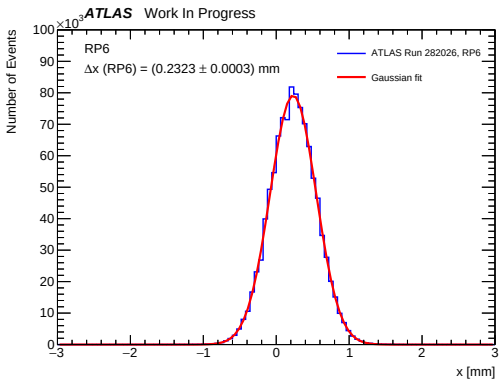

Figure 10.4: Gaussian fit to the horizontal track positions in RP6 (B7R1U) to determine the horizontal offset Δx.

The vertical alignment is found from the LVDT measurements. However an additional correction may be applied, as the inner and outer detectors may have a small relative offset. This offset can be found by considering the correlation of the vertical track position of the inner detector versus the difference between the vertical track position of the outer detector and the inner detector. This can then be fitted with a linear function,

$$y_{245\text{ m}} - y_{237\text{ m}} = a \times y_{237\text{ m}} + b \tag{10.1}$$

where, if no offset is present, should cross the origin, i.e. $b = 0$. This is illustrated in Figure 10.5 and Figure 10.6. The vertical positions will then be corrected by the offset b as such:

$$y_{237\text{ m}} = y_{237\text{ m}} + \frac{b}{2}, \qquad y_{245\text{ m}} = y_{245\text{ m}} - \frac{b}{2} \tag{10.2}$$

as it is not known which of the detectors are misaligned.

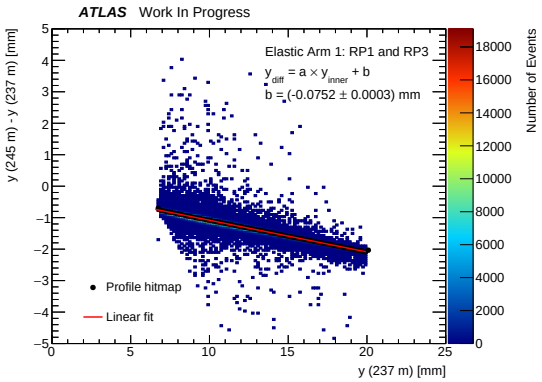

Figure 10.5: Correlation of reconstructed vertical track position versus vertical local angle $\theta_y \approx y_{\text{outer}} - y_{\text{inner}}$ for the elastic arm in RP1 (B7L1U) and RP3 (A7L1U).

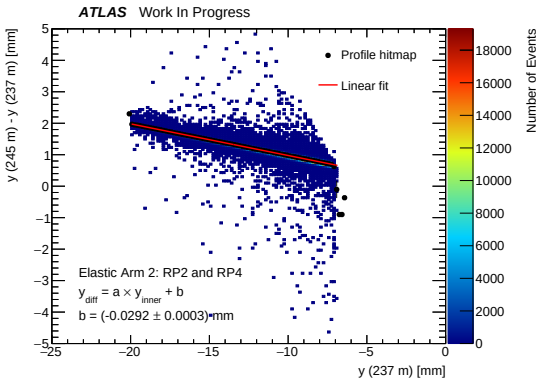

Figure 10.6: Correlation of reconstructed vertical track position versus vertical local angle $\theta_y \approx y_{\text{outer}} - y_{\text{inner}}$ for the elastic arm in RP2 (B7L1L) and RP4 (A7L1U).

The alignment procedure as outlined here, should optimally be performed in multiple iterations until a convergence is met. This is because the elastic event selection will depend on the alignment through the correlation cuts and vice versa. However, in this study, a simple alignment procedure with just a single iteration has been performed. The track based alignment will also depend on input from the optics and the elastic track reconstruction efficiency. None of these have been worked out yet and hence the final results for the alignment are not finished. In a more complete alignment, the distance measurements between the upper and lower ALFA Roman Pots in each station would be used instead of the LVDT measurements, as they would be more accurate. The distance measurements would be based on readouts of the overlap detectors.

Table 10.1: Track-based alignment parameters used to align the ALFA detectors in this study. The LVDT measurements are from [76] with an uncertainty of about 100 μm.

Detector	LVDT $y_{meas.}$ [mm]	Δx [mm]	θ_z [mrad]
RP1	5.71 ± 0.10	0.6148 ± 0.0004	5.132 ± 0.173
RP2	-6.02 ± 0.10	-0.1617 ± 0.0004	0.030 ± 0.179
RP3	6.47 ± 0.10	0.7178 ± 0.0003	3.352 ± 0.119
RP4	-6.53 ± 0.10	0.4805 ± 0.0003	-1.151 ± 0.122
RP5	6.28 ± 0.10	0.1850 ± 0.0003	-0.576 ± 0.123
RP6	-6.77 ± 0.10	0.2323 ± 0.0003	0.066 ± 0.121
RP7	5.18 ± 0.10	0.2275 ± 0.0004	1.197 ± 0.178
RP8	-6.54 ± 0.10	0.3351 ± 0.0004	-0.137 ± 0.177

10.3 SINGLE DIFFRACTIVE EVENT SELECTION CUTS

After performing the alignment of the ALFA detector for our run we can now turn towards selecting single diffractive events for analysis. This section will describe the cuts used to obtain a nearly clean sample of single diffractive events. The selection criteria will mirror what we used in our simulation framework in Section 8.6.

10.3.1 *Luminosity Blocks*

The events in our data run has been first selected from an ATLAS good-runs-list (GRL) which signals whether the detector was in a good enough condition such that the lumi-block containing the given event can be used for physics analysis.

On the ALFA side, there exists specialized criteria for a good lumi-block. First, the ALFA Roman Pots must be in the final position for data taking. Second, the duration of the lumi-block must be more than 60 s. Third, the dead time of the ALFA and ATLAS detectors must be less than 5% of the lumi-block duration. The lumi-blocks in run 282026 passing the ALFA criteria are found from ref. [47] to be 5 - 8 and 10 - 238.

10.3.2 *Bunch Crossing Identifiers (BCID)*

Each bunch crossing is given a unique ID called a bunch crossing ID or BCID. Not all bunches in a given beam will have a collision with a bunch in the other beam. These are called unpaired bunches and may give a signal in the ALFA detector due to beam background or beam

halos. The unpaired bunches for our run can be found from ref. [47] and are removed to reduce the background.

10.3.3 *Signal in ALFA*

The ALFA SD event selection criteria requires exactly one reconstructed track in each of the two ALFA detectors of one of the four arms. The number of U and V plates used in the track reconstruction was required to be $N_U, N_V > 5$ out of the total 10 plates for both U and V. This is to ensure a well-reconstructed track. The distributions of hits in the U and V plates are shown in Figure 10.7. All other detector arms are required to be empty. The reconstructed hit coordinates in the transverse plane is required to be within an edge cut defined by the ALFA and beam screen region as illustrated in Figure 8.14. Hits outside the overlap region between ALFA and the beam screen are expected to be from beam background.

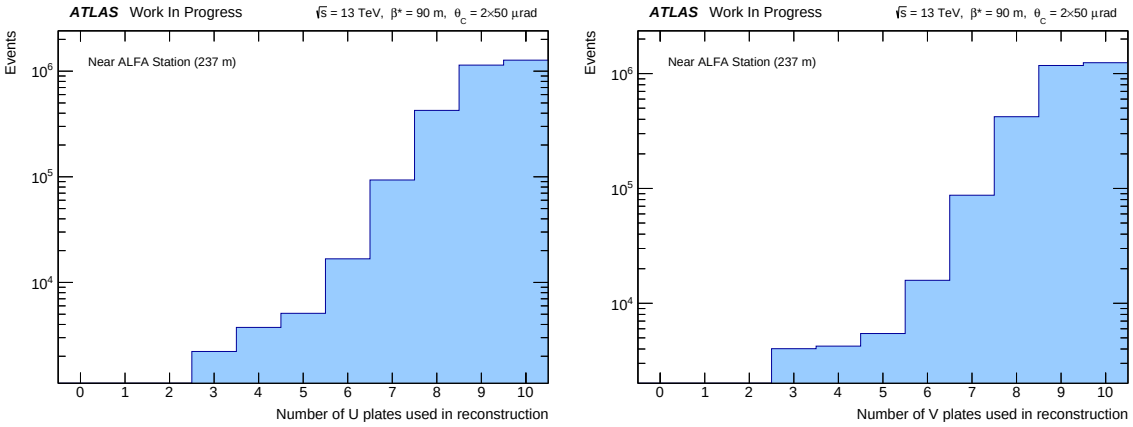

(a) Distribution of hits in the U plates.

(b) Distribution of hits in the V plates.

Figure 10.7: Number of hits in each ALFA detector plate for the stations at $z = 237$ m.

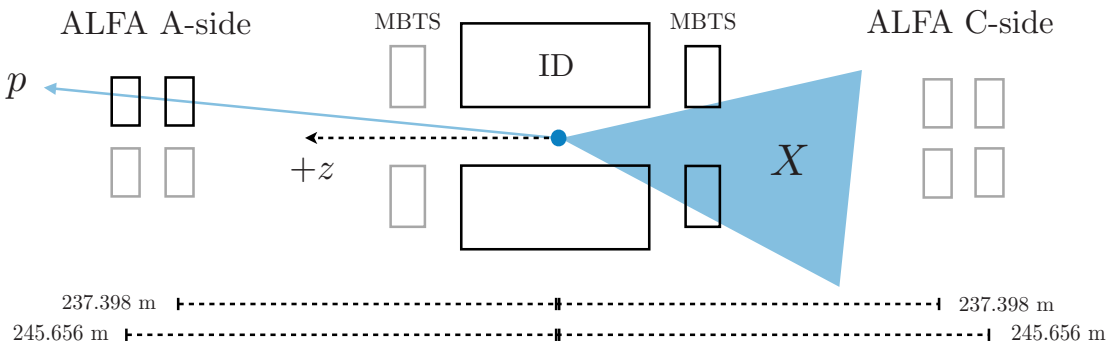

Figure 10.8: Simplified illustration of the signal diffractive event selection using ALFA and ATLAS.

10.3.4 *Signal in the MBTS*

The MBTS is used to signal activity in the ATLAS detector for minimum bias samples. Combined L1 trigger items for the MBTS and the ALFA detector has been used to trigger on events where 1 or 2 MBTS segments has fired on the opposite side of the ALFA detectors with a reconstructed track. The combined L1 triggers are

`L1_MBTS_1_A_ALFA_C`, `L1_MBTS_1_C_ALFA_A`,
`L1_MBTS_2_A_ALFA_C`, `L1_MBTS_2_C_ALFA_A`

and has been used to select single diffractive events. In addition, the event selection requires at least one MBTS segment (on the opposite side of the ALFA hit) with a deposited charge Q over a certain signal threshold (set to 0.15 pC). The deposited charge Q in one of the MBTS segments on the A-side is shown in Figure 10.9 for paired and unpaired bunches. Unpaired bunches will have no collisions at the interaction point and any charge deposited in the MBTS will therefore be background or noise. The charge deposited from the MBTS background will mainly be below the chosen signal threshold and is also present for the paired bunches. A veto on signals on the side with the ALFA hit can also be imposed but has been found to significantly reduce the amount of events, resulting in low statistics. The MBTS veto has therefore not been included in the event selection.

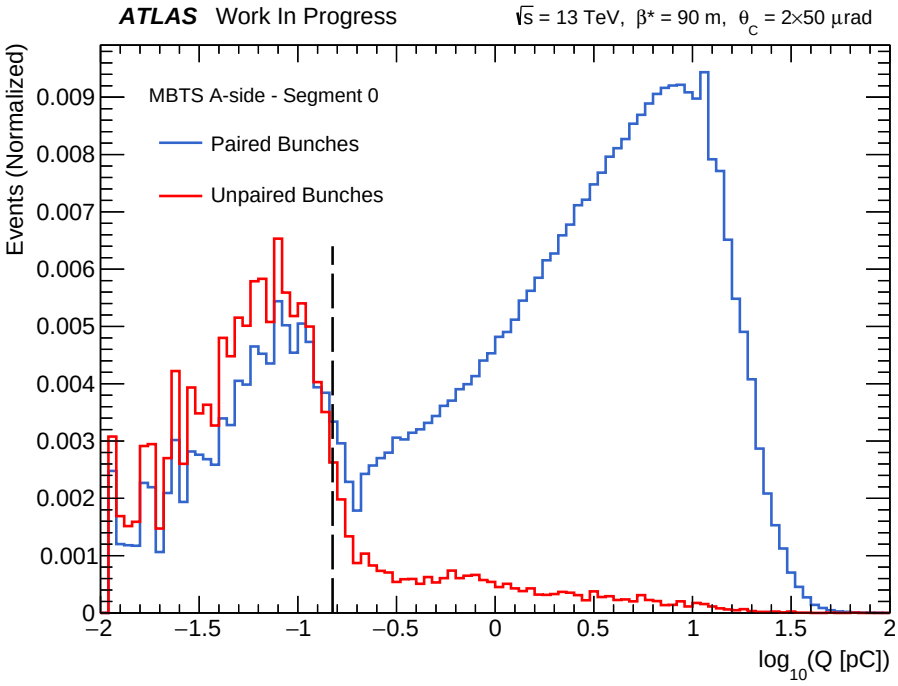

Figure 10.9: Distribution of the collected charge Q in MBTS segment 0 on the A-side for paired and unpaired bunches. The 0.15 pC signal threshold is illustrated by a dashed line.

10.3.5 *Signal in the ATLAS Inner Detector*

We require a reconstructed vertex in the ATLAS inner detector as the primary vertex is important for the precise reconstruction of the proton kinematics. The average number of pile-up collisions was $\langle\mu\rangle \approx 0.0863$, as discussed in Section 5.4, and there are therefore a small probability of more than one collision happening for any given bunch crossing. Assuming a Poisson distribution the probability of k collisions happening in a given bunch crossing can be estimated as

$$P(k \text{ collisions}) = \frac{e^{-\langle\mu\rangle}\langle\mu\rangle^k}{k!} \tag{10.3}$$

Hence, the probability of two collisions happening in a given bunch crossing is suppressed by a factor

$$\frac{P(1 \text{ collision})}{P(2 \text{ collisions})} = \frac{e^{-\langle\mu\rangle}\langle\mu\rangle^1/1!}{e^{-\langle\mu\rangle}\langle\mu\rangle^2/2!} \approx 23 \tag{10.4}$$

compared to the probability of just one collision. A requirement of exactly one reconstructed vertex is imposed to ensure a clean sample and to reduce background from pile-up.

The reconstruction of the primary vertex requires at least two tracks. The following cuts are imposed on the reconstructed charged tracks to tighten the quality of the tracks:

- $p_T \geq 100$ MeV,
- $|\eta| < 2.5$,
- require tracks to have at least one hit in the B-layer (first pixel layer) if they pass a module that is expected to be active,
- if a B-layer hit is not expected then require at least one hit in the pixel detector,
- $|d_0| < 1.5$ mm (transverse distance of track origin to the primary vertex),
- $|z_0| \sin\theta < 1.5$ mm (longitudinal distance of track origin to the primary vertex),
- χ^2 probability > 0.01 for reconstructed tracks with $p_T > 10$ GeV,
- a requirement of SCT hits with regard to the track p_T:
  - $n_{\text{SCT}} > 2$, for $p_T < 200$ MeV,
  - $n_{\text{SCT}} > 4$, for 200 MeV $< p_T <$ 300 MeV,
  - $n_{\text{SCT}} > 6$, for $p_T > 300$ MeV,

The track selection criteria are similar to those of previous minimum-bias analyses at the ATLAS detector [77].

The number of reconstructed vertices for events that have passed the ALFA and MBTS cuts are shown in Figure 10.10. A large fraction of events either does not have a reconstructed vertex or have more than one. In events with more than one reconstructed vertex it is unclear which vertex the diffractively scattered proton originated from.

The coordinates of the reconstructed primary vertices are shown in Figure 10.11 - 10.13. The vertex distributions have been fitted with Gaussian distributions and the resulting mean values and standard deviations corresponds reasonably well with the beam spot measurements in Equation 5.7 - 5.9.

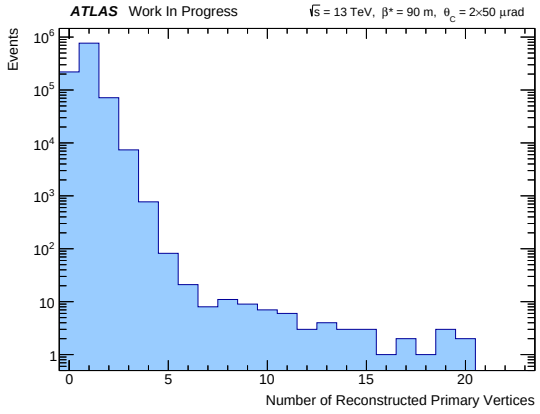

Figure 10.10: Distribution of reconstructed vertices in the ATLAS inner detector for events passing the ALFA and MBTS cuts.

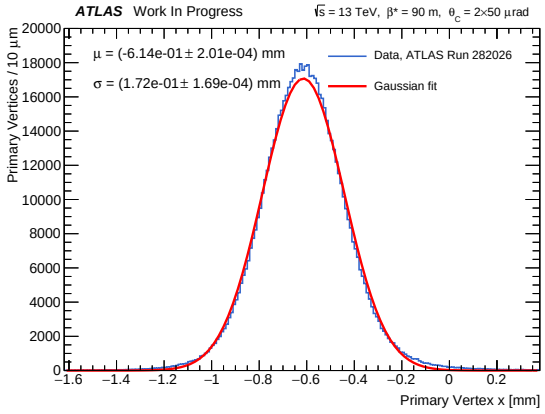

Figure 10.11: Reconstructed primary vertex x-coordinate plotted with a Gaussian fit.

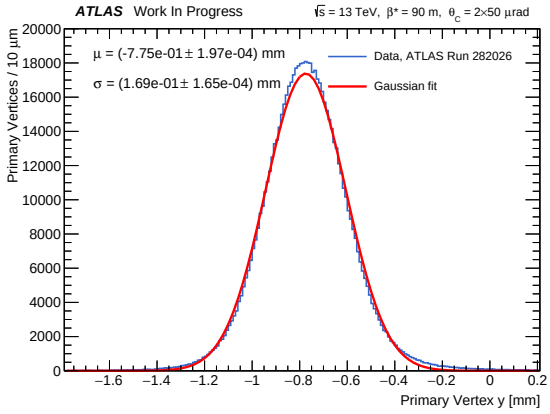

Figure 10.12: Reconstructed primary vertex y-coordinate plotted with a Gaussian fit.

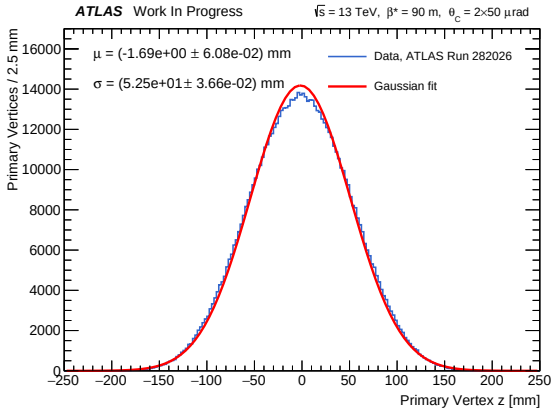

Figure 10.13: Reconstructed primary vertex z-coordinate plotted with a Gaussian fit.

The uncertainties given by the primary vertex reconstruction in the inner detector can be used in `ALFAReco` instead of the beam spot uncertainties for additional accuracy. These are shown in Figure 10.14 and 10.15.

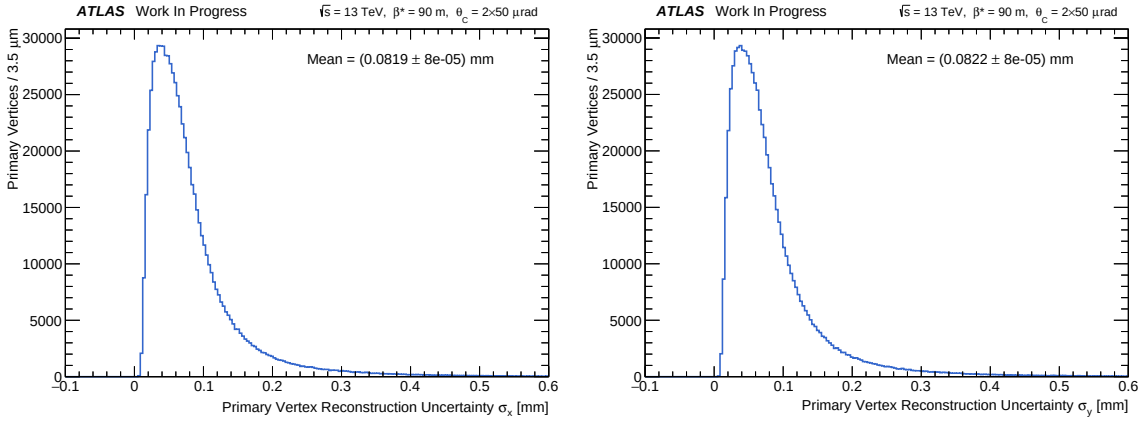

(a) Reconstruction uncertainty for x. **(b)** Reconstruction uncertainty for y.

Figure 10.14: Distribution of the primary vertex reconstruction uncertainties.

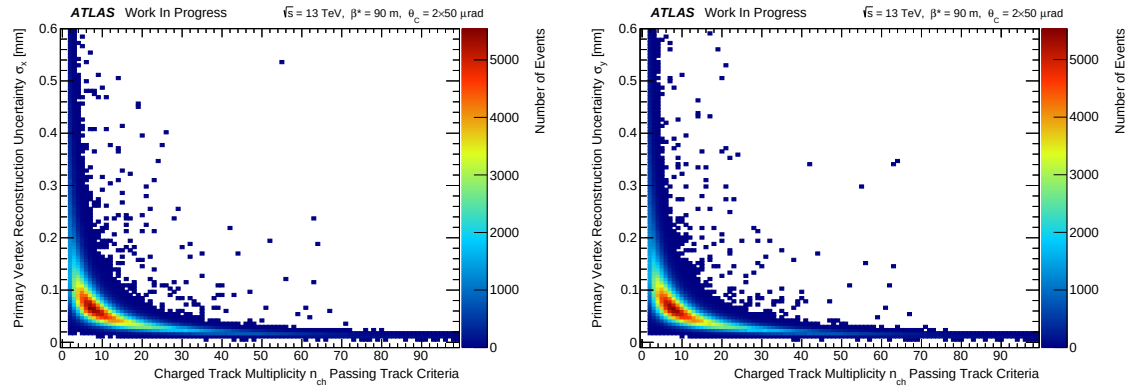

(a) Reconstruction uncertainty for x. **(b)** Reconstruction uncertainty for y.

Figure 10.15: The primary vertex reconstruction uncertainties as functions of the number of charged ID tracks that passed the track criteria.

10.3.6 *Signal in the ATLAS Calorimeter System*

Reconstructed topo-cluster jets in the ATLAS calorimeter system has not been included in the data analysis, as there were some problems with the jet cleaning algorithms. The calorimeter system can extend the pseudorapidity coverage for the particles from the diffractively dissociated system up to $|\eta| < 4.9$ from the inner detector coverage of $|\eta| < 2.5$. Therefore requiring a signal in the calorimeter instead of the inner detector will increase the number of observed single diffractive events. However, unlike the inner detector the calorimeter does not reconstruct a primary vertex which is necessary for a precise proton reconstruction. The calorimeter is therefore not of vital importance for our analysis of single diffractive events.

10.3.7 *Reconstruction of Proton Kinematics*

Finally the kinematics of the proton at the interaction is reconstructed by using `ALFAReco` with the produced `ALFAReco` parameter file for $\sqrt{s} = 13$ TeV, $\beta^* = 90$ m, and $\theta_C = 2 \times 50$ μrad as described in Section 8.4. The reconstructed track hit positions in both the near and far ALFA detectors in one of the four armlets along with the reconstructed primary vertex with uncertainties by the ATLAS inner detector is given as input to the `ALFAReco` reconstruction code.

As described in Section 8.4 the `ALFAReco` parameterization was generated assuming a beam spot position at $(x_{BS}, y_{BS}) = (0, 0)$ in the LHC coordinate system. However, the actual beam spot position was measured by the ATLAS inner detector and is listed in Equation 5.7 - 5.8. Hence, the actual beam spot position is given as input to `ALFAReco` for correction. Note that both the measurement of the primary vertex per event as well as the measurement of the beam spot are done by the ATLAS inner detector measurement and is therefore in the ATLAS coordinate system. Ideally, one should transform the ALFA inner detector measurements to the LHC coordinate system. Unfortunately, no information about the difference between the two coordinate systems has been found. The measurements from the ATLAS inner detector has therefore been used as if they given in the LHC coordinate system which will result in a systematic error on the reconstructed proton kinematics.

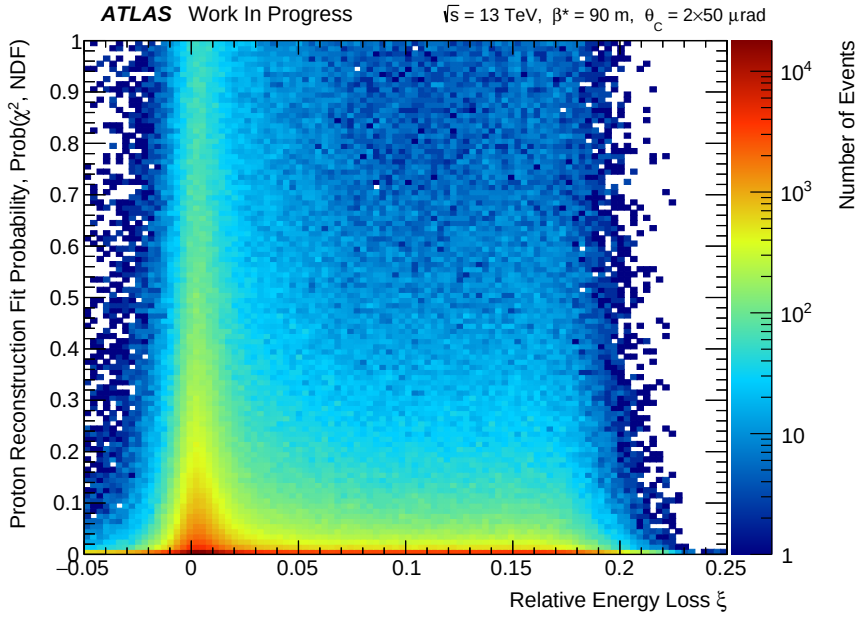

Figure 10.16: Correlation between the reconstructed ξ and the `ALFAReco` reconstruction fit probability for data.

The reconstruction fit performed by `ALFAReco` may fail if convergence in Minuit is not achieved. Events with a failed proton reconstruction will be discarded.

10.3.8 *Resulting Cutflow*

In Table 10.2 the resulting cutflow is presented. Requiring exactly one reconstructed track in ALFA will reduce the number of events significantly, as will the requirement of a hit in the MBTS on the opposite side, and the requirement of a single good reconstructed primary vertex.

Table 10.2: Cutflow table for the single diffractive event selection in run 282026. Listing number of events passing each cut.

Cut	Number of Events
Total events in data sample	14822415
GRL and ALFA lumi-block cuts	14439022
Only paired bunches	14226546
Exactly one track in ALFA	2983052
Hit in one of the four arms	2958803
$N_U > 5$ and $N_V > 5$	2924248
ALFA and beam screen edge cut	2848701
Hit in opposite side of MBTS	1067264
Exactly one primary vertex	767522
At least two good tracks in the ID	749186
Successful Proton Reconstruction	748909

In Table 8.4 it was listed that about 21.6% of simulated single diffractive events would survive the detector acceptance in the simulation framework. Assuming that about 20% of all pp interactions are single diffractive (see Equation 4.10), we can estimate the final number of selected events to be $14822415 \cdot 20\% \cdot 21.6\% \approx 640328$, which is closer than anticipated to the actual number of 748909. The discrepancy in the event count may be caused by the Pomeron flux parameterizaton since the accepted event count does depend on the model parameters as seen in Table 9.1 and 9.2. The discrepancy may also in part be explained by background. The possible background sources will be investigated in the following sections.

10.4 BACKGROUND SOURCES

Even with the event selection cuts, the resulting selected single diffractive sample will not be completely free of background. Some of the possible background sources was discussed in Section 9.2. However, additional sources of background may exist that were not possible to simulate with the developed simulation framework. This section will discuss these possible background sources.

Elastic events with only one of the elastically scattered protons leaving a reconstructed track in the ALFA detector while a non-diffractive pile-up event giving a signal in the ATLAS detector. The relative event count of this background will depend on the track reconstruction efficiency of ALFA, the pile-up rate, and the exact cross-sections for the different types of pp interactions.

The vacuum inside the LHC beam pipes play an important role in the performance and operation of the accelerator. Residual gas in the beam pipes can lead to not only a degradation of the beam quality but can also be a source of background. Protons originating from *beam-gas interactions* can be detected in the ALFA detector in coincidence with a pile-up event in the ATLAS inner detector and MBTS.

The beam particles may interact with magnet material or collimation instrumentation which results in a *beam halo* – a collection of particles that do not move on the designed trajectory but will follow upstream parallel to the beam. Some of the beam halo can also originate from the beam-gas interactions. Charged particles from the beam halo may leave a signal in ALFA along with some activity in ATLAS.

Low energy decay products from collision debris either from the actual (in time) collision or the ones before (out of time) may give a signal in the ATLAS inner detector and MBTS. This background is called *afterglow*. Finally, instrumental noise in ALFA and/or the MBTS may make up some of the background.

A full study of the background sources is beyond the scope of this thesis, as it requires a full simulated Monte Carlo sample with knowledge of the cross-sections as well as the acceptances and efficiencies of the ALFA and ATLAS detectors. Some of the beam halo background will be studied later but a full understanding of the beam related backgrounds may require a FLUKA simulation [78, 79].

10.5 COMPARISON OF DATA AND SIMULATION

The distributions of hits from the reconstructed tracks in the ALFA detector for selected events are shown in Figure 10.17. There are significantly more hits with $x > 0$ than in the simulated single diffractive hitmaps in Figure 8.28. This is most likely due to background sources as discussed in the previous section.

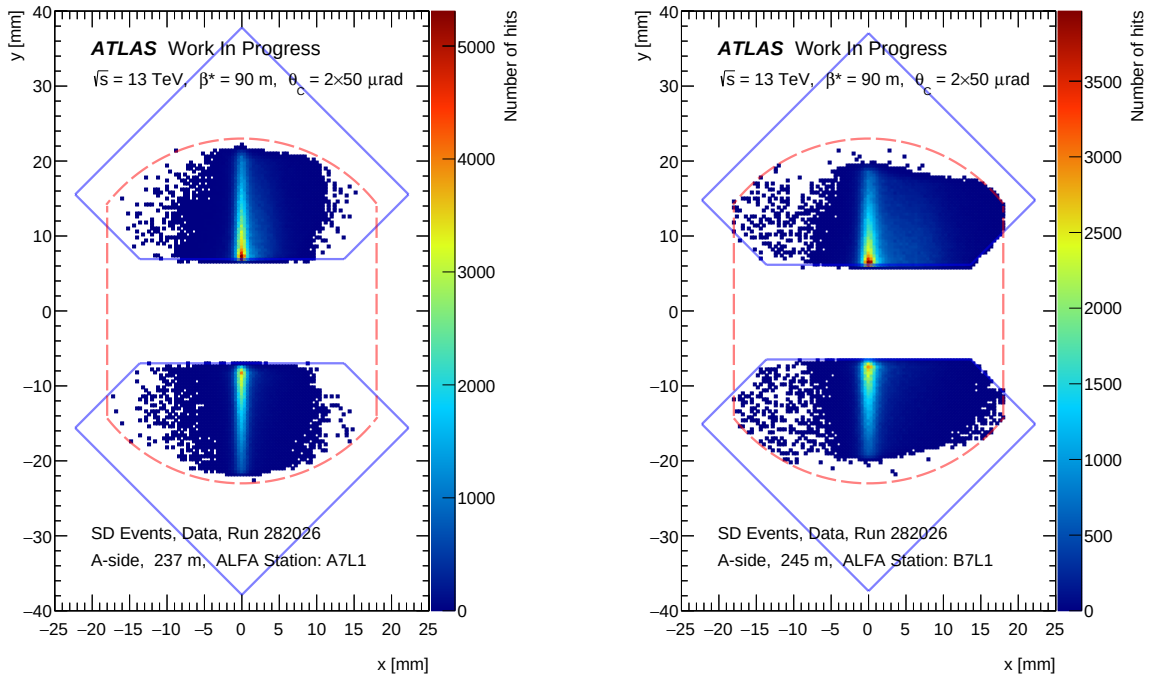

(a) Near station: $z = 237$ m.

(b) Far station: $z = 245$ m.

Figure 10.17: Hitmaps of single diffractively scattered protons from data run 282026 in the ALFA stations on the A-side. Overlaid with the outline of the ALFA main detector (solid blue line) and the LHC beam screen (dashed red line).

In the Δx plot in Figure 10.18 a much larger tail towards larger differences in the x-coordinates between the near and far stations is seen for data. This is also seen by a much larger and more pronounced diffractive 'banana' shape in the correlation plot between the local angle θ_x and the x-coordinate for the near station in Figure 10.20.

A secondary ellipse which is narrow in θ_x but spread out in x is observed in data. This secondary ellipse is not observed in the simulated single diffractive events in Figure 9.18 and is due to beam background as we shall see later.

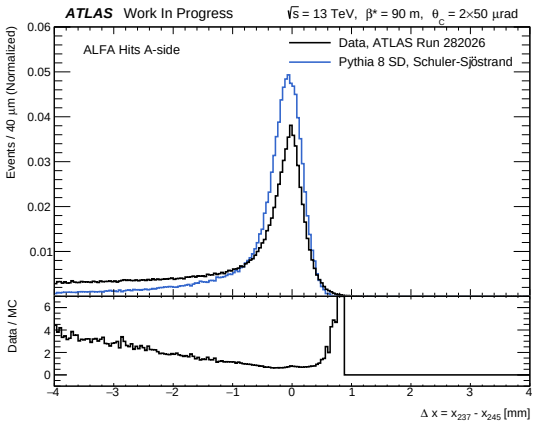

Figure 10.18: Difference in the proton hit x-coordinate between the near and far ALFA station, $\Delta x = x_{237\,\mathrm{m}} - x_{245\,\mathrm{m}}$, on the A-side.

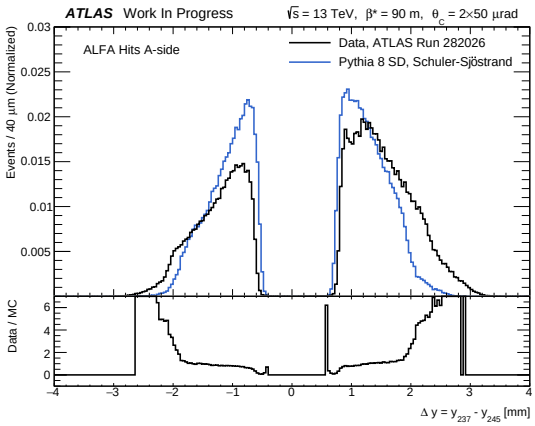

Figure 10.19: Difference in the proton hit y-coordinate between the near and far ALFA station, $\Delta y = y_{237\,\mathrm{m}} - y_{245\,\mathrm{m}}$, on the A-side.

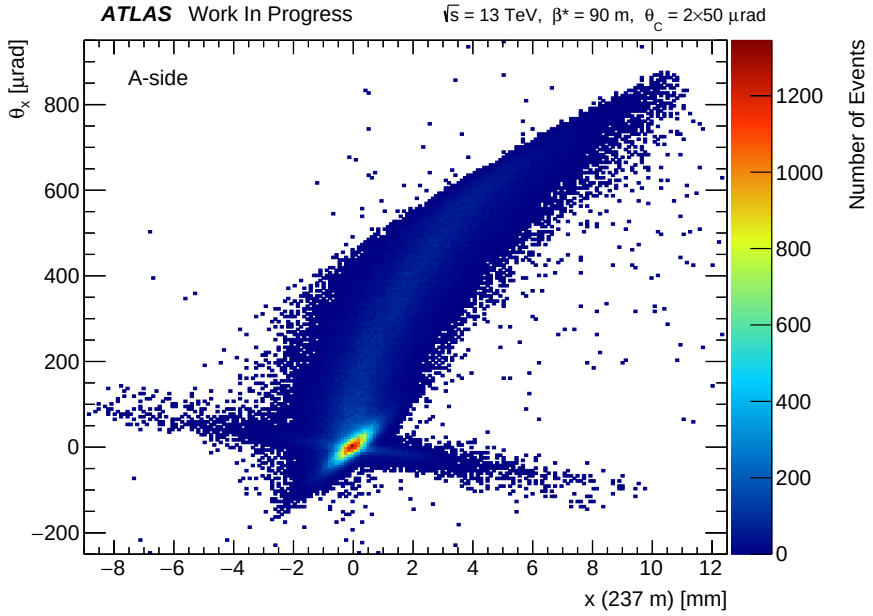

Figure 10.20: Correlation of the single diffractive hit x-coordinate versus the local angle θ_x for the A-side.

The distribution of the reconstructed relative energy loss ξ is shown in Figure 10.21. A large number of protons with a negative energy loss, corresponding to an energy larger than the beam energy, are observed for data but not seen in simulation. These protons corresponds to the hits with a negative x-coordinate.

Regge theory predicts that the single diffractive cross-section falls rapidly with the relative energy loss ξ,

$$\frac{\mathrm{d}\sigma^{\mathrm{SD}}}{\mathrm{d}\xi \mathrm{d}t} \sim \xi^{-1-\varepsilon} \qquad \text{for} \quad s \gg |t| \tag{10.5}$$

This behavior is modelled by the Pomeron flux parameterizations in Pythia as shown in Equation 4.81, 4.82, and 4.84. However, a flat plateau (or shoulder) is present for larger ξ values in data which is in disagreement with the expectation from Regge theory. The expected non-diffractive and double diffractive background as shown in Figure 9.14 is not large enough to explain this plateau. This plateau needs to be understood before the fit procedure to discern the best Pomeron flux model parameters can be applied to data.

The distribution of the reconstructed squared momentum transfer t is shown in Figure 10.22. Significantly more events with a high t value are observed in data compared to simulation. The expected non-diffractive and double diffractive background in Figure 9.15 is again not large enough to describe the discrepancy.

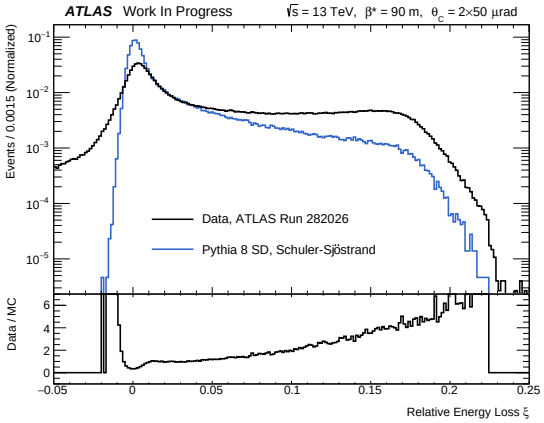

Figure 10.21: Distribution of the reconstructed ξ for data and simulation with the Schuler-Sjöstrand parameterization.

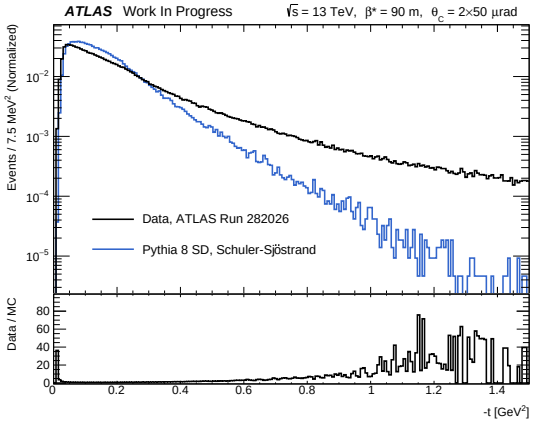

Figure 10.22: Distribution of the reconstructed t for data and simulation with the Schuler-Sjöstrand parameterization.

The correlation plot between the reconstructed ξ and t is shown in Figure 10.23. Several structures in the correlation plot for data are observed that are not present in the single diffractive simulation plot in Figure 9.3.

First, a 'boomerang' shape around $\xi \simeq 0$ and extending to higher t values is observed. This is due to beam background and will be investigated later.

Second, a large number of events is observed at low t values but large ξ values compared to the single diffractive simulation. This cluster of events corresponds to the shape of the non-diffractive and double diffractive background in Figure 9.21 and 9.22. This is a part of the origin of the observed flat plateau in ξ.

Finally, a more pronounced 'wing' structure going from low ξ and t values to higher values are observed in data than in simulation. This wing structure may be the primary contribution to the large discrepancy observed in the t distribution at large t values.

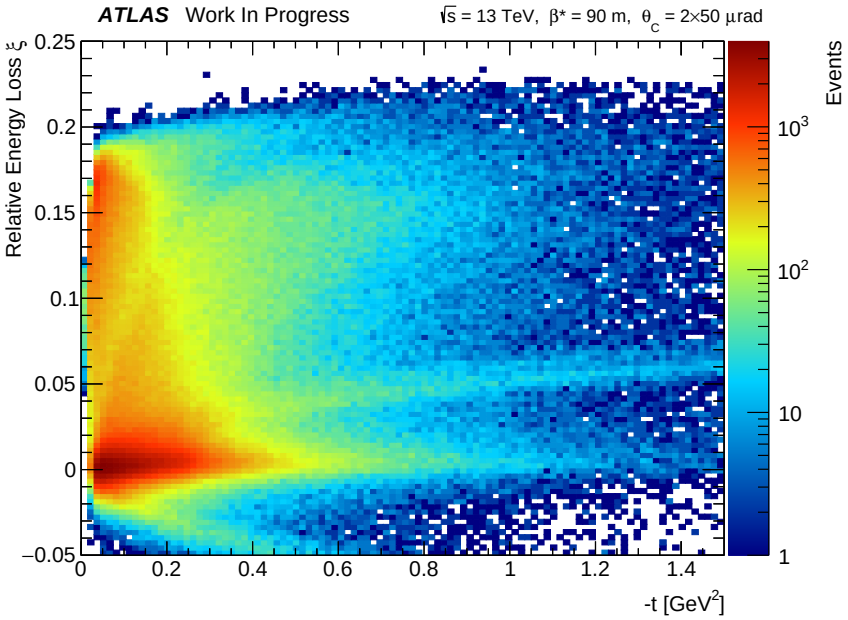

Figure 10.23: Correlation plot of the reconstructed ξ and t for data.

The cluster and the wing structure seems to be a consequence of the kinematic acceptance of the ALFA detector, since both the cluster and the wing structure are visible in the ξ vs. p_T acceptance plot in Figure 8.20a. The correlation between ξ and p_T for data is shown in Figure 10.24 and the ALFA acceptance in the same ranges is shown in Figure 10.25, where two bands give rise to the cluster and wing structures.

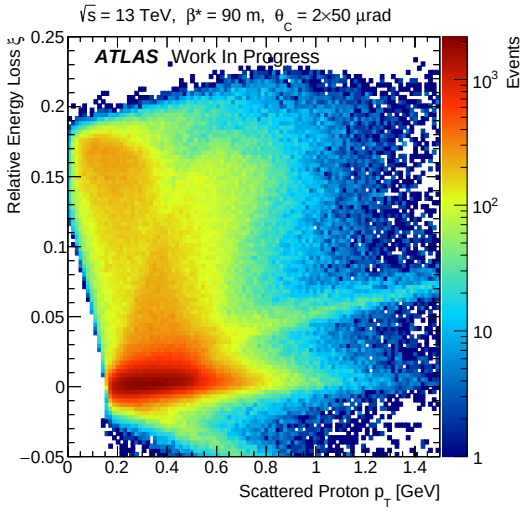

Figure 10.24: Correlation plot of the reconstructed ξ and p_T for data.

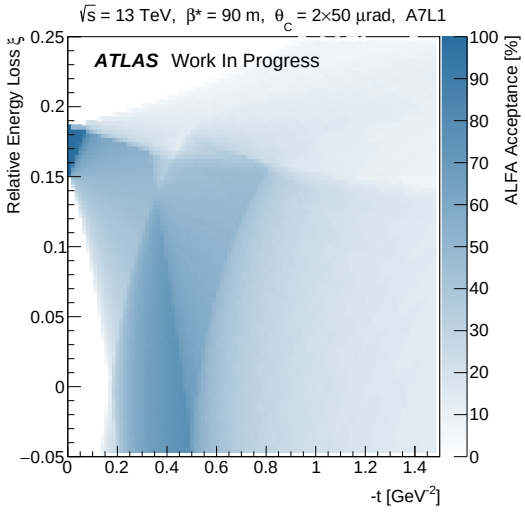

Figure 10.25: Two-dimensional acceptance plot of the ALFA acceptance for ξ vs. p_T.

The resulting ξ vs. t distribution for data (or alternatively ξ vs. p_T) seems to be a mapping of the underlying physics (or *truth*) distri-

butions onto the kinematic acceptance regions of the ALFA detector. The underlying physics distributions may then be a combination of the single diffractive signal along with the double diffractive and non-diffractive backgrounds as well as the beam background. This is illustrated in Figure 10.26. The expected sizes of the double diffractive and non-diffractive background from the simulation in Figure 9.14 and 9.15 may have been underestimated. The fit procedure in Section 9.4 could be modified such that the relative normalizations of the background sources (N_{SD}/N_{DD} and N_{SD}/N_{ND}) could be fitted as free parameters, along with ε and α'.

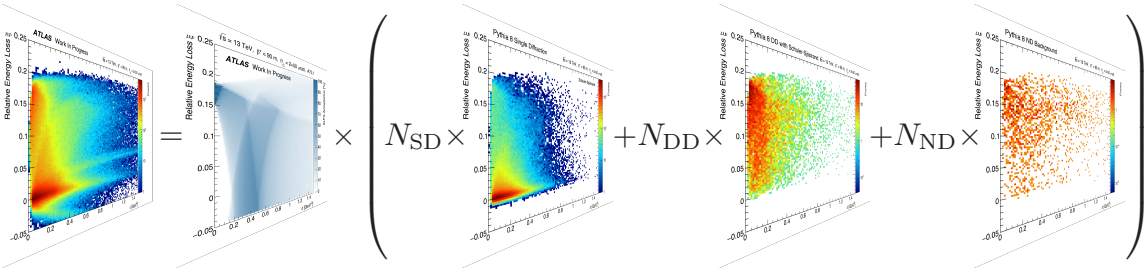

Figure 10.26: Illustration of the mapping of the underlying physics distribution for the SD signal and the DD and ND background as mapped onto the kinematic acceptance region. The contribution from the beam background is not shown.

A cut can be performed on the 'goodness' of the `ALFAReco` reconstruction fit. The fit probability as a function of ξ is shown in Figure 10.16. The distributions of the reconstructed ξ and t for data for different ranges of the fit probability are shown in Figure 10.27 and 10.28. Some of the beam background at negative ξ is seemingly removed with the cut on the reconstruction fit probability but other than that it is seen that the cut will not have any significant effect on the shape of the distribution. Most notably is the flat plateau at large ξ which is still present.

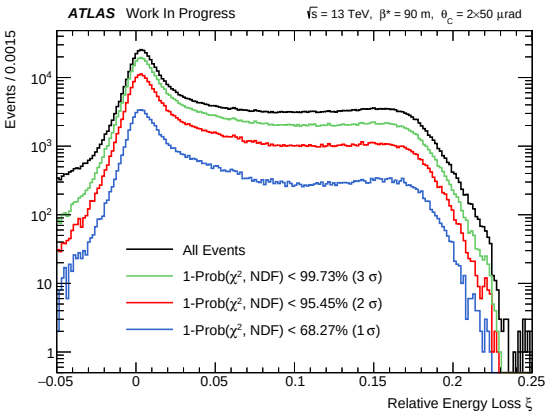

Figure 10.27: Distribution of the reconstructed ξ for data for different ranges of the 'goodness' of the reconstruction fit.

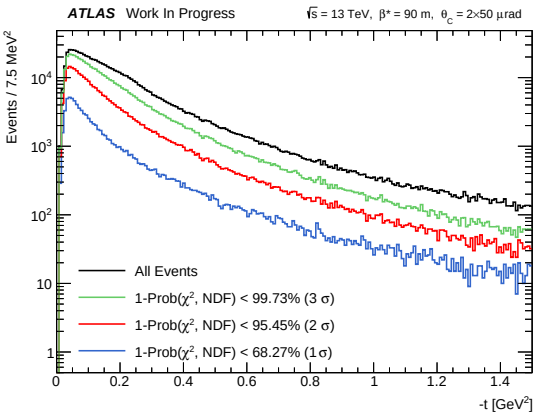

Figure 10.28: Distribution of the reconstructed t for data for different ranges of the 'goodness' of the reconstruction fit.

The number of charged tracks in the ATLAS inner detector after the single diffractive event selection is shown in Figure 10.29. The charged multiplicity in the simulated single diffractive events for both MPI toggled on and off is also shown. Data seems to peak around 4 charged tracks while simulation peaks at 11. The cause of this could be that some of the quality requirements of the charged tracks in the data analysis was not included in the simulation. A full GEANT4 simulation may be needed to test for this. Data seems to indicate that MPIs does happen in the diffractively dissociated system.

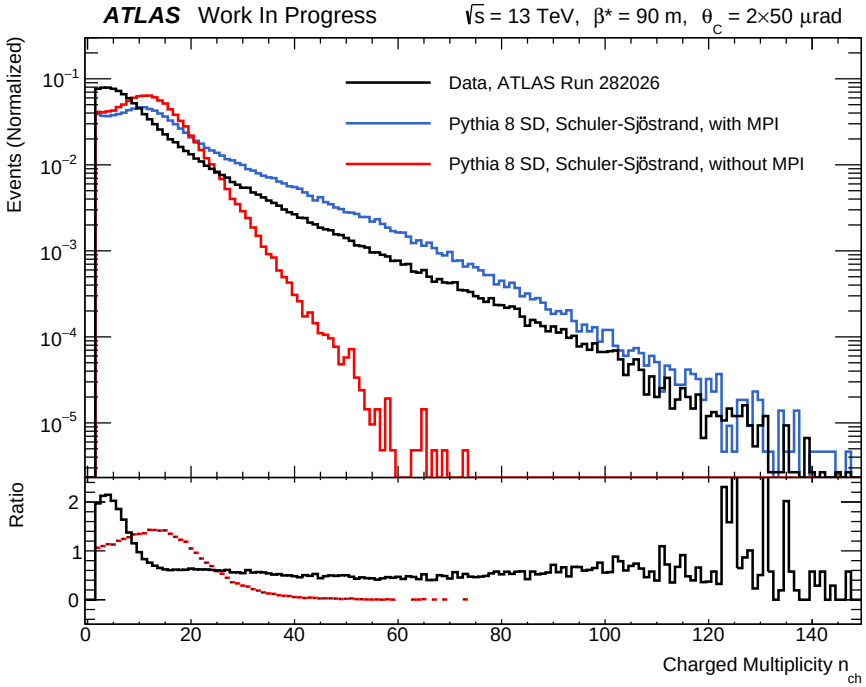

Figure 10.29: Distribution of the charged track multiplicity n_{ch} in the ATLAS ID for data compared to simulations with and without MPI.

Certain structures in the distributions (most notably the flat plateau in ξ) are observed in data but not in simulation. These structures and effects must be accounted for before the fit procedure to discern the Pomeron flux parameters can be used on data. The following sections will investigate some possible sources of background that may give rise to these structures.

Additional data distributions (including p_x, p_y, p_T, and $|\eta|$) are shown in the Appendix in Section B.3.

10.6 RANDOM UNCORRELATED COINCIDENCES

Charged particles from the beam background (beam-gas interactions and beam halo) may hit the ALFA detector and leave a reconstructed track. Such a track could coincide with some activity in ATLAS – e.g. a non-diffractive event – and could contribute to the background in the single diffractive event selection. This background contribution is called *Random Uncorrelated Coincidences* (RUCs).

It is possible to study this accidental coincidence background by selecting unpaired bunches in the data run. Unpaired bunches will not contain any pp collisions as no bunch crossing is happening. Hence, any signal in ALFA present in unpaired bunches will be from beam background. The distribution of the hits from reconstructed tracks in the ALFA detector in unpaired bunches are shown in Figure 10.30. The differences in the x- and y-coordinates are shown in Figure 10.31 and 10.32, respectively. The beam background is distributed in an ellipse that is seemingly symmetric in the x-direction in contrast to the single diffractive signal.

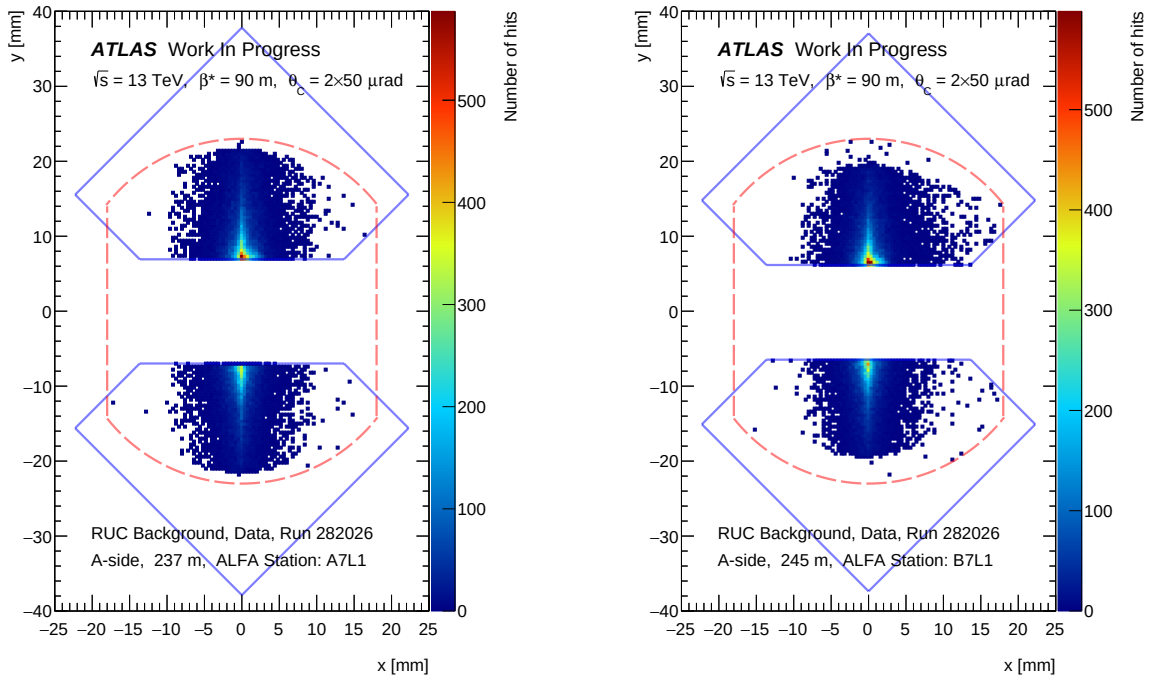

(a) Near station: $z = 237$ m.

(b) Far station: $z = 245$ m.

Figure 10.30: Hitmaps of beam background particles from unpaired bunches in data run 282026 in the ALFA stations on the A-side. Overlaid with the outline of the ALFA main detector (solid blue line) and the LHC beam screen (dashed red line).

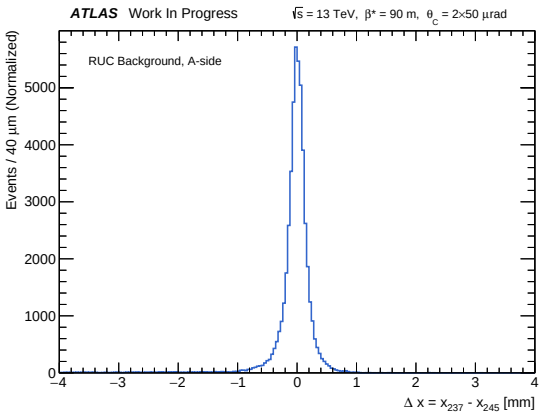

Figure 10.31: Difference in the beam background particle hit x-coordinate between the near and far ALFA station, $\Delta x = x_{237\,\mathrm{m}} - x_{245\,\mathrm{m}}$, on the A-side.

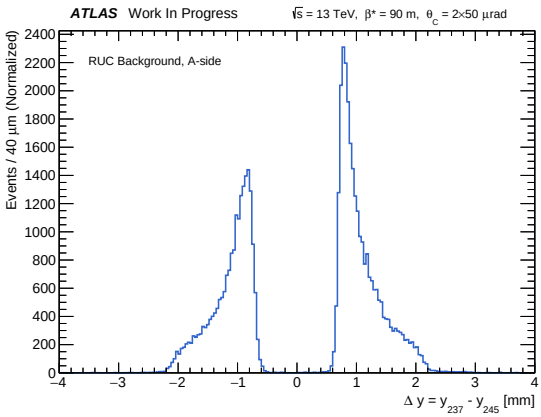

Figure 10.32: Difference in the beam background particle hit y-coordinate between the near and far ALFA station, $\Delta y = y_{237\,\mathrm{m}} - y_{245\,\mathrm{m}}$, on the A-side.

The correlation plot of the local angle θ_x vs. the x-position of the reconstructed tracks in the near station is shown in Figure 10.33. Most of the beam background is distributed in an ellipse that is narrow in θ_x but is spread out in x. This is also reflected in the hitmap in Figure 10.30a and the Δx plot in Figure 10.31. This ellipse is not visible in the simulated single diffractive signal in Figure 9.18.

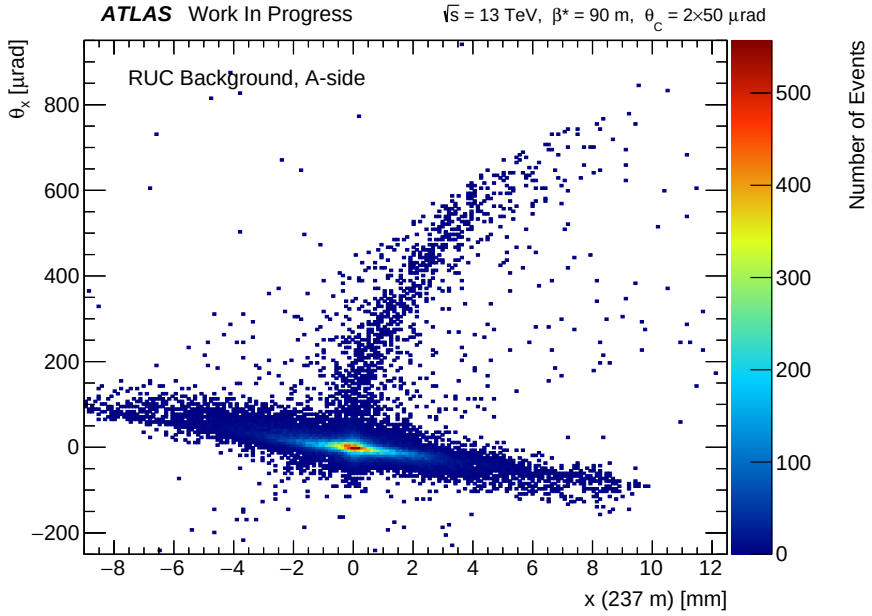

Figure 10.33: Correlation of the beam background particle hit x-coordinate versus the local angle θ_x for the A-side.

The hit positions have been given to `ALFAReco` along with the average values of the primary vertex coordinates in Figure 10.11 - 10.13 and the average vertex reconstruction uncertainties in Figure 10.14 to

study how the beam background is distributed in ξ and t. The distribution of the beam background in ξ is shown in Figure 10.34. The beam background can explain the prevalence of events for $\xi < 0$ that was observed in data that was not observed in simulation. The distribution of the beam background in t is seen in Figure 10.35, where the beam background seems to flatten out for high t values.

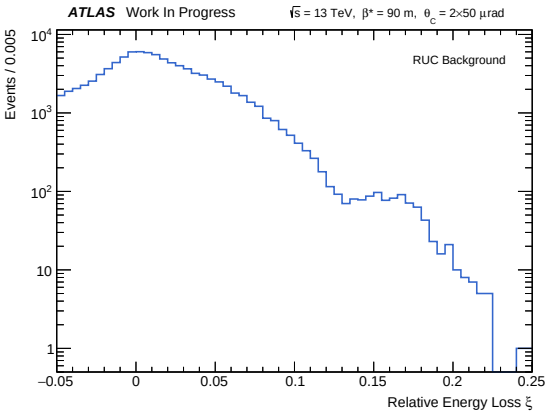

Figure 10.34: Distribution of the reconstructed ξ for the beam background particles in unpaired bunches.

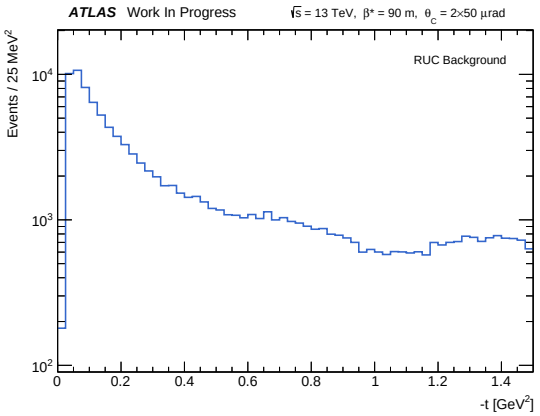

Figure 10.35: Distribution of the reconstructed t for the beam background particles in unpaired bunches.

The correlation plot between ξ and t is seen in Figure 10.36. The beam background from RUCs forms a 'boomerang' shape around $\xi \simeq 0$ extending towards larger t values. This boomerang shape was also observed in the selected single diffractive sample in Figure 10.23.

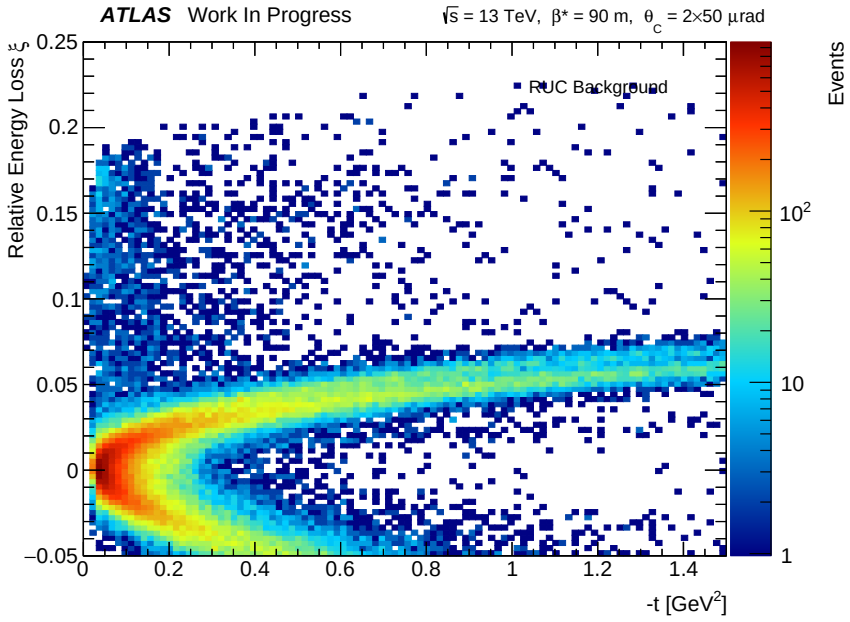

Figure 10.36: Correlation of the reconstructed ξ and t for the beam background particles in unpaired bunches.

The beam background is perhaps most easily distinguishable in the correlation plot of θ_x vs. x in Figure 10.33, as some of the beam background ellipse lies outside the 'elastic' ellipse and the diffractive banana shape. The size of the beam background can be estimate by choosing a RUC selection region in the shape of a side-band as illustrated on Figure 10.37 and 10.38. The RUC selection region is chosen well outside the signal region (as seen on Figure 9.18) and will only contain background events. The background events can then be scaled such that the integral of events inside the selection region for the RUC background sample matches that of the data sample.

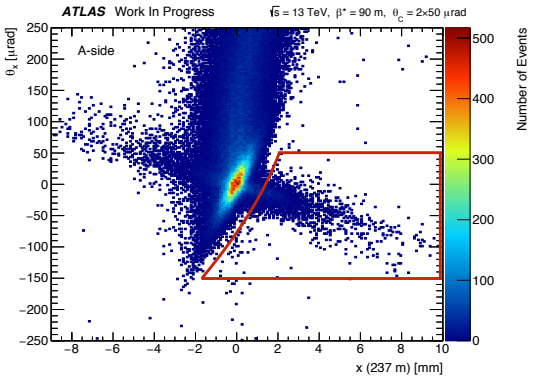

Figure 10.37: Correlation between the local angle θ_x and the near station hit x-coordinate for the selected data sample with the RUC selection region.

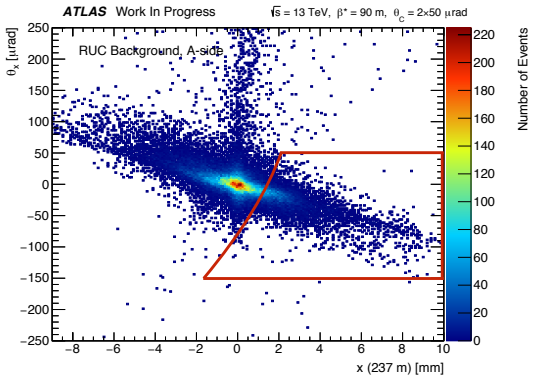

Figure 10.38: Correlation between the local angle θ_x and the near station hit x-coordinate for the RUC beam background sample with the RUC selection region.

Alternatively, the size of the beam background from RUCs can be estimated by considering events with a relative proton energy loss $\xi < -0.02$ as no single diffractive signal event will be in this region.

Once the RUC beam background has been correctly scaled relative to the data sample, the beam background can be subtracted from the data sample distributions. The resulting ξ and t distributions are shown in Figure 10.39 and 10.40.

While the RUC beam background can account for the events with $\xi < -0.02$ it can not account for all of the flat plateau at large ξ values. Nor can the beam background account for all of the observed discrepancy in data and simulation at large t values. The events with large ξ and t values are of particular interest as they are particularly sensitive to the Pomeron flux parameterization as seen in Section 9.1.

In the ξ distribution after beam background subtraction in Figure 10.39 it seems that the Gaussian shape around $\xi \simeq 0$ is slightly wider for data than for simulation. This could hint that the detector resolution of the far ALFA stations are larger than the estimated 40 μm due to energy-dependent shower effects from multiple scattering.

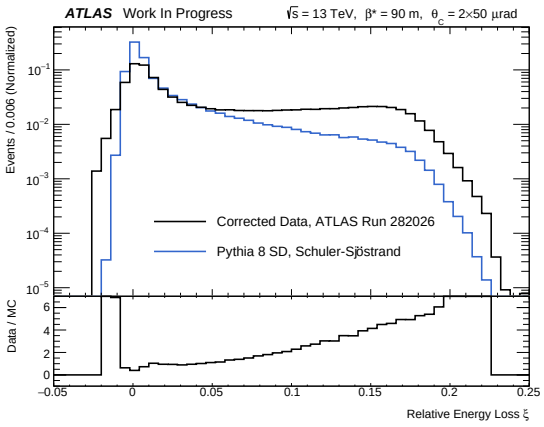

Figure 10.39: Distribution of the reconstructed ξ for data corrected for beam background compared to simulation with the Schuler-Sjöstrand parameterization.

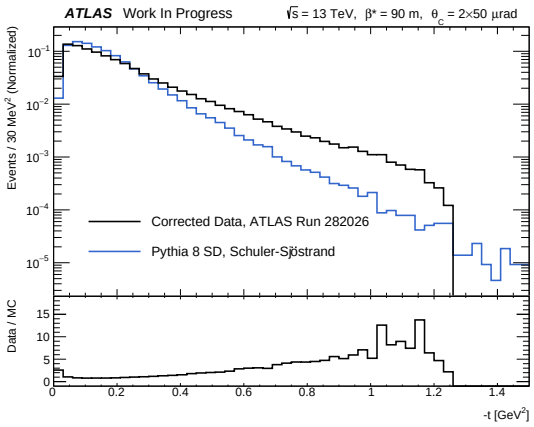

Figure 10.40: Distribution of the reconstructed t for data corrected for beam background compared to simulation with the Schuler-Sjöstrand parameterization.

10.7 BACKGROUND REDUCTION WITH LUCID

The pseudorapidity coverage of the LUCID detector is $5.6 < |\eta| < 5.9$ [80] while the ALFA detector covers $9 \lesssim |\eta| \lesssim 13$ (see Figure 8.39). Hence, a single diffractively scattered proton that hits the ALFA detector will not hit the LUCID detector as well. However, the spray of particles from the single diffractively dissociated system may hit the LUCID detector on the opposite side. This is illustrated in Figure 10.41.

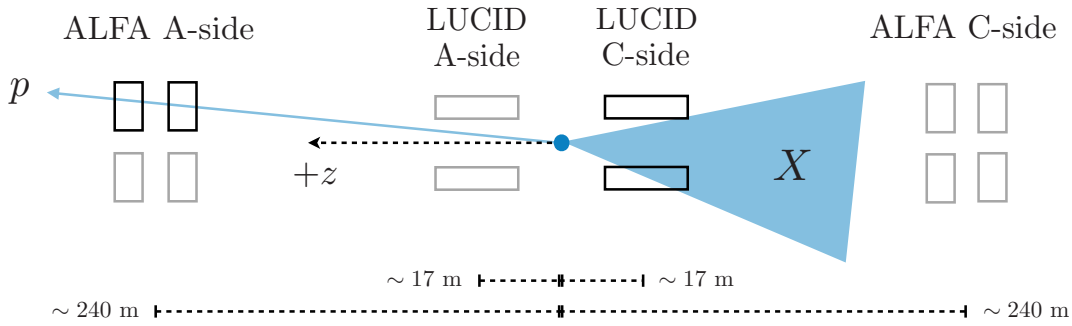

Figure 10.41: Simplified illustration of a single diffractive event signature in ALFA and LUCID.

In non-diffractive and double diffractive events with a reconstructed track in ALFA, there may be hits in LUCID on the same side as the ALFA hit, since we have sprays of particles in both directions. This is not expected in the single diffractive signal and a LUCID cut can therefore be used to remove background events.

After the MBTS selection, an extra cut has been imposed using the LUCID detector. The L1 trigger item `L1_LUCID` will pass for a given event if LUCID on either the A-side or the C-side has been fired during the event. When knowing on which side the ALFA detector was hit, we can use the combined LUCID and ALFA L1 trigger items,

`L1_LUCID_A_ALFA_C`,
`L1_LUCID_C_ALFA_A`

to see whether LUCID fired on the opposite side of the ALFA hit. If LUCID fired on the same side as the ALFA hit, the event is counted as background. If LUCID did not fire on either side then the event is discarded.

Let us first investigate the background events that are removed by the LUCID cut. The correlation between the local angle θ_x and the x-coordinate of the hit position in the near station for the LUCID background is shown in Figure 10.42. It is seen that some of the beam background is removed by the LUCID cut, as the secondary ellipse is present. The LUCID cut will also remove a significant portion of the diffractive 'banana' shape at higher θ_x values.

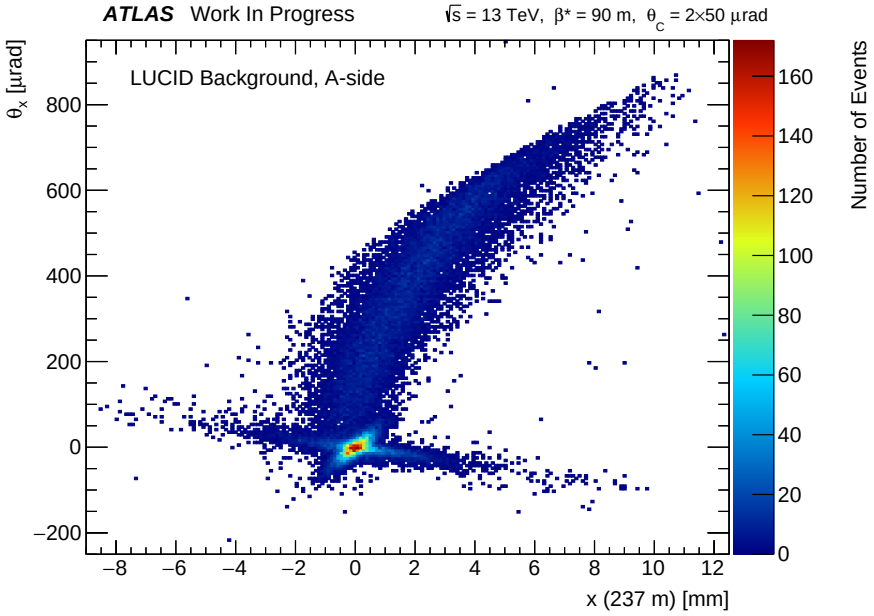

Figure 10.42: Correlation of the LUCID background hit x-coordinate versus the local angle θ_x for the A-side.

The distributions of the reconstructed ξ and t are shown in Figure 10.43 and 10.44 for the LUCID background events. The LUCID background seem to include some of the beam background with $\xi < -0.02$. Furthermore, the LUCID background may explain some

of the flat plateau observed at large ξ values. However, the LUCID background does not seem to be able to explain the background at large t values.

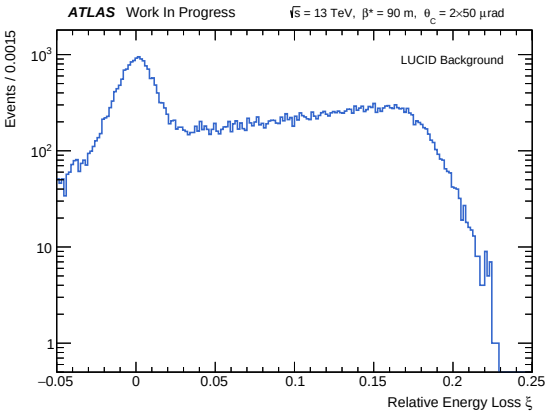

Figure 10.43: Distribution of the reconstructed ξ for the LUCID background.

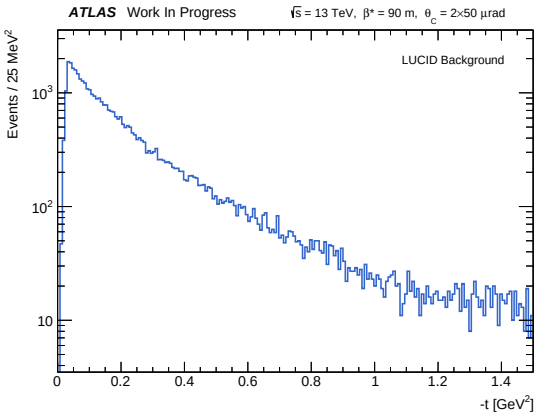

Figure 10.44: Distribution of the reconstructed t for the LUCID background.

The correlation between ξ and t for the LUCID background events is shown in Figure 10.45. Here the beam background 'boomerang' shape is visible along with a significant amount of events at $\xi \simeq 0$ and very low t values that may originate from beam background as well. Besides the beam background, the LUCID background also shows a very similar distribution of events to that of the non-diffractive and double diffractive background in Figure 9.21 and 9.22 with a large amount of events at large ξ and low t values.

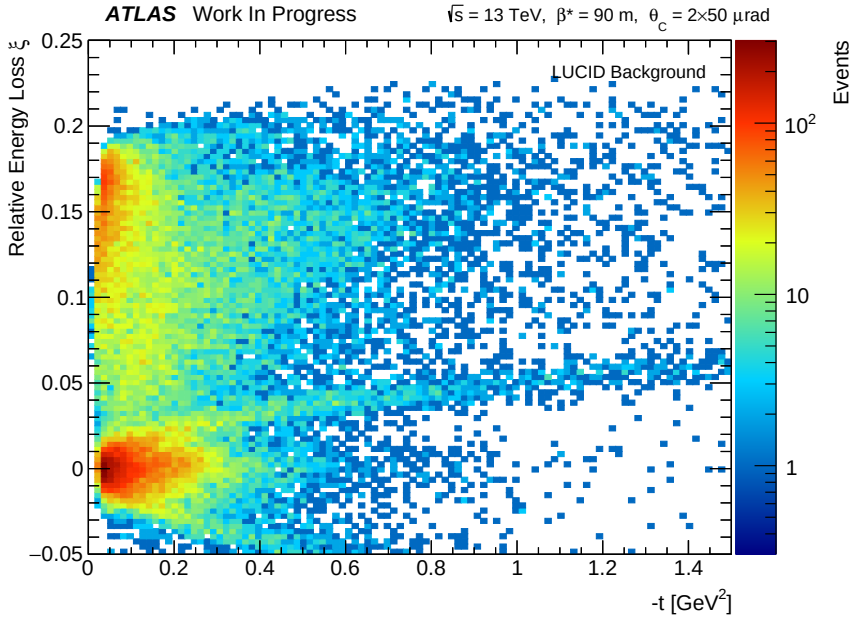

Figure 10.45: Correlation of the reconstructed ξ and t for the LUCID background.

The distributions of the reconstructed ξ and t of the selected single diffractive sample after the LUCID cut are shown in Figure 10.46 and 10.47. It is seen that the LUCID cut may not be strict enough and will not remove all of the expected background.

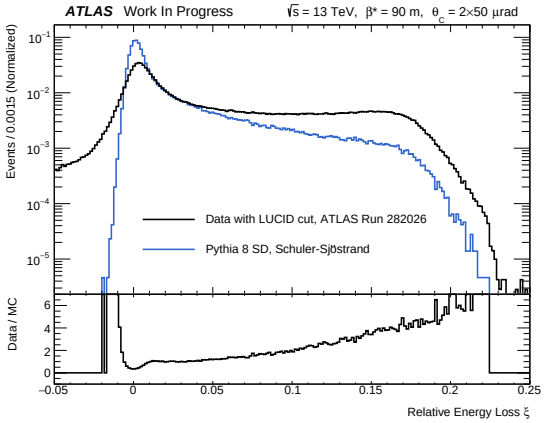

Figure 10.46: Distribution of the reconstructed ξ for data with the LUCID cut compared to simulated events.

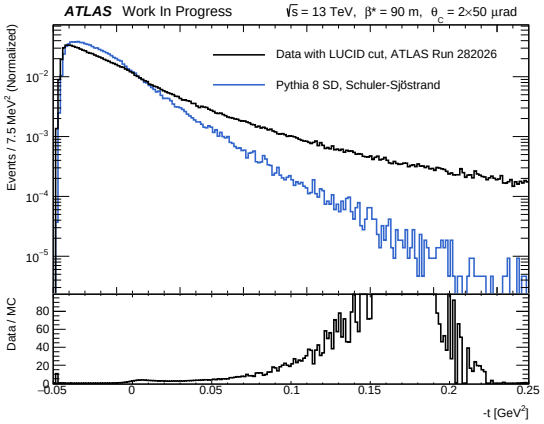

Figure 10.47: Distribution of the reconstructed t for data with the LUCID cut compared to simulated events.

The relative scale of the beam background from RUCs compared to the single diffractive signal could be estimated since the beam background was easily separated from the signal in the θ_x vs. x correlation plot (as well as in the ξ distribution). This made it possible to subtract the beam background from the data distributions.

The background causing the flat plateau for large ξ values may be caused by non-diffractive and double diffractive background events. Unfortunately, these background events are not easily separated from the signal events and hence the relative scale is not known. The LUCID cut may not be strict enough to remove the expected background. Since the exact cause and relative scale of the expected background at large ξ and t values is not known, the fit procedure to discern the Pomeron flux parameters can not be applied on data.

The flat plateau in ξ has been observed before at the ALFA detector for $\sqrt{s} = 8$ TeV [69, 81]. The flat plateau has also been observed at other experiments, such as the CERN ISR [82] and the CERN SPS [83] both around $\sqrt{s} = 540$ GeV. Hence, the flat plateau seems to be energy independent and could be a detector or accelerator effect.

10.8 ELECTROWEAK GAUGE BOSONS IN DIFFRACTIVE SYSTEMS

The common phenomenological approach to diffraction is based on the Ingelman-Schlein [5] approach of a Pomeron with a partonic substructure. In this view, the Pomeron often takes the form of a glue-ball state. Similar to the proton, the Pomeron would then, when probed at high energy, exhibit a sea of virtual quarks and gluons. Due to the possibility of virtual quarks in the Pomeron, diffractively dissociated systems may contain electroweak gauge bosons, $W^{\pm}$ and Z^0, as per the electroweak vertices, $q\bar{q} \rightarrow W^{\pm}/Z^0$, as shown in Figure 2.1. The production of W's and Z's in the diffractively dissociated proton will therefore be a sign of a partonic substructure of the Pomeron. The process is illustrated for single diffraction in the Feynman diagram of Figure 10.48.

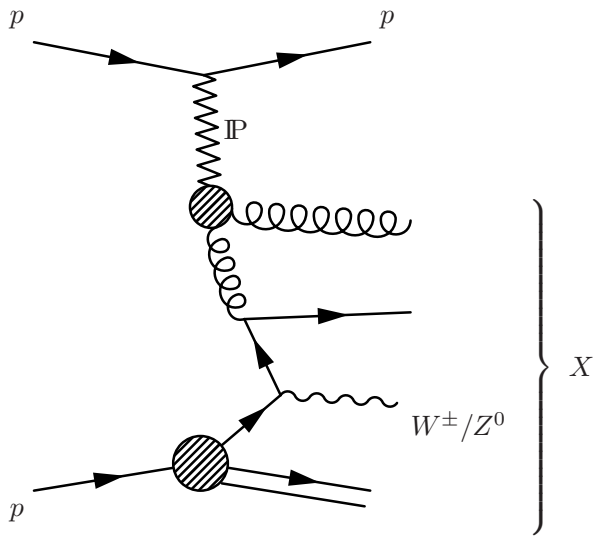

Figure 10.48: Feynman diagram of the production of a $W^{\pm}$ or Z^0 in a single diffractive pp event with a partonic Pomeron.

The existence and prevalence of W and Z bosons in the diffractively dissociated system can be studied by considering the distribution of the invariant mass M_X of the system and whether statistical significant 'bumps' (which can be fitted to Breit-Wigner distributions) at $m_Z \approx 91.2$ GeV and $m_W \approx 80.4$ GeV [14] are observed. However, the M_X distribution is bounded by the ξ acceptance of the ALFA detector. Furthermore, it is expected from Regge theory that the single diffractive cross-section follows a $1/M_X^2$ dependence so that high mass diffractively dissociated systems rarely occurs.

11 CONCLUDING REMARKS

11.1 SUMMARY AND OUTLOOK

The primary goal of this thesis has been to understand the effects of the phenomenological Pomeron flux parameterizations (available in the Monte Carlo event generator PYTHIA 8) on final-state observables in single diffractive events, in order to fit measured distributions leading to constraints on the Pomeron flux parameterizations and their allowed parameter space.

A fast detector response simulation of the ALFA and ATLAS detector has been developed for the purposes of studying diffractive pp scattering at $\sqrt{s} = 13$ TeV. The developed simulation framework is able to handle the beam transport of diffractively scattered protons. Knowledge about the magnetic lattice in the LHC beam pipe section between the ATLAS interaction point and the ALFA Roman Pots have been used to parameterize the hit position of the scattered proton in the ALFA detector in the transverse plane to the beam, as functions of the energy and the horizontal and vertical components of the interaction point and momentum. Furthermore, the simulation framework imposes the kinematic acceptance of the ALFA detector which was found to be approximately $\xi \lesssim 0.22$, with a pseudorapidity coverage of $9 \lesssim |\eta| \lesssim 13$.

The simulation framework has been used in a phenomenological study of single diffraction. The relative energy loss ξ was found to be the observable most sensitive to the Pomeron flux parameter ε while the transverse momentum p_T of the scattered proton was found to be the observable most sensitive to the α' parameter. Using this information, a statistical fit procedure to determine the Pomeron flux parameters has been developed and tested on several generated test samples. It was found that the developed fit procedure is generally able to estimate the parameters within at least 2σ of the uncertainty from the fit minimization for most of the test samples.

Data recorded at $\sqrt{s} = 13$ TeV, $\beta^* = 90$ m, and $\theta_C = 2 \times 50$ μrad at the ATLAS experiment in the Run 2 period has been analysed. Event selection cuts have been applied in order to obtain as clean and pure a single diffractive sample as possible. However, even after the event selection, several structures in the measured distributions from data indicates background not predicted by the simulation framework.

Background from beam related sources materialize as a secondary ellipse in the correlation between the local angle θ_x and the hit position $x_{237\,\mathrm{m}}$, and as a 'boomerang' shape in the correlation between the reconstructed ξ and t. It is possible to separate the beam background from the single diffractive signal in these two channels and thereby estimate the relative normalization in order to subtract the beam background.

In addition to the beam background, a flat plateau at large ξ values is observed which is expected to be a result of an observed 'cluster' and 'wing' structures in the correlation between the reconstructed ξ and t. These structures correspond to the expected shape of the double diffractive and non-diffractive background as mapped onto the kinematic acceptance of ALFA. However, the estimated size of the background from the simulation framework is not large enough to explain what is seen in data. It is possible that the simulation framework underestimates this background. This could be caused by the simulation framework not being able to transport negatively charged particles from the interaction point to the ALFA detectors. In addition, the expected single diffractive, double diffractive, and non-diffractive cross-sections in Equation 4.8 - 4.11 may differ from the actual cross-sections. Unfortunately, it has not been possible to find a channel in which this background could be separated from the single diffractive signal in order to estimate the relative normalization scale. Due to the large discrepancy between the shape of the simulated and measured distributions, it has not been possible to use the fit procedure on data. It may be possible to include the background normalization as a free parameter in the fit procedure along with ε and α'. The fit procedure could then, besides fitting the Pomeron flux parameterization, also estimate the size of the background.

The ALFA detector provides a great opportunity to study diffractive pp scattering at high energies. The data analysis presented in this thesis is still at a preliminary level. Effective optics and a final alignment using distance measurements from the overlap detectors will reduce systematic errors and improve the reconstruction of the proton kinematics. The use of reconstructed topo-cluster jets in the calorimeter in the event selection may reduce background. Finally, a full Monte Carlo simulation of the ALFA detector and the LHC magnetic lattice between the interaction point and the ALFA Roman Pots will make it possible to properly study the beam background as well as the double diffractive and non-diffractive background.

11.2 PROSPECTS OF FURTHER RESEARCH

High-p_T interactions with the production of heavy resonances and/or hard QCD jets are the main interest of many studies at both ATLAS and CMS. But the possibility of tagging protons in the extreme forward direction with the ALFA detector (or alternatively the TOTEM experiment [84] at IP5) opens up for a lot of potential studies of soft QCD processes such as diffractive scattering. A potential prospect of further research into diffractive pp-scattering is the study of *multiple rapidity gaps* in single diffractive events.

In a normal single diffractive event, the dissociated system of particles is expected to behave as essentially a non-diffractive event, where any smaller rapidity gaps within the system are expected to be exponentially suppressed. However, if we allow for the possibility of double pomeron exchange in single diffractive events, we should be able to observe an additional rapidity gap in the system. This is illustrated in the Feynman diagram in Figure 11.1 along with the expected final-state. Studying the second largest rapidity gap in single diffractive events in data could give information on the nature of the Pomeron as well as the factorization of the single diffractive cross-section with regard to the Pomeron flux factor.

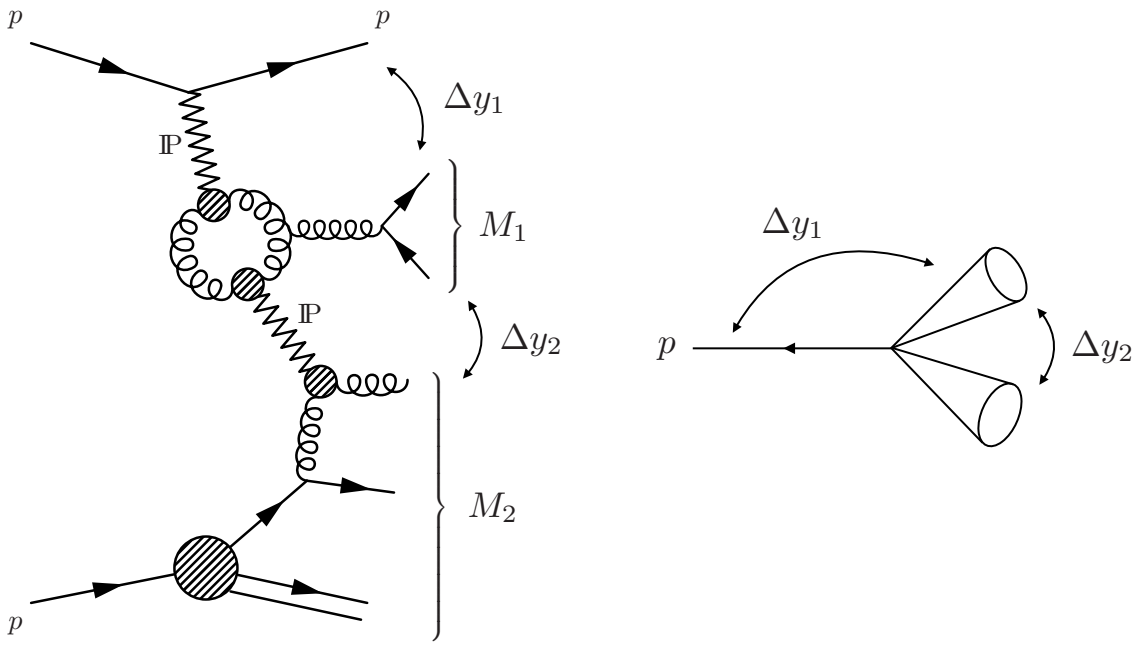

Figure 11.1: Left: Possible Feynman diagram of a single diffractive event with double pomeron exchange. Right: Final-state of a single diffractive event with two rapidity gaps.

Part V

APPENDIX

A

BEAM TRANSPORT PARAMETERS

The parameterization of the u-coordinate ($u = \{x, y\}$) of the proton at the ALFA Roman Pots can be written as

$$u_{\mathrm{RP}}\left(u_{\mathrm{IP}}, \frac{p_{u,\,\mathrm{IP}}}{p}, \frac{\Delta p}{p}\right) = F_u\left(\frac{\Delta p}{p}\right) \cdot u_{\mathrm{IP}} + G_u\left(\frac{\Delta p}{p}\right) \cdot \left[\frac{p_{u,\,\mathrm{IP}}}{p}\right] + H_u\left(\frac{\Delta p}{p}\right) \tag{A.1}$$

where F_u, G_u, and H_u are all functions of the momentum loss $\frac{\Delta p}{p}$,

$$F_u\left(\frac{\Delta p}{p}\right) = f_{u,\,0} + f_{u,\,1} \cdot \left(\frac{\Delta p}{p}\right) + f_{u,\,2} \cdot \left(\frac{\Delta p}{p}\right)^2 + f_{u,\,3} \cdot \left(\frac{\Delta p}{p}\right)^3 + f_{u,\,4} \cdot \left(\frac{\Delta p}{p}\right)^4 \tag{A.2}$$

and

$$G_u\left(\frac{\Delta p}{p}\right) = g_{u,\,0} + g_{u,\,1} \cdot \left(\frac{\Delta p}{p}\right) + g_{u,\,2} \cdot \left(\frac{\Delta p}{p}\right)^2 + g_{u,\,3} \cdot \left(\frac{\Delta p}{p}\right)^3 + g_{u,\,4} \cdot \left(\frac{\Delta p}{p}\right)^4 \tag{A.3}$$

and

$$H_u\left(\frac{\Delta p}{p}\right) = h_{u,\,0} + h_{u,\,1} \cdot \left(\frac{\Delta p}{p}\right) + h_{u,\,2} \cdot \left(\frac{\Delta p}{p}\right)^2 + h_{u,\,3} \cdot \left(\frac{\Delta p}{p}\right)^3 + h_{u,\,4} \cdot \left(\frac{\Delta p}{p}\right)^4 \tag{A.4}$$

Giving in total 30 parameters for each station and beam setting. The parameters are listed in Table A.1 and A.2. Note that the units and uncertainties on the parameters are not listed.

Table A.1: Beam transport parameters for $\theta_C = 0$ μrad.

$\sqrt{s} = 13$ TeV, $\beta^* = 90$ m, $\theta_C = 0$ μrad				
	Station 1: A245	Station 2: A237	Station 3: C237	Station 4: C245
$f_{x,0}$	-1.0922	-1.2399	-1.2400	-1.0922
$f_{x,1}$	3.8050	2.6336	2.6333	3.8044
$f_{x,2}$	10.463	7.8948	7.8920	10.467
$f_{x,3}$	14.747	11.499	11.488	14.744
$f_{x,4}$	9.9386	7.0032	7.0585	9.7079
$g_{x,0}$	-1.5727×10^4	-1.0293×10^4	-1.0292×10^4	-1.5725×10^4
$g_{x,1}$	-7.9407×10^4	-8.8003×10^4	-8.8004×10^4	-7.9399×10^4
$g_{x,2}$	2.3461×10^5	1.6264×10^5	1.6260×10^5	2.3454×10^5
$g_{x,3}$	4.7062×10^5	3.4906×10^5	3.4901×10^5	4.7083×10^5
$g_{x,4}$	1.7591×10^6	1.2619×10^6	1.2615×10^6	1.7575×10^6
$h_{x,0}$	2.6980×10^{-4}	1.9743×10^{-4}	1.7418×10^{-4}	2.6463×10^{-4}
$h_{x,1}$	10.830	-5.0019	-5.0039	10.825
$h_{x,2}$	1.6609×10^2	1.1428×10^2	1.1419×10^2	1.6605×10^2
$h_{x,3}$	2.4108×10^2	1.7271×10^2	1.7315×10^2	2.4106×10^2
$h_{x,4}$	1.1875×10^3	8.2300×10^2	8.2161×10^2	1.1870×10^3
$f_{y,0}$	-2.1014×10^{-2}	9.7387×10^{-3}	9.7317×10^{-3}	-2.1011×10^{-2}
$f_{y,1}$	-10.716	-11.779	-11.781	-10.719
$f_{y,2}$	-23.104	-27.260	-27.266	-23.114
$f_{y,3}$	-27.132	-40.286	-40.301	-27.158
$f_{y,4}$	-78.576	-1.1735×10^2	-1.1735×10^2	-78.646
$g_{y,0}$	2.5231×10^5	2.7781×10^5	2.7784×10^5	2.5238×10^5
$g_{y,1}$	-3.6878×10^5	-3.4770×10^5	-3.4770×10^5	-3.6877×10^5
$g_{y,2}$	-7.9352×10^5	-8.7960×10^5	-8.7974×10^5	-7.9409×10^5
$g_{y,3}$	-1.0256×10^6	-1.1317×10^6	-1.1315×10^6	-1.0226×10^6
$g_{y,4}$	-2.3563×10^6	-4.0249×10^6	-4.0273×10^6	-2.3696×10^6
$h_{y,0}$	0	0	0	0
$h_{y,1}$	0	0	0	0
$h_{y,2}$	0	0	0	0
$h_{y,3}$	0	0	0	0
$h_{y,4}$	0	0	0	0

Table A.2: Beam transport parameters for $\theta_C = 2 \times 50$ μrad.

$\sqrt{s} = 13$ TeV, $\beta^* = 90$ m, $\theta_C = 2 \times 50$ μrad				
	Station 1: A245	Station 2: A237	Station 3: C237	Station 4: C245
$f_{x,0}$	-1.0922	-1.2399	-1.2400	-1.0922
$f_{x,1}$	3.8047	2.6338	2.6332	3.8038
$f_{x,2}$	10.468	7.8929	7.8914	10.472
$f_{x,3}$	14.759	11.493	11.493	14.760
$f_{x,4}$	9.7578	7.0732	7.0727	9.5396
$g_{x,0}$	-1.5727×10^4	-1.0293×10^4	-1.0292×10^4	-1.5725×10^4
$g_{x,1}$	-7.9406×10^4	-8.8003×10^4	-8.8004×10^4	-7.9399×10^4
$g_{x,2}$	2.3458×10^5	1.6263×10^5	1.6260×10^5	2.3454×10^5
$g_{x,3}$	4.7097×10^5	3.4911×10^5	3.4904×10^5	4.7088×10^5
$g_{x,4}$	1.7580×10^6	1.2617×10^6	1.2615×10^6	1.7574×10^6
$h_{x,0}$	2.7749×10^{-4}	1.8427×10^{-4}	1.7775×10^{-4}	2.7497×10^{-4}
$h_{x,1}$	10.829	-5.0010	-5.0051	10.825
$h_{x,2}$	1.6610×10^2	1.1426×10^2	1.1422×10^2	1.6606×10^2
$h_{x,3}$	2.4100×10^2	1.7283×10^2	1.7294×10^2	2.4103×10^2
$h_{x,4}$	1.1877×10^3	8.2271×10^2	8.2217×10^2	1.1871×10^3
$f_{y,0}$	-2.1037×10^{-2}	9.7374×10^{-3}	9.7521×10^{-3}	-2.1007×10^{-2}
$f_{y,1}$	-10.715	-11.779	-11.781	-10.719
$f_{y,2}$	-23.110	$-27.261e$	-27.263	-23.113
$f_{y,3}$	-27.146	-40.286	-40.287	-27.155
$f_{y,4}$	-78.444	-1.1734×10^2	-1.1746×10^2	-78.672
$g_{y,0}$	2.5231×10^5	2.7781×10^5	2.7784×10^5	2.5238×10^5
$g_{y,1}$	-3.6878×10^5	-3.4770×10^5	-3.4770×10^5	-3.6877×10^5
$g_{y,2}$	-7.9385×10^5	-8.7959×10^5	-8.7970×10^5	-7.9409×10^5
$g_{y,3}$	-1.0223×10^6	-1.1318×10^6	-1.1319×10^6	-1.0226×10^6
$g_{y,4}$	-2.3663×10^6	-4.0246×10^6	-4.0261×10^6	-2.3694×10^6
$h_{y,0}$	13.708	15.087	15.089	13.712
$h_{y,1}$	12.555	17.015	16.977	12.539
$h_{y,2}$	9.1016	17.697	17.627	9.0876
$h_{y,3}$	-8.7326	2.5076	2.4771	-8.6634
$h_{y,4}$	4.3438	35.585	35.358	4.3734

B

DISTRIBUTIONS

B.1 ACCEPTANCE PLOTS IN ξ, p_x, AND p_y FOR $\theta_C = 2 \times 50$ μRAD

Below are the 2D projections of the LHC and ALFA acceptance plots in ξ, p_x, and p_y. Notice that p_x and p_y are in the LHC coordinate system. Hence, the beam is at $p_x = 0$ and $p_y = -0.325$ GeV.

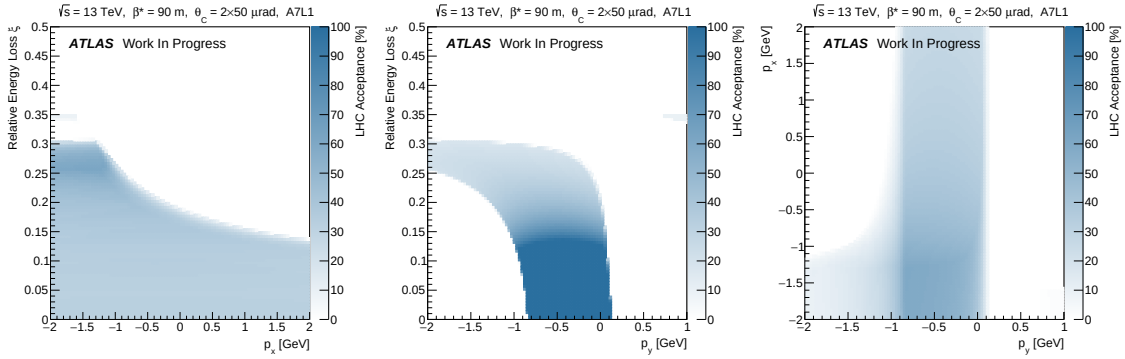

(a) ξ vs. p_x. **(b)** ξ vs. p_y. **(c)** p_x vs. p_y.

Figure B.1: Two-dimensional projections of the LHC acceptance plots for $\theta_C = 2 \times 50$ μrad.

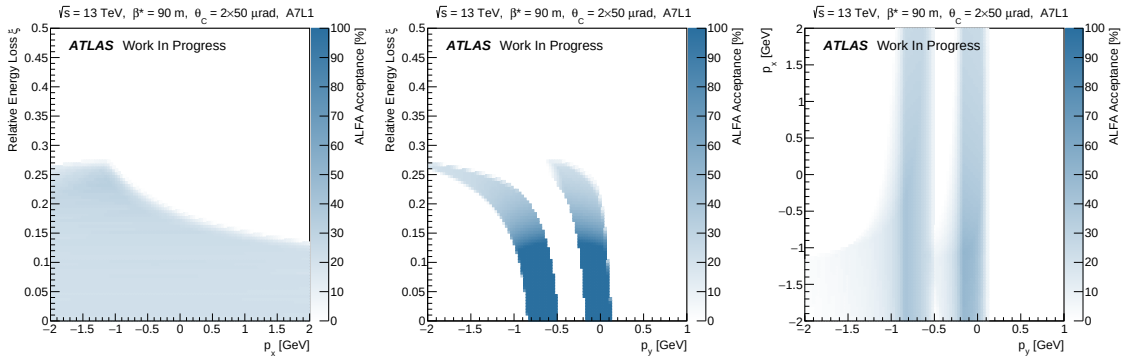

(a) ξ vs. p_x. **(b)** ξ vs. p_y. **(c)** p_x vs. p_y.

Figure B.2: Two-dimensional projections of the ALFA acceptance plots for $\theta_C = 2 \times 50$ μrad.

B.2 OBSERVABLES SENSITIVE TO MODEL PARAMETERS

The sensitivity plots for the absolute pseudorapidity $|\eta|$ of the diffractively scattered proton are shown in Figure B.3. It is seen that $|\eta|$ is primarily sensitive to α'.

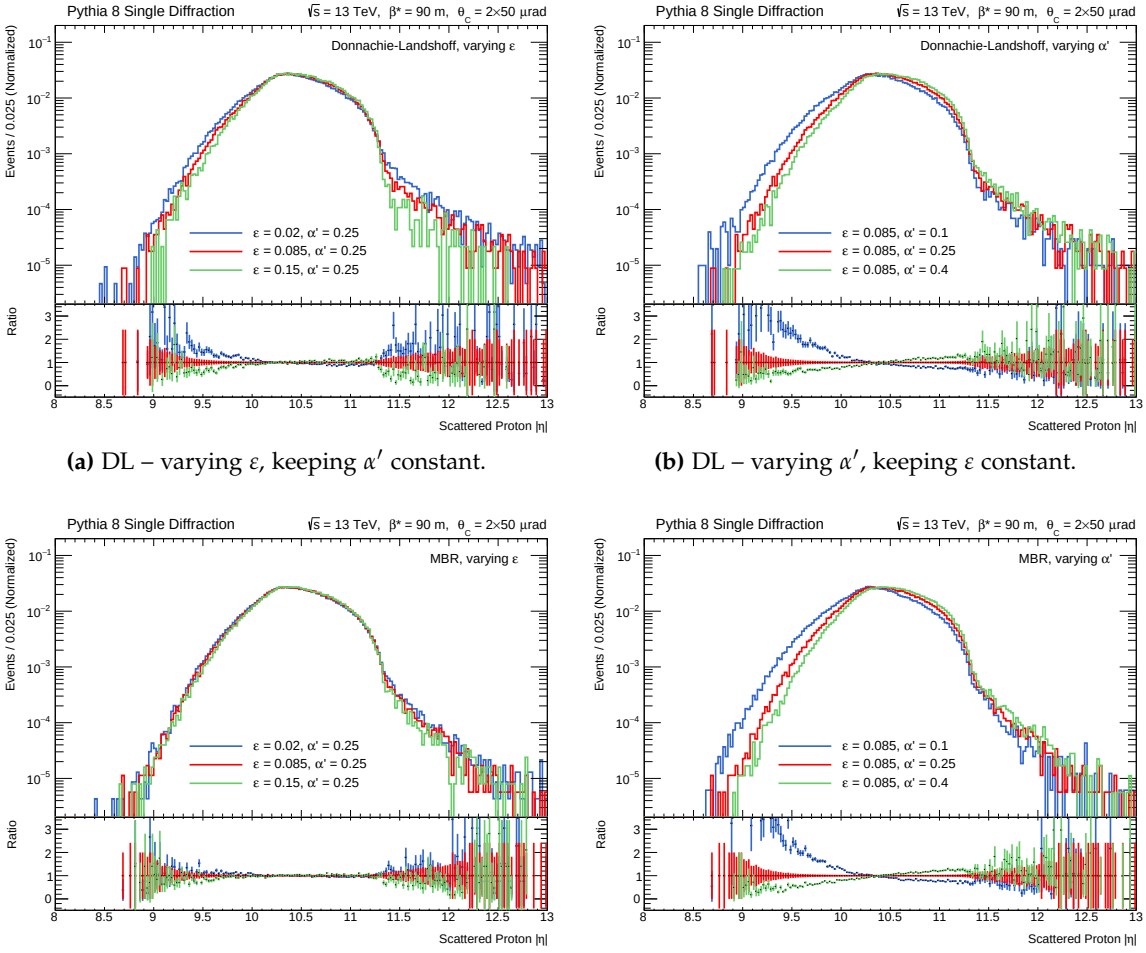

(a) DL – varying ε, keeping α' constant.

(b) DL – varying α', keeping ε constant.

(c) MBR – varying ε, keeping α' constant.

(d) MBR – varying α', keeping ε constant.

Figure B.3: Absolute pseudorapidity $|\eta|$ distributions for different values of the model parameters, ε and α'.

The sensitivity plots for the charged multiplicity n_{ch} in the diffractively dissociated system are shown in Figure B.4. It is seen that n_{ch} is primarily sensitive to ε, especially at low multiplicities.

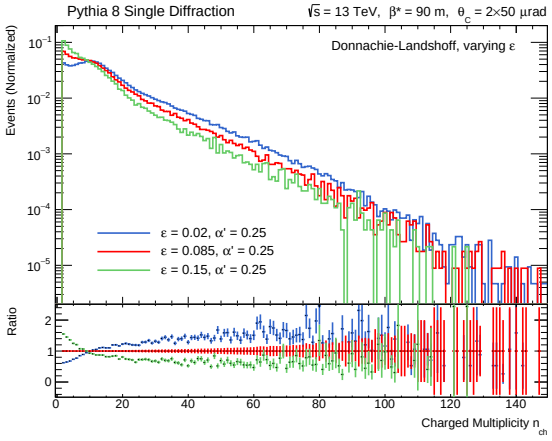

(a) DL – varying ε, keeping α' constant.

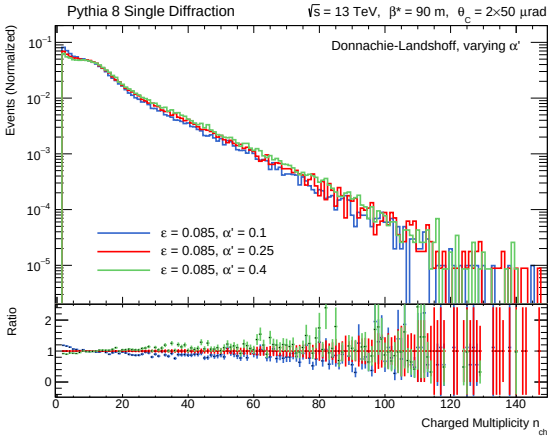

(b) DL – varying α', keeping ε constant.

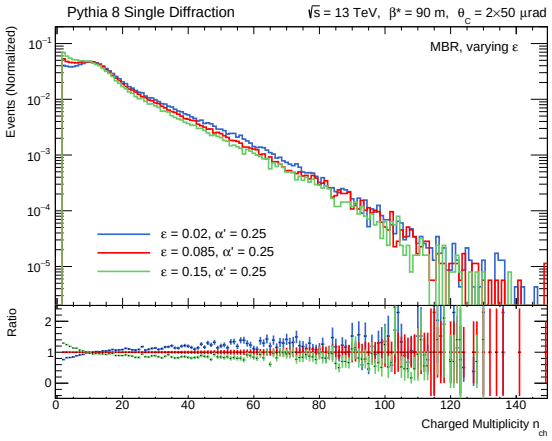

(c) MBR – varying ε, keeping α' constant.

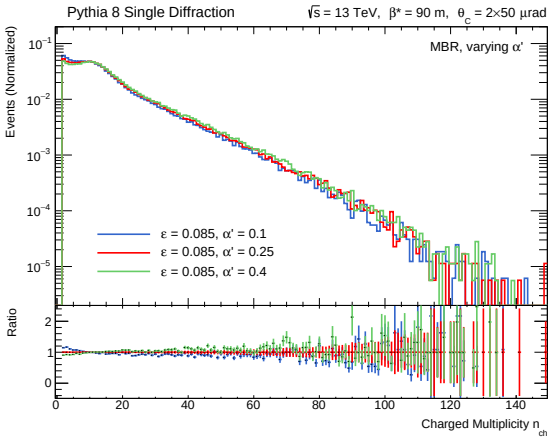

(d) MBR – varying α', keeping ε constant.

Figure B.4: Charged multiplicity n_{ch} distributions for different values of the model parameters, ε and α'.

B.3 COMPARISON PLOTS OF DATA AND SIMULATION

Additional final-state distributions for selected single diffractive events in data run 282026 are shown in Figure B.5 - B.8. The data distributions are plotted alongside simulated single diffractive events with the Schuler-Sjöstrand Pomeron flux parameterizations. Note that discrepancies between data and simulation may be explained by background as explained in Chapter 10.

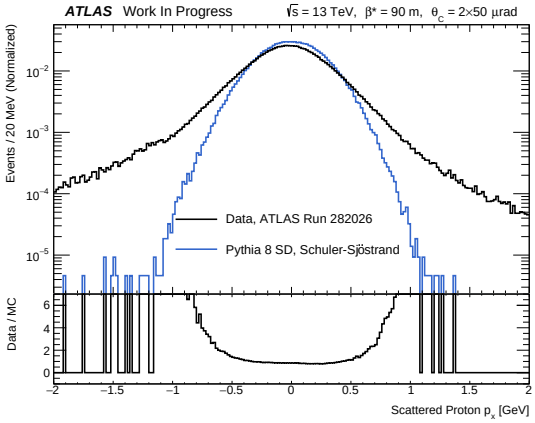

Figure B.5: Distribution of the reconstructed p_x for data and simulation with the Schuler-Sjöstrand parameterization.

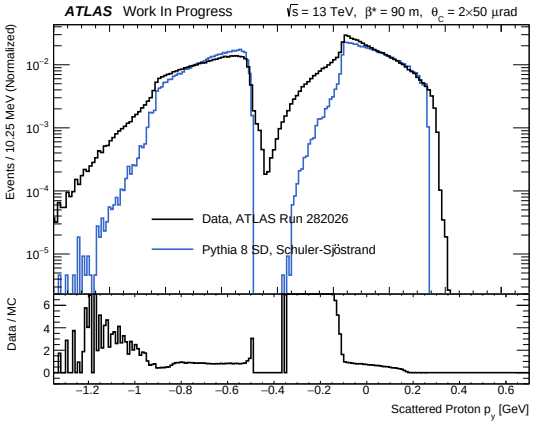

Figure B.6: Distribution of the reconstructed p_y for data and simulation with the Schuler-Sjöstrand parameterization.

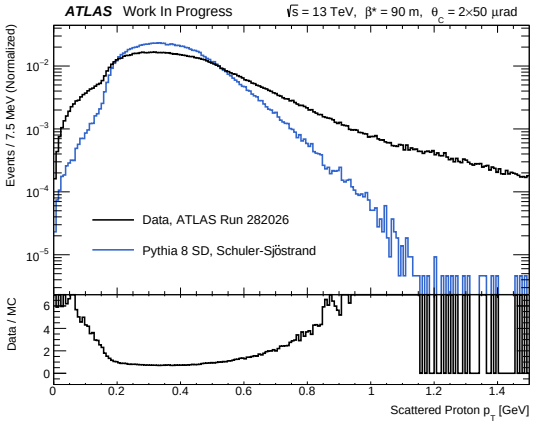

Figure B.7: Distribution of the reconstructed p_T for data and simulation with the Schuler-Sjöstrand parameterization.

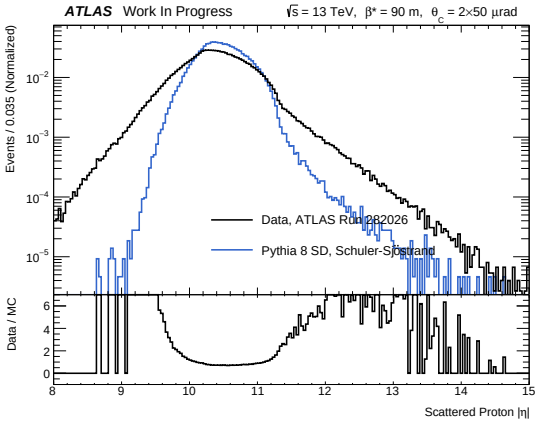

Figure B.8: Distribution of the reconstructed $|\eta|$ for data and simulation with the Schuler-Sjöstrand parameterization.

BIBLIOGRAPHY

[1] Quote by J. D. Bjorken. From a talk given at the 75th anniversary celebration of the Max-Planck Institute of Physics, Munich, Germany, December 10th, 1992. As quoted in: Beam Line, Winter 1992, Vol. 22, No. 4.

[2] A. Hobson. *Tales of the Quantum: Understanding Physics' Most Fundamental Theory*. First Edition. Oxford University Press, 2017.

[3] ATLAS Collaboration. *Observation of a new particle in the search for the Standard Model Higgs boson with the ATLAS detector at the LHC*. Phys. Lett. B 716 (2012) 1. [arXiv:1207.7214v2 [hep-ex]].

[4] CMS Collaboration. *Observation of a new boson at a mass of 125 GeV with the CMS experiment at the LHC*. Phys. Lett. B 716 (2012) 30. [arXiv:1207.7235v2 [hep-ex]].

[5] G. Ingelman and P. Schlein. *Jet Structure in High Mass Diffractive Scattering*. Phys. Lett. B152 (1985) 256.

[6] T. Sjöstrand, S. Mrenna, and P. Skands. *PYTHIA 6.4 Physics and Manual* and *A Brief Introduction to PYTHIA 8.1*. JHEP05 (2006) 026, Comput. Phys. Comm. 178 (2008) 852.

[7] A. Buckley, J. Butterworth, D. Grellscheid, H. Hoeth, L. Lonnblad, J. Monk, H. Schulz, F. Siegert. *Rivet user manual*. February, 2013. [arXiv:1003.0694v8 [hep-ph]]. https://rivet.hepforge.org/.

[8] D. Griffiths. *Introduction to Elementary Particles*. Second, Revised Edition. Wiley-VCH, 2008.

[9] M. Thomson. *Modern Particle Physics*. First Edition. Cambridge University Press, 2013.

[10] B. R. Martin and G. Shaw. *Particle Physics*. Manchester Physics series. John Wiley and Sons, Ltd, 3rd edition, 2008.

[11] M. Srednicki. *Quantum Field Theory*. 8th printing, Cambridge University Press, 2014.

[12] M. E. Peskin and D. V. Schroeder. *An Introduction to Quantum Field Theory*. Westview Press, 1995.

[13] P. Skands. *Introduction to QCD*. January, 2015. [arXiv:1207.2389v4 [hep-ph]].

[14] C. Patrignani et al. (Particle Data Group). *Review of Particle Physics*. Chin. Phys. C, 40, 100001 (2016).

[15] S. Bethke. *Experimental Tests of Asymptotic Freedom*. June, 2006. Prog. Part. Nucl. Phys. 58:351-386. [arXiv:hep-ex/0606035v2].

[16] D. Green. *High PT Physics at Hadron Colliders*. Cambridge Monographs on Particle Physics, Nuclear Physics, and Cosmology 22. Cambridge University Press, 2005.

[17] T. Sjöstrand. Particle Physics Phenomenology. Lecture slides, Lund University, 2015. http://home.thep.lu.se/~torbjorn/ppp2015.html.

[18] A. Buckley, et al. *General-purpose event generators for LHC physics*. January, 2011. [arXiv:1101.2599v1 [hep-ph]].

[19] J. M. Campbell, J. W. Huston, and W. J. Stirling. *Hard Interactions of Quarks and Gluons: a Primer for LHC Physics*. Rept. Prog. Phys. 70:89, 2007. [arXiv:hep-ph/0611148v1].

[20] M. Bahr, et al. *Herwig++ Physics and Manual*. Eur. Phys. J. C58:639-707, 2008. [arXiv:0803.0883v3 [hep-ph]].

[21] T. Gleisberg, et al. *Event generation with SHERPA 1.1*. JHEP 0902:007, 2009. [arXiv:0811.4622v1 [hep-ph]].

[22] B. Andersson, G. Gustafson, G. Ingelman and T. Sjöstrand. *Parton Fragmentation and String Dynamics*. Phys. Rep. 97 (1983) 31.

[23] B. R. Webber. *A QCD Model for Jet Fragmentation including Soft Gluon Interference*. Nucl. Phys. B238 (1984) 492.

[24] V. Barone and E. Predazzi. *High-Energy Particle Diffraction*. Springer, Heidelberg, Germany, 2002.

[25] E. Predazzi. *Diffraction: Past, Present and Future*. Lectures given at Hadrons VI, Florianopolis, Brazil, March 1998. [arXiv:hep-ph/9809454v1].

[26] P. D. B. Collins. *An Introduction to Regge Theory and High Energy Physics*. Cambridge Monographs on Mathematical Physics, Cambridge University Press, 1977.

[27] A. Donnachie, H. G. Dosch, P. V. Landshoff, and O. Nachtmann. *Pomeron Physics and QCD*. Cambridge Monographs on Particle Physics, Nuclear Physics, and Cosmology, Cambridge University Press, 2002.

[28] J. C. Collins. *Light-cone Variables, Rapidity and All That*. May, 1997. [arXiv:hep-ph/9705393v1].

[29] S. Navin. *Diffraction in PYTHIA*. May, 2010. LUTP-09-23, MCnet/10/09. [arXiv:1005.3894v1 [hep-ph]].

[30] G. A. Schuler and T. Sjöstrand. *Hadronic diffractive cross sections and the rise of the total cross section*. March, 1994. Phys. Rev. D 49, 2257.

[31] M. L. Good and W. D. Walker. *Diffraction Dissociation of Beam Particles*. Phys. Rev. 120, 1857. December, 1960.

[32] A. T. Doyle. *Diffraction: QCD Effects in Colour Singlet Exchange*. Talk presented at the 25th SLAC Summer Institute, SLAC. August 1997. Preprint available at: http://www.ppe.gla.ac.uk/preprints/97/13/.

[33] A. Donnachie and P. V. Landshoff. *Total Cross Sections*. Phys. Lett. B 296 (1992) 227-232. [arXiv:hep-ph/9209205v1].

[34] D. A. Fagundes, M. J. Menon, and P. V. R. G. Silva. *Bounds on the rise of total cross section from LHC7 and LHC8 data*. March, 2017. [arXiv:1703.07486v1 [hep-ph]].

[35] A. Donnachie and P. V. Landshoff. *pp and $\overline{p}p$ Elastic Scattering*. January, 1984. Nucl. Phys. B231 (1984) 189.

[36] M. Arneodo. *Nuclear effects in structure functions*. May, 1994. Physics Reports 240 (1994) 301—393.

[37] C. O. Rasmussen and T. Sjöstrand. *Hard Diffraction with Dynamic Gap Survival*. JHEP 1602 (2016) 142. [arXiv:1512.05525v1 [hep-ph]].

[38] C. O. Rasmussen. *Hard Diffraction in Pythia 8*. December, 2015. [arXiv:1512.05872v1 [hep-ph]].

[39] R. Ciesielski, and K. Goulianos. *MBR Monte Carlo Simulation in PYTHIA8*. August, 2012. [arXiv:1205.1446v2 [hep-ph]].

[40] O. S. Brüning, P. Collier, P. Lebrun, S. Myers, R. Ostojic, J. Poole, and P. Proudlock. *LHC Design Report*. CERN, Geneva, 2004. CERN-2004-003-V-1. [CDS:782076].

[41] L. Evans and P. Bryant (editors). *LHC Machine*. JINST, **3** S08001, 2008. [inSPIRE:796247].

[42] P. Hansen. *Particle Detectors and Accelerators. Lecture Notes*. Second Edition. University of Copenhagen, September, 2015.

[43] J. Rossbach and P. Schmüser. *Basic Course on Accelerator Optics*. Conf. Proc. C9209071 (1992) 17-88. [inSPIRE:347558].

[44] S. Baird. *Accelerators for Pedestrians*. AB-Note-2007-014. CERN-AB-Note-2007-014. PS-OP-Note-95-17-Rev-2. CERN-PS-OP-Note-95-17-Rev-2. CERN, Geneva, 2007. [CDS:1017689].

[45] The public results of ATLAS luminosity measurements. https://twiki.cern.ch/twiki/bin/view/AtlasPublic/LuminosityPublicResults.

[46] ATLAS Collaboration. *Pile-up subtraction and suppression for jets in ATLAS*. August, 2013. ATLAS-CONF-2013-083. [CDS:1570994].

[47] The ATLAS Run Query page. https://atlas-runquery.cern.ch/.

[48] ATLAS Beam Spot page. https://atlas-beamspot.cern.ch/jobfiles/data15_13TeV.00282026.express_express/DB_BEAMSPOT.x354_c870/data15_13TeV.00282026.express_express-DB_BEAMSPOT.x354_c870.PlotBeamSpot.pdf.

[49] S. H. Stark. *Study of forward elastic pp scattering at $\sqrt{s} = 8$ TeV with the ALFA detector*. January, 2017. PhD Thesis, Niels Bohr Institute, University of Copenhagen.

[50] G. Baud, B. Dehning, J. Emery, J-J. Gras, A. Guerrero, E. Piselli. *Performance Assessment of Wire-Scanners at CERN*. September, 2013. CERN-ACC-2013-0308. [CDS:1638354].

[51] LHC eLogBook. https://op-webtools.web.cern.ch/elogbook/?lgbk%5B%5D=60.

[52] ATLAS Collaboration. *The ATLAS Experiment at the CERN Large Hadron Collider*. JINST, **3** S08003, 2008. [inSPIRE:796888].

[53] ATLAS Collaboration. *Measurement of the total cross section from elastic scattering in pp collisions at $\sqrt{s} = 7$ TeV with the ATLAS detector*. [arXiv:1408.5778v2 [hep-ex]].

[54] H. Grote, F. Schmidt, L. Deniau, G. Roy. *The MAD-X Program (Methodical Accelerator Design) Version 5.02.09 User's Reference Manual*. April, 2016. http://mad.web.cern.ch/mad/.

[55] GEANT4 Collaboration. *Nuclear Instruments and Methods in Physics Research*. A 506 (2003) 250-303. *IEEE Transactions on Nuclear Science*. 53 No. 1 (2006) 270-278. *Nuclear Instruments and Methods in Physics Research*. A 835 (2016) 186-225. http://geant4.cern.ch/.

[56] CMS Collaboration. *The CMS experiment at the CERN LHC*. JINST, **3** S08004, 2008. [inSPIRE:796887].

[57] ATLAS IBL Community for the ATLAS Collaboration. *ATLAS Insertable B-Layer Technical Design Report*. September, 2010. CERN-LHCC-2010-013. ATLAS-TDR-19. [CDS:1291633].

[58] F. Meloni, A. Milov, S. Pagan-Griso, K. Prokofiev, A. Wildauer. *Vertexing Performance Data vs MC comparison for LPCC*. September, 2011. ATL-COM-PHYS-2011-1312. https://atlas.web.cern.ch/Atlas/GROUPS/PHYSICS/IDTRACKING/PublicPlots/ATL-COM-PHYS-2012-474/.

[59] R. E. Kwee. *Development and Deployment of an Inner Detector Minimum Bias Trigger and Analysis of Minimum Bias Data of the ATLAS Experiment at the Large Hadron Collider*. September, 2011. PhD Thesis, Humboldt-Universität zu Berlin.

[60] ATLAS Collaboration. *ATLAS Forward Detectors for Measurement of Elastic Scattering and Luminosity*. Technical Design Report. CERN-LHCC-2008-004. CERN, 2008. [CDS:1095847].

[61] S. Jakobsen, P. Fassnacht, P. Hansen, and J. B. Hansen. *Commissioning of the Absolute Luminosity For ATLAS detector at the LHC*. December, 2013. PhD Thesis, Niels Bohr Institute, University of Copenhagen. [CDS:1637195].

[62] S. Jakobsen. *Upgrade of ATLAS-ALFA for Run2*. ATLAS Slides, 2016. ATL-FWD-SLIDE-2016-267. [CDS:2156404].

[63] ATLAS Collaboration. *ATLAS Forward Detectors for Measurement of Elastic Scattering and Luminosity – Technical Design Report*. January, 2008. ATLAS-TDR-18. CERN-LHCC-2008-004. [CDS:1095847].

[64] Webpage for ATLAS research in Giessen by H. Stenzel. February, 2007. Accessed on April, 2017. http://www.physik.uni-giessen.de/atlas/research.htm.

[65] M. Dobbs, J. B. Hansen, L. Garren, L. Sonnenschein. *HepMC 2: a C++ Event Record for Monte Carlo Generators*. May, 2010. http://lcgapp.cern.ch/project/simu/HepMC/. https://hepmc.web.cern.ch/hepmc/.

[66] K. Kreutzfeldt. *Measurement of elastic proton-proton scattering at $\sqrt{s} = 7$ TeV with the ALFA sub-detector of ATLAS at the LHC*. December, 2014. PhD Thesis, Physikalisches Institut, Justus-Liebig-Universität Gießen.

[67] M. Trzebiński on behalf of the ATLAS Collaboration. *Towards a Total Cross Section Measurement with the ALFA Detector at ATLAS*. September, 2014. Acta Physica Polonica B, vol. 44 (2013), p. 1623-1628. [arXiv:1409.4866v1 [physics.ins-det]].

[68] F. Pfeiffer. *Simulation of the ATLAS ALFA detector in comparison with testbeam data*. May, 2010. CERN-THESIS-2010-112. [CDS:1291227].

[69] S. S. Mortensen. *Kinematic reconstruction of diffractive processes – with tagged protons in the ALFA detector at* $\sqrt{s} = 8$ *TeV*. August, 2013. Master's Thesis, Niels Bohr Institute, University of Copenhagen.

[70] F. James and M. Winkler. *Minuit User's Guide*. June, 2004. `http://seal.web.cern.ch/seal/documents/minuit/mnusersguide.pdf`.

[71] H. Akima. *A New Method of Interpolation and Smooth Curve Fitting Based on Local Procedures*. October, 1970. Journal of the ACM, 17(4):589-602.

[72] ATLAS Collaboration. *Rapidity gap cross sections measured with the ATLAS detector in pp collisions at* $\sqrt{s} = 7$ *TeV*. Eur.Phys.J. C72 1926, 2012. `[arXiv:1201.2808v2 [hep-ex]]`.

[73] M. Diehl and O. Nachtmann. *Optimal observables for the measurement of three gauge boson couplings in* $e^+e^- \to W^+W^-$. September, 1994. Phys. C - Particles and Fields (1994) 62: 397. doi:10.1007/BF01555899.

[74] M. Dobbs. *Probing the Three Gauge-boson Couplings in* 14 *TeV Proton-Proton Collisions*. April, 2002. PhD Thesis, University of Victoria. CERN-THESIS-2002-048. `[CDS:613333]`.

[75] R. J. Barlow. *Statistics: A Guide to the Use of Statistical Methods in the Physical Sciences*. John Wiley and Sons, Ltd, Reprinted, 1999.

[76] ATLAS DCS Data Viewer. `https://atlas-ddv.cern.ch/DDV.html`.

[77] ATLAS Collaboration. *Charged-particle multiplicities in pp interactions measured with the ATLAS detector at the LHC*. February, 2011. New J. Phys. 13:053033, 2011. `[arXiv:1012.5104v2 [hep-ex]]`.

[78] T. T. Böhlen, F. Cerutti, M. P. W. Chin, A. Fassò, A. Ferrari, P. G. Ortega, A. Mairani, P. R. Sala, G. Smirnov and V. Vlachoudis. *The FLUKA Code: Developments and Challenges for High Energy and Medical Applications*. Nuclear Data Sheets 120, 211-214 (2014).

[79] A. Ferrari, P. R. Sala, A. Fassò, and J. Ranft. *FLUKA: a multi-particle transport code*. CERN-2005-10 (2005), INFN/TC_05/11, SLAC-R-773.

[80] Sara Diglio on behalf of the ATLAS Collaboration. *The ATLAS Forward Physics Program*. December, 2013. ATL-GEN-PROC-2013-005. `[CDS:1639613]`.

[81] M. A. Medici. *Diffraction with ALFA and ATLAS at* $\sqrt{s} = 8$ *TeV*. August, 2013. Master's Thesis, Niels Bohr Institute, University of Copenhagen.

[82] CHLM Collaboration. *Inelastic diffractive scattering at the CERN ISR*. January, 1976. Nucl. Phys. B108 (1976) 1-29. [inSPIRE:3424].

[83] UA4 Collaboration. *Single diffraction dissociation at the CERN SPS collider*. December, 1983. Phys. Lett. 136B (1984) 217-220. [inSPIRE:194837].

[84] The TOTEM Collaboration. *The TOTEM Experiment at the CERN Large Hadron Collider*. 2008 JINST 3 S08007.